La collana della Scuola di Alta Formazione Dottorale accoglie le migliori tesi di dottorato dell'Università degli Studi di Bergamo, insignite della dignità di stampa e sottoposte a procedura di *blind peer review*.

The present publication aspires to be a comprehensive research on the main aspects of open-wheeled racing car aerodynamics. Starting from the comprehension of ground effect principles, the work moves towards the simulation of a modern F1 car. The vehicle aerodynamics is numerically investigated from many points of view: different setups and operating conditions are taken into account in order to fully characterize the behaviour of the vehicle and evidence any possible critical aspects. The considered 2017 F1 car, as expression of current FIA Technical Regulations, has proved to be poorly suited to working in slipstream: as a result, both the approach to a vehicle ahead and the overtaking manoeuvre are difficult and unsafe. In light of this, the core of the research is directed towards the aerodynamic development of the original car, with the aim of improving its performance both in freestream and, above all, in wake flows.

Umberto Ravelli graduated in Automotive Engineering in 2013 from the University of Modena and Reggio Emilia with full marks and honours. After a brief working experience in motorsport industry, he moved to the University of Bergamo, where he received the Ph. D. in Engineering and Applied Sciences (2019 - XXXI cycle): the focus of the research activity was on designing aero components and investigating new solutions for improving the performance of a F1 car, both in freestream and wake flows. He is currently teaching Flight Mechanics in a technical college.

ISBN: 978-88-97413-38-7
DOI: 10.6092/978-88-97413-38-7

Umberto Ravelli AERODYNAMICS OF A 2017 FORMULA 1 CAR

21

Collana della Scuola di Alta Formazione Dottorale
- 21 -

Umberto Ravelli

AERODYNAMICS OF A 2017 FORMULA 1 CAR
Design Improvements in Freestream and Wake Flows

UNIVERSITÀ
DEGLI STUDI
DI BERGAMO

2021

Collana della Scuola di Alta Formazione Dottorale

- 21 -

Collana della Scuola di Alta Formazione Dottorale

Diretta da Paolo Cesaretti

Ogni volume è sottoposto a *blind peer review*.

ISSN: 2611-9927

Sito web: https://aisberg.unibg.it/handle/10446/130100

Umberto Ravelli

AERODYNAMICS OF A 2017 FORMULA 1 CAR
Design Improvements in Freestream and Wake Flows

Università degli Studi di Bergamo

2021

Aerodynamics of a 2017 Formula 1 Car: Design Improvements in
Freestream and Wake Flows /
Umberto Ravelli. – Bergamo :
Università degli Studi di Bergamo, 2021.
(Collana della Scuola di Alta Formazione Dottorale; 21)

ISBN: 978-88-97413-38-7
DOI: 10.6092/978-88-97413-38-7

Progetto grafico: Servizi Editoriali – Università degli Studi di Bergamo

via Salvecchio, 19
24129 Bergamo
Cod. Fiscale 80004350163
P. IVA 01612800167

https://aisberg.unibg.it/handle/10446/175304

Acknowledgements

The first thanks are addressed to my academic supervisor, Prof. Marco Savini, who gave me the freedom to work on unusual research topics, such as ground effect aerodynamics and racing cars.

We acknowledge the CINECA award under the LISA initiative, for the availability of high-performance computing resources and support.

Special thanks to Nicolas Perrin and his team for sharing their F1 project.

I am grateful to ©OptimumG for providing the lap-time simulation software OptimumLap.

I also would like to thank the F1 aerodynamicist Willem Toet, with whom I exchanged ideas in the last part of my research.

At last but not at least, my gratitude goes to my family, for the constant support.

“Beh, se ce lo consiglia Varzi, prendiamolo pure questo Tazio Nuvolari.
E che Dio ce la mandi buona.”
Vittorio Jano, Alfa Romeo designer

Table of contents

Introduction

In this publication an extensive numerical analysis of open-wheeled racing car aerodynamics is presented. The whole CFD workflow, from meshing to calculation, was carried out by the open-source software OpenFOAM®, in the steady RANS framework. After investigating the mechanisms behind ground effect by means of simple test cases, including a diffuser-equipped blunt body and a single element wing, attention was focused on the 2017 Formula 1 car designed by the British constructor ©PERRINN. The validation of the numerical results in terms of drag, downforce, efficiency and front balance was accompanied by a qualitative study of the flow around the car. Axial vorticity plays a key role in the generation of downforce and the use of ground effect improves the efficiency of the overall vehicle. In the second step of the research, it was found that front and rear ride height have a strong influence on the dynamic behaviour of the car. Since racing implies a close interaction with other vehicles, the core of the research was devoted to evaluation and subsequent improvement of aerodynamic performance in wake flows. Tandem-running simulations at different distances between lead and following cars put in evidence that running in slipstream results in a strong worsening of downforce and a dramatic change in front balance.

To overcome these limitations, the baseline vehicle was subjected to a targeted aerodynamic development. Among the tested aero packages, one in particular provided encouraging results: it ensures higher downforce and efficiency than the baseline configuration while fulfilling, at the same time, the goal of reducing the above-mentioned performance worsening in slipstream. The concepts behind the effectiveness of the new design deal with a better management of the chaotic flow underneath the car; moreover, underbody and rear wing adjustments contribute to generation of a shorter and narrower wake. Overall, an easier approach to the lead car and a safer overtaking could be achieved through small modifications to 2017 F1 Technical Regulations, without disrupting the current F1 car layout. As a further check of the robustness of the new design proposals, all the developed aerodynamic configurations have been tested in yawed flow. Finally, the last section of the research aimed at quantifying the lap-time performance of the vehicles equipped with the new aero packages, since each track requires specific levels of downforce and efficiency. Results in terms of aerodynamic specifications are in line with those typically encountered in current F1 grand prix races.

Chapter 1. State of the Art and Overall Plan

The present publication aspires to be a comprehensive research on the main aspects of open-wheeled racing car aerodynamics. Starting from the comprehension of ground effect principles, the work moves towards the simulation of a modern F1 car. The vehicle aerodynamics is numerically investigated from many points of view: different setups and operating conditions are taken into account in order to fully characterize the behaviour of the vehicle and evidence any possible critical aspects.

The considered 2017 F1 car, as expression of current FIA Technical Regulations, has proved to be poorly suited to working in slipstream: as a result, both the approach to a vehicle ahead and the overtaking manoeuvre are difficult and unsafe. In light of this, the core of the research is directed towards the aerodynamic development of the original car, with the aim of improving its performance both in freestream and, above all, in wake flows. Further indications about driveability and safety of the new aerodynamic configurations have been attained by means of sideslip angle analysis.

The entire numerical analysis has been conducted through steady RANS calculations, carried out by the open-source software OpenFOAM®. The meshing procedure for complex and realistic geometries was found to suffer from some criticalities, such as the layer addition algorithm, but it allows for high-level automation in creating meshes for different test cases; concerning the fluid dynamic simulation, it can be said that a high degree of freedom in the numerical setup goes hand in hand with greater difficulties in interpreting the final results. Nevertheless, OpenFOAM® was chosen for facilitating the repeatability of the simulations and filling the gap between academic and industrial research, which usually deals with commercial codes.

The original contribution of this research, compared to published literature, lies in the analysis of a complex industrial topic by means of research approaches typical of the academic world: consolidated theoretical know-how and empirical evidences were used to develop, test and integrate new aero devices, for the purpose of improving F1 car aerodynamics in slipstream, both in terms of safety and pure performance.

Nevertheless, for further development, it would be desirable to have access to experimentally measured performance for validation purposes, in order to reach definitive conclusions on the behaviour of complex aero devices in different operative conditions, within the strict limits imposed by the protection of industrial secrets.

1.1 State of the Art

1.1.1 Ground Effect Aerodynamics

Investigation of ground effect aerodynamics is crucial in automotive industry, in order to improve performance of road vehicles and racing cars. Over the past 50 years, this branch of aerodynamics has considerably grown, thanks to wind tunnel testing first and then to computational fluid dynamics (CFD), involving both automotive industry and universities.

In the ‘80s, the benefits of using ground effect to improve downforce were already known by F1 engineers. Wright (1982), director of Team Lotus International, summarized the features of the ground effect Formula 1 cars of that era: special attention had been given to the relationship between ground clearance and lift coefficient. As a result, development of the car underbody focused on achieving the highest possible negative lift at the highest possible lift/drag ratio [Wright, (1982), p.389]. The progress made from the late ‘70s to the early 2000’s in aerodynamics of open-wheel race cars is well described by Zhang et al. (2006): despite numerous changes in technical regulations (Figure 1), the ground effect components of the vehicle, such as step plane and diffuser, still play a crucial role in generating downforce and they are much more efficient than other aerodynamic devices (for instance the rear wing).

Owing to geometry complexity, interaction between different components and variability of the operating conditions, race cars are characterized by tricky flow physics: the analysis of individual components, such as diffuser and front wing, is a prerequisite towards a better insight into the overall flow field and the entire vehicle design (Zhang et al., 2006).

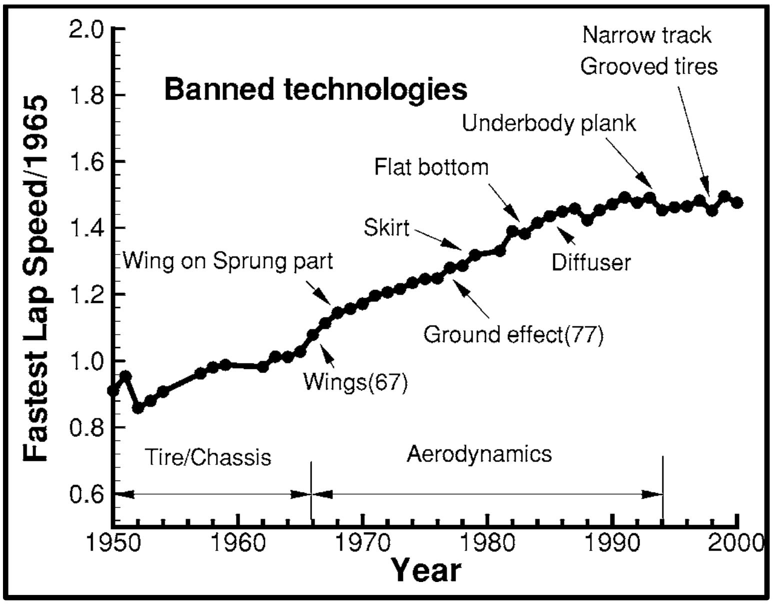

Figure 1: An example of average race speed evolution since 1965 (Zhang et al., 2006)

1.1.2 Experiments on Blunt Bodies

Ground effect aerodynamics of road-vehicle-related blunt bodies was investigated experimentally by George (1981). Detailed data about lift, drag, pitching moment were measured in different conditions: with and without simulated wheels, underbody roughness, proximity to a stationary or moving ground. The results showed that these variables have a strong influence on the aerodynamic performance of the vehicle, so they should be carefully kept into account during the design process. Three types of flows are typical of this kind of bodies: fully attached flow, reversed delta wing-type vortices and separation with presence of recirculation zones.

Two years later, the same author focused on the flow field under Venturi-type bodies, which was found to be highly three-dimensional: the longitudinal vortices under the body help to prevent two-dimensional separation. The optimum ground clearance for generating downforce should be that required to take advantage of both the Venturi effect and the longitudinal vortices in order to keep the diffuser flow attached. This optimum height is larger for larger angle of the diffuser, because more lateral inflow is needed to generate stronger vortices (George and Donis, 1983).

In recent years, research into blunt body aerodynamics has accelerated owing to the need to improve aerodynamic performance of modern vehicles in terms of stability and fuel consumption. A lot of researchers from Southampton University put their efforts into the understanding of vortex structures underneath the diffuser (Mahon et al., 2004) and behind the bluff body (Zhang et al., 2004). In the former paper, it was concluded that edge vortices enhance the downforce as the ride height is reduced until a maximum value of downforce is achieved (Figure 2a). The latter paper contains a detailed investigation about the variation of downforce as function of the diffuser-equipped blunt body ride height: four regions can be identified, as shown in Figure 2b. In the force enhancement region (a), a pair of contra-rotating vortices exists in the cross-plane between the upswept surface and the ground. In the force plateau region (b) the vortices increase in size, but their strength is weakened. The force reduction region (c) is characterised by vortex breakdown whereas the diffuser is starved of mass flow in the loss of downforce region (d). These experimental studies put in evidence that similar blunt bodies in ground effect can show very different downforce trends depending on the amplitude of the diffuser angle and the presence or absence of endplates: one of the major differences consists in the presence of an hysteresis in the force reduction region, mainly caused by a combination of flow separation and vortex breakdown (Figure 2b).

Jowsey and Passmore (2013) carried out an extensive research on diffuser equipped blunt bodies in ground effect. Particular attention was given to the link between the diffuser angle and the lift coefficient: the optimum value for the downforce lies between 13° and 16°, where a local flow separation can be observed at the diffuser inlet. The downforce starts decreasing above 16° and the diffuser is stalled over 25°. Improvement of downforce with minimal increase in drag can be observed with multiple channel diffusers, especially in the range 16°-19°. Cogotti (1998) carried out a detailed examination on a full-scale simplified car model: different wheels, various ground clearances and four wind tunnel configurations were tested (moving ground and rotating wheels, moving ground only, rotating wheels only, all static).

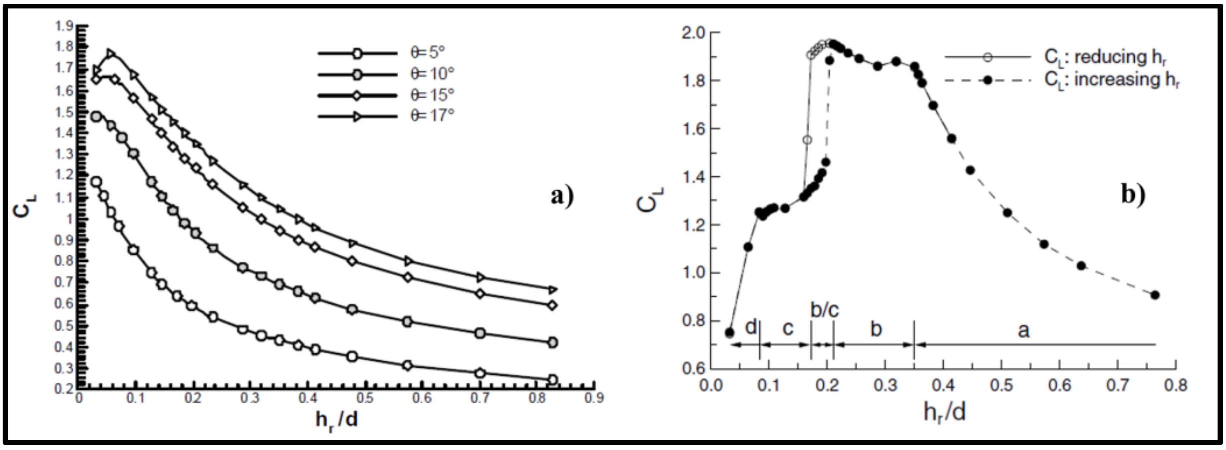

Figure 2: Lift coefficient of the body as function of dimensionless ride height: a) Mahon et al., 2004, b) Zhang et al., 2004

The influence of the floor on wind tunnel simulations has been investigated by several researchers. Carr (1988) came to the conclusion that vehicle models with low ground clearance and a smooth diffuser-equipped underbody develop higher downforce when tested with a moving ground instead of with a stationary wind-tunnel floor. In the paper by Howell and Hickman (1997) it was established that the fixed floor is inadequate, especially when accuracy in drag measurement is needed. An estimation of the difference between moving ground and fixed ground measurement was provided by Bearman et al. (1988): floor movement increases downforce by about 30% and reduces drag by 8% on one-third scale passenger car models.

1.1.3 Experiments on Slender Bodies

In recent years, several experiments on downforce-generating wings in ground effect were carried out at Southampton University. At first, performance characteristics and flowfield phenomena of a single element wing were investigated (Zerihan and Zhang, 2000): the collected data showed that a reduction of the wing ride height leads to higher level of downforce. This trend continues until the ground clearance is less than 20% of the chord. Closer to the ground (less than 10% of the chord) the wing stalls and the downforce drops. In two subsequent papers, the effects of Gurney flaps (Zerihan and Zhang, 2001) and tip vortices (Zhang et al., 2002) on downforce were studied by means of different experimental methods, including particle image velocimetry (PIV), laser Doppler anemometry (LDA), pressure and force balance measurements as well as surface flow visualization. Afterwards the attention was focused on multi element wings. The interaction between the main element and the flap is crucial in determining the performance of the entire wing. As shown in Figure 3, three regions can be identified on the downforce-vs-height curve (Zhang and Zerihan, 2003): as the wing is moved from the freestream toward the ground, the downforce rapidly increases (region a) and the flow is characterized by the tip vortex off the edge of the side plate; the increase in downforce continues, until the edge vortex breaks down at a critical height (region b); below the ride height where the maximum downforce is reached, the flow massively separates and the downforce is reduced (region c).

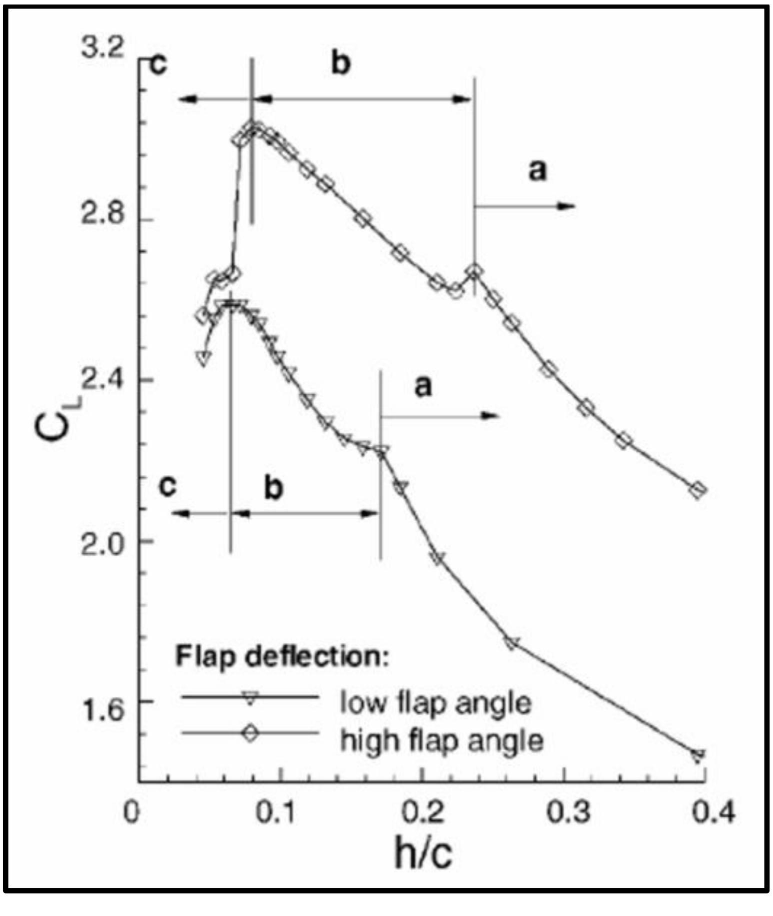

Figure 3: Lift coefficient of the double element wing as function of dimensionless ride height (Zhang and Zerihan, 2003)

Another paper from Southampton University (Kuya et al., 2009) investigated the implementation of vortex generators for separation control on the suction side of the wing in ground effect. Counter-rotating and co-rotating configurations of vortex generators were tested: the former suppresses flow separation at the centre of each device pair whereas the latter induces horseshoe vortices between each device, where the flow is separated.

In recent years, aerodynamics of wings in ground effect has been investigated in realistic on-track conditions, including roll, yaw and immersion in the wake of a leading car. It was found that small roll angles (< 3°) can increase downforce and small yaw angles (< 5°) cause a small decrease in downforce and increase in drag; on the contrary, a wing operating in wake flow suffers from a significant reduction in downforce (Correia, 2016).

1.1.4 Experiments on Scale Models and Real Vehicles

The overall features of vehicle aerodynamics are often measured and analysed by means of scale-model testing, to limit fan power requirements and running costs. These savings allow car manufacturers to invest in advanced testing techniques, such as “adaptive wall technology”: the shape of the test section automatically changes in response to the pressure measured along the tunnel walls, in order to reduce the so-called “blockage effect” (McBeath, 2006).

However, experimental research on vehicle aerodynamics does not confine itself to studying simplified scale models: the very first example of full-scale wind tunnel dedicated to real vehicle investigations was built in 1939, near Stuttgart, under the direction of W. Kamm. Low-blockage test section and high velocity flow are advantageous for the development of fast vehicles, for instance race cars, even when Reynolds number effects are no longer expected (Hucho et al., 1998).

1.1.5 The Role of CFD in Vehicle Aerodynamics

While the advent and progress of the computer industry, computational fluid dynamics (CFD) began to support wind tunnel testing. The increasing success of CFD is prompted by some of its interesting peculiarities. CFD solution of the physical-mathematical model is almost always faster and cheaper than experimental testing; moreover, in CFD, all non-dimensional quantities can be exactly matched, while experiments generally try to match the Reynolds Number regime (Linfield and Mudry, 2008).

One of the areas where CFD has reached its highest peak is motorsport: on the one hand, aerodynamic simulations are crucial for designing and developing increasingly fast vehicles; on the other hand, the extreme research of performance in motor racing is the catalyst behind the development of sophisticated and reliable numerical procedures and innovative Computer Aided Design (CAE) tools. Looking at the Formula 1 experience during the period from 1990 to 2010, simulations evolved from the inviscid panel method to 1 billion cell calculations of entire cars, including analysis of transient behaviour and overtaking (Hanna, 2012). Nowadays CFD and wind tunnels are used together in a synergic iterative process where one technique fills the gaps left by the other: in fact, in certain areas, computed and measured results may differ and it is not clear which provides the best real-world results (Linfield and Mudry, 2008). As witnessed by the Swiss Formula 1 team Sauber Motorsport AG, the CFD technology is applied in many stages of the car development: early concept phase, engine and brake cooling, single component design and complete system design and interactions (Larsson et al., 2005).

From the point of view of the required computational resources, the complexity of the geometry and the resulting numerical issues, the simulation of realistic open-wheeled cars is really challenging. For this reason, F1 teams, car manufacturers and researchers often rely on commercial software that provide user-friendliness, flexibility and reliability: the longer you spend time on pre-processing and debugging, the lesser you can focus on design and physics comprehension. Examples of these studies can be found in the following papers by Perry and Marshall (2008), Larsson (2009) and Chandra et al. (2011): in the first two works, ANSYS software package is used to investigate the impact of 2009 FIA technical regulations on the aerodynamic performance of F1 cars, while the last work puts in evidence the capability of StarCCM+ tools in the managing of complex surfaces, including overlapping edges, non-manifold surfaces, holes, and gaps. The use of commercial packages is worthwhile in the case of complicated procedures, such as aerodynamic optimization, which require reliable algorithms (Zaya, 2013) and interaction between different softwares (Lombardi et al., 2009).

In addition to CFD commercial solutions, there are open-source codes able to execute both the meshing phase and the fluid dynamic calculation: one of the most popular is OpenFOAM®. This free-license tool is successfully used and developed by academic researchers (Nebenführ, 2010) and automotive industries (Islam et al., 2009) in order to predict the aerodynamic performance of road cars. However, due to some criticalities connected to meshing accuracy and numerical stability, it is not widespread in high level motorsport applications.

1.2 Overall Plan

The preliminary stage of the work consists in understanding the basics of diffuser-equipped blunt bodies and inverted wings in ground effect: both were tested at different ride heights and diffuser angles/angles of attack. In this respect, experimental data from Loughborough and Southampton University were taken into account, in order to validate drag and lift coefficients provided by incompressible RANS-type simulations. Some important conclusions were obtained: the k-ωSST turbulence model provides better predictions of blunt body flow fields; conversely, the Spalart-Allmaras (S-A) model produces more accurate results when applied to slender bodies. From a numerical point of view, the coupled solver was found to be faster and more reliable than the segregated one, at the expense of greater computational effort. From a physical point of view, the qualitative results of the simulations put in evidence typical three-dimensional vortical structures characterizing the behaviour of downforce generating devices and other fluid-dynamic phenomena such as separation in adverse pressure gradient and viscous effects.

The next step of the research is devoted to applying the above described learnings on numerical modelling to a realistic open-wheeled racing car: the 2017 F1 vehicle designed by ©PERRINN was designated for this purpose. Despite some geometrical simplifications related to internal flows, the 3D model maintained all the features and the details characterizing its external aerodynamics. The complexity of the geometry made it necessary to develop a complex and reliable CFD procedure, including CAD cleaning, surface and volume mesh automatization, simulation setup and post-processing. The S-A turbulence model provided the best matching with the reference performance coefficients provided by ©PERRINN: drag, downforce, front balance and efficiency predictions were calculated with less than 10% margin of error. The study of the single components showed that front and rear wing contribute more or less to a quarter of total downforce each; the remaining percentage is attributable in large part to the underfloor. The latter component, consisting of step plane, plank and diffuser, was found to be very efficient, due to the use of Venturi and ground effects. The tyres are the mains source of pressure drag, whilst the rear wing is the main responsible for induced drag. The post-processing activity showed that production of axial vorticity is one of the most important mechanisms for generation of downforce: in this respect, the front wing plays a key role in controlling the downstream flow.

The second step of the PERRINN F1 car analysis was to investigate the influence of front and rear ride height on aerodynamic performance. The simulation outputs demonstrated that small setup modifications (within a range of 15 mm on the front and 10 mm on the rear), lead to substantial downforce improvements and increase in front balance (> 5%) at the cost of negligible extra-drag. Lower front ride height allows the front wing to better exploit the benefits of ground effect, whilst a parallel increase in rear ride height leads to a greater area ratio of the underfloor. To sum up, increase in rake angle results in higher values of downforce and front balance, so long as the flow underneath the car does not separate because of the adverse pressure gradient.

After analysing the ©PERRINN F1 car under ideal operating conditions, the focus was shifted to its aerodynamic behaviour in slipstream. This particular off-design circumstance is really common during a race and heavily influences driveability and safety. Two vehicles were tested at four different distances in order to evaluate the performance losses affecting the following car. The results of the tandem-running simulations testified that 2017 Technical Regulations did not resolve the controversial issue of overtaking. In proximity to the leader, the following car loses more than half of the overall downforce and is subjected to a serious increase in front balance, undermining braking effectiveness and vehicle stability in high-speed corners. Also, the approach to the leader is difficult, because running in wake flow weakens the performance of the following cars over long distances (> 20 m). Unfortunately, the benefits resulting from drag reduction on long straights are not able to counterbalance the above described criticalities. Looking deeper into the performance results, it can be noted that the front wing suffers much less than other aerodynamic devices from working in slipstream: rear wing performance constantly deteriorate during the approach phase, while the underfloor evidences an abrupt downforce loss in close proximity to the lead vehicle. The qualitative analysis of the results confirmed that the following car is fed by low-energy, rotational flow, whose streamlines diverted from the original direction: therefore, most of the axial vortical structures responsible for the generation of downforce are heavily weakened.

At this point, the research moved to a higher level: efforts focused on aerodynamic development of the baseline vehicle, for the purpose of improving aerodynamic performance both in freestream and wake flows by means of cheap, targeted and readily applicable changes. Different devices were designed, tested and integrated on the car: in light of the previous results, the front wing was modified in accordance with the 2017 Technical Regulations, whilst underfloor, rear wing and other bodywork components underwent several adjustments: some of them are inspired by the past, while others are completely original, thus constituting the most relevant contribution to the current state-of-the-art. Three different aerodynamic configurations were obtained, in order to meet the performance requirements of low, medium and high-downforce tracks. All three new aerodynamic packages simultaneously improved efficiency and downforce of the original car: the low-downforce vehicle (F1UR4LD) is characterized by the highest efficiency (+13% compared to the baseline), while the high-downforce layout (F1UR4HD) enhanced the level of available downforce by 48%; the medium-downforce vehicle (F1UR4MD) is instead a compromise solution between the above described configurations.

The analysis of the conceived vehicles in freestream was followed by a detailed performance evaluation in wake flow. In fact, the main goal of the new aerodynamic configurations was to make current F1 cars safer and more performing in slipstream. All the considered advanced layouts proved to be more robust than the baseline in terms of downforce loss; nevertheless, low and medium downforce vehicles, as well as the first version of the car, suffer from unacceptable front balance variations. The high-downforce vehicle, instead, showed much better performance than the original one: when the distance from the lead car is about 2.5 m, the front balance increase goes from +20% to +14%, the downforce loss from -53% to -39% and the efficiency loss from -30% to -

22%. The results are even better for greater distances, making the approaching phase much easier: when the distance between the two vehicles is about 5.5 m, the downforce loss goes from -44% to -25%, the front balance increase from +34% to +12% and the efficiency loss from -30% to -13%. At a distance of about 11 m, the downforce loss goes from -25% to -12%, the front balance increase from +20% to +5% and the efficiency loss from -13% to -6%.

These encouraging results can be attributed to specific features of the design. The entire bodywork was equipped with several aerodynamic add-ons, in order to achieve a more uniform distribution of the downforce sources. The underbody was made more suitable for working with low-energy and chaotic flow, by means of specific devices restoring the low-pressure cores on the bottom of the car (vortex generators at the step plane inlet and a convergent guide vane in correspondence of the diffuser). In addition, the above described devices have the important function of narrowing the underbody wake in span direction. The interaction between the new three-element rear wing and the supplementary beam wing enhances the diffuser extraction, preventing flow separation; apart from that, the new rear wing assembly, in cooperation with tyre ramps and T-wings, shields the following car against the underbody low-energy flow by means of a strong upward deflection: as a consequence, the resulting wake is very short. To summarize, a narrow and short wake ensures that clean and high-energy flow is able to fill the gap between the two vehicles and reach the following car more easily.

Besides the slipstream off-design condition, racing cars are continually exposed to direction changes. During cornering the flow is not perfectly aligned with the car, generating the so-called sideslip angle: in racing applications its value is similar to the tyre slip angle (5°÷8°). The baseline vehicle and the three new configurations were tested in the above described conditions so as to evaluate their capability of providing adequate aerodynamic performance and measure the newly generated side force. To stress the vehicles in critical circumstances, high values of sideslip angle (10° and 20°) were set up in the numerical simulations. At worst, the downforce decrease related to the new aerodynamic configurations is about 10%, whereas the original car is subject to a 15% loss in vertical load. Most importantly, the cornering stability of the new vehicles can benefit from a constant or decreasing front balance. The monitoring of the side force indicated that its magnitude increases in parallel with the sideslip angle and the downforce level of the vehicle, up to 24% of the total drag. A deeper analysis of the results put in evidence the asymmetrical behaviour of the vehicle: the left and the right sides of the car are characterized by different values of front balance, provided that the respective centres of pressure tend to align with the freestream flow.

The last part of the research is not CFD-oriented but aims at evaluating the track performance of the new developed vehicles. OptimumLap, a free-software developed by the American company

©OptimumG, was used to perform lap-time simulations on different circuits of the F1 World Championship: making use of a quasi-steady-state point mass vehicle model, it was possible to match every track with the most suitable aerodynamic configuration. The model setup includes general vehicle data, aerodynamic coefficients, engine map, gear ratios and tyre parameters. With a few exceptions, it was found that performance of current F1 cars are “grip limited” rather than “power limited”: as a consequence, the best aerodynamic setup usually requires high levels of downforce in most of the considered tracks. At last, some of the most characteristic circuits were analysed in detail to evidence the influence of downforce on braking performance, lateral and longitudinal acceleration, cornering speed and top speed.

Chapter 2. Understanding the Basics of Racing Car Aerodynamics

The main purpose of this preliminary research is to assess the capability of OpenFOAM in predicting aerodynamic performance of blunt and slender devices for automotive and motorsport applications such as a diffuser-equipped blunt body and a F1 single element front wing in ground effect. Reynolds Averaged Navier-Stokes (RANS) simulations were carried out at different values of ride height and diffuser angle (α)/angle of attack (AOA): predictions of integral quantities such as drag (C_D) and lift (C_L) coefficients were validated against the available set of experimental data from Loughborough and Southampton Universities.

Pressure and velocity equations arising from the incompressible flow assumption were solved both with segregated and coupled approach, in order to achieve the best possible matching with experimental results in almost all cases of ground clearance (h) and diffuser angle.

The k-ωSST turbulence model was chosen for simulating the blunt body aerodynamics, owing to its documented capabilities in predicting this type of fluid flow. Concerning the front wing simulations, both k-ωSST and S-A turbulence models were employed and compared with each other.

2.1 Geometrical Features

The first step of the procedure consists in the virtual modelling of both the diffuser-equipped blunt body and the front wing. These CAD models are replicas of the wind tunnel bodies used for the experiments at Loughborough and Southampton University, respectively. Shape and dimension of the models under consideration are depicted in Figures 4 and 5.

The blunt body looks like a rectangular hexahedron: it is 0.8 m long, 0.4 m wide and its height is 0.31 m. The frontal area is characterized by bevels, whose radius is 0.064 m, in order to avoid massive premature flow separation. The diffuser region covers 25% of the body length, and it is bounded by 0.0125 m thick endplates (Jowsey and Passmore, 2010).

The wing is a component from the Tyrrell 026, the car with which the Tyrrell Formula One team competed in the 1998 Formula One season (Zerihan and Zhang, 2000). Chord and spanwise length are 0.2234 m and 1.1 m respectively, thus leading to an aspect ratio of about 4.9.

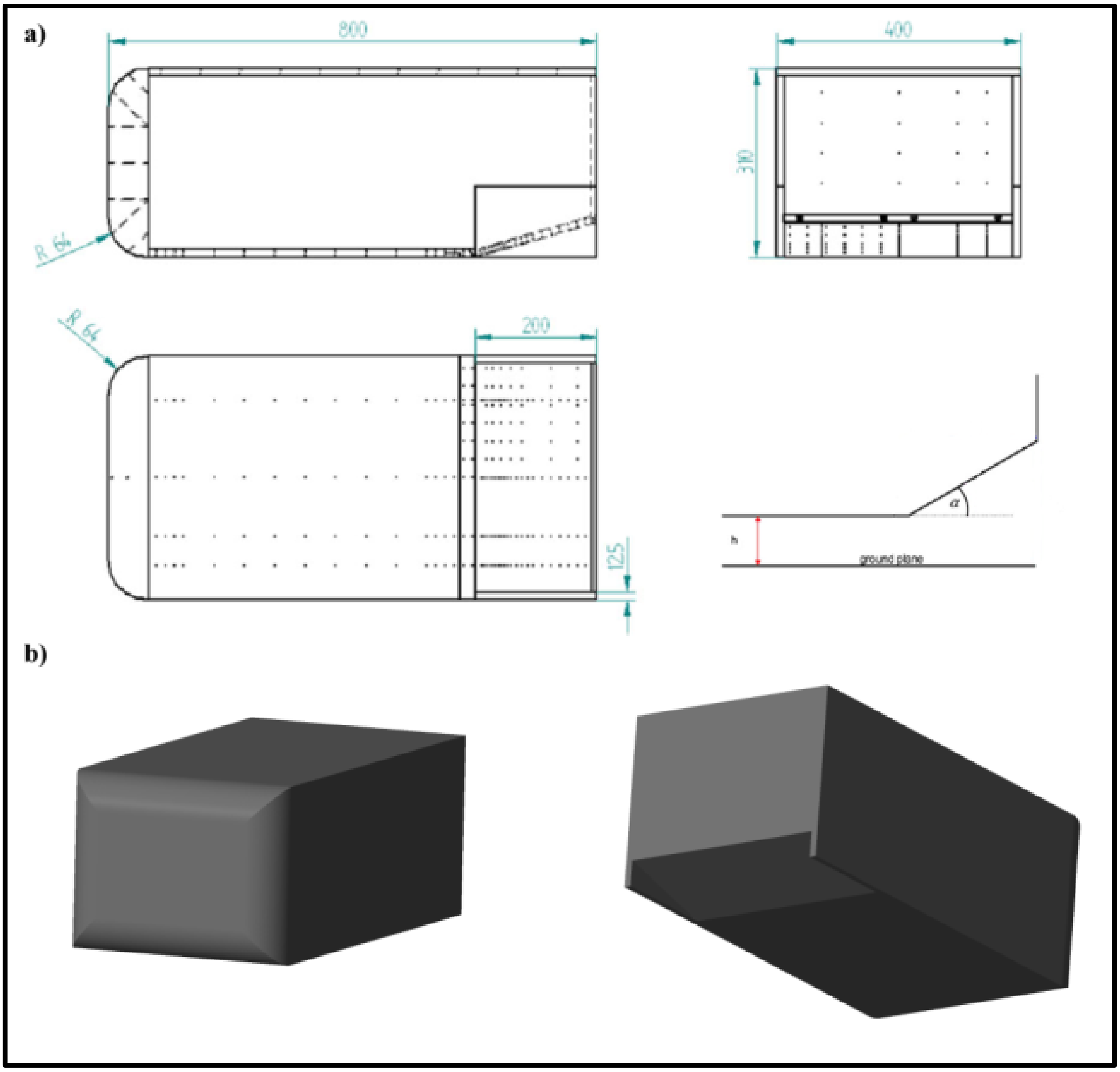

Figure 4: Blunt body model: a) technical drawing (Jowsey and Passmore, 2010) and b) 3D CAD model of the blunt body

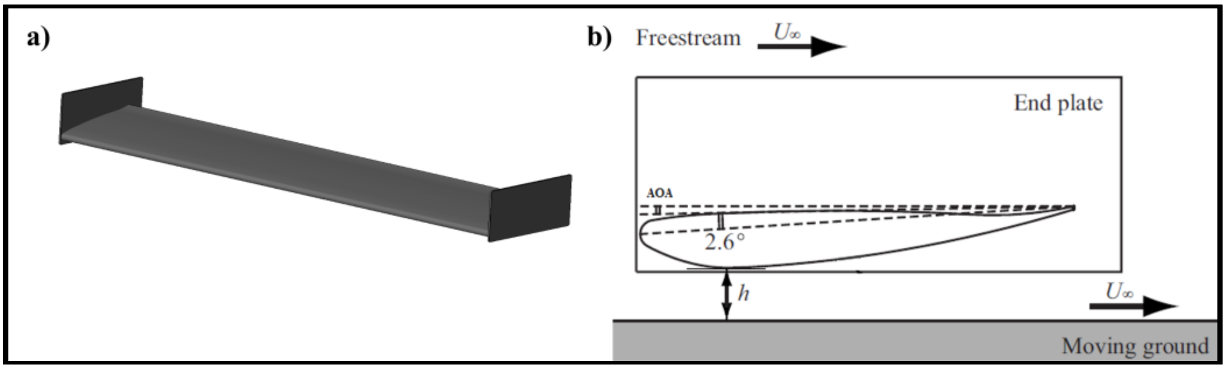

Figure 5: Wing model: a) 3D CAD model and b) drawing of the front wing (readjustment of image from Kuya et al., 2009)

2.2 Simulation Tools

The 3D CAD models need to be converted in STereoLithography format, in order to be processed by the OpenFoam meshing tool. The meshing utility, called SnappyHexMesh, allows for a non-graphical, fast and flexible procedure for every kind of geometry, especially in external aerodynamics applications. On the other hand, an untrained user might experience some difficulties in controlling layer addition and complex surface edges, due to serious issues of cell skewness and non-orthogonality. Thus, for a CFD beginner, grid generation by means of commercial software products might be easier to handle.

The fluid dynamic calculation was performed by means of OpenFOAM®: the choice fell on the most popular open-source CFD code, in order to facilitate the repeatability of the simulations and fill the gap between academic and industrial research, which often relies on commercial softwares. The software package is composed by a series of C++ libraries divided in two families: solvers and utilities (Nebenführ, 2010). Many degrees of freedom are available in the case setup: the user can decide time and space discretization schemes of the Navier-Stokes equation terms as well as the choice of the solver for each variable.

Both meshing and calculations were carried out using Galileo, the Italian Tier-1 cluster for industrial and public research, available at CINECA SCAI. The meshing processes were executed by means of 1 computational node, which is composed by 16 cores (8GB/core); the calculations were instead performed using 2 nodes.

2.3 Diffuser-Equipped Blunt Body

2.3.1 Mesh and Simulation Setup

The entire domain is about 6.5 times the length of the body. Height and width of the mesh comply with the size of the working section of the Loughborough University wind tunnel (1.92 x 1.32 m^2), in order to replicate the experimental conditions. The distance between the inlet and the frontal face of the body is about 1.5 times the body length (L). The outlet of the virtual wind tunnel was located well downstream the body (about 4 times the body length), so that atmospheric pressure could be reasonably imposed (Figure 6a). A few tests at the lowest ride height (28 mm) and the highest diffuser angle (13°) have been carried out to study the influence of side wall boundary condition on final results: the use of slip rather than wall condition did not alter the predictions of drag and lift coefficients. Therefore, the slip condition was chosen for the entire simulation set because allows us to save memory and CPU time in comparison to a boundary layer discretization. Moreover, since the ground of the wind tunnel was fixed, a boundary layer profile was imposed at the inlet section matching the published experimental values (Figure 6b). Table 1 summarizes the experimental conditions required to properly define the numerical setup (Jowsey and Passmore, 2010).

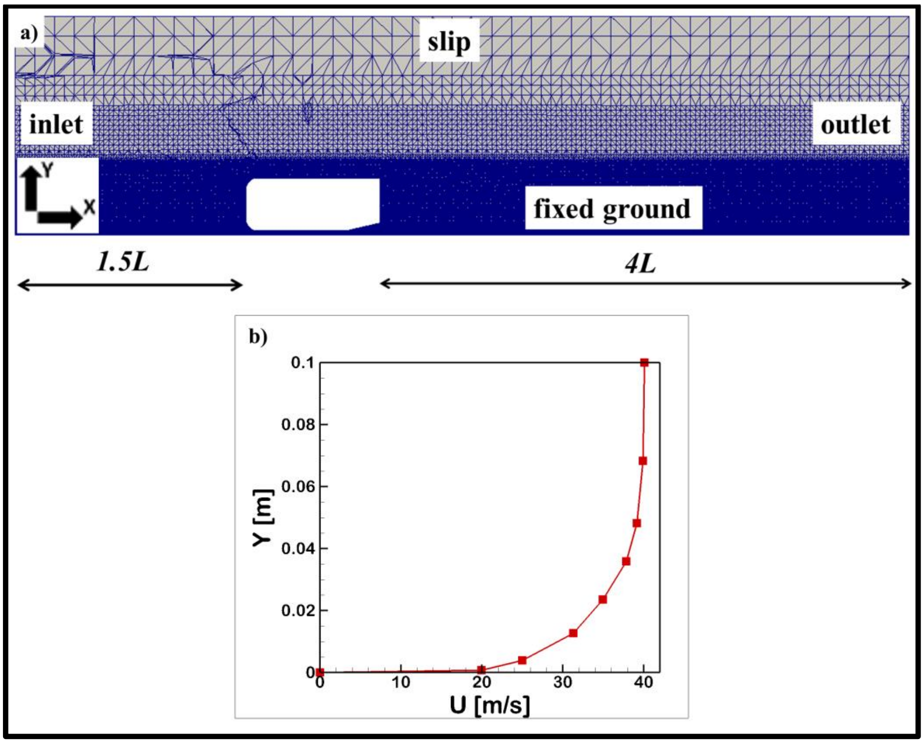

Figure 6: Mesh and inlet setup: a) midspan slice of the blunt body mesh and b) inlet boundary layer profile

The first mesh contained about 16 million cells. The height of the first cell at solid surfaces and the expansion ratio of the adjacent layers were 0.5 mm and 1.2, respectively, so as to obtain an average y^+ value in the first cell of about 30. In stagnation regions, such as the frontal area of the body, and in fully separated region, e.g. the rear base area, y^+ falls well below the average value. On streamlined surfaces, such as the underbody and the upper bodywork, the first cell is placed in the boundary layer log-law region ($y^+ > 30$). This mesh was refined around the body and behind it, to grasp the features of the wake flow and the ground boundary layer. Particular attention was given to the underbody and diffuser exit regions. The total CPU time for mesh creation, calculated as the product of the real-time and the number of required processors, was about 7.5 hours.

The chosen turbulence model was the k-ωSST (Menter, 1994) with high-Reynolds number wall treatment. Two turbulence variables are introduced: the turbulent kinetic energy (k) and the specific dissipation rate (ω). In short, this turbulence model is intended to offer the best of k-ω and k-ε models: it behaves like the k-ω model in the inner part of the boundary layer, and like the k-ε in the outer part close to the freestream. The performance of the low-Re option was also assessed: the increase in the computational effort due to mesh refining at the wall was not counterbalanced by any accuracy improvement, since C_D and C_L predictions were very similar to those obtained from the high-Re approach. Thanks to the data reported in Table 1, it was possible to set the inlet turbulence variables according to the formulas written in Table 2. The turbulence length scale (l_t) was assumed to be the diameter of the largest vortex in the flow, namely the height of the blunt body. Use of shorter inlet turbulence length scales, and hence higher values of ω, showed negligible differences in the results.

Symbol	*Parameter*	*Value*
ρ	Air density	1.165 kg/m^3
L	Characteristic length (body length)	0.8 m
U_∞	Freestream velocity	40 m/s
$Re_{(L)}$	Reynolds number	2.27 x 10^6
I	Turbulence intensity	0.15%
δ	Boundary layer thickness	0.06 m
δ_1	Displacement thickness	0.0094 m
δ_2	Momentum thickness	0.0055 m

Table 1: Experimental data necessary to setup the numerical simulation of the blunt body - data from Loughborough University (Jowsey and Passmore, 2010)

Symbol	*Turbulent Variable*	*Formula*	*Value*
k	Turbulent kinetic energy	$\frac{3}{2}(\mathrm{I}u_\infty)^2$	≈ 0.005 m^2/s^2
ω	Specific dissipation rate	$2.35\frac{\sqrt{k}}{l_t}$	≈ 0.5 1/s

Table 2: Inlet turbulence variables of the k-ωSST model – blunt body case

The simple algorithm (Semi-Implicit Method for Pressure-Linked Equations) available in OpenFOAM® was chosen, because it is suitable for incompressible, steady, turbulent flows (https://openfoamwiki.net). The GAMG (Geometric Algebraic Multi Grid) solver was employed for the pressure equation, whilst smoothSolver was used with velocity and turbulence variables. Approximately, the initial 500 iterations were executed with 1st order discretization whereas the remaining iterations were executed with 2nd order schemes. Gradient, divergence and Laplacian terms of the Navier-Stokes equations (written in differential form) were discretized by means of the Gauss scheme; at cell interfaces, the chosen interpolation scheme was linear (centred or upwind). Depending on the quality of the mesh, it is possible to select enhanced versions of the above-mentioned schemes both for scalars and vectors. The chosen convergence criteria were the following: the scaled pressure residual had to be lower than 10^{-5} and aerodynamic coefficients had to remain reasonably stable (± 1% in the last 200 iterations).

A 3x3 simulation pattern was carried out: each of the three diffuser angles (7°, 10°, 13°) was tested in three different ride heights (28 mm, 36 mm, 44 mm). Experimental and numerical data were compared in terms of drag and lift coefficients. Moreover, the same simulation pattern was replicated both with segregated and coupled solver, keeping the same turbulence model. On average, the CPU times required by segregated and coupled methods to reach convergence were 13.5 and 11 hours, respectively: every pseudo time-step executed by the coupled solver required more computational effort, but a smaller number of iterations were needed to complete the simulation. Mesh sensitivity was performed on the following cases: 13° - 44 mm and 13° - 28 mm. Two meshes with similar structure were tested, but with different levels of refinement (24.6 vs 16.5 million cells). Since drag and lift coefficients did not substantially change, the coarsest mesh was used for running the simulations.

2.3.2 Aerodynamic Performance

Once the most appropriate mesh has been established, every k-ωSST RANS simulation, performed with the segregated solver (seg.), was replicated with the coupled solver (cou.) and numerical outputs (num.) were compared to the experimental results (exp.). As shown in Tables 3, 4 and 5, the accuracy of predictions consistently improved, in particular in the most critical cases, i.e. low ground clearance and large diffuser angle: coupled calculations had average percentage error (e%) well below 5%, except for the 10° - 28 mm case.

		28 mm				
		exp.	*num.*		*e %*	
			seg.	*cou.*	*seg.*	*cou.*
7°	C_D	0.36	0.33	0.37	8.7	2.7
	C_L	-0.69	-0.72	-0.72	4.3	4.3
10°	C_D	0.38	0.36	0.40	5.4	5.1
	C_L	-0.87	-0.97	-0.95	10.9	8.8
13°	C_D	0.39	0.37	0.41	5.3	5.0
	C_L	-0.99	-1.14	-1.00	14.1	1.0

Table 3: Results of the blunt body simulations, h = 28 mm

		36 mm				
		exp.	*num.*		*e %*	
			seg.	*cou.*	*seg.*	*cou.*
7°	C_D	0.36	0.31	0.36	14.9	0
	C_L	-0.64	-0.64	-0.64	0	0
10°	C_D	0.37	0.34	0.38	8.5	2.7
	C_L	-0.80	-0.86	-0.84	7.2	4.9
13°	C_D	0.38	0.35	0.39	8.2	2.6
	C_L	-0.95	-1.05	-0.94	10.0	1.1

Table 4: Results of the blunt body simulations, h = 36 mm

		44 mm				
		exp.	*num.*		*e %*	
			seg.	*cou.*	*seg.*	*cou.*
7°	C_D	0.35	0.31	0.35	12.1	0
	C_L	-0.58	-0.58	-0.57	0	1.7
10°	C_D	0.36	0.32	0.36	11.8	0
	C_L	-0.73	-0.76	-0.75	4.0	2.7
13°	C_D	0.37	0.34	0.38	8.5	2.7
	C_L	-0.88	-0.94	-0.89	6.6	1.1

Table 5: Results of the blunt body simulations, h = 44 mm

Looking at the lift coefficient results of the 13° cases, the accuracy of the segregated method got worse as the ground clearance got smaller; on the contrary, the coupled method was found to be reliable at every ride height.

In Figure 7 the centre line pressure coefficient (C_P) distribution is plotted versus the non-dimensional body length (x/L), varying the ride height at fixed angle. In all cases the matching between numerical results and experimental data underneath the body is very good. Two peaks of negative relative pressure can be seen. The first minimum, which is located at $x/L \approx 0.05$, is due to the acceleration of the freestream flow at the entrance of the gap between the ground and the body; the second one, located at $x/L = 0.75$, is caused by suction around the diffuser.

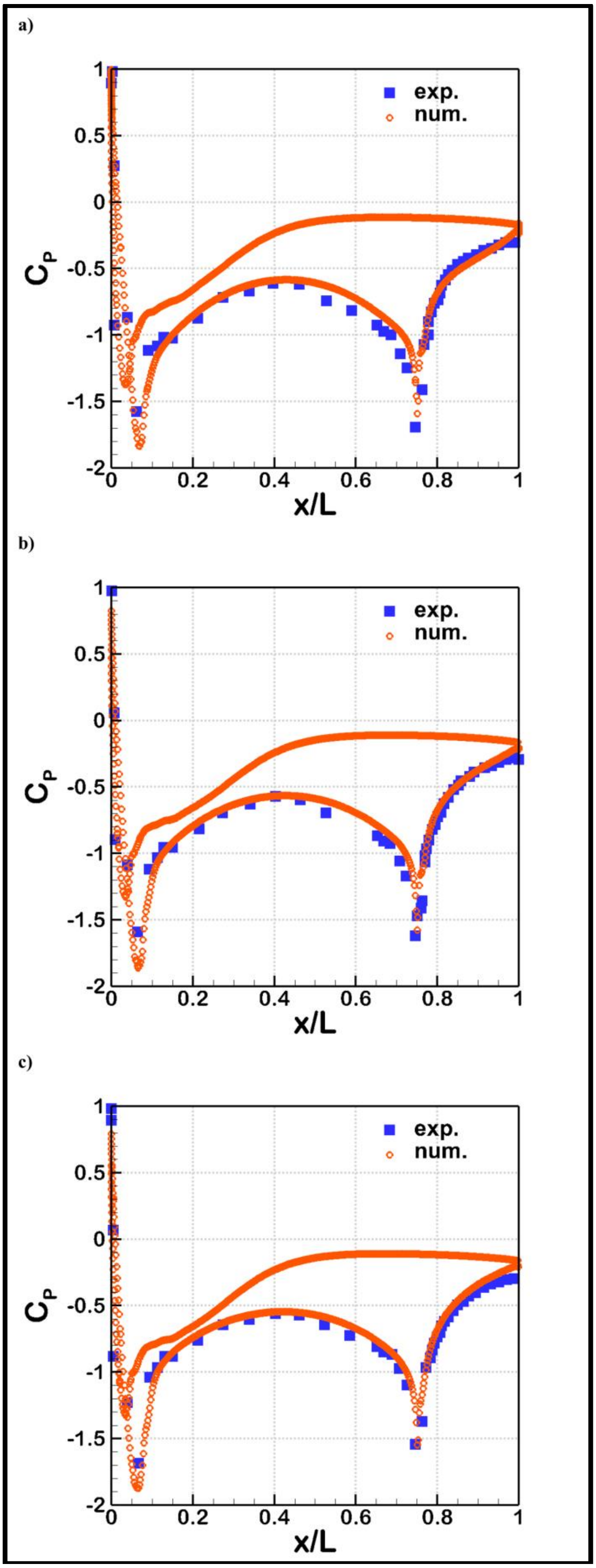

Figure 7: C_P as a function of x/L: a) α = 13°, h = 28 mm; b) α = 13°, h = 36 mm; c) α = 13°, h = 44 mm

The value of the second minimum of pressure is the main difference among the three cases: despite the diffuser angle is the same (13°), a smaller ground clearance determines a higher diffuser area ratio and, consequently, higher downforce, as long as there is no massive separation inside the diffuser.

In all three cases, slight discrepancy can be observed between experimental and numerical data at the diffuser exit (x/L=1): the k-ωSST RANS simulations overestimate the diffuser pressure recovery and, as a consequence, the base pressure of the blunt body at mid-span. In spite of this, the numerical predictions of C_D and C_L are really close to experimental measurements.

Figure 8 illustrates the streamwise velocity field at midspan. Some typical zones can be identified. The wake is in the same order of magnitude as the body height and occupies the base region: the value of the base pressure is the main cause of blunt body drag. At the leading edge the flow separates and generates a recirculation bubble on the body roof, leaving an enlarged boundary layer downstream. Right below the wake, there is the flow region identified by the diffuser extraction. If the associated boundary layer has enough kinetic energy to overcome the adverse pressure gradient, the flow remains attached to the diffuser surface; otherwise it separates and affects the performances of the underbody in terms of both drag and downforce.

Ahead of the stagnation area, a horseshoe vortex starts to envelop the body, as can be seen in Figures 9a, 10 and 11. Comparing the cases with same ground clearance and different diffuser angle, one can see how, increasing diffuser angle, the anticipated near-ground separation forces upward the flow coming from the diffuser, thereby shrinking the wake in the base region. Comparing the cases with same diffuser angle and different ground clearance, it can be observed that, for bigger ride heights, the extent of the rear wake is larger where the diffuser extraction is weaker. These two observations put in evidence that the fluid dynamic structures connected with downforce (flow coming from the underbody) interact with those linked with drag (wake in the base region).

More details about the wake can be observed in Figure 9b: the pressure contours show two cores of low-pressure behind the body. The streamlines confirm that the wake consists of two recirculation bubbles: the clockwise one comes from the upper side of the body whereas the counter-clockwise one derives from the upswept flow at the diffuser outlet. Moreover, the displacement induced by the diffuser flow can be noticed when looking at the upper streamline.

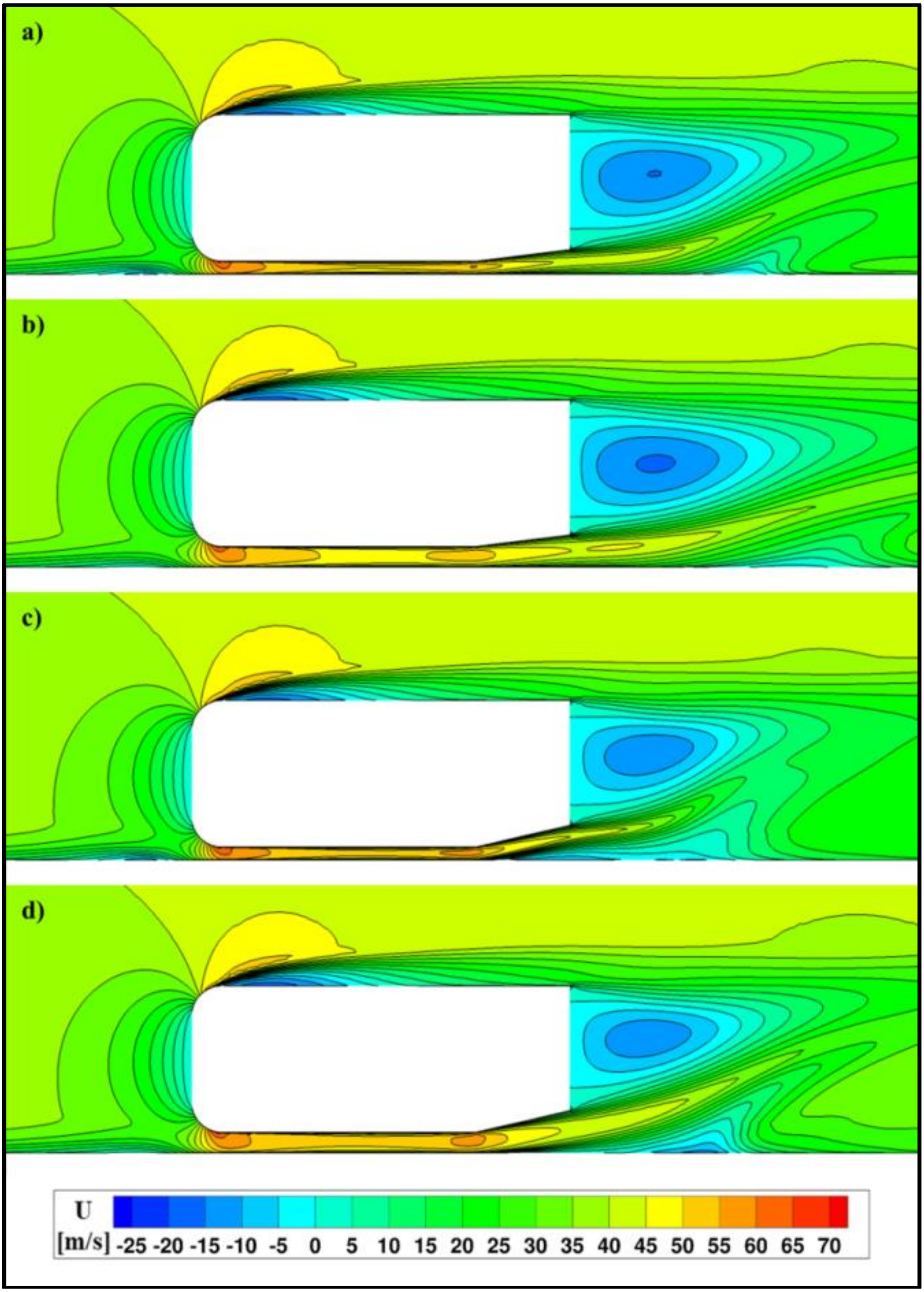

Figure 8: Streamwise velocity field at midspan: a) 7°, 28 mm; b) 7°, 44 mm; c) 13°, 28 mm; d) 13°, 44 mm

The rear views of the body show noteworthy axial vortices: Venturi vortices, strictly connected with the generation of downforce, and the horseshoe vortices, linked with the ground proximity of the body. Both axial vorticity (Figure 10) and Q-criterion (Figure 11) are useful for visualizing these structures. The iso-surfaces of the variable Q [$1/s^2$], the second invariant of the velocity gradient tensor, are good indicators of turbulent flow structures.

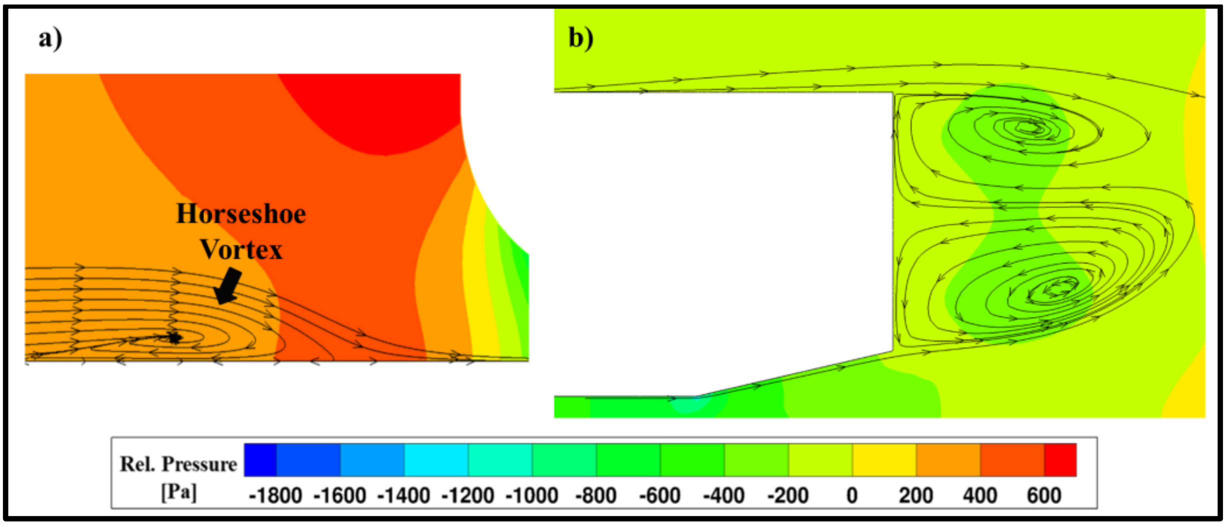

Figure 9: Pressure contours and streamlines at midspan (13°, 28 mm): a) Underbody inlet detail, b) Base region

The Venturi vortices begin to develop at the diffuser inlet because of the pressure difference between the underbody and the region at the side of the diffuser itself. They increase their energy along the diffuser sidewall and survive downstream of the diffuser. Close to every main vortex there is a secondary counter rotating structure due to the interaction with the ground boundary layer. As shown by the streamwise vorticity contours, a bigger diffuser angle translates into a larger diameter of the Venturi vortices. The horseshoe vortices start from the stagnation area and envelop the body. The smaller the ground clearance, the more persistent the horseshoe vortices: in the 28 mm cases, these material tubes continue to exist beyond the rear of the body, whereas in the 44 mm cases they breakup near the entrance.

After describing the global features of the flow, attention was focused on the diffuser region affected by the Venturi vortices: for a better understanding of this physical phenomenon, the case at lowest ride height and larger diffuser angle (13° - 28 mm) was used as an example. Figure 12 (pressure coefficient versus non-dimensional body length) and Figure 13 (plots of streamwise and spanwise velocity) refer to a longitudinal slice at 80% of the half width of the body.

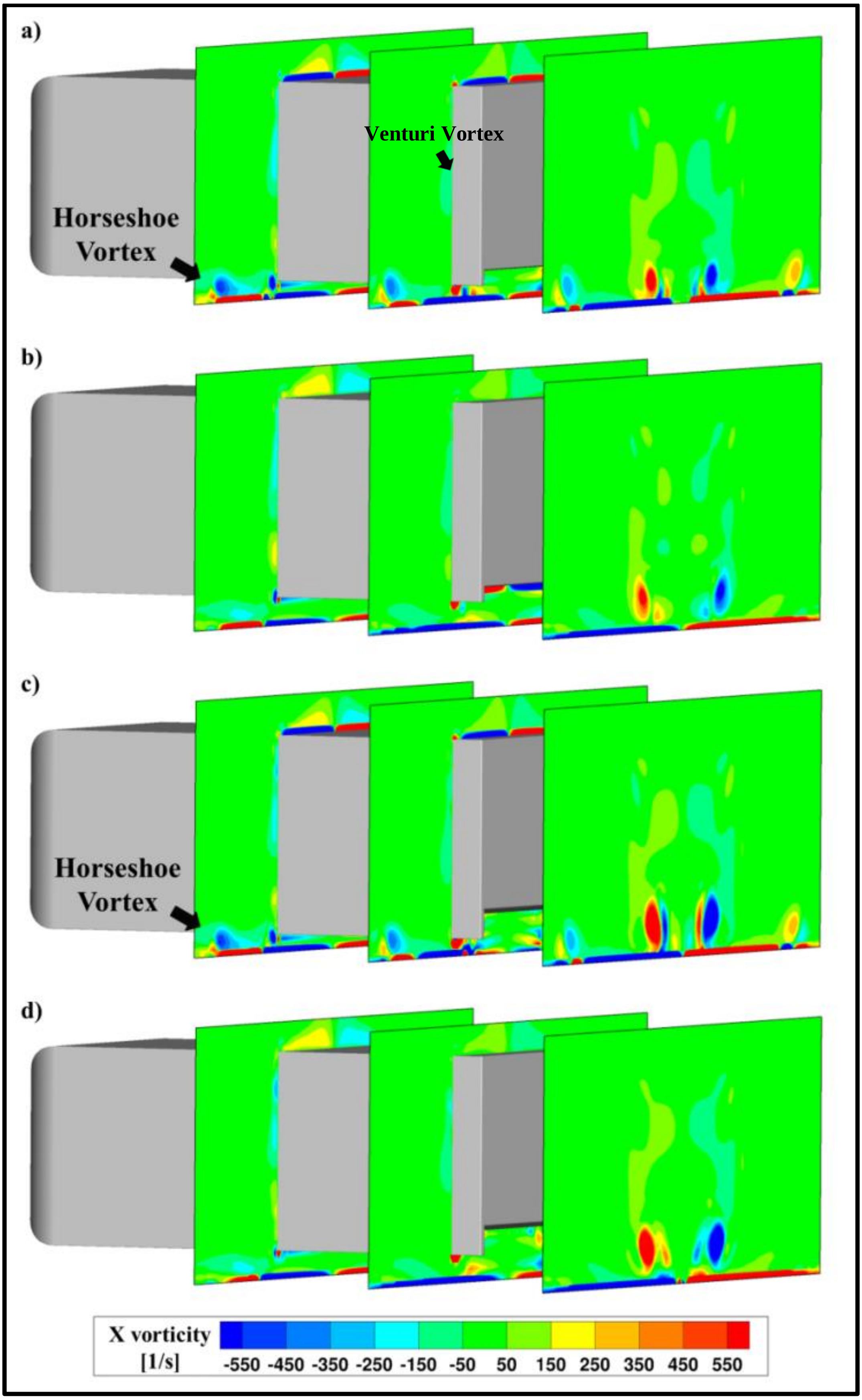

Figure 10: Axial vorticity in three cross sections (x/L=0.6, 0.95, 1.3): a) 7°, 28 mm; b) 7°, 44 mm; c) 13°, 28 mm; d) 13°, 44 mm

Figure 12 shows that the pressure profile on the diffuser surface (x/L > 0.75) is bumpy and irregular as a symptom of unsteadiness. Looking at the two peaks of negative relative pressure, it can be noted that the one located at x/L = 0.05 is weaker than its counterpart at midspan (-1.5 versus -1.85 in Figure 7a), whilst the other minimum at the beginning of the diffuser (x/L = 0.75) maintains more or less the same value of its counterpart at midspan (about -1.6) thanks to the Venturi vortex that keeps the underbody flow confined.

As highlighted in Figure 13, this vortex starts at the beginning of the diffuser and develops while converting streamwise velocity into spanwise velocity. The coloured streamlines of Figure 14 illustrate the above mentioned three-dimensional vortical flow field.

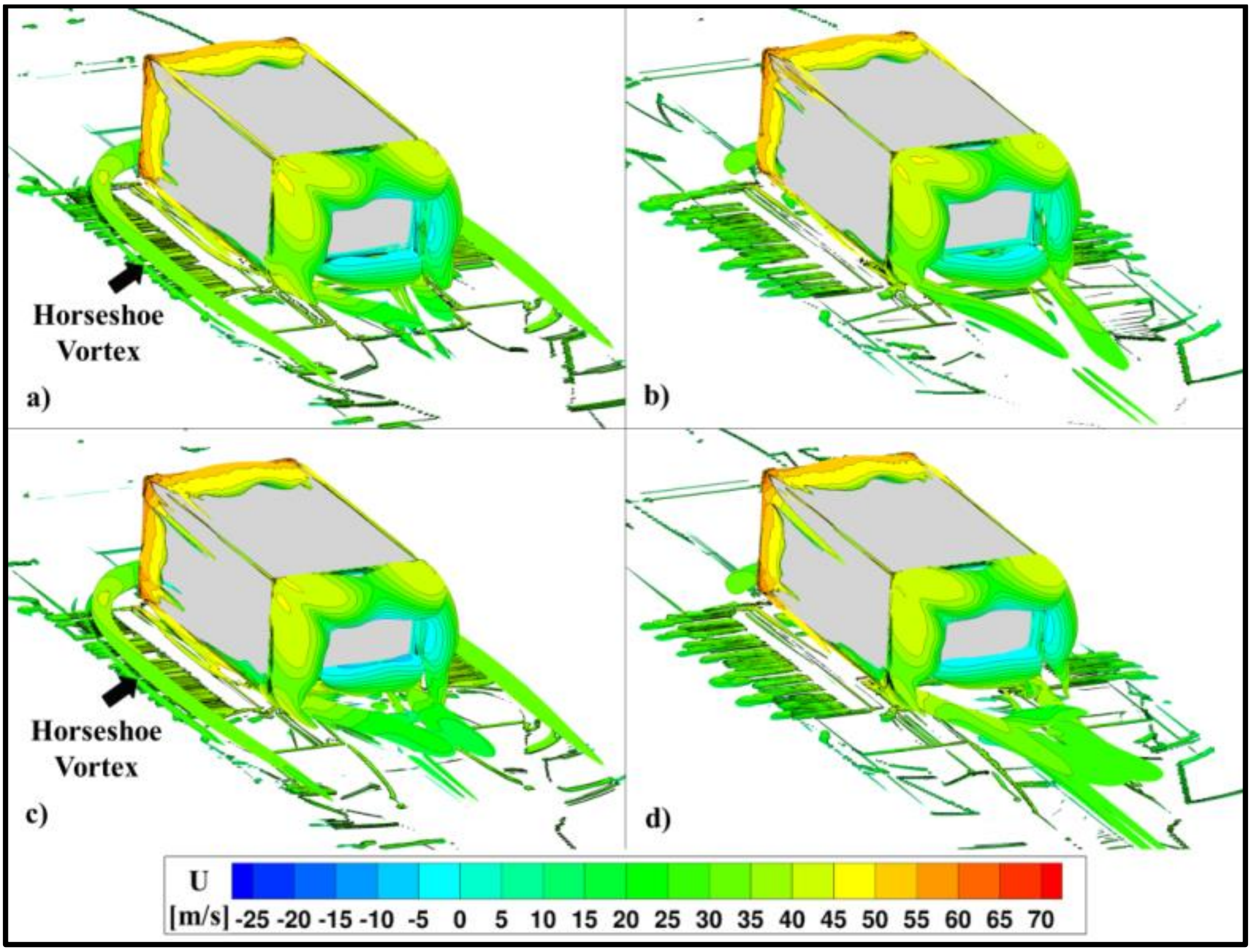

Figure 11: Iso-contours of Q coloured with streamwise velocity: a) 7°, 28 mm; b) 7°, 44 mm; c) 13°, 28 mm; d) 13°, 44 mm

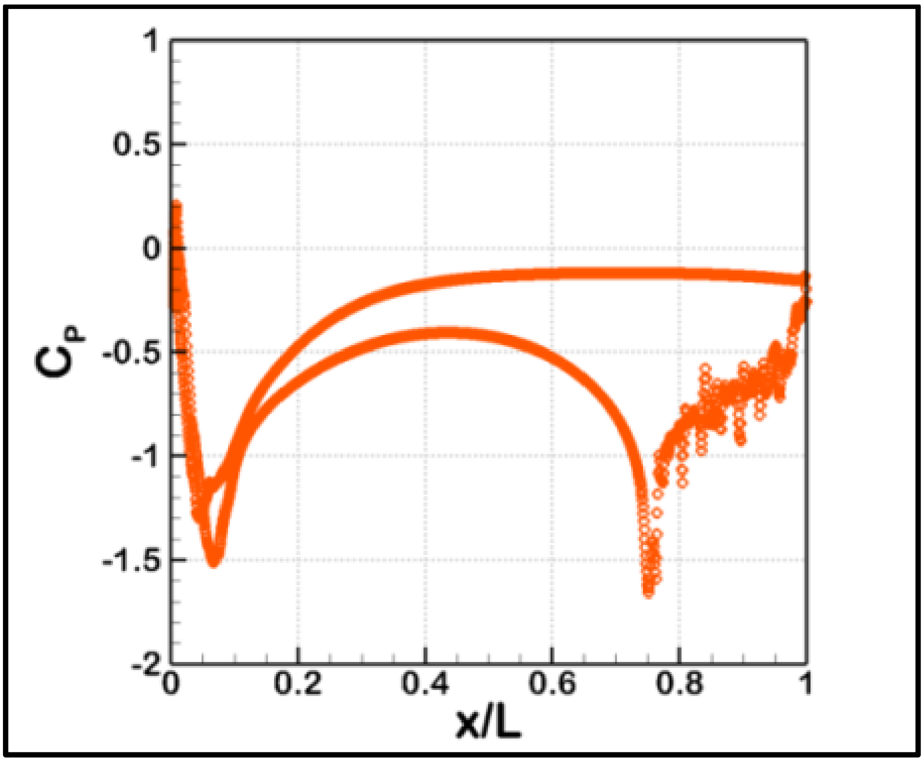

Figure 12: C_P as a function of x/L - slice at 80% of the half width of the body

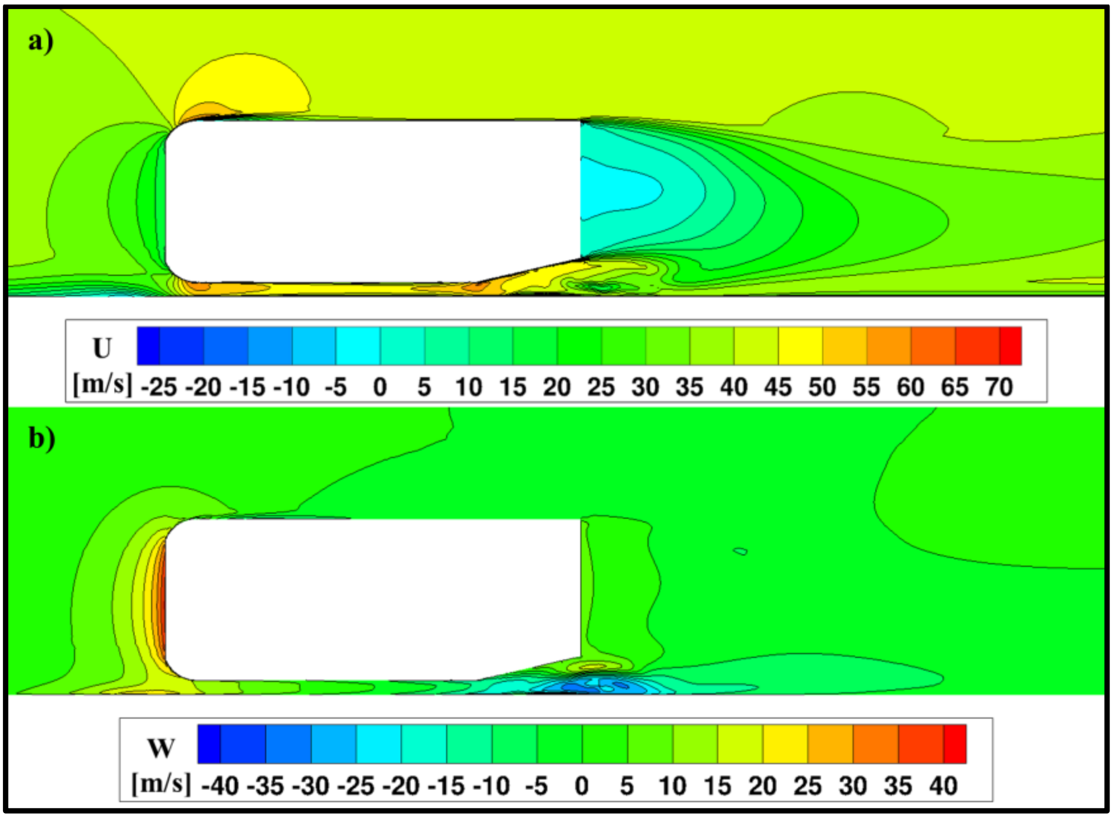

Figure 13: Slice at 80% of the half width of the body: a) streamwise velocity field; b) spanwise velocity field

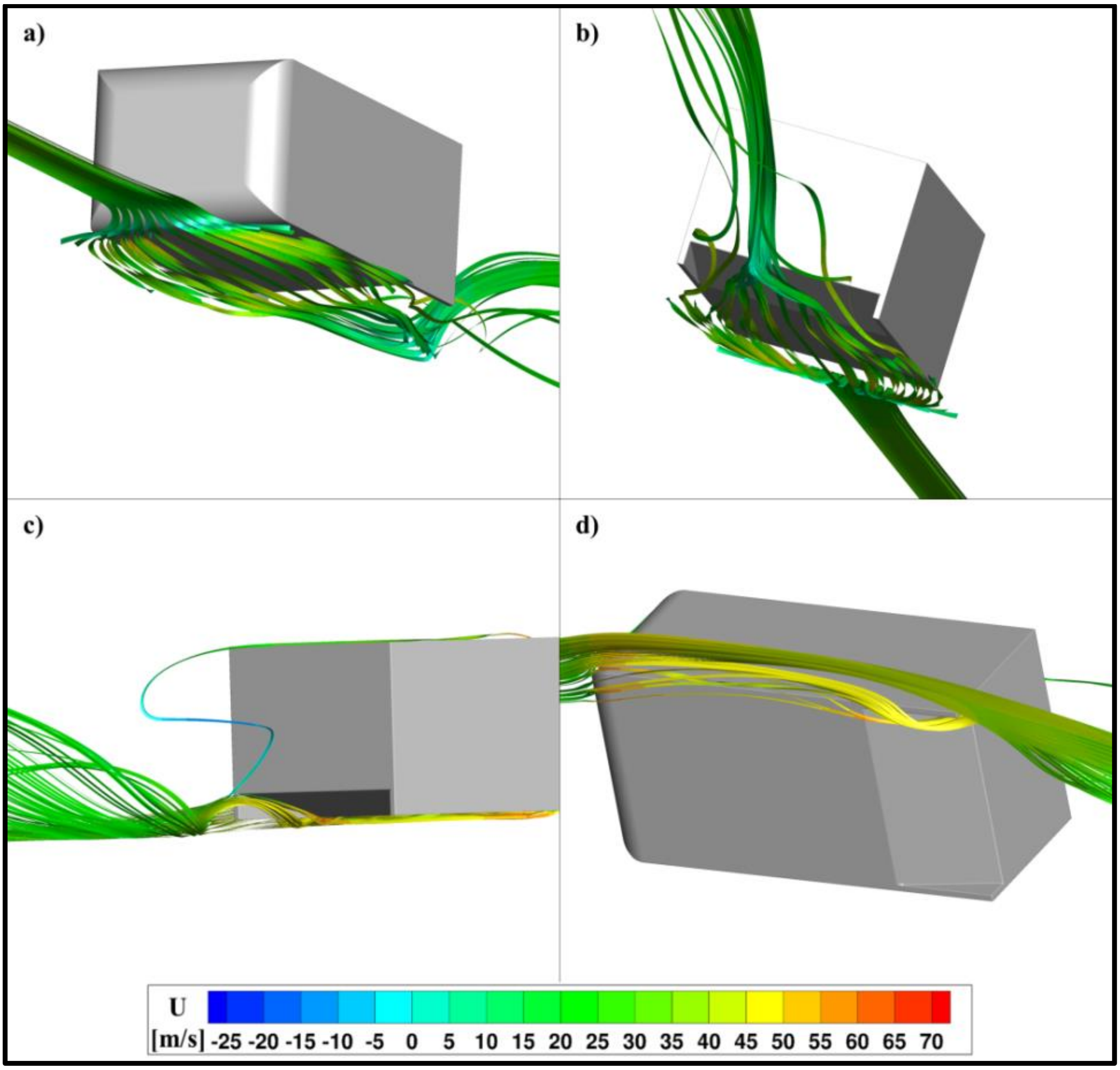

Figure 14: Streamlines coloured with streamwise velocity (case: α = 13°, h = 28 mm) in different views: a) front-bottom view, b) rear-bottom view, c) rear-side view, d) side-bottom view

2.4 Front Wing

2.4.1 Mesh and Simulation Setup

The mesh in streamwise direction is 2.4 m long. The leading edge of the wing lies 0.65 m from the inlet (about 3 times the wing chord, c). The distance between the trailing edge and the outlet patch is about 1.5 m (about 7 times the wing chord). As in the previous case, width and height of the volume mesh comply with the size of the working section of the Southampton University wind tunnel (2.1 x 1.5 m^2), where experiments had been performed. See Figure 15 for more details.

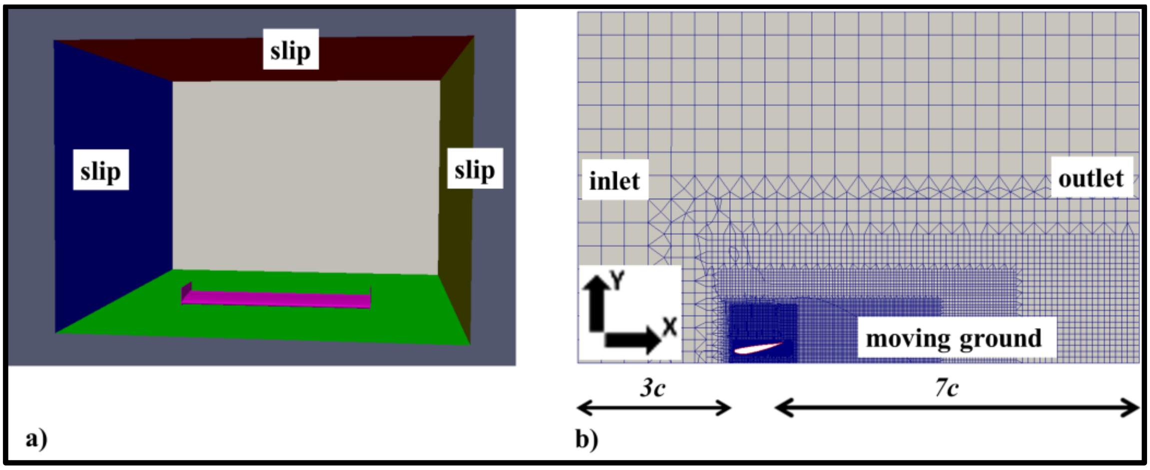

Figure 15: Mesh of the wing: a) external boundaries and b) midspan slice of the volume mesh

Five refinement regions were defined: special care was taken to the volume between the suction side of the wing and the ground. The first cell height on the wing surface was 0.6 mm (about 2.5 x 10^{-3} times the wing chord): this value led to an average y^+ value of about 30. As in the previous case, the leading and trailing edge regions are characterized by lower values of y^+. The total amount of cells was about 11 million. The total CPU time for mesh creation was about 5 hours. The experimental wind tunnel had a moving ground: as a result, there was no boundary layer imposed at the inlet section. Basically, the boundary conditions of the front wing case were the same as previously described: the only differences concerned the uniform inlet velocity and the moving ground. In light of previous tests, slip condition was imposed on the side walls of the virtual wind tunnel. All the data necessary to model the wing and fix the boundary conditions are summarized in Table 6. As confirmed by many papers in the published literature, the k-ωSST model is suited for predicting blunt body aerodynamic features. This might not be always true dealing with slender body aerodynamics. Another turbulence model, i.e. S-A, was considered for comparison. The S-A model is based on an additional equation including the turbulent eddy viscosity. It was developed for aerospace applications and aerodynamic flows (Spalart and Allmaras, 1992). It usually shows a good behaviour for boundary layer in adverse pressure gradient, even though it is not calibrated for general industrial flows.

Table 7 summarizes the inlet turbulent variables, both for the k-ωSST and S-A model. The turbulence length was assumed to be of the same order of magnitude of the wing chord. Algorithms, equation solvers and the entire numerical setup were the same as those used in the blunt body simulations.

A 2x4 simulation pattern was carried out: each of angle of attack (1°, 5°) was tested in four different ride heights (40, 50, 70, 100 mm). Experimental and numerical data were compared in terms of C_D and C_L. This group of simulations was aimed at comparing the results of k-ωSST to the ones from the S-A model. On average, S-A simulations reduced the CPU time by about 40% as compared to the k-ωSST ones (5.5 vs 9 hours), because S-A model has one less equation to solve and requires less iterations to get convergence.

A mesh sensitivity analysis was carried out with 5° - 40 mm case and S-A model. Two mesh sizes were tested, focusing on the refinement box between the body and the ground and the region downstream of the trailing edge.

Symbol	*Parameter*	*Value*
ρ	Air density	1.209 kg/m^3
c	Chord	0.2234
U_∞	Freestream velocity	30 m/s
$Re_{(c)}$	Reynolds number	0.45 x 10^6
I	Turbulence intensity	< 0.2%

Table 6: Experimental data necessary to setup the numerical simulation of the wing - data from Southampton University (Zerihan and Zhang, 2000)

Symbol	*Turbulent Variable*	*Formula*	*Value*
k	Turbulent kinetic energy	$\frac{3}{2}(Iu_\infty)^2$	≈ 0.003 m^2/s^2
ω	Specific dissipation rate	$2.35\frac{\sqrt{k}}{l_t}$	≈ 0.5 1/s
$\tilde{\nu}$	Turbulent viscosity (S-A)	$\sqrt{\frac{3}{2}}Iu_\infty l_t$	≈ 0.012 m^2/s

Table 7: Inlet turbulence variables of the k-ωSST and S-A model – wing case

Experiments were performed in conditions of fixed (fi.) and free (fr.) transition. In the former case, the switchover from laminar to turbulent boundary layer was induced by a strip located at 10% of the chord on both surfaces of the wing; in the latter case, the boundary layer became turbulent without any external forcing. Since the CAD model of the wing had no strips and, to the authors' knowledge, OpenFOAM® does not easily allow the transition point to be fixed on the wing, the numerical results had to be compared with the free transition experimental outputs (Zerihan and Zhang, 2001).

2.4.2 Aerodynamic Performance

The wing was tested at four different ride heights (40, 50, 70, 100 mm) and two values of AOA (1° and 5°). Tables 8 and 9 summarize the results in terms of drag and lift coefficients.

	1°							
	C_L *fi exp*	C_L *fr exp*	C_L *num k-ωSST*	C_L *num S-A*	C_D *num k-ωSST*	C_D *num S-A*	*e% fr k-ωSST*	*e% fr S-A*
40 mm	-1.12	-1.42	-1.30	-1.36	0.068	0.082	8.82	4.32
50 mm	-1.08	-1.25	-1.25	-1.26	0.064	0.078	0.00	0.80
70 mm	-0.98	-1.08	-1.13	-1.11	0.058	0.072	4.52	2.74
100 mm	-0.88	-0.95	-1.00	-0.98	0.054	0.067	5.13	3.11

Table 8: Results of the wing simulations, AOA = 1°

	5°							
	C_L *fi exp*	C_L *fr exp*	C_L *num k-ωSST*	C_L *num S-A*	C_D *num k-ωSST*	C_D *num S-A*	*e% fr k-ωSST*	*e% fr S-A*
40 mm	-1.36	-1.84	-1.58	-1.62	0.116	0.132	15.20	12.72
50 mm	-1.38	-1.73	-1.64	-1.59	0.105	0.123	7.19	8.43
70 mm	-1.34	-1.54	-1.48	-1.47	0.093	0.113	3.97	4.65
100 mm	-1.27	-1.38	-1.36	-1.33	0.087	0.105	1.46	3.69

Table 9: Results of the wing simulations, AOA = 5°

In six out of eight cases (ride heights from 50 to 100 mm), the S-A and k-ωSST are essentially equivalent in terms of drag and lift coefficients. The S-A model works better than k-ωSST when the ground clearance is very small (40 mm) and, as a consequence, both the adverse pressure gradient on the suction side of the wing and the acceleration of the flow between the wing and the ground are very high: this feature could probably make the S-A model better than the k-ωSST model in typical cases of motorsport applications, such as high cambered wings. Other benefits of the S-A model are related to its numerical features: it is very stable and typically requires a smaller number of iterations than the k-ωSST model to reach convergence.

Figure 16 shows the longitudinal velocity field at midspan for four combinations of angle of attack (1°, 5°) and ground clearance (40, 100 mm). Predictions from S-A are shown on the left whereas results from k-ωSST are depicted on the right. The wing in ground effect behaves almost like a converging-diverging nozzle, in which the walls are made up of the suction side of the wing and the ground itself. The variations of ride height and angle of attack contribute to change the area ratio of this “nozzle” and therefore the features of the flow: when the angle of attack increases and the ground clearance gets smaller, the area ratio of the nozzle becomes larger.

Reduction in ground clearance causes higher flow acceleration and, consequently, lower pressure. This results in more downforce and more drag, because of the reduced pressure insisting on the rear suction side of the airfoil. Moving from 1° to 5° angle of attack, the effects are similar to those just described here. When the ride height is very low and the angle of attack is high, separation and recirculation of the flow on the suction side of the wing occur (see negative longitudinal velocity in 5° - 40 mm case). When angle of attack increases but the ground clearance is high, the separation of the flow is much less pronounced.

The differences between the two models in terms of drag and lift coefficients are confirmed by qualitative results: k-ωSST underestimates lift coefficient because is less resistant to flow separation than S-A in extreme conditions (5° - 40 mm). This might be the reason why the drag coefficient calculated by k-ωSST is smaller than the one calculated by S-A model. Looking at the velocity contours, it can also be noted that an earlier separation does not allow the flow to reach high speed on the suction side of the wing, compromising the generation of downforce.

Figures 17 and 18 refer to the wake generated by the wing in the following operating conditions: 1° - 50 mm, 1° - 100 mm. These combinations of AOA and ride heights are particularly interesting because numerical outputs can be compared with experimental results (Zhang and Zerihan, 2002). While moving along the X-axis, and thus away from the trailing edge, the wake is getting shorter in chord-wise direction and thicker in Y-direction, because of the viscous dissipation of the wake structures. Lower ride height leads to deeper wakes in X-direction, because the flow on the suction side of the wing is subjected to a stronger adverse pressure gradient. S-A and k-ωSST turbulence models predicted comparable velocity profiles, consistently with the fact that also the global performance coefficients are similar in these combinations of AOA and ride height (see Table 8). Both the turbulence models slightly overestimate the size of the wake both in X and Y-directions.

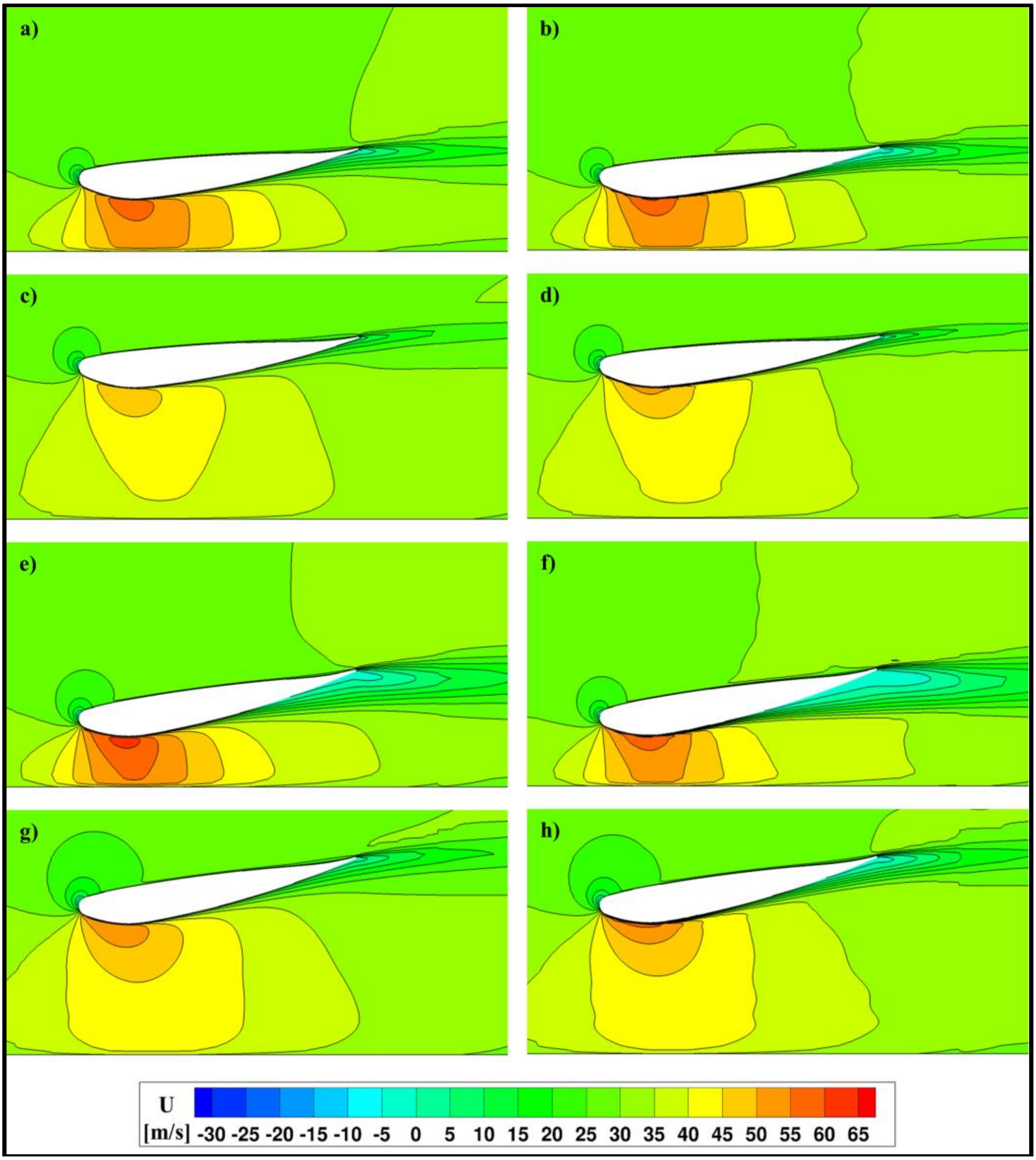

Figure 16: Streamwise velocity field at midspan: a) S-A, 1°, 40 mm; b) k-ωSST, 1°, 40 mm; c) S-A, 1°, 100 mm; d) k-ωSST, 1°, 100 mm; e) S-A, 5°, 40 mm; f) k-ωSST, 5°, 40 mm; g) S-A, 5°, 100 mm; h) k-ωSST, 5°, 100 mm

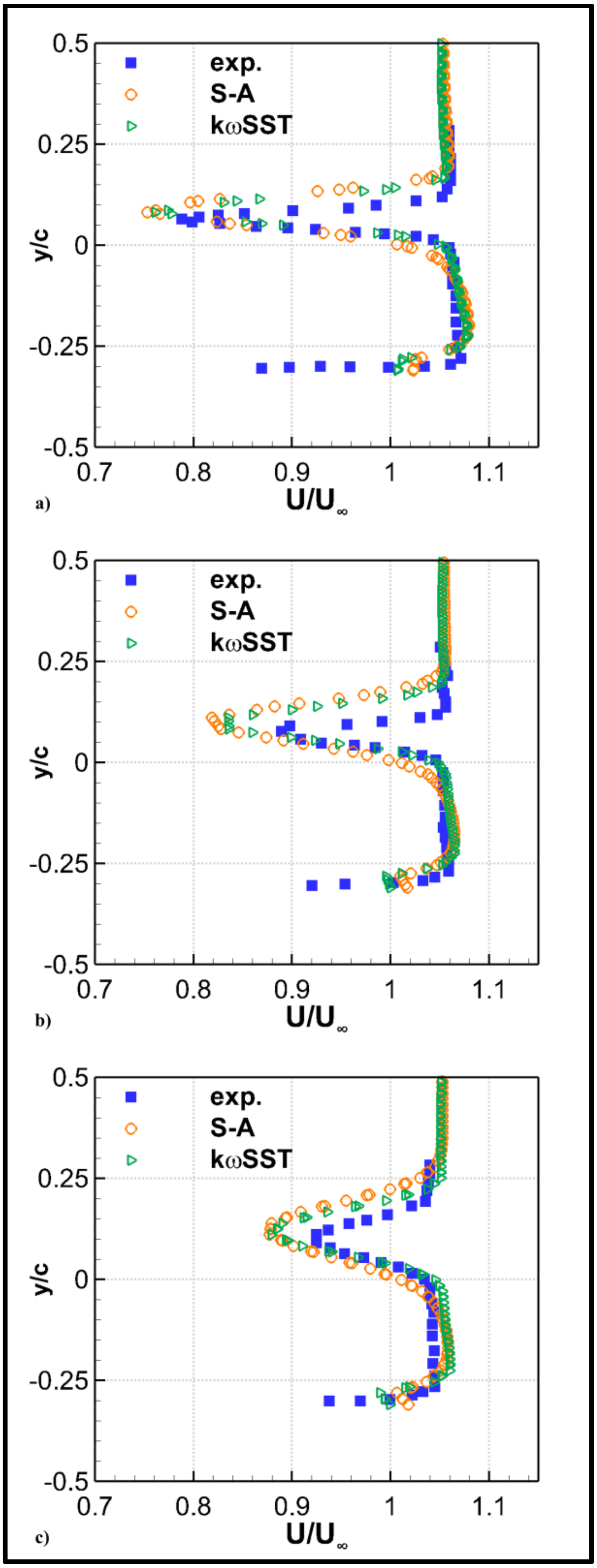

Figure 17: Mean flow wake profiles at midspan (1° - 50 mm) at different distances from the wing leading edge: a) x/*c* = 1.5; b) x/*c* = 2; x/*c* = 3

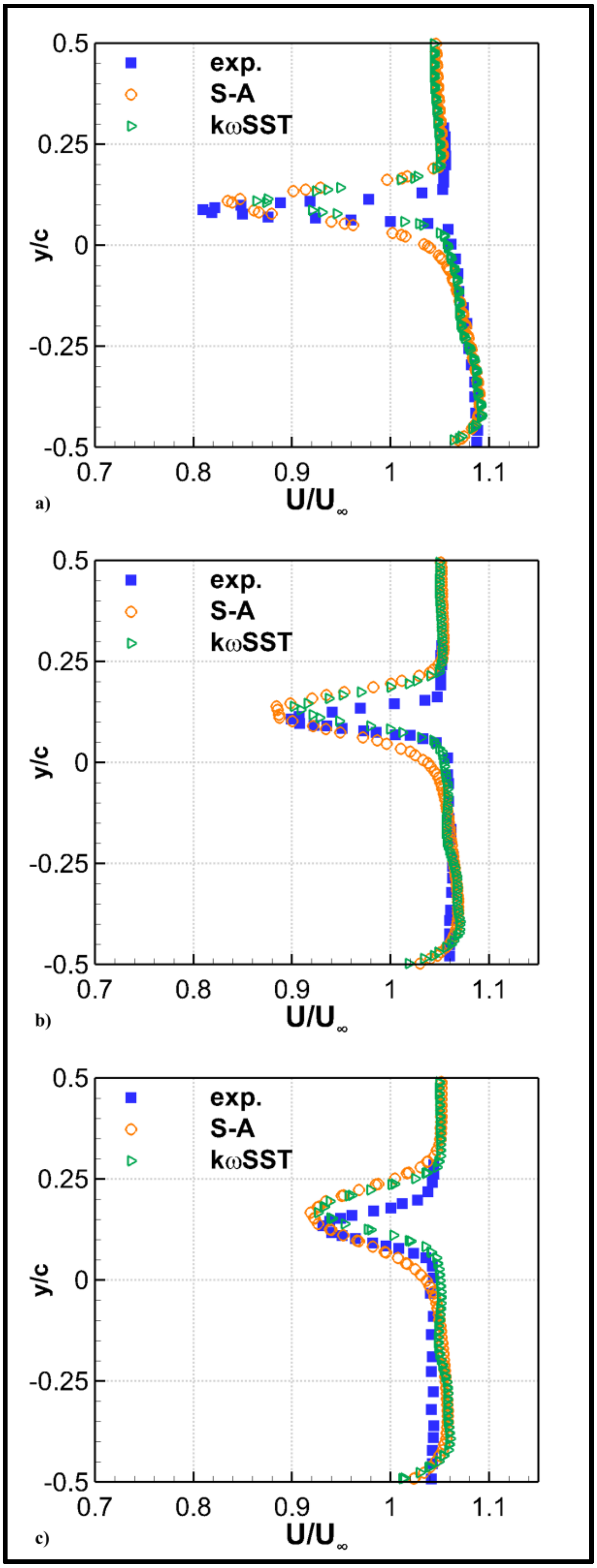

Figure 18: Mean flow wake profiles at midspan (1° - 100 mm) at different distances from the wing leading edge: a) x/*c* = 1.5; b) x/*c* = 2; x/*c* = 3

Both the longitudinal vorticity contours (Figure 19) and the iso-surfaces of Q-criterion (Figure 20), have been computed using the S-A model. Figure 19 shows two axial vortices detaching from the wing side plate: both depend on the difference of pressure between the region outside the plate and the wing itself. The biggest vortex is located on the suction side of the wing, the smallest one on the pressure side. When the ride height is lower, a secondary counter rotating vortex can be identified between the suction side vortex and the ground. Figure 20 supports the previous observations and shows two-dimensional flow separation on the suction side of the wing in 5° - 40 mm case.

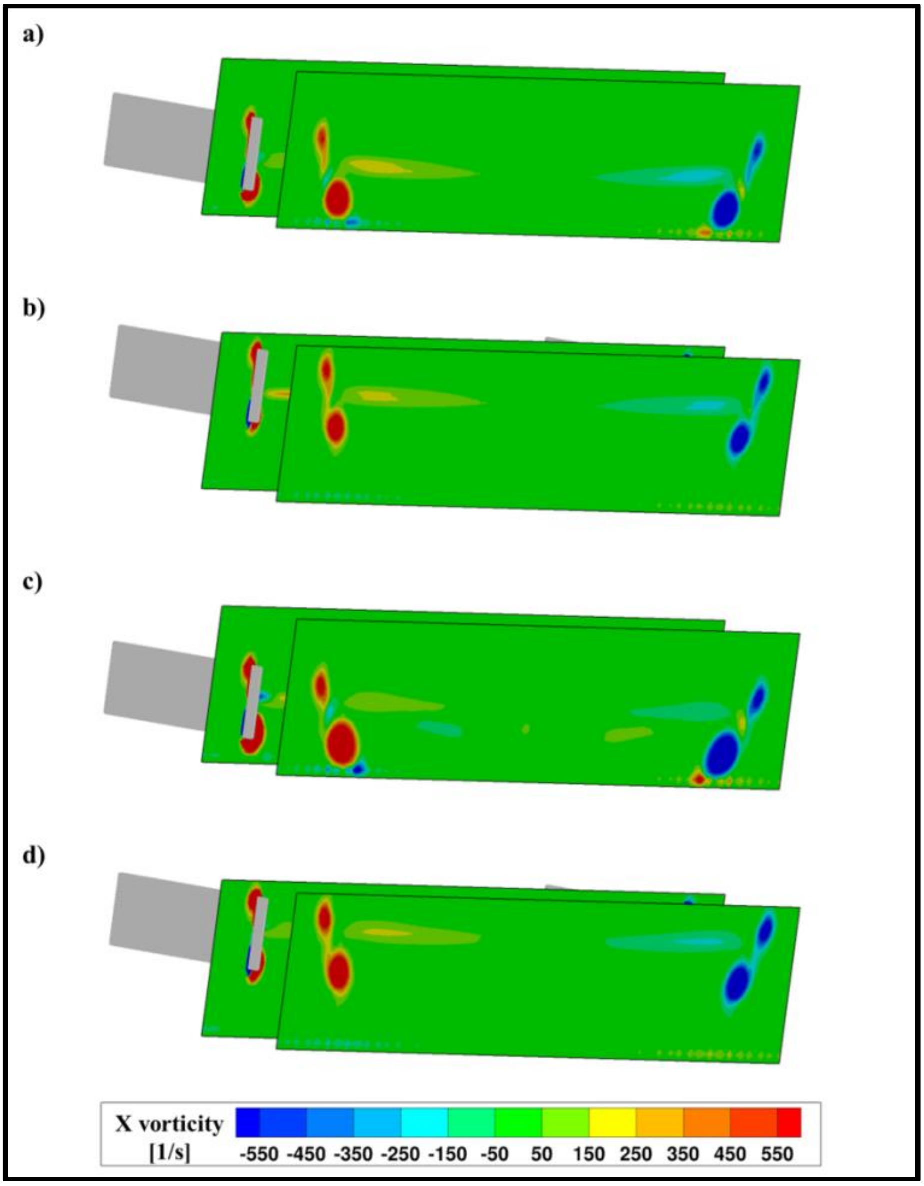

Figure 19: Axial vorticity in two cross sections at trailing edge and at half chord from trailing edge – S-A model: a) 1°, 40 mm; b) 1°, 100 mm; c) 5°, 40 mm; d) 5°, 100 mm

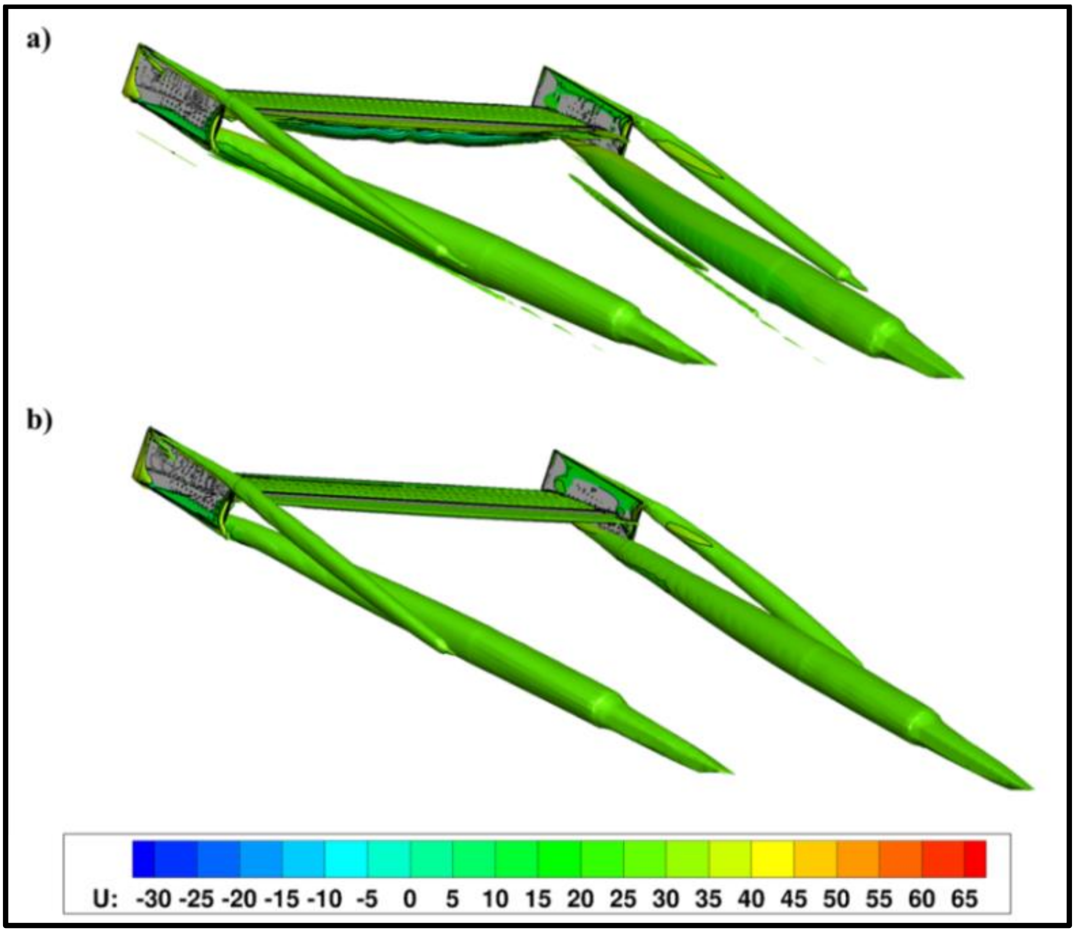

Figure 20: Iso-contours of Q coloured with streamwise velocity (S-A model): a) 5°, 40 mm; b) 5°, 100 mm

As in the blunt body investigation, the attention focused on the region near the endplates, where the flow is highly three-dimensional and characterised by tip vortices. The 5° - 40 mm case was chosen for this purpose. Figure 21 shows the comparison between two pressure coefficient profiles: the former calculated at midspan ($Z/Z_{max} = 0$), the latter at 80% of the half span ($Z/Z_{max} = 0.8$). Looking at the minima of relative pressure at $x/c_{ax} = 0.2$, where c_{ax} is the axial chord, one can see that the wing generates less downforce near the endplates, due to the presence of the tip vortices that equalize the pressure on both the sides of the wing. On the other hand, as indicated by C_p values at the trailing edge, it seems that the tip vortex on the suction side helps to prevent flow separation in adverse pressure gradient.

The streamwise velocity contours in Figure 22 confirm that the wing section at midspan is characterized by higher acceleration and earlier separation of the flow than the section near the endplate.

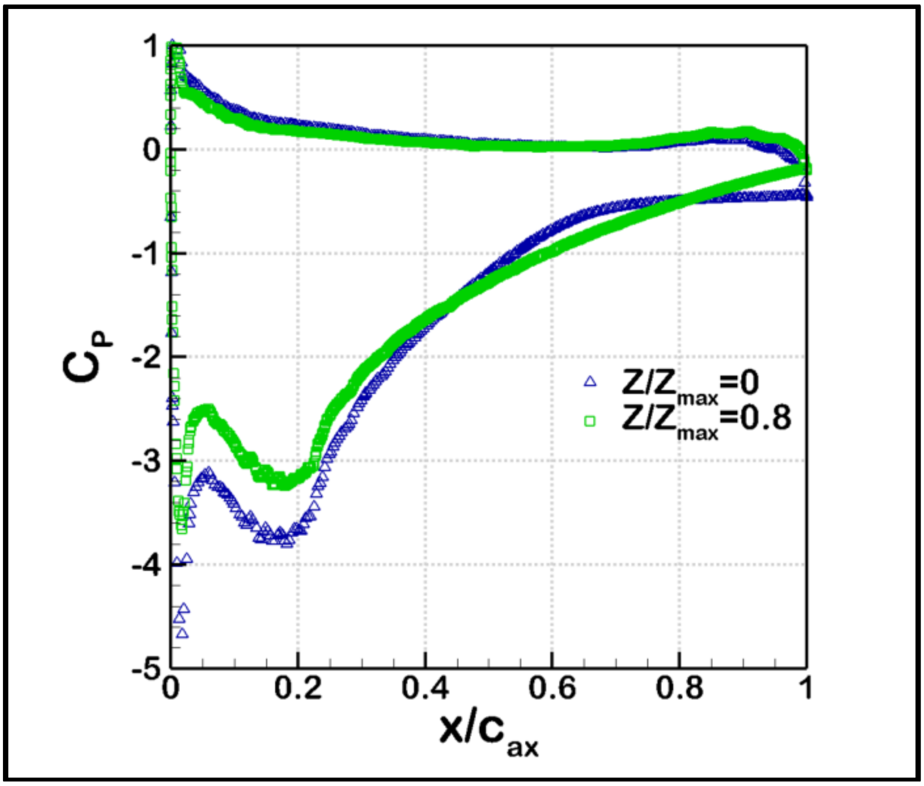

Figure 21: C_P versus x/c_{ax}: comparison between midspan (Z/Zmax = 0) and slice at 80% of the half span (Z/Zmax = 0.8)

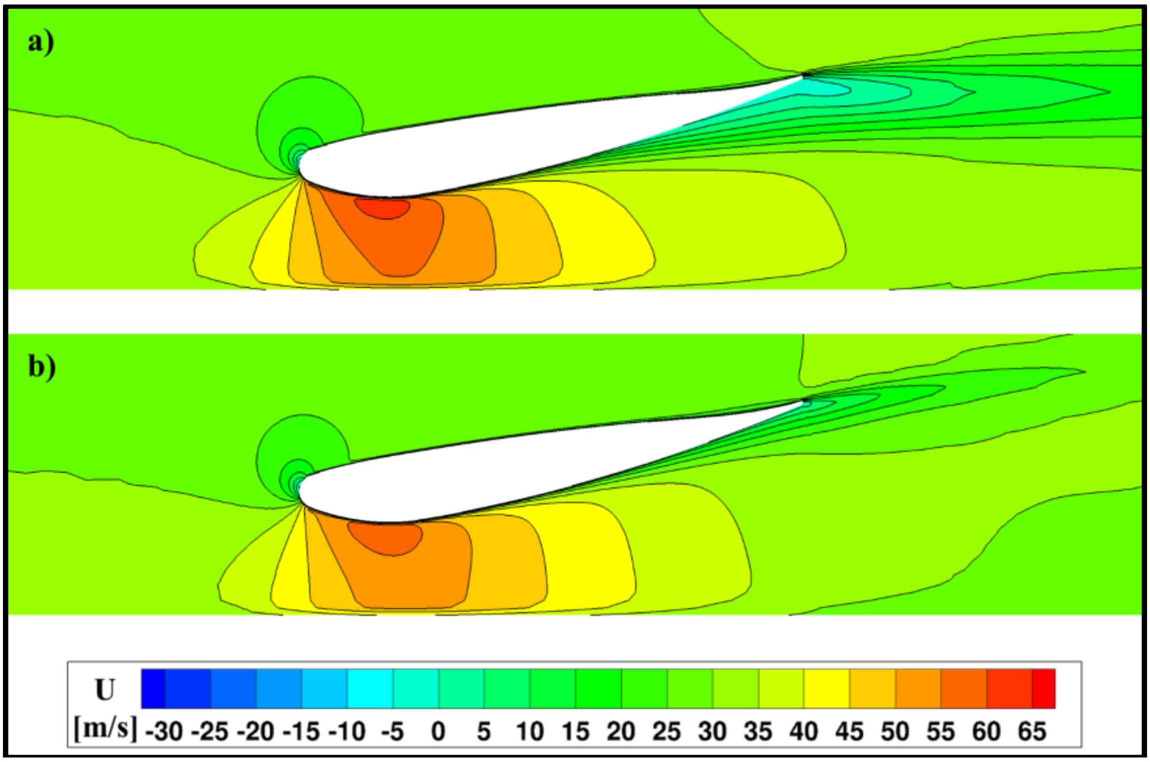

Figure 22: Streamwise velocity field (S-A model): a) midspan; b) 80% of the half span

Finally, the coloured streamlines of Figure 23 illustrate the most important vortical structures affecting the flow around the wing.

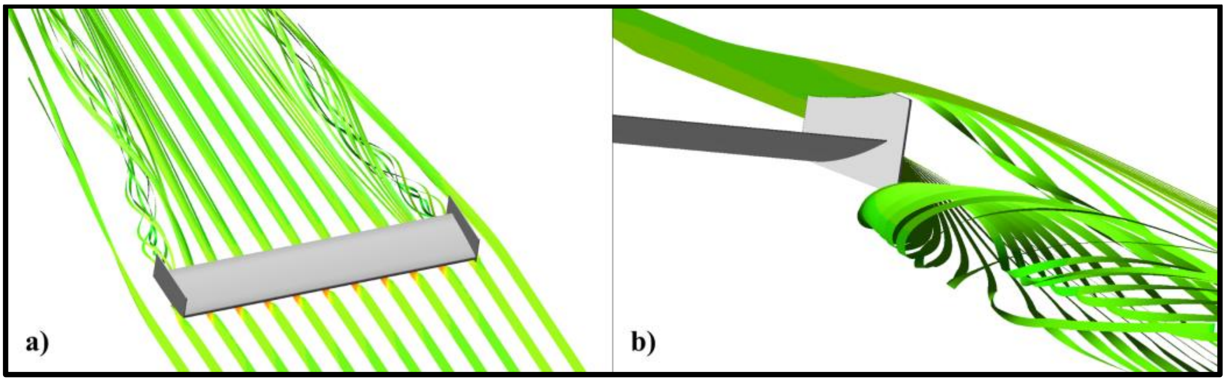

Figure 23: Streamlines in different views (5°, 40 mm): a) front-upper view, b) rear-bottom view

2.5 Conclusions

The open-source software OpenFOAM® was used for investigating incompressible external aerodynamics. The attention was drawn to motorsport/automotive applications: a diffuser-equipped blunt body and a F1 front wing in ground effect were both studied under the assumption of steady flow, taking into account turbulence with RANS approach. In both test cases, results of CFD simulations turned out to be very close to the experimental values, thereby providing the effectiveness of numerical investigations in the context of race car aerodynamics.

Concerning the blunt body simulations, the results put in evidence that the coupled solver improves significantly the performances of the k-ωSST turbulence model, better suited to solve strongly separated flow fields than a one-equation turbulence model like the S-A.

With regard to the front wing case, the comparison between k-ωSST and S-A models led to the conclusions that, in many configurations of angle of attack and ground clearance, both lift and drag predictions of the two models are similar. However, when the ride height is very low (40 mm), the S-A model gives better predictions of C_D and C_L than k-ωSST. Moreover, in every tested configuration, the S-A model was found to be more robust and provided faster convergence. The findings concerning prediction capabilities and numerical behaviour of the turbulence models are not necessarily general but pertained to the OpenFOAM® usage for the current applications.

This numerical investigation led to a better understanding of typical phenomena that characterize aerodynamics of downforce generating devices in ground effect, such as three-dimensional structures (Venturi vortex, horseshoe vortex, tip vortex), separation in adverse pressure gradients and viscous effects. They play a key role in improving the design of aerodynamics components at least as much as the correct prediction of global integral parameters like drag and lift coefficients:

these are typically the only outcomes of standard experimental campaigns, leaving to CFD the important task to illustrate in detail the underlying complex flow physics.

The present study can also be viewed as a preparatory step toward the numerical investigation of a F1 car. Since an open-wheeled racing car is a mix of blunt and slender components, the choice between S-A and k-ωSST turbulence models is not easy when simulating phenomena connected with ground effect and generation of downforce: when bluff body effects prevail, the k-ωSST model is expected to be the right option; on the contrary, when wings and high adverse pressure gradients dominate the physical phenomena, it is likely that S-A model might be the right choice. In both cases the use of the coupled approach is useful to reach faster convergence and better accuracy, especially when dealing with complex fluid dynamic phenomena, such as massive separation and vortex shedding.

Chapter 3. Aerodynamic Simulation of a 2017 F1 Car

In light of the results achieved in Chapter 2, it is easy to understand that open-wheeled race car aerodynamics is unquestionably challenging insofar as it involves many physical phenomena, such as slender and blunt body aerodynamics, ground effect, vortex management and interaction between different aero devices. In the current chapter, the external aerodynamics of a 2017 F1 car was numerically investigated. The vehicle project was developed by PERRINN (Copyright © 2011 - Present PERRINN), an engineering community founded by Nicolas Perrin in 2011. The racing car performance was quantitatively evaluated in terms of drag, downforce, efficiency and front balance. The main goals of this part of the research are the following: formulating a reliable workflow from CAD model to post-processing on the basis of the lessons learnt from Chapter 2 and understanding the complex flowfield around the vehicle.

3.1 Geometrical Features and CAD Pre-Processing

The design of the full scale CAD model of the PERRINN F1 car, whose wheelbase (WB) measures 3.475 m, complied with the 2017 FIA Technical Regulations and is equipped with all the most important aerodynamic devices characterizing the modern open-wheel racing cars (Figure 24). All the geometrical details concerning the external aerodynamic components of the car were maintained, whereas some simplifications regarding internal flows, wheel rims and brake ducts were introduced.

Figure 24: Rendering of the 2017 F1 car by PERRINN (image from gpupdate.net)

The first pre-processing phase was to clean the original model in iges or step format, in order to fix the most common topology defects, such as overlapping edges and surface cracks. Particular attention was also put on some critical regions of the model, whose quality determines the success of the final meshing procedure: thickness of wing strakes, slots, turning vanes and vortex generators thickness does not exceed 1.5 mm. Moreover, some surface details, such as front suspension arms, flap connections and the intersection between ground and tyres, were partially re-designed in order to avoid problems of cell skewness or non-orthogonality.

Once a smooth surface was obtained, the vehicle was divided into components, so as to analyse separately the behaviour of each part of the car body (Figure 25): the most important ones in terms of downforce generation are the front wing, the underbody (including the step plane and the rear diffuser), the plank and the rear wing. The front wing is composed by a main plane and 3 flaps; its outer region is characterized by an endplate, a winglet cascade and a turning vane. The side areas of the underbody are flat, whilst the middle region is characterized by a plank (or skid block) working very close to the ground. The rear end of the vehicle is equipped with a multi-channel diffuser and a double element wing (Ravelli and Savini, 2018).

The next step was to adjust the front ride height (FRR) and the rear ride height (RRH) of the vehicle, in order to attain the prescribed setup (FFR = 20 mm; RRH = 50 mm): in this position, the minimum distance between the plank and the ground is 13 mm. Further details on the setup issue will be discussed extensively in Chapter 5. The intersection between the tyres and the ground leads to the creation of a contact patch, which can vary depending on the front and rear ride height of the vehicle. These regions are particularly critical from a meshing point of view, because of high-skewness cells and non-orthogonality issues: in this regard, a 1.5 mm thick collar was designed between the tyre and the ground.

As in the previous chapter, the last stage of the pre-processing procedure was to export every component in STereoLithography format (stl), in order to be processed by SnappyHexMesh: the final triangle mesh of the full vehicle consists of about 5 million elements. Many commercial CAD software are able to convert the original model in this format, but it is preferable to use only those providing a detailed control on the output file, since the quality of the stl model is directly connected to the quality of the volume mesh and hence the accuracy of the final fluid dynamic results. A final check of the stl file is recommended in order to control orientation, surface closure, quality of triangles and edges: Netfabb Basic 5.2.0, a free software provided by Autodesk®, was used to perform this task.

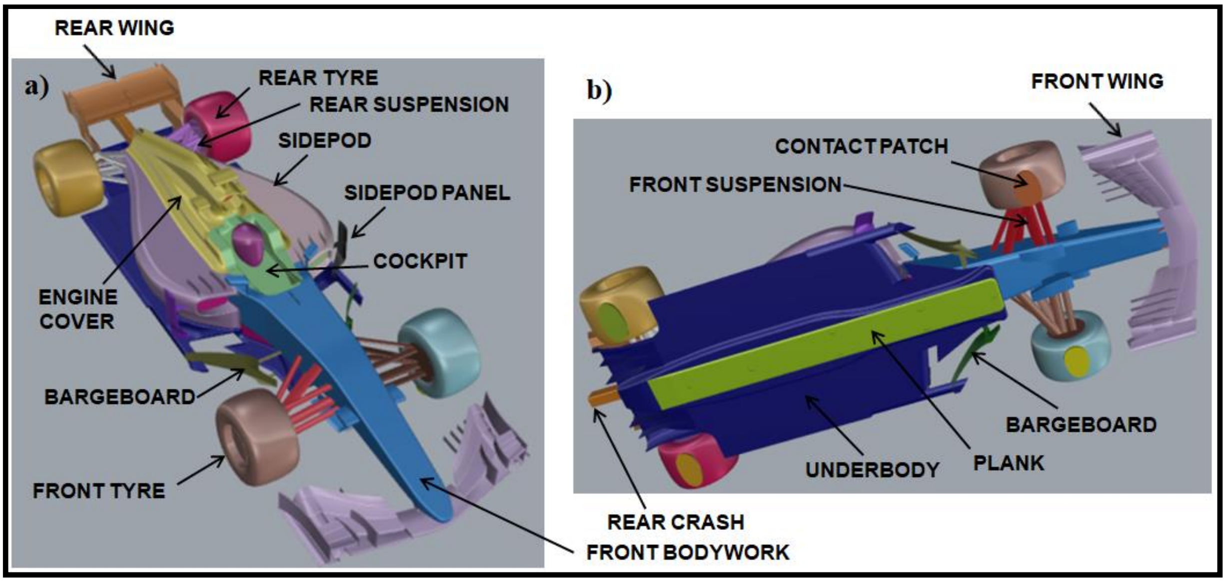

Figure 25: Geometry in stl format - a) top view, b) bottom view

3.2 Simulation Tools

Both meshing and calculation were carried out using the A1 partition of Marconi, the new Tier-0 cluster system available at SCAI Cineca and based on the Lenovo NeXtScale platform (http://www.hpc.cineca.it). The SnappyHexMesh processes were executed by means of 6 computational nodes, each of which is composed of 16 cores (8GB/core); the OpenFOAM® calculations were instead performed using 14 nodes. The post-processing operations were carried out by means of Pico, a machine equipped with two 128GB RAM visualization nodes.

3.3 Mesh and Simulation Setup

The domain length is about 18 times the wheelbase (WB) of the vehicle: the distance between the inlet and the front axle is about 4.6 times the WB, while the outlet of the virtual tunnel, where the atmospheric pressure is imposed, is located well downstream of the car, i.e. 13.8 times the WB (Figure 26).

Since the simulation is steady and the vehicle is perfectly symmetrical, only half car was taken into account: the distance between the longitudinal symmetry plane and the sidewall is about 16 times the half-width of the car. The height of the domain is 16 times the height (h) of the vehicle. Slip condition was imposed on the side wall and the ceiling of the wind tunnel, while the ground was moving at the same speed imposed at the inlet, for the purpose of comparison with the reference calculation made by ©PERRINN. Angular velocity and rotational axis of the wheels were also defined.

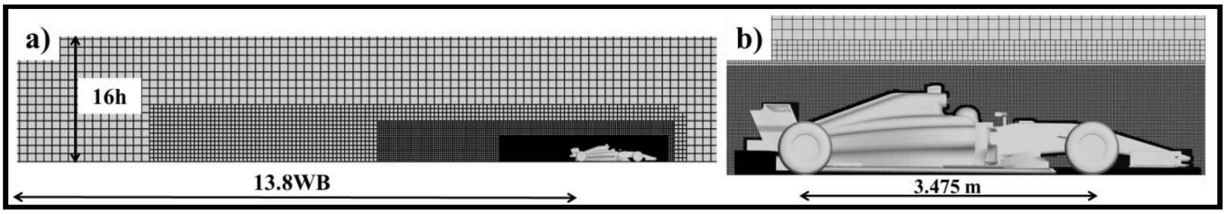

Figure 26: Volume mesh – a) symmetry plane, b) details of the refinement boxes around the car

The main features of the mesh are as follows: the height of the first cell at all solid surfaces is 0.6 mm, with a layer expansion ratio of 1.2. The resulting average value of y^+ is about 40: this number involves the use of wall functions, as is currently done in industrial applications. In order to better catch the features of the fluid dynamic phenomena, many refinement boxes were designed. Special attention was put on the huge wake region and the devices responsible for downforce: the multi-component ground effect front wing, the rear wing composed of a high-cambered main plane and a high angle-of-attack flap, and finally the underfloor, where the flow reaches top speed.

As suggested by the results achieved in Chapter 3, two turbulence models were taken into account: k-ωSST and S-A. The k-ωSST model has proved to be reliable and suitable for a wide variety of industrial applications. However, also the S-A is still exploited and developed for the purpose of simulating complex physical phenomena, such as different regimes of Mach flows, particle dispersion, internal flows. Besides the well-known aerospace applications, including slender body aerodynamics and turbomachinery flows, it has been recently used for bluff body aerodynamics, such as blunt trailing-edge airfoils (Cooperman et al., 2010) and simplified car body (Guilmineau, 2008). All the data needed to define the numerical setup and initialize the turbulent variables of both simulations are summarized in Table 10.

Since the wake of the vehicle is subjected to a strong upward deflection, the size of the largest eddy is larger than the height of the vehicle therefore car wheelbase was chosen as turbulent length scale. The incompressible RANS simulations were performed by the coupled version of the simpleFoam algorithm, which is faster and more stable than the segregated one, at the cost of more computational resources. The GAMG solver was used for the pressure equation, whilst smoothSolver was applied for velocity and turbulent variables. The entire calculation was executed with 2nd order discretization schemes.

Convergence was assumed to be reached whenever the scaled pressure and velocity residuals were lower than 10^{-4} and the aerodynamic coefficients remained stable (± 1% in the last 500 iterations).

Variable	*Value*
Freestream velocity (u_∞)	50 m/s
Air density (ρ)	1.225 kg/m^3
Turbulent intensity (I)	0.15%
Wheelbase of the vehicle (WB)	3.475 m
Reynolds Number (Re_{WB})	$12 \cdot 10^6$

Table 10: Physical conditions of the simulation

Three different meshes were tested (140 mln, 120 mln, 90 mln cells): since the results in terms of global performance did not change significantly, the coarse one was chosen for the research.

3.4 Results and Discussion

The comparison between numerical predictions and reference data from ©PERRINN database deals with drag (SCx), downforce (SCz), aerodynamic efficiency (Cz/Cx) and front balance (FB), where S [m^2] is the frontal area of the car and FB is the ratio between the downforce on the front axle (Cz_{front}) and the total downforce ($Cz = Cz_{front} + Cz_{rear}$). From this point, a new reference system was defined, as commonly used for racing car applications. Drag is still pointing in the X-direction, but lift is parallel to the Z-axis. As a consequence, the width of the car extends along the Y-axis (Figure 27).

The k-ωSST turbulence model predicted a premature separation of the flow on the suction side of the wings and along the diffuser: as a result, both downforce and drag coefficients were underestimated respectively by 20% and 11%. On the opposite, S-A showed a better behaviour for boundary layer in adverse pressure gradient (Ravelli and Savini, 2018): as summarized in Table 11, the results of the coupled RANS simulation with S-A model agree with the reference data. The percentage errors in drag and downforce predictions are respectively 6% and 7%, whilst the front balance coefficient differs by 10% from reference datum. After proper validation, Figure 28 summarizes the contribution of the main vehicle components to the vertical load (SCz).

The bottom of the car, composed of the underbody and the plank, generates more or less 58% of the overall downforce, whilst the front and the rear wing provide respectively the 26.3% and the 27.5% of the total contribution. Also, the front bodywork has a beneficial effect in terms of downforce; on the contrary, sidepod and engine cover generate undesirable lift because they deflect the flow downwards. Concerning SCx, Figure 29 shows that that wheels are responsible for approximately 30% of total drag, dominated by the pressure losses in the wake.

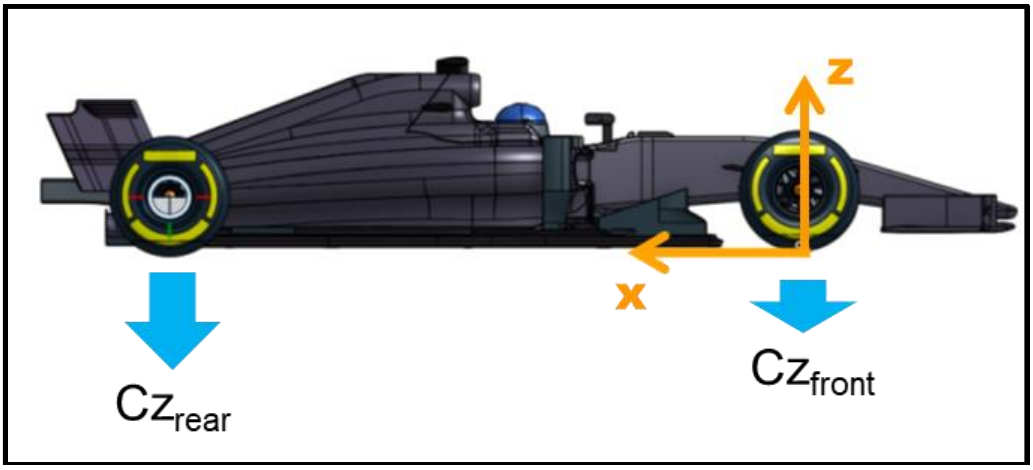

Figure 27: Definition of the new reference system

	SCx [m^2]	*SCz [m^2]*	*Cz/Cx*	*FB*
Reference data	1.23	-3.59	2.92	0.448
S-A results	1.16	-3.35	2.89	0.403
Error %	5.7	6.7	1.0	10.0

Table 11: Comparison between numerical results and reference data (S-A model)

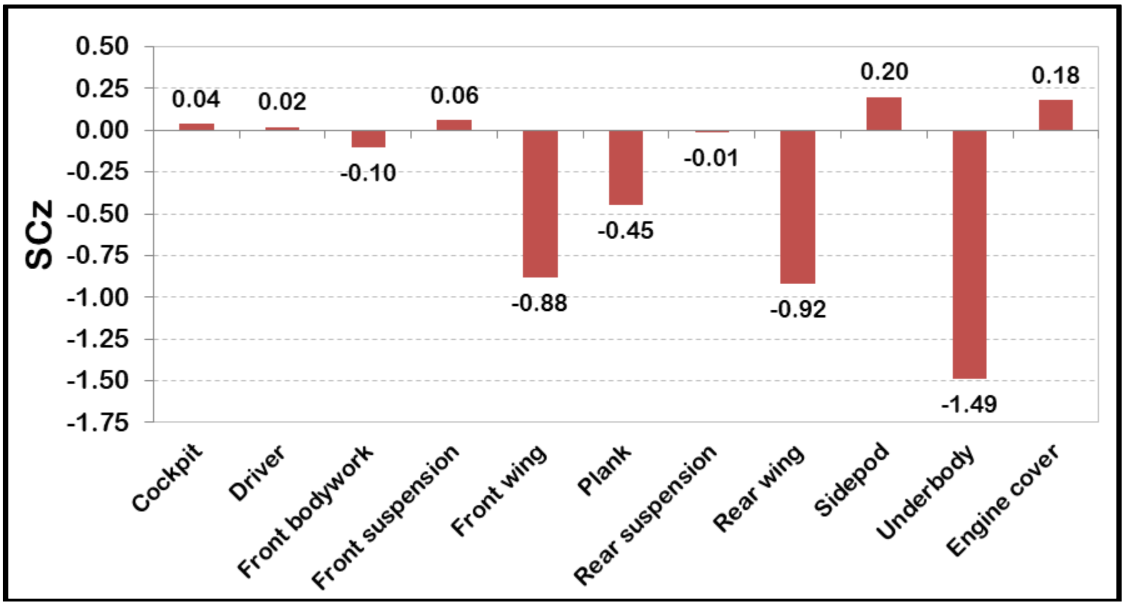

Figure 28: Contribution to lift/downforce of the main components of the car

The underbody is the most efficient aerodynamic device, because it makes extensive use of ground effect and Venturi effect to generate downforce; in contrast, the rear wing is characterized by a low aspect ratio and hence suffers from a large production of induced drag. The front wing efficiency is halfway between the underfloor and the rear wing: the benefits resulting from ground effect are counterbalanced by the presence of high angle-of-attack flaps and the generation of vortical structures aimed at managing the flow towards the underbody. Despite the complexity of the suspension geometry, its contribution to drag is only 3%, owing to the fact that arm sections are streamlined like a wing profile.

Figure 30 illustrates the pressure coefficient (C_P) on the surface of the car. The bottom of the bodywork is characterized by typical low-pressure cores at the front region of the plank (where the ground clearance is the smallest), and in correspondence of underbody and rear diffuser inlets. In close proximity to the rear tire disturbance, pressure increases and the ground effect benefits are lost.

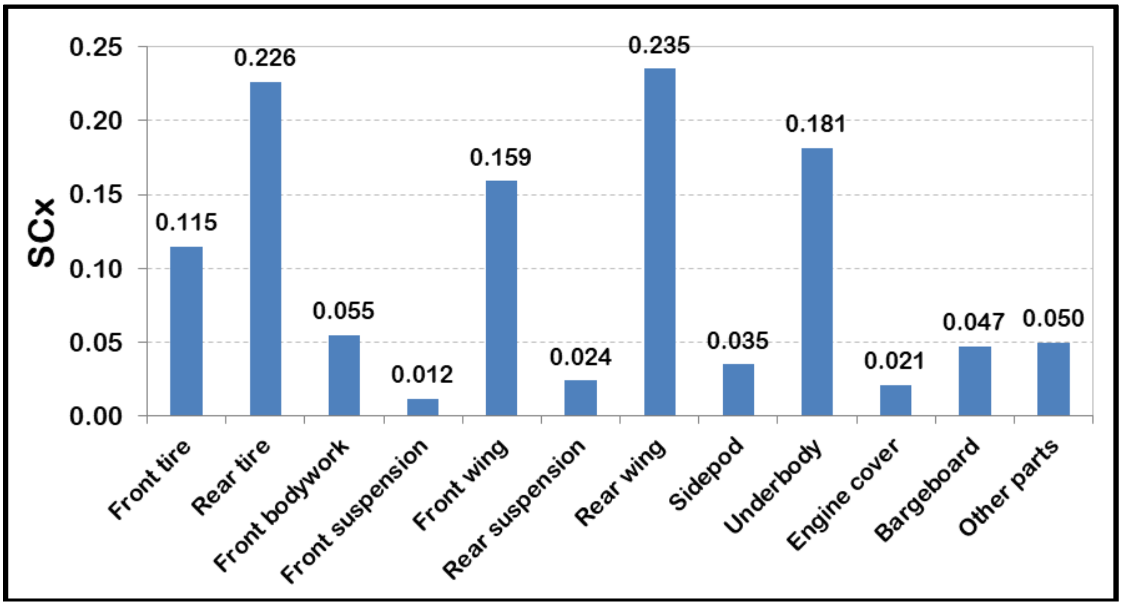

Figure 29: Contribution to drag of the main components of the car

The upper view shows the contribution to downforce of the front bodywork, due to the shape of the nose cone, and the stagnation areas in front of cockpit and rear tyres. As regards the wings, it can be noted that the rear wing generates downforce mainly due to the high camber of the airfoil design and their high angle-of-attack; on the contrary the front wing makes use of ground effect to accelerate the flow on the suction side.

Both generation of downforce and induced drag are strictly connected with the management of axial vorticity: an overall view of these three-dimensional rotational structures can be identified by the iso-surface of the scalar Q [$1/s^2$]: this variable, defined as the second invariant of the velocity gradient tensor, allows detection of the regions where the Euclidian norm of the vorticity tensor prevails over that of the rate of strain (Haller, 2005).

In light of the above, Figures 31 and 32 show respectively the iso-contour of Q and the axial vorticity plot in four significant cross sections: immediately downstream of the front wing (X = -

0.65 m, section 1), in correspondence of the bargeboard (X = 1 m, section 2) , at the diffuser outlet (X = 3.7 m, section 3) and just downstream of the rear wing (X = 4 m, section 4).

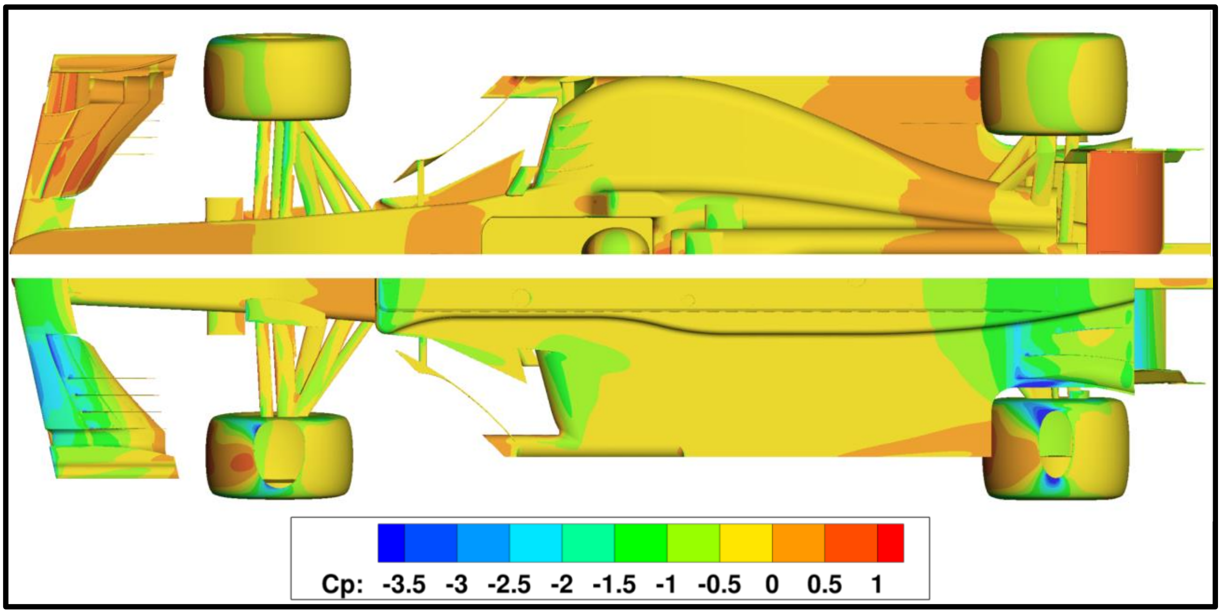

Figure 30: Pressure coefficient (Cp) contours – top and bottom view

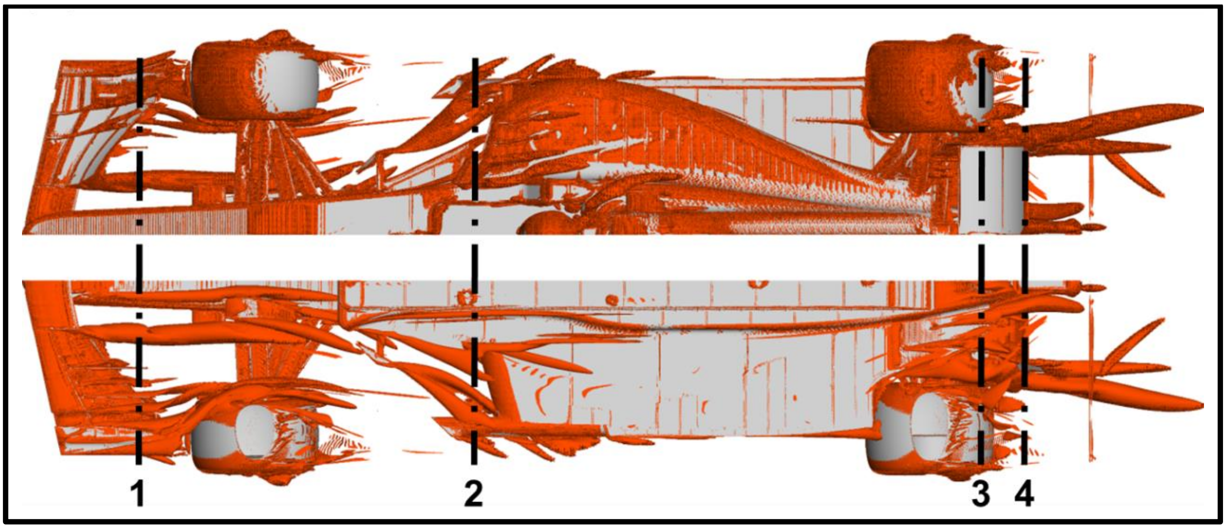

Figure 31: Iso-contour of Q = 50000 1/s2 and cross sections – top and bottom view

The former plot is useful to understand shape, position and persistency of the three-dimensional vortical structures; the latter provides information about the strength and the rotation axis of the vortices. In Figure 32 the X-axis points inside or outside the cross section, according to the reported symbol.

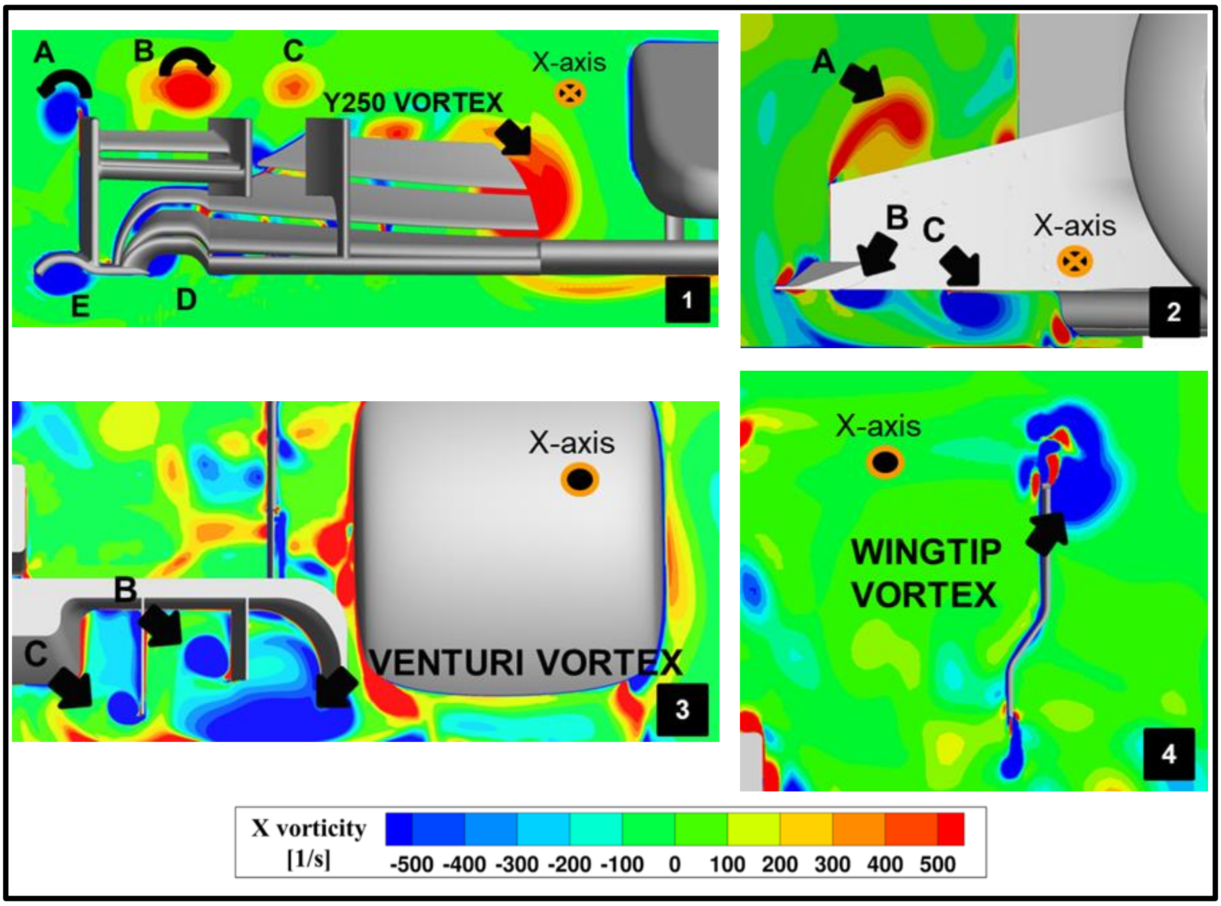

Figure 32: Axial vorticity contours – cross sections: X = -0.65 m (1), X = 1 m (2), X = 3.7 m (3) and X = 4 m (4)

The first cross section clearly shows the dual function of the front wing: in fact, it generates not only downforce but also axial vortices aimed at bypassing the front tires and energizing the flow feeding the downstream devices. Vortices 1A, 1B, 1C, 1D and 1E are created respectively by the main endplate, the cascade winglet endplate, the turning vane, the endplate foot and the wing tunnel: depending on the pressure field they are immersed in, the vortex tubes rotate clockwise or counter clockwise. The biggest diameter vortex, as indicated in Figure 32, is the so called “Y250 vortex”, because of its position on the Y-axis. It develops between the neutral middle section and the multiple flaps of the front wing, aiming at governing the flow towards the underbody inlet.

Moving downstream, one can see the vortex system characterizing the middle region of the vehicle (cross section 2). The bargeboard, apart from shielding the underbody from the tire wake, generates a pair of counter-rotating vortices: the upper one (2A) travels down the sidepod and acts as an aerodynamic skirt, sealing the low-pressure area underneath the car; the lower one (2B) energizes the flow underneath the vehicle, in cooperation with the vortex generated by the delta-shaped part of the step plane (2C). The above described flow structures develop along the entire step plane and make the underbody flow highly three-dimensional: the low-pressure core of these sort of fluid dynamic tubes contributes to the generation of downforce, in absence of side skirts isolating the underfloor. The management of the flow underneath the car will be explored in greater detail in Chapter 6.

The car rear-end is dominated by the flow structures associated with the functioning of diffuser and rear wing. Cross section 3 puts in evidence a series of three vortices confined within their respective diffuser channels. The largest one is the Venturi vortex, developing at the side of the diffuser due to the pressure difference between the bottom of the car and the region outside it; the smaller vortices (3B and 3C) are instead generated by the diffuser fences. It can be also observed that each vortex tube is coupled with a secondary structure rotating in the opposite direction, because of its interaction with the ground boundary layer. Finally, section 4 shows the wingtip vortex detaching from the rear wing: its size and persistency (Figure 31) are strictly connected with the production of high induced drag. As depicted in Figure 32, the endplates slots try to mitigate this phenomenon, thus equalizing the pressure difference between the flow within the endplate and the side region.

3.5 Conclusions

Aerodynamic performance of a F1 2017 car designed by ©PERRINN was analysed by the open-source software OpenFOAM®. The meshing phase was particularly tricky because of the sophisticated geometry of the vehicle. In view of the simulation complexity, a coupled approach was chosen to avoid numerical instability in the very first iterations and reduce the number of iterations to reach convergence. The results of the S-A RANS incompressible calculation were found to be in good agreement with the reference data in terms of drag, downforce, efficiency and front balance.

F1 car aerodynamics involves slender and blunt bodies interacting with each other and the generation of downforce is achieved in different ways: by means of inverted multi-element wings, ground effect of the underbody, Venturi effect of the diffuser and vorticity management alongside the entire vehicle bodywork. The contributions of front and rear wing to downforce are 26.3% and 27.5%, respectively; most of the remaining percentage is attributable to the underbody. Front and rear wheels are the main source of pressure drag, because they generate a huge wake. The rear wing is primarily responsible for induced drag, as a result of axial vortices detaching from the wingtips. The front wing deserves a comment of its own: in addition to local generation of downforce, it plays a key role in improving the performance of the underbody by means of creation and management of dedicated vortical structures. It appears that ground effect is the most convenient way to generate downforce: in fact, the underbody is more efficient than the front wing, and the front wing is in turn more efficient than the rear wing.

Chapter 4. Influence of Ride Height on Aerodynamic Performance

The understanding of F1 car aerodynamics consists of different steps. Firstly, the behaviour of the isolated vehicle in baseline position should be analysed, in order to grasp the basic properties of the flow field (see Chapter 4); then, changes in racing setup should be taken into account, for the purpose of testing the consistency of the aerodynamic design and determining the so called "aeromap" of the vehicle.

In this chapter, the 2017 F1 car designed by ©PERRINN (Copyright © 2011 - Present PERRINN) was modelled in different combinations of front ride height (FRH) and rear ride height (RRH). The results of the simulations put in evidence that small setup modifications lead to remarkable changes in the aerodynamic features of the vehicle and, consequently, in its dynamic behaviour.

4.1 Definition of Front and Rear Ride Height

For the purpose of defining the settings of a F1 car, in terms of front (FRH) and rear ride height (RRH), attention needs to be paid to its underfloor. As shown in Figure 33, the flat side of the underbody, which is called "step plane", is connected to the "reference plane" (XY) by means of a transition region. The middle section of the underbody consists of the plank, i.e. a phenolic resin block (formula1-dictionary.net), which can touch the ground as a result of the typical movements of the chassis, such as heave and pitch.

The ride heights of the vehicle are measured starting from the reference plane (XY) and moving alongside the Z-axis. The front ride height is measured at the front axle, where the origin of the coordinate system is located; the rear ride height is measured at the rear axle (Figure 34).

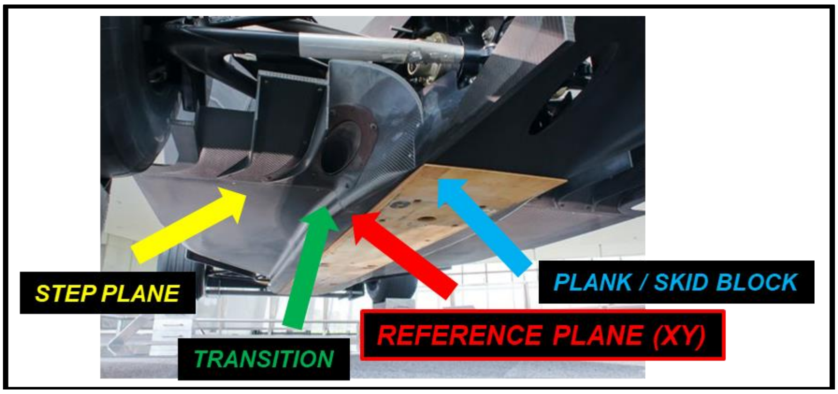

Figure 33: Underbody of the Honda RC-F1 2.0X (Honda Collection Hall, Motegi, Japan)

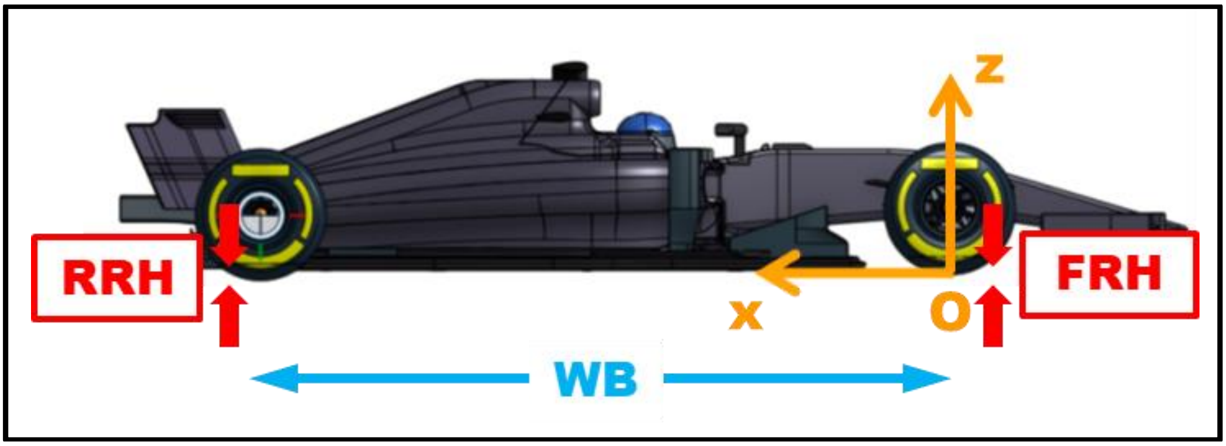

Figure 34: Definition of FRH, RRH and coordinate system of the vehicle

The distance between the two measurement points is equal to the wheelbase (WB) of the vehicle. The difference between the RRH and the FRH is strictly related to the rake angle (α), according with the following:

$$\alpha = \tan^{-1}\left(\frac{RRH - FRH}{WB}\right)$$

Equation 1: Definition of the rake angle (α)

The desired rake angle can be obtained by rotating the chassis around the Y-axis. Then the front and the rear ride heights can be fixed by translating the vehicle bodywork along the Z-axis. In racing applications, RRH is always greater than FRH (formula1-dictionary.net), leading to a positive rake angle. Figure 35 displays a few examples of vehicle setup: depending on the aerodynamic project of the car, different teams choose different rake angles and ride heights.

4.2 Mesh and Simulation Setup

The changes in ride heights led to different contact patches between the tires and the ground. Accordingly, the refinement boxes were translated according to the new positions of the chassis, in order to achieve mesh uniformity. No further adjustments were needed. Further details on simulation tools, mesh and simulation parameters can be found in the previous Chapter (sections 4.2 and 4.3).

4.3 Results and Discussion

The simulation set is composed by twelve setups: each of the four FRH (10, 15, 20, 25 mm) was tested in three RRH cases (45, 50, 55 mm). Results are collected in Table 12: as in the previous analysis, Cx and Cz are multiplied by frontal area of the car (S). It should be remembered that front balance (FB) is the ratio between the downforce acting on the front axle and the overall downforce generated by the vehicle. The baseline setup is 20 mm on the front and 50 mm on the rear (20-50): the related results are marked in bold.

Figure 35: Rake angle comparison (image from formula1-dictionary.net)

It can be observed that drag variation does not exceed 2% of the baseline value within the considered ride height range. On the other hand, downforce and front balance are affected by significant changes (6% and 7.5%, respectively): these results highlight the importance of free practice sessions and lap-time simulations in order to unlock the potential of the vehicle, when looking for the best setup.

		RRH [mm]								
		SCx [m^2]			SCz [m^2]			FB [%]		
		45	50	55	45	50	55	45	50	55
FRH [mm]	10	1.17	1.15	1.18	3.24	3.23	3.48	41.4	43.3	41.4
	15	1.14	1.17	1.18	3.17	3.27	3.46	42.0	40.1	40.5
	20	1.16	**1.16**	1.17	3.27	**3.35**	3.46	40.1	**40.3**	39.9
	25	1.14	1.15	1.16	3.14	3.22	3.37	39.2	39.1	38.9

Table 12: SCx, SCz and FB calculated in different combinations of FRH and RRH

Four out of eleven setups ensure a higher downforce (SCz) than the baseline, namely 25-55, 20-55, 15-55, 10-55. These setups are characterized by the same rear ride height (55 mm), whilst the front ride height ranges from 25 to 10 mm. Under the condition of constant rear ride height, a decrease in the front ride height results in higher rake angles. These cause an increase in downforce and front balance, thus leading to a forward shift of the centre of pressure.

Table 13 focuses on these four remarkable setups, showing the force contributions given by the main aerodynamic devices of the vehicle: front wing, rear wing and underfloor, consisting of plank and underbody. The results related to the baseline setup (20-50) are marked in bold.

Through a better exploitation of the ground effect, lower front ride heights allow the front wing to generate more downforce even more efficiently: this continuous performance improvement occurs as long as the considered front ride height is large enough to avoid massive flow separation and vortex breakdown, as described by Zhang and Zerihan (2003).

The rear wing does not work in ground effect and the considered setups have constant rear ride height; furthermore, the progressive increase in rake angle has negligible effects on the angle of attack of the rear wing: as a consequence, the related force contribution remains almost constant.

		Front Wing		Rear Wing		Plank + Underbody	
		SCx [m^2]	SCz [m^2]	SCx [m^2]	SCz [m^2]	SCx [m^2]	SCz [m^2]
setup	20-50	**0.159**	**0.886**	**0.235**	**0.923**	**0.190**	**1.940**
	10-55	0.165	0.956	0.239	0.920	0.198	1.985
	15-55	0.163	0.923	0.239	0.921	0.196	1.985
	20-55	0.160	0.895	0.237	0.920	0.194	2.006
	25-55	0.157	0.869	0.236	0.920	0.195	1.939

Table 13: Force contributions from front wing, rear wing and underfloor at different setups

Conversely, the performance of the underfloor does not show a clear trend, when decreasing the front ride height. In fact, the flow underneath the car is influenced by different factors, such as the position of the front wing, the minimum ground clearance at the underbody inlet and the rake angle. When working very close to the ground, the front wing acts like a disturbance for the flow feeding the bottom of the car. Furthermore, the combination of front ride height, rear ride height and rake angle determines the ratio between the outlet and the inlet areas of the underbody, which operates like a huge diffuser. As depicted by different authors (Cooper et al., 1998), enlarging the area ratio is beneficial for improving downforce performance, as long as the flow does non separate because of the increasingly adverse pressure gradient ad the rear end of the vehicle (Jowsey and Passmore, 2010): since the downforce generated by the underfloor does not drop sharply when changing the front ride height, it is reasonable to assume that the vehicle is not affected by early flow separation or diffuser stall.

4.4 Conclusions

All things considered, the search for the best setup is a crucial part of the aerodynamic development: as witnessed by numerical results, a variation of few millimetres in front and rear ride height may seriously affect the performance of the car, both in terms of overall downforce and front balance, which is closely linked to vehicle dynamics and driveability. As regards the behaviour of the most important aerodynamic devices, it can be concluded that the rear wing is not significantly influenced by the setup; however, ride height and rake angle play a key role in establishing the operating conditions of front wing and underbody, whose aerodynamic behaviour is closely interdependent.

Chapter 5. Slipstream Effects on Aerodynamic Performance

Despite the aerodynamic setup is optimised for freestream low-turbulence flows, F1 cars run in off-design conditions, namely in wake flows, for most of the race. When two vehicles race in close proximity to each other, the lead car can dramatically affect the flow feeding the following car, which experiences a noteworthy change in its aerodynamic performance.

2017 Technical Regulations have deeply modified the appearance and the aerodynamic behaviour of F1 cars. Both mechanical and aerodynamic grip have increased significantly: wider suspension tracks and tyres have been accompanied by wider step plane and diffuser, larger bargeboards and wings (Piola and Somerfield, 2016). As a result, 2017 cars are much faster than those from 2016, but there is no guarantee that the new aerodynamic package shows a good behaviour when operating in wake flows. A robust aerodynamic performance in slipstream is crucial for allowing safer and easier overtaking, thus deserving special attention.

Several studies regarding the aerodynamic behaviour of sport and stock cars in slipstream or in critical stability conditions have been conducted over the last decades. Romberg et al. (1971) investigated from an experimental point of view the performance of a NASCAR vehicle in drafting and passing situations, focusing on the influence of aerodynamics phenomena on car handling. Dominy et al. (2000) examined the pitch sensitivity of late ‘90s Le Mans Prototype Race Cars, which made extensive use of ground effect to generate downforce.

There are also few academic studies investigating the behaviour of open-wheeled racing cars in wake flows. Notable amongst those are the paper by Dominy (1990) and the recent analysis by Newbon et al. (2017). The former dealt with an experimental investigation of the interaction between two F1 cars from the late ‘80s. The measured downforce loss characterizing the slipstreaming car is significant (-36%), but much lower than that affecting a 2017 F1 car running in wake flow, on equal terms (-57%). The front balance was also subjected to a dramatic change but, unlike the case of 2017 F1 cars, the centre of pressure moved rearwards. The latter explored, both experimentally and numerically, the behaviour of a simplified Grand Prix car, whose geometry is compatible with the late ’90s F1 Technical Regulations: the documented results are in line with those provided by Dominy (1990), both in terms of downforce loss and front balance shift. Special mention should be given to the numerical investigation carried out by Dynamic Flow Solutions Ltd., which focuses on a F1 car designed according to the 2017 FIA Technical Regulations (McBeath, 2017). Unlike the vehicles from ‘80s (Dominy, 1990) and ‘90s (Newbon et al., 2017), current F1 cars are characterized by a huge number of sophisticated aero devices, which make use of axial vortices to create downforce. Results of the simulations put in evidence a dramatic downforce loss, mostly concentrated on the rear axle. This last work has been taken as a starting point for the pursuit of the current investigation.

After the ride height analysis described in Chapter 5, the following section of the research embraces the slipstream investigation in order to quantify any change in the aerodynamic behaviour of a F1 car during a race weekend, depending on the driver necessities, truck conditions and interaction with other vehicles. As proven by the results of the numerical simulations, the changes in the aerodynamic behaviour of a F1 car running in slipstream are so great that the fine tuning of the vehicle setup is completely disrupted. Tandem-running simulations were performed with no sideway offset, based on an assessment of the worst case condition for the following car. This study is an original contribution to this topic, especially when dealing with the complexity of a real F1 car (©PERRINN 2017 F1), under the current FIA Technical Regulations.

The aerodynamic performance was evaluated in terms of drag and downforce coefficients, efficiency and front balance. Emphasis was placed on the comparison between the vehicle in freestream flow and the vehicle operating in wake flow, both in terms of pure performance and safety.

5.1 Mesh and Simulation Setup

The size of the virtual wind tunnel used for the slipstream investigation is the same as that for the isolated vehicle simulations: previous tests on the single vehicle, in a range of different positions along the X-axis, demonstrated that the reduced distance between the mesh outlet and the rear-end of the 2nd vehicle is adequate for providing reliable results in terms of global performance coefficients (drag, downforce, front balance and efficiency). The number of cells required for double vehicle meshes is approximately 180 million, which is twice that of the single vehicle. Figure 36 shows two slices of the volume mesh applied for the slipstream analysis, putting in evidence the refinement boxes around the vehicles. The distance (d) between the two car is measured from the rear crash of the lead car to the nose cone of the following car. The boundary conditions of the following car are the same as those used for the lead car.

5.2 Results and Discussion

Two identical vehicles were examined in tandem-running simulations, at four different distances: 0.5L, L, 2L, 4L, where L is the total length of the vehicle (5.38 m). The baseline setup was assumed for this analysis (20-50).

Table 14 shows drag (SCx), downforce (SCz), efficiency (Cz/Cx) and front balance (FB) of the car in 2nd place (P2) and the percentage change of the aforementioned performance coefficients with respect of the isolated vehicle in freestream flow. For the sake of clarity, the data collected in the right table are also represented in graphical form (Figure 37).

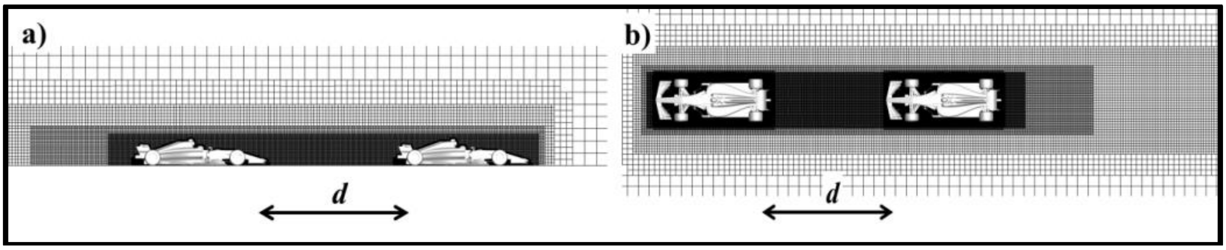

Figure 36: Detail of the mesh domain – a) side view of the symmetry plane, b) top view of the ground

P2 car	*SCx [m²]*	*SCz [m²]*	*Cz/Cx*	*FB*
0.5L	0.79	-1.44	1.8	0.54
L	0.89	-1.89	2.1	0.57
2L	0.97	-2.46	2.5	0.50
4L	1.05	-2.79	2.7	0.47

P2 car	*SCx [m²]*	*SCz [m²]*	*Cz/Cx*	*FB*
0.5L	-32%	-57%	-38%	+35%
L	-23%	-44%	-28%	+42%
2L	-16%	-27%	-14%	+25%
4L	-9%	-17%	-7%	+18%

Table 14: Performance coefficients related to the car in 2nd place and percentage change with respect of the isolated vehicle in freestream flow

The results reveal that the approach to the lead car is already challenging at a distance of 4L (more or less 21 meters): the following car undergoes a 17% reduction in overall downforce, in the face of a 9% decrease in drag. As the distance between the two vehicles decreases, the aerodynamic performance of the following car is getting worse and worse: in close proximity to the leader (d = 0.5L), it loses more than 55% of total downforce in the face of a 32% decrease in drag. In addition to a dramatic loss of downforce, the driver of the P2 car experiences more oversteer because of significant increases in front balance (from 18 to 42%). The combination of these two factors leads to safety problems during braking and high-speed cornering.

Given that the weight distribution of 2017 F1 car is around 45% on the front axle (McBeath, 2017), the aerodynamic front balance should not exceed 45% for safety and stability issues: however, this is not the case when the car is working in slipstream (FB values range from 47% to 54%).

The dynamic behaviour of the vehicle in high-speed corners is sketched in Figure 38. When the centre of pressure (CoP) is behind the centre of gravity (CoG), the yawing moment given by the aerodynamic forces counterbalances the driver’s steering input and thereby stabilizes the vehicle.

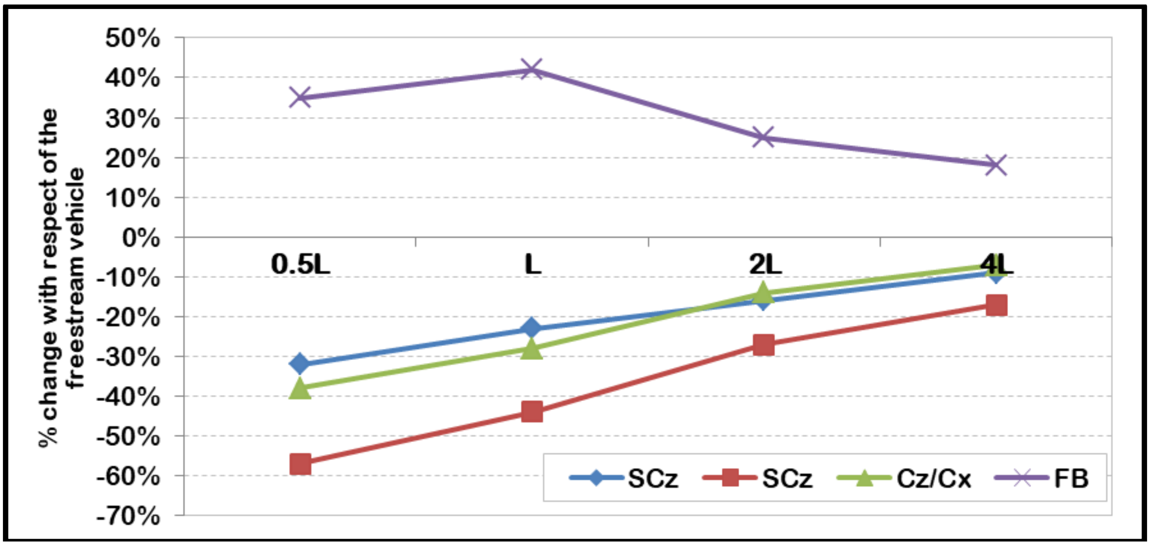

Figure 37: Percentage change of the P2 car performance with respect of the freestream vehicle

On the contrary, when the CoP is ahead of the CoG, the yawing moment tends to increase the sideslip angle: any longitudinal or lateral irregularity (bumps, wind gusts…) makes the vehicle unstable, forcing the driver to steering corrections (Casiraghi, 2010).

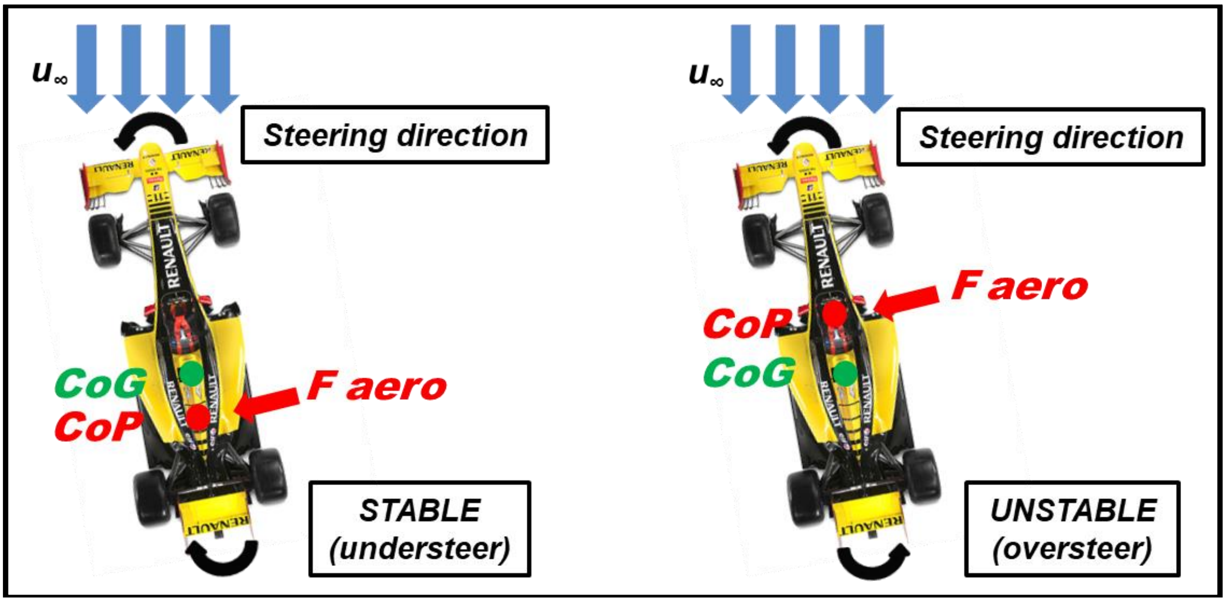

Figure 38: Influence of the centre of pressure (CoP) position on vehicle stability

To sum up, the overall prediction is consistent with that obtained by Dynamic Flow Solutions Ltd. (McBeath, 2017), in terms of performance changes in downforce, drag, efficiency losses and front balance shift.

Then, the analysis focused on the most important aerodynamic components mounted on the vehicle. Table 15 collects the data related to drag and downforce generated by the front wing in slipstream.

Front Wing - P2 car	*SCx [m^2]*	*SCz [m^2]*
0.5L	0.13	-0.63
L	0.16	-0.80
2L	0.17	-0.85
4L	0.17	-0.88

Front Wing - P2 car	*SCx [m^2]*	*SCz [m^2]*
0.5L	-19%	-28%
L	-0%	-9%
2L	+6%	-3%
4L	+6%	-0%

Table 15: Performance of the front wing in 2nd place: absolute values and percentage change with respect of the isolated vehicle in freestream flow

The front wing loses a significant amount of downforce (-28%) only when it is in close proximity to the lead car (d = 0.5L): for greater distances, the downforce loss is minimal. When distance between the two vehicles equals 2L or 4L, the drag generated by the front wing mounted on the following car is slightly greater than that of the front wing operating in freestream, perhaps because of the turbulent flow conditions. On the opposite, when the cars are very close to each other, the drag of the front wing sharply decreases because the car in 2nd position is operating inside the wake of the lead car.

As reported in Table 16, slipstream heavily penalizes the rear wing, that starts to lose a large amount of downforce pretty far from the leader (-28% when d = 4L). The performance loss is progressive and reaches its peak at the minimum distance between the two cars (-55% when d = 0.5L). Since the drag decreases at the same rate as the downforce, the rear wing efficiency remains nearly constant. So far, results indicate that rear wing suffers more than front wing in slipstream: the lack of downforce in the car rear-end explains the increase in front balance and the related forward shift of the centre of pressure.

The most surprising outputs come from the analysis of the underfloor, including the underbody and the plank (Table 17). The downforce generated by the underfloor drops sharply as the distance between the two cars decreases. Moreover, since drag diminishes slower than downforce, the underfloor efficiency progressively declines, when approaching the lead car.

The underfloor is the component that suffers the most from running in close proximity to the lead car, since the downforce loss exceeds 60% at the minimum distance of d = 0.5L. It follows that generating downforce by means of the underfloor is not suitable for overtaking. This conclusion may sound strange, because in the late ‘70s and early ‘80s F1 cars were able to race closely and overtaking each other, despite the underbody played a key role in generation of downforce. The explanation can be found in the adjustments of technical regulations which have occurred in F1 over the last 40 years, as clearly illustrated by Somerfield and Piola (2017). Here the major steps in the evolution of aero regulations are briefly recalled.

Rear Wing - P2 car	*SCx [m^2]*	*SCz [m^2]*
0.5L	0.12	-0.41
L	0.13	-0.43
2L	0.16	-0.56
4L	0.19	-0.66

Rear Wing - P2 car	*SCx [m^2]*	*SCz [m^2]*
0.5L	-50%	-55%
L	-46%	-53%
2L	-33%	-39%
4L	-21%	-28%

Table 16: Performance of the rear wing in 2nd place: absolute values and percentage change with respect of the isolated vehicle in freestream flow

Underfloor - P2 car	*SCx [m^2]*	*SCz [m^2]*
0.5L	0.10	-0.75
L	0.13	-1.08
2L	0.16	-1.42
4L	0.17	-1.62

Underfloor - P2 car	*SCx [m^2]*	*SCz [m^2]*
0.5L	-47%	-61%
L	-32%	-44%
2L	-16%	-27%
4L	-11%	-16%

Table 17: Performance of the underfloor in 2nd place: absolute values and percentage change with respect of the isolated vehicle in freestream flow

At the beginning of the “Ground Effect Era”, F1 underbodies exploited the ground effect by means of wing-shaped sidepods and sideskirts sealing the flow underneath the vehicle. Lotus 78 (Figure 39) and 79 (Figure 40) may be considered as the most representative of this era. Vortex generation and management did not play a significant role in generation of downforce: the front wing was characterized by an essential geometry; furthermore, bargeboards, diffuser strakes and other types of vortex generators were not mounted on the vehicle.

As a result of the implementation of these principles, the flow downstream of the lead vehicle was basically clean and two-dimensional: the following car was therefore able to generate an adequate amount of downforce. However, the extreme use of ground effect was linked with some serious safety problems. Any damage to the sideskirts or bump on the track could cause an abrupt loss of downforce, which entirely depended on the sealing effect of the underbody low-pressure area and the extremely low ride height. In this respect, the drivers experienced an annoying phenomenon known as “porpoising”, a sort of resonance resulting from the uninterrupted heaving of the car. Lastly, high g-forces made suspensions prone to breaking.

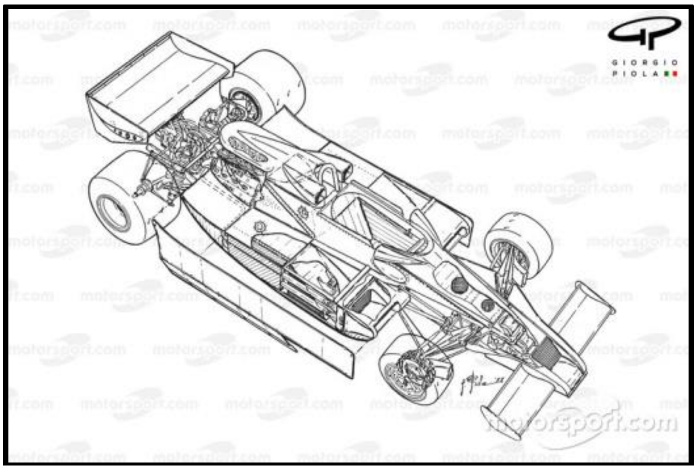

Figure 39: Lotus 78 1977 detailed overview (photo by Piola)

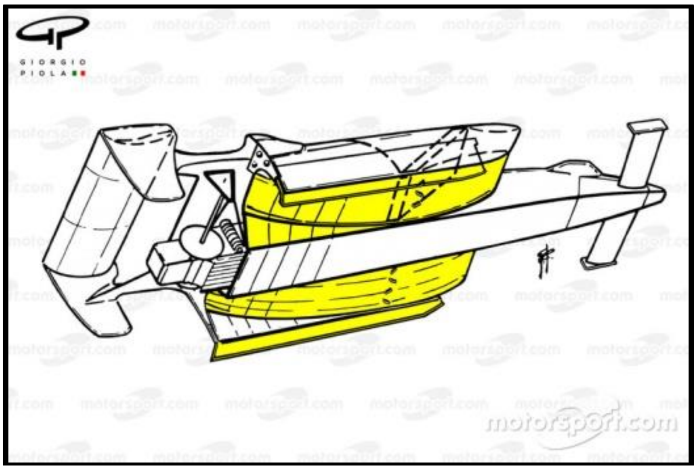

Figure 40: Lotus 79 ground effect tunnels (photo by Piola)

From the early ‘80s, FIA gradually changed the technical regulations, for the purpose of removing the original ground effect from F1 cars: sideskirts were banned, a mandatory ground clearance was introduced and, finally, the sidepod Venturi channels were replaced by flat bottom and diffuser. In order to control the increasing performance, ‘90s were characterized by further modifications to the technical regulations, such as the introduction of plank, step plane and restrictions to the diffuser geometry. Since the underbody ground effect was no longer available in its original and more effective version, new ways to generate downforce were badly needed. As already seen in Chapter 4, current F1 cars make extensive use of streamwise vortices for sealing the low-pressure region underneath the car and feeding the underfloor. The entire vehicle is involved in generation and management of axial vorticity (from front wing add-ons to diffuser strakes, from bargeboards to underbody inlet devices), that is why flow downstream of the lead vehicle is highly swirling and three-dimensional. The following car, which owes its aerodynamic effectiveness to correct position, strength and persistence of the axial structures around its bodywork, is not designed for managing chaotic flows: consequently, its sophisticated aerodynamic devices do not work properly, thus causing a dramatic loss of downforce. In this regard, the following section investigates in detail the features of the wake flows. Figure 41 shows the streamwise velocity (U) contours on the symmetry plane.

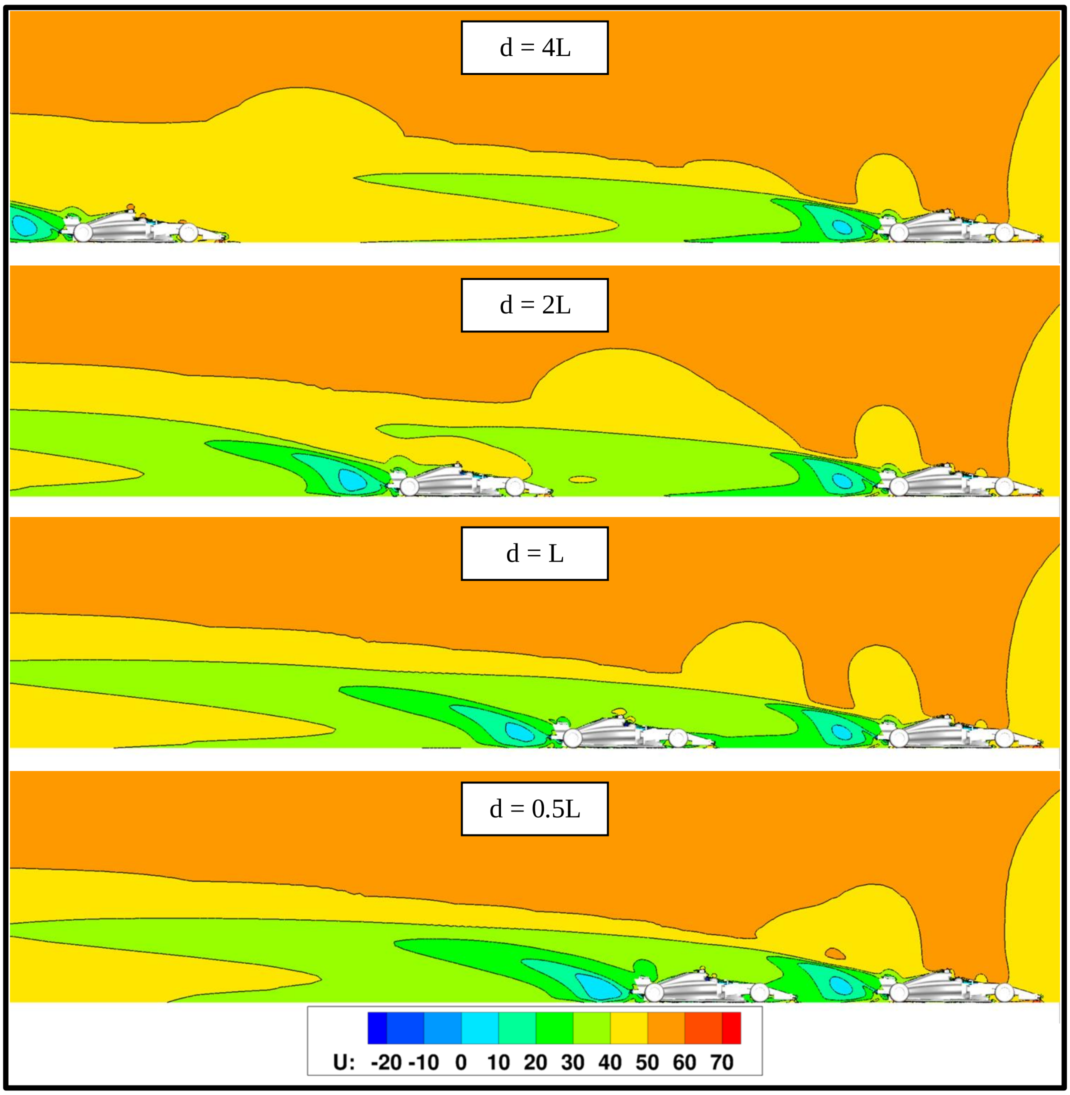

Figure 41: Streamwise velocity plot (U) on the symmetry plane (XZ plane) – d = 4L, 2L, L, 0.5L

It is clear that the car in 2nd position is fed by low kinetic energy flow: when the gap between the two vehicles is greater than 20 meters (d = 4L), the wake of the lead car is capable to affect the downstream flowfield.

When the distance between the two vehicles is lower than 2L, a unique wake structure can be detected: the streamwise velocity of the flow feeding the P2 car ranges from 20 m/s to 30 m/s (from 40% to 60% of the freestream flow).

Figure 42 displays the streamwise velocity (U) contours on a plane parallel to the ground, at Z = 0.1 m. This slice is noteworthy because it intercepts an important part of the flow feeding the front wing and coming out from the diffuser. As the distance between the two vehicles decreases, the separation region behind the P2 car becomes more evident. For d = 0.5L, the presence of reversed flow can be seen close to the diffuser outlet. Shifting attention to the lead car, it can be noted that the shape of its wake is not greatly affected by the approach of the following car.

This qualitative result is supported by quantitative evidences: in fact, the performance coefficients of the car in 1st position undergo a variation of about 1÷2% only when the distance between the two vehicle is equal to 0.5L.

Attention now turns to the streamline plots, in order to analyse the functioning of the main components of the vehicle, i.e. front wing, rear wing and underfloor. The streamlines feeding the car in 1st position (P1) and the car in 2nd position (P2) help to understand the difference between the performance in freestream and wake flows. For comparison purposes, Figure 43 shows the streamlines feeding the front wing mounted on the car running in freestream flow. As easy to guess, the flow is perfectly aligned in X-direction and it is characterized by freestream undisturbed velocity (50 m/s). The streamlines feeding the front wing of the P2 car at different distances (d = 4L, 2L, L, 0.5L) are plotted in Figure 44.

When d = 4L, the streamlines impinging on the front wing show the same velocity magnitude as the freestream flow and they are almost perfectly aligned with it. This portion of flow is not affected by any energy loss, because the streamlines bypass the lead car from each side, without interacting with any upstream device. Even when the distance is halved, flow energy and streamline direction are still preserved. At d = L (5.38 m), streamlines begin to be deflected inboard by the wake of the P1 car: despite this, the swept front wing still shows a robust behaviour. At the minimum working distance (d = 0.5L), the streamlines feeding the middle region of the wing are characterized by rotational low-speed flow, coming from the wake of the leading car: luckily, the mid-section of the front wing does not generate downforce, in accordance with the FIA Technical Regulations.

The same comparison between the isolated vehicle and the car operating in slipstream has been conducted focusing on the rear wing (Figures 45 and 46).

Under normal conditions, the rear wing is fed by perfectly aligned streamlines (Figure 45), as well as the front wing. As documented by Figure 46, the streamlines feeding the P2 rear wing are characterized by a slight inboard deflection when the distance between the vehicles is equal to 4L and 2L, but the loss of downforce is significant. It might be that the rear wing is more sensitive to the streamline direction than the front wing because of the low aspect ratio, the straight shape and the presence of huge endplates. At lower distances ($d \leq L$), the rear wing works with low-energy rotational flow passing through the vehicle bodywork: the velocity of the streamlines feeding the rear wing is roughly halved compared to that of the freestream flow. This evidence indicates that the entire aerodynamic system of the P2 car has been heavily disrupted by the leading car.

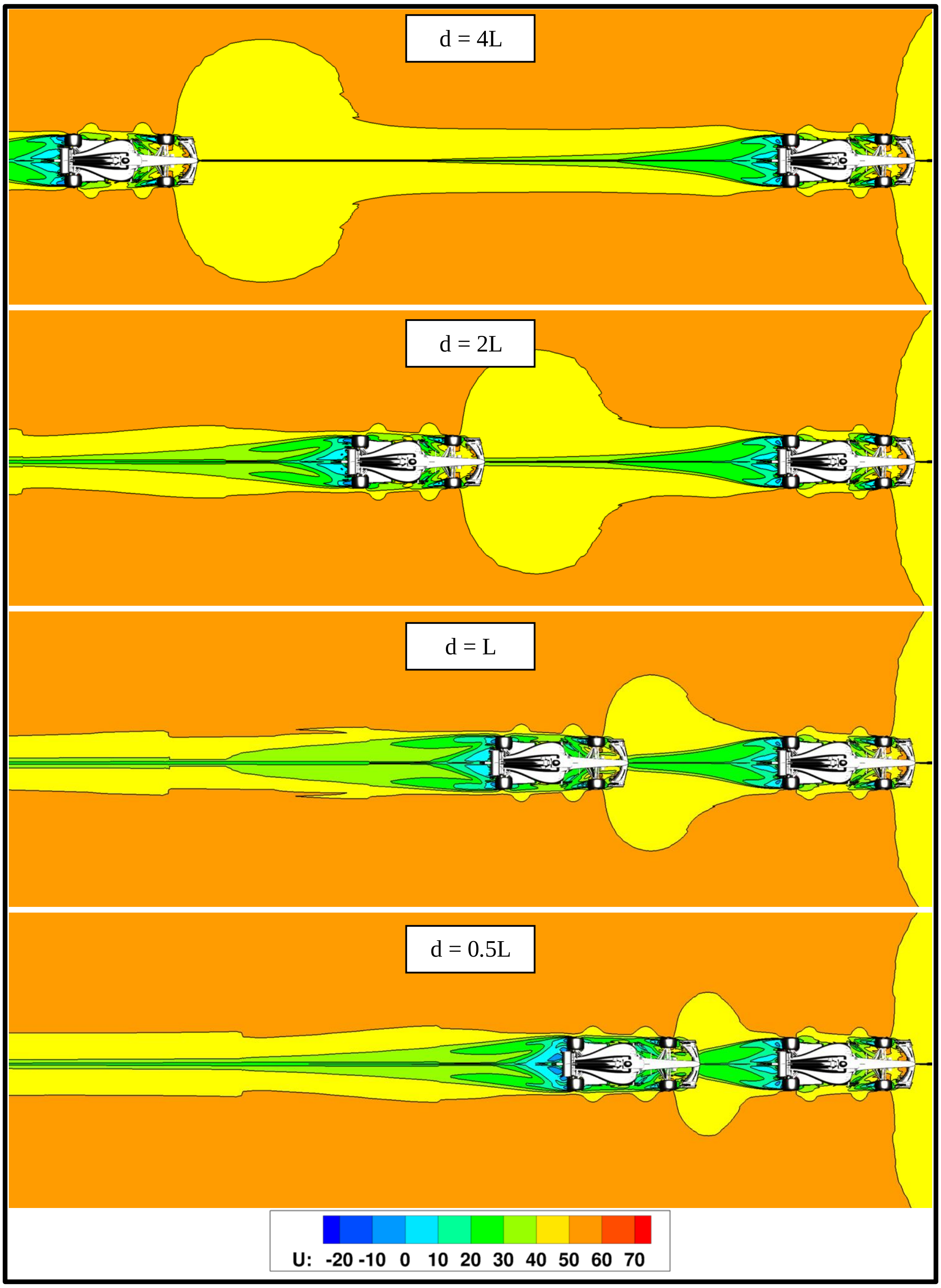

Figure 42: Streamwise velocity plot (U) on XY plane (Z = 0.1 m) – d = 4L, 2L, L, 0.5L

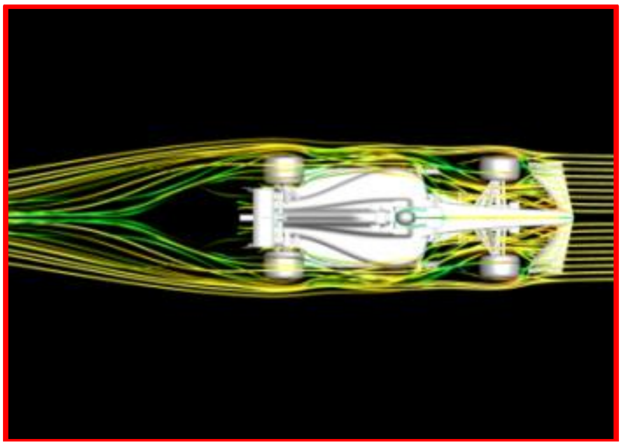

Figure 43: Streamlines feeding the front wing – isolated vehicle (P1)

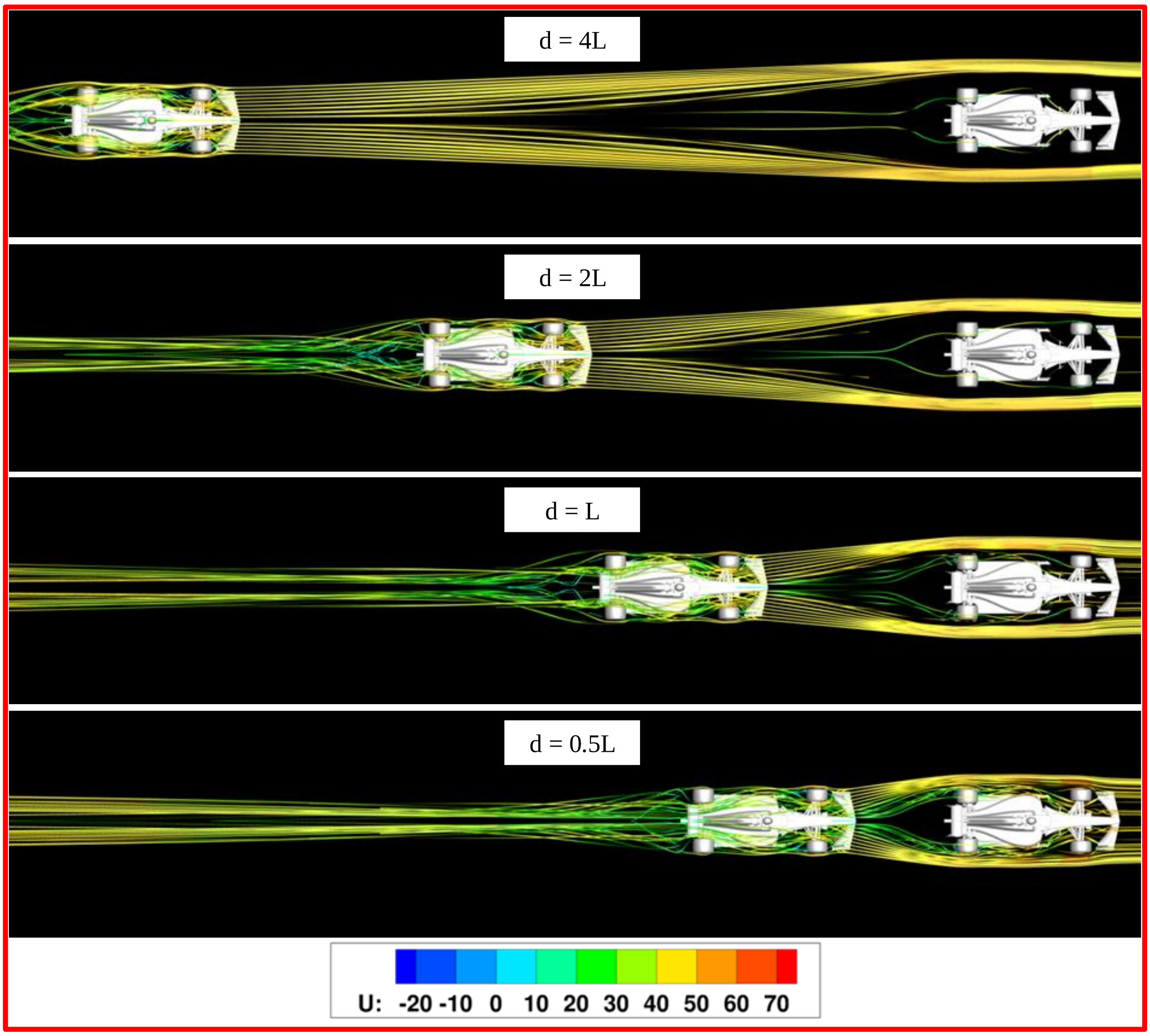

Figure 44: Streamlines feeding the front wing – following car (P2) – d = 4L, 2L, L, 0.5L

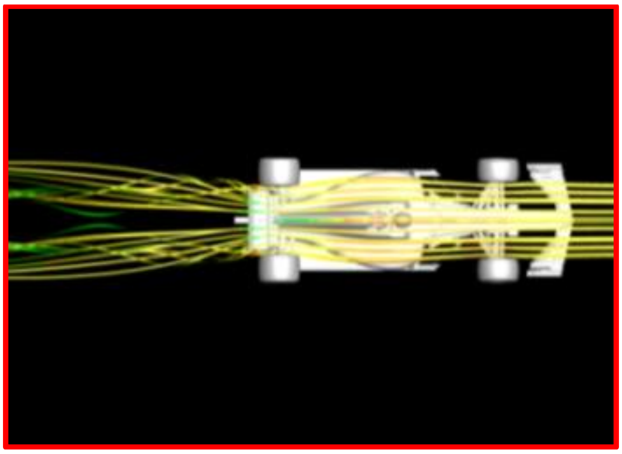

Figure 45: Streamlines feeding the rear wing – isolated vehicle (P1)

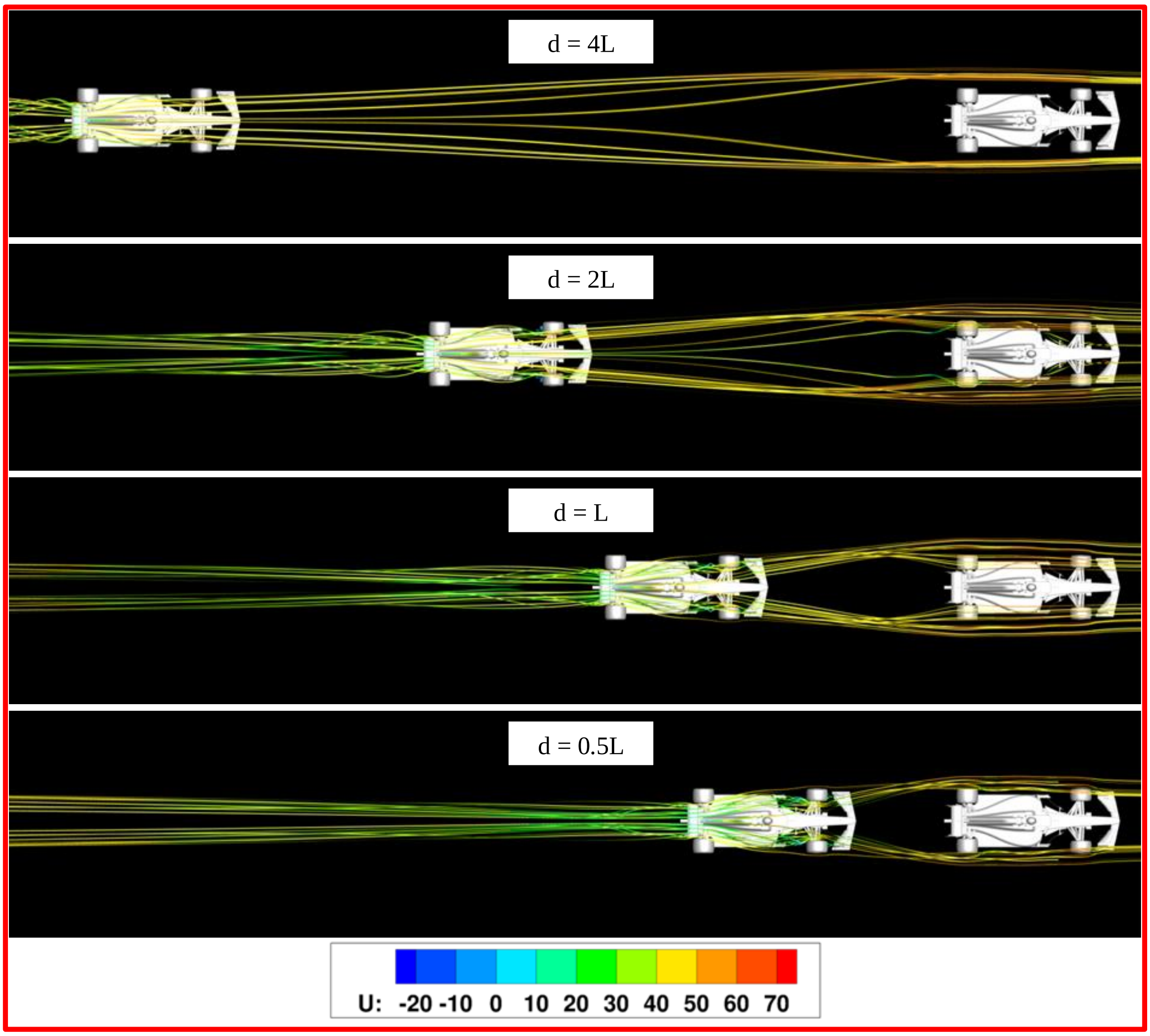

Figure 46: Streamlines feeding the rear wing – following car (P2) – d = 4L, 2L, L, 0.5L

Finally, Figures 47 and 48 describe how the underfloor works in freestream and wake flows, respectively. In design condition the underbody is fed by energized flow coming from the front wing and bypassing the front tyre. The streamlines are not straight: as seen previously, generation and management of vortices characterize current F1 underbodies. When d = 4L, most of the streamlines feeding the P2 underbody bypasses the lead car from each side and preserve the freestream flow energy. Moreover, the observed inboard deflection is negligible. When the distance is halved, the underbody performance starts worsening because of the increasing inboard deflection and the mutual disturbance of the streamlines.

Once the vehicles are very close to each other, the middle section of the underfloor is fed by low-energy and rotational flow coming from the lead car, thus causing huge performance losses. The central section of the underfloor is particularly sensitive to wake flows, because it works much closer to the ground than the front wing. In the baseline configuration (20-50) the ground clearance of the front wing is 86 mm, while the smaller gap between the step plane and the floor is only 13 mm: the low energy and highly-rotational flow cannot be squeezed through such a small slot, hence causing a significant downforce loss.

Pressure coefficient (C_P) plots are useful to appreciate how changes in the flow structure result in local performance losses (Figures 49 and 50). The gradual but significant performance loss of the rear wing is well documented: the approach to the lead car compromises the functioning of both its pressure and suction side. Also, the contribution to downforce from the stagnation region in front of the rear wheels is decreasing little by little. Conversely, the front wing is proven to be more robust when running in slipstream. Looking at the bottom view, one can notice the progressive disappearance of the typical low-pressure cores at the underbody inlet. Moreover, the diffuser contribution to downforce gets worse and worse, until it becomes negligible.

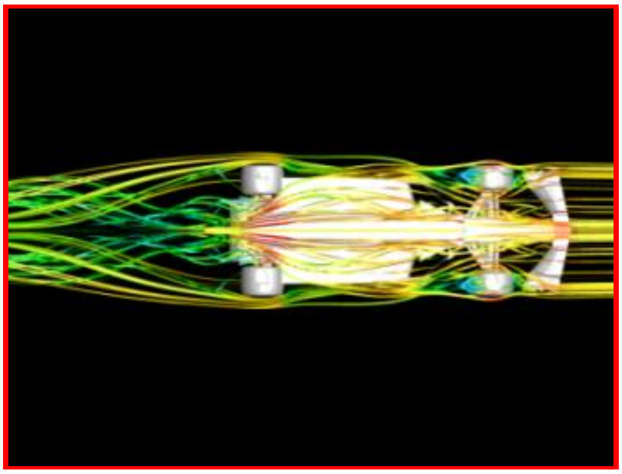

Figure 47: Streamlines feeding the underfloor – isolated vehicle (P1)

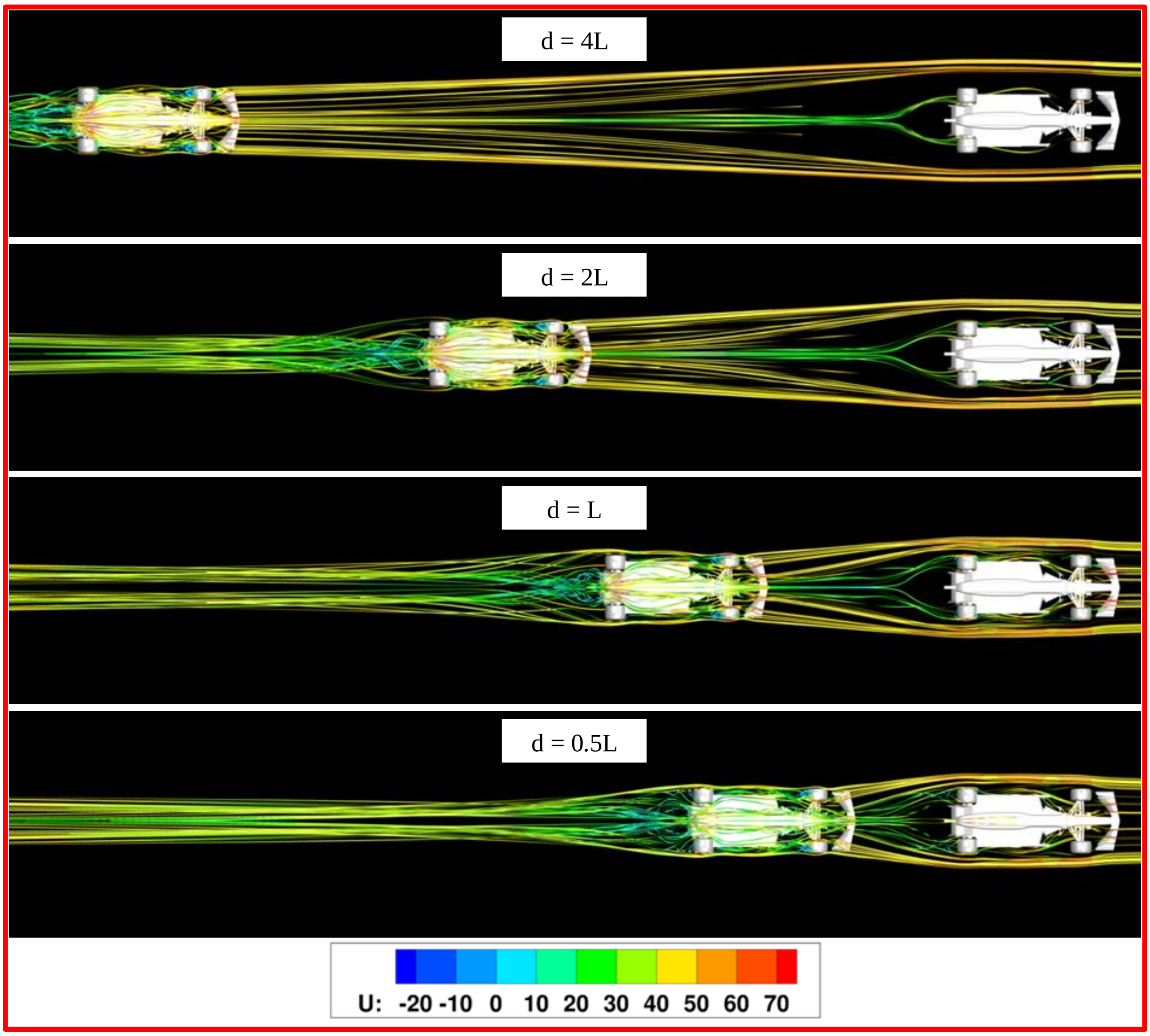

Figure 48: Streamlines feeding the underfloor – following car (P2) – d = 4L, 2L, L, 0.5L

The last contribution to the comprehension of the aerodynamic phenomena related to slipstream comes from the iso-contour of the scalar Q [$1/s^2$], defined as the second invariant of the velocity gradient tensor (see Figures 51 and 52). It is useful for disclosing shape, position and persistency of the three-dimensional axial vortices, which are of crucial importance in the downforce generation processes. As already described in Chapter 4, axial vortices can have different functions: they can be useful for bypassing obstacles (such as the front tires), sealing portion of fluid or entraining fresh flow from the side of the vehicle, creating low-pressure cores underneath the car. Vortex size and strength are strongly affected by running in close proximity to another vehicle. The wingtip vortices detaching from the rear wing of the following car are less persistent than those from the vehicle running in freestream flow (see Figure 31): since they are strictly connected to the pressure difference between the upper and the lower side of the wing, their premature deterioration indicates significant losses of downforce. In other words, the strength of the wingtip vortices is a direct consequence of the vertical load generated by the wing itself. The vortex system coming from the diffuser walls loses a large part of its strength as the distance between the vehicles decreases. Slipstreaming conditions also undermine the effectiveness of the counter-rotating vortices generated by the bargeboard. Concerning the front-end of the vehicle, it can be observed that the flow structures generated by the central section of the front wing, such as the Y250 vortex, are more affected by the wake flow than the ones produced by the side of the wing.

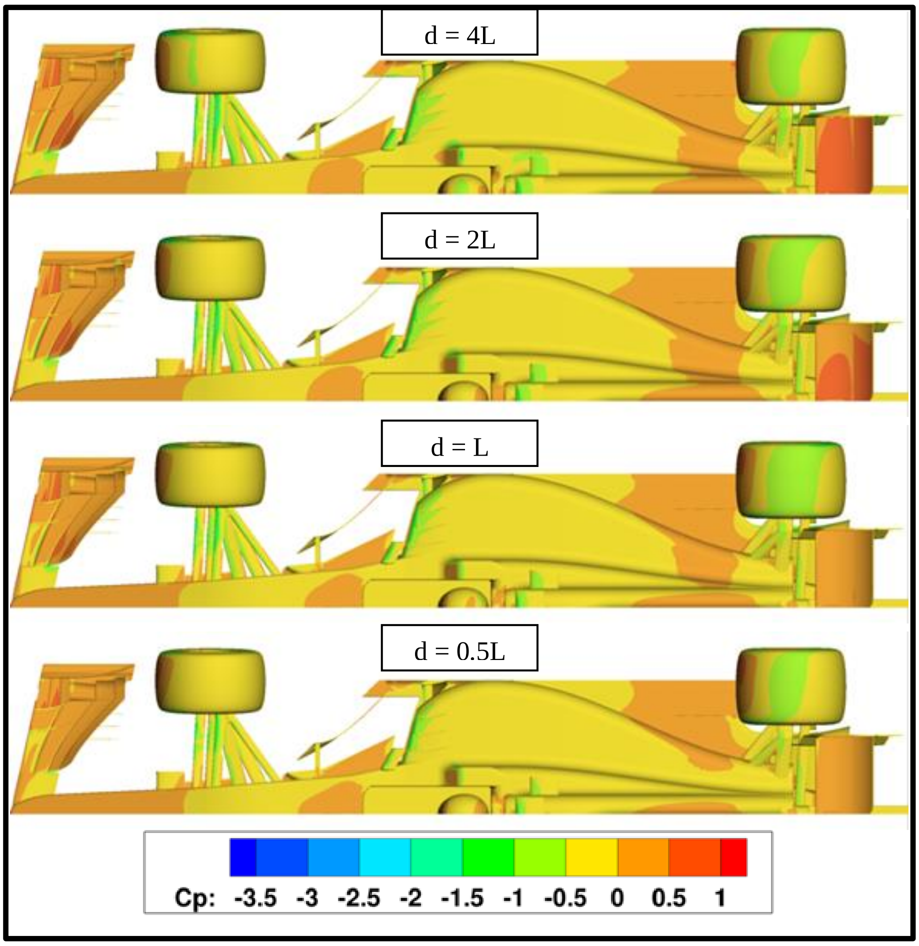

Figure 49: Pressure coefficient (Cp) plot related to the P2 car – top view – d = 4L, 2L, L, 0.5L

5.3 Conclusions

Every effort made in finding the best setup and hence optimizing the lap-time in freestream conditions may vanish when the vehicle runs in wake flows: the results of the slipstream simulations clearly show that 2017 aerodynamic configuration has made F1 cars considerably faster but, on the other hand, the overtaking issue is still unsolved.

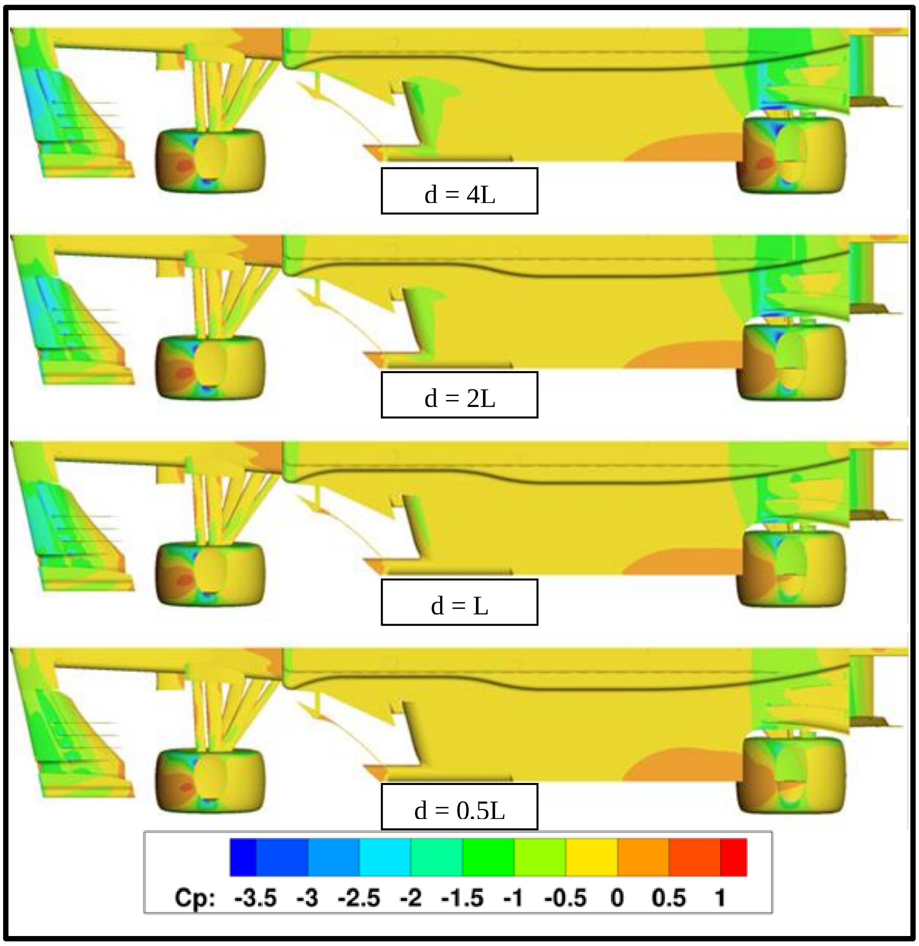

Figure 50: Pressure coefficient (Cp) plot related to the P2 car – bottom view – d = 4L, 2L, L, 0.5L

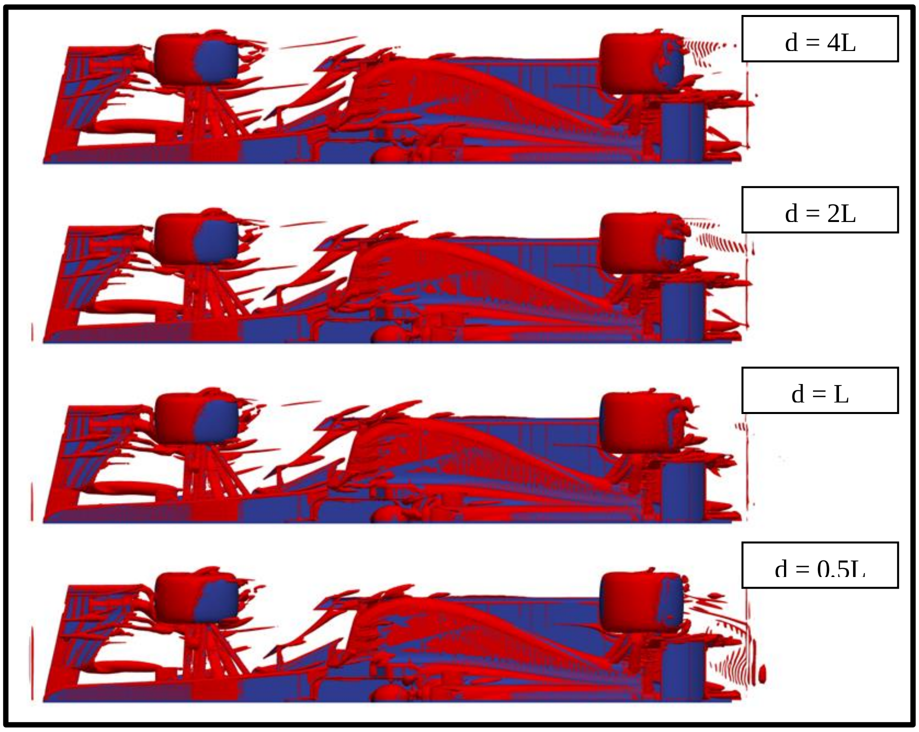

Figure 51: Iso-contour of Q = 50000 1/s2 related to the P2 car – top view – d = 4L, 2L, L, 0.5L

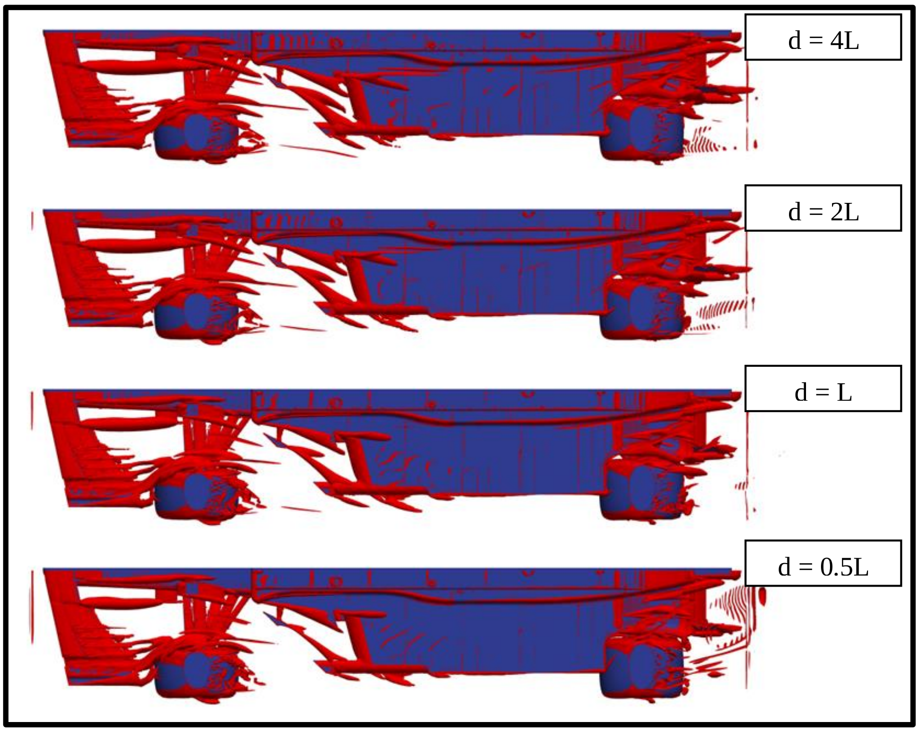

Figure 52: Iso-contour of Q = 50000 1/s2 related to the P2 car – bottom view – d = 4L, 2L, L, 0.5L

The loss of downforce in slipstream is still a major problem and, as if that was not enough, the driver experiences a significant change in the dynamic behaviour of the vehicle: the centre of pressure shifts forward and hence the front balance rises above the desired level of 0.45, which corresponds to the vehicle weight distribution.

The above described performance worsening undermines the opportunity of approaching the lead car in high-speed corners and breaking safely during the overtaking manoeuvre. Other adverse consequences of running in close proximity to the leader are related to the thermal management of the vehicle: both tires and engine may suffer from overheating, thus reducing their lifespan.

Chapter 6. Aerodynamic Development of the Baseline Vehicle

After having analysed in detail the aerodynamic behaviour of the original 2017 F1 car (F1base) designed by ©PERRINN, this chapter is devoted to aerodynamic development of that vehicle. Starting from the baseline geometry, different devices were designed, integrated on the vehicle and numerically tested. Three different aero packages were developed, in order to meet the performance requirements of low (F1UR4LD), medium (F1UR4MD) and high-downforce (F1UR4HD) tracks.

In light of the information provided by the tandem-running simulations (Chapter 6), few components, such as the front wing, were developed in accordance with 2017 FIA Technical Regulations. Conversely, other devices were designed following the technical guidelines of past F1 seasons or exploring new paths, with the aim of improving the robustness of the aerodynamic design in wake flows. However, the fundamentals behind the current F1 car aerodynamics were not turned upside down: the final goal of the research is to find simple, effective and easy to implement aerodynamic solutions for the purpose of improving overtaking, without compromising lap-time performance and raising development costs.

In this chapter all the devices related to the new aerodynamic configurations are described in detail. The related set of CFD simulations evaluated the performance of the new vehicles in freestream flow; the slipstreaming behaviour of the new aerodynamic configurations will be analysed later on, in a separate section (see Chapter 8).

6.1 Description of the New Components

6.1.1 Front Wing

As shown in Figure 53, the baseline front wing underwent a lot of changes, which are common to all the configurations. In the light of the above post-processing of the performance predictions related to the baseline car (F1base), two of the four fences mounted on the first flap were removed (Figure 54). Specifically, the inboard mounted fences were not able to generate any useful vortex in addition to disrupting the flow profile on the suction side of the flap. The span of the cascade winglets was extended by 60 mm: as a consequence, the turning vane mounted on the main plane was moved from the original position by 40 mm along the Y-axis. In addition, the angle of incidence of the cascade endplate and the turning vane was increased up to 25°, for the purpose of increasing the vortex strength bypassing the front tyres.

Inside the main endplate of the wing, an extra high-cambered small profile was added (Figure 55). The external side of the main endplate now comes with a new appendix, which was intended to double the endplate foot. A Gurney flap was also introduced on the upper component of the wing tunnel.

The geometry of the flaps makes the difference between the three types of wing. The low-downforce configuration (F1UR4LD) is characterized by a main plane and three flaps: the span of the 2nd and the 3rd flap was reduced by means of a cut in proximity to the FIA control section. The medium-downforce wing assembly (F1UR4MD) preserves the original profile geometry, but the 2nd and the 3rd flaps are characterized by a lower angle of attack (-1.5° and -2°, respectively). The high-downforce configuration (F1UR4HD) provides for the installation of a small extra profile, equipped with a Gurney flap.

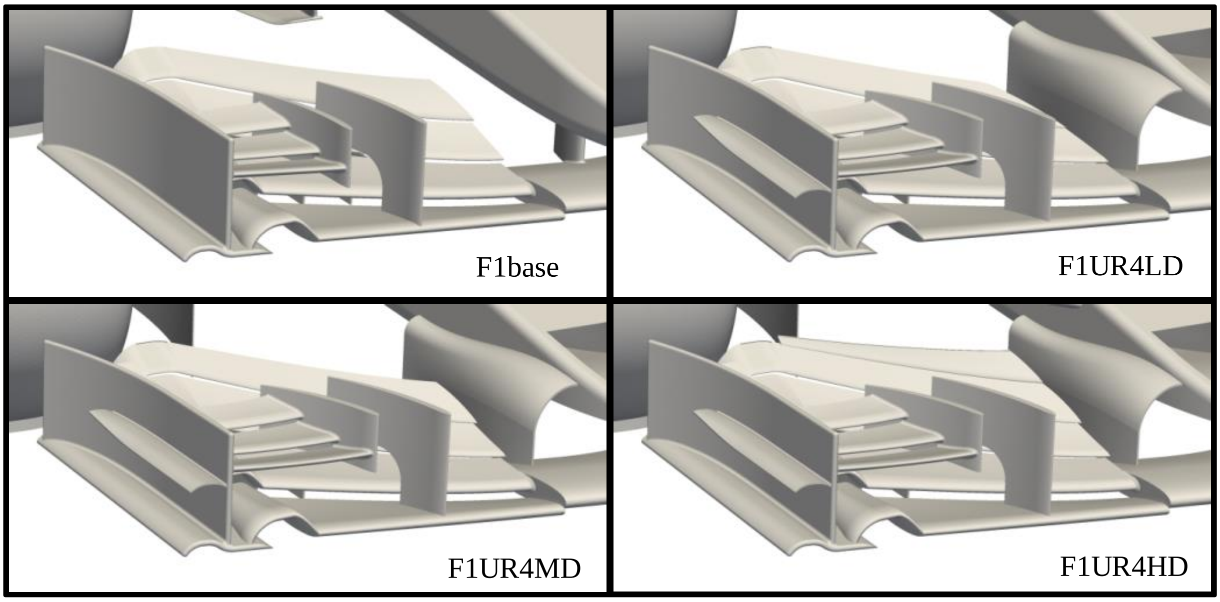

Figure 53: Front wing details - baseline, low (LD), medium (MD) and high-downforce (HD) configurations

6.1.2 Nosecone and Front Bodywork

The nose pylons were completely redesigned (Figure 55): thanks to their streamlined shape, they generate a convergent channel, in order to accelerate the flow towards the underbody. The front-end of the bodywork was thinned down, allowing a larger amount of fresh flow to feed the bottom of the car. In accordance with the same principle, a duct was obtained into the nose cone.

The turning vanes under the front bodywork were removed. The differences between the three configurations consist in the design of the canards: only one appendix with different angle of attack was mounted on low and medium-downforce vehicles; the high-downforce configuration is characterized by a double canard (Figure 56).

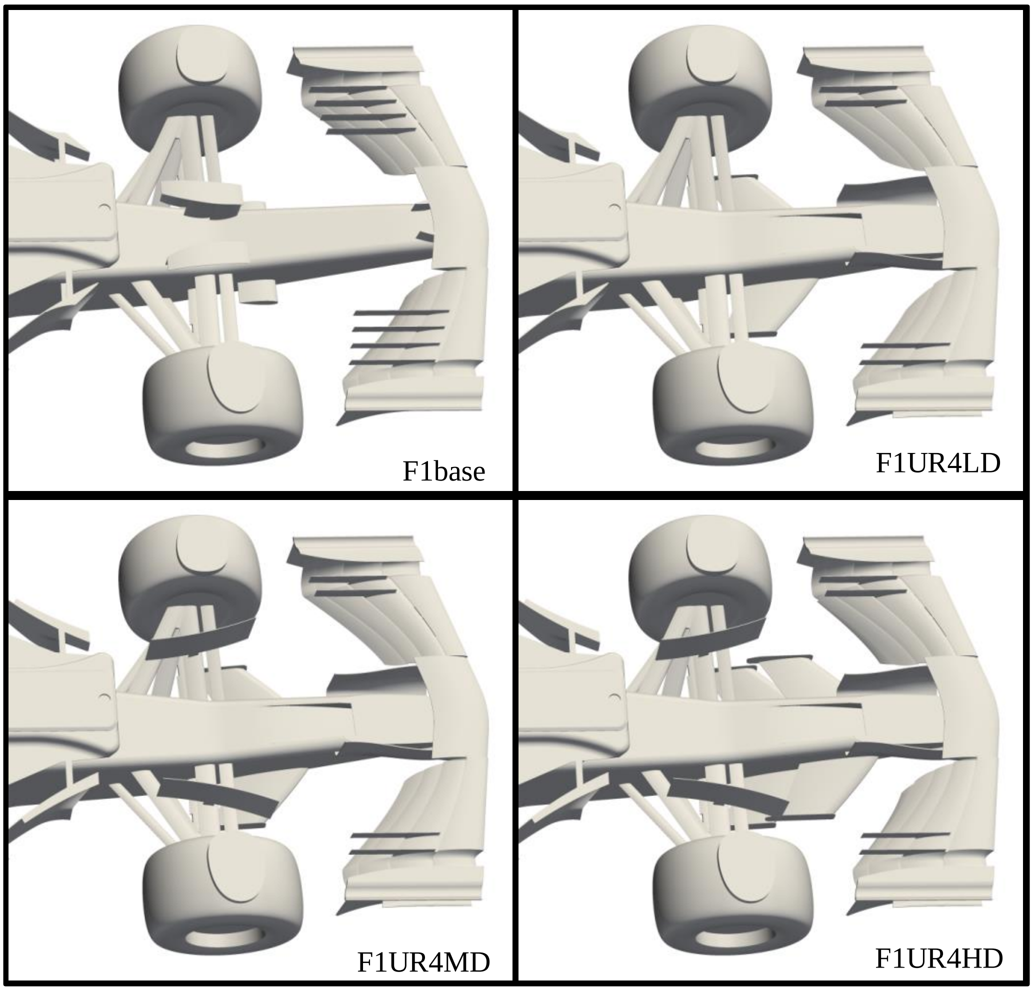

Figure 54: Front-end of the vehicle (bottom view) - baseline, low (LD), medium (MD) and high-downforce (HD) configurations

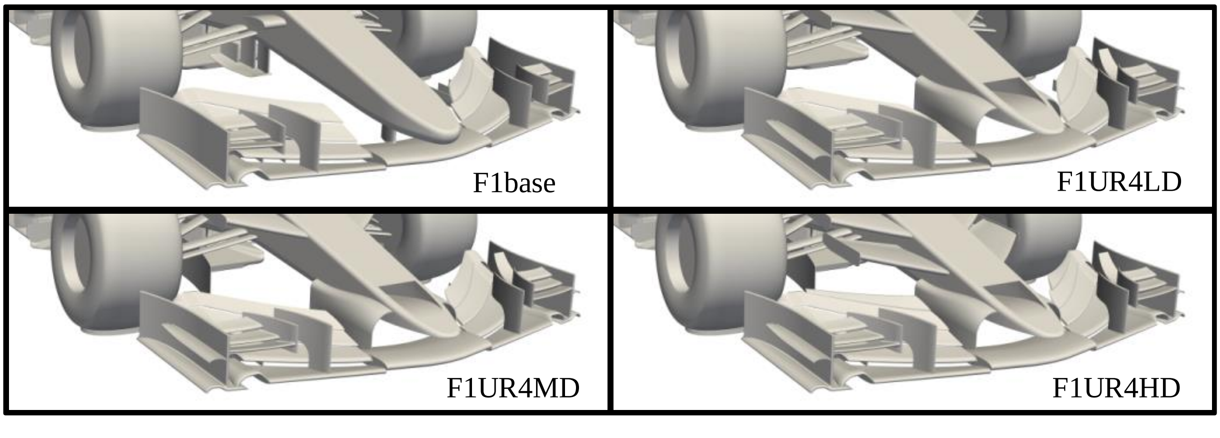

Figure 55: Front-end of the vehicle - baseline, low (LD), medium (MD) and high-downforce (HD) configurations

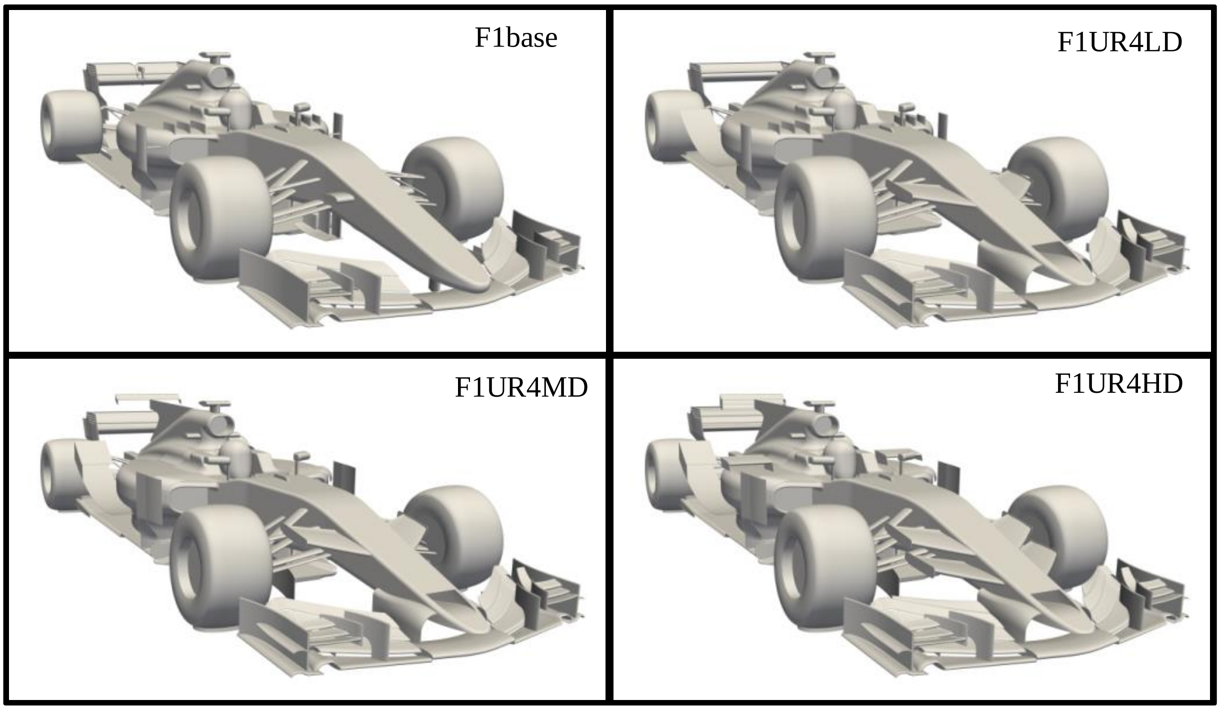

Figure 56: Front view of the entire vehicle - baseline, low (LD), medium (MD) and high-downforce (HD) configurations

6.1.3 Front and Rear Suspension

There are no changes in the low-downforce suspensions with respect to the baseline design. Medium and high-downforce vehicles introduce a turning vane mounted on the lower wishbone of the front suspension (Figure 54) and a small wing profile on the toe link of the rear suspension, clearly visible in the F1UR4MD vehicle shown in Figure 59.

6.1.4 Sidepod and Engine Cover

The front part of the sidepod is usually characterized by flow-control devices, in order to smooth the air enveloping the vehicle bodywork. The low-downforce car maintained the original configuration of the sidepod panel assembly. In medium and high-downforce vehicles, the side panel was lengthened and the vortex generators on the top of the sidepod were replaced by a couple of guide vanes. Concerning the rear-end of the sidepod, the F1UR4LD vehicle was modified by means of a single-component tyre ramp; for all the other configurations, a double-deck tyre ramp was designed. Finally, a winglet was mounted on the side of the F1UR4HD cockpit. The low-downforce engine cover maintained the original design; on the contrary, F1UR4MD and F1UR4HD configurations were equipped with shark fin and T-wing assembly (single element for the medium-downforce and triple element for the high-downforce vehicle). See Figure 57 for further details.

6.1.5 Underbody

In light of the tandem-running simulation results, the bottom of the car was subjected to an extensive review. All the configurations were equipped with convergent guide vanes at the diffuser inlet and vortex generators (VG) at the underbody inlet (single VG for the low-downforce setup; four VGs for medium and high-downforce aero packages). As a result of preliminary tests, it was found that the optimum angle of incidence of the vortex generators is 25°. The original appendix mounted in close proximity to the rear tyre was replaced with a horizontal lip, acting like a sort of Gurney flap.

F1UR4MD and F1UR4HD were enhanced through other devices: two extra expansion areas were added to the step plane; the main diffuser channels were redesigned together with the strakes; an array of small vortex generators was added at the diffuser inlet. A duct was designed for the purpose of blowing the new diffuser nolder, on the upper side of the underbody (Figures 58 and 59).

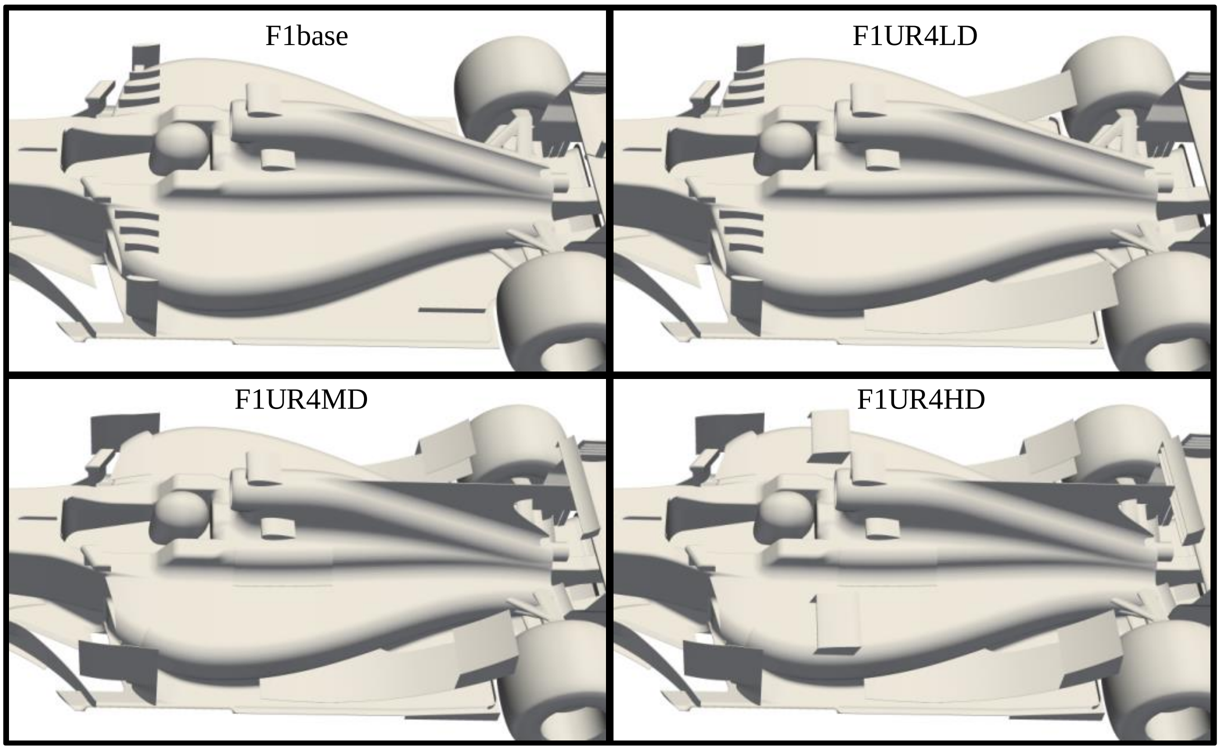

Figure 57: Sidepods and engine cover - baseline, low (LD), medium (MD) and high-downforce (HD) configurations

6.1.6 Rear Wing

Figure 60 shows the rear-end of the vehicle (rear wing assembly, rear crash, diffuser outlet). The angle of attack of the low-downforce rear wing structure was decreased by 7° compared to the baseline vehicle. The medium-downforce vehicle maintained the original wing configuration (angle of attack of the wing assembly = 22°, effective flap angle = 42°). The high-downforce rear wing is made up of a main plane (Be 112-205) and two flaps (Be 122-125 and Be 152-105). In this regard, the reader is referred to the handbook by Benzing (2012) for more details. The entire wing compound has an angle of attack of 25°; the effective flap angles are 59° and 72°, respectively. The wing position of the F1UR4HD configuration was raised by 50 mm in Z-direction, for the purpose of installing a beam wing on the rear crash.

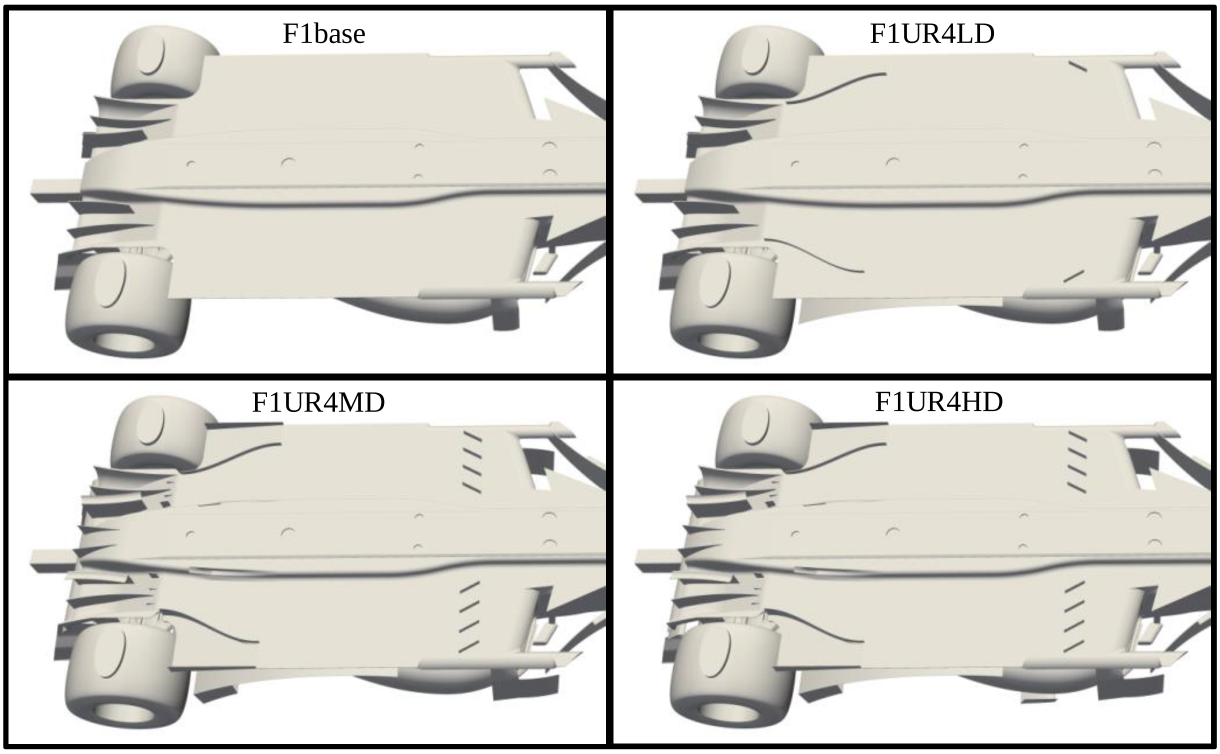

Figure 58: Underbody details - baseline, low (LD), medium (MD) and high-downforce (HD) configurations

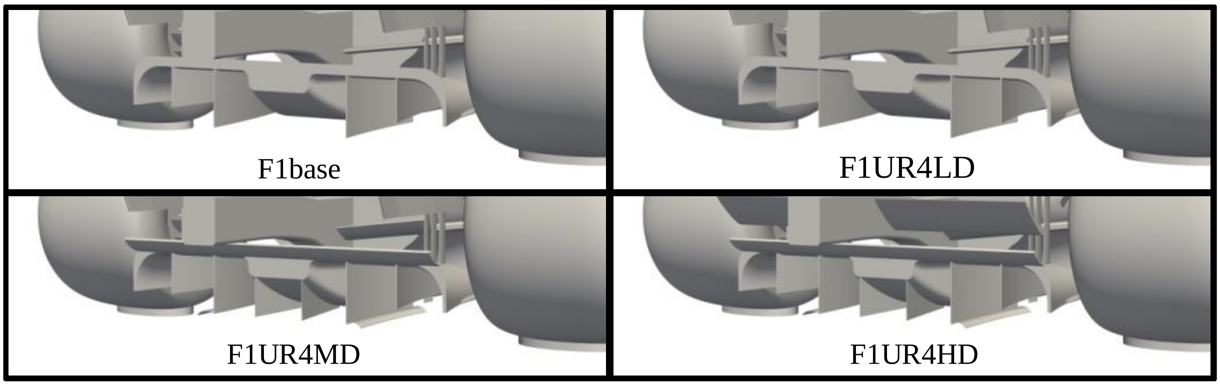

Figure 59: Diffuser details - baseline, low (LD), medium (MD) and high-downforce (HD) configurations

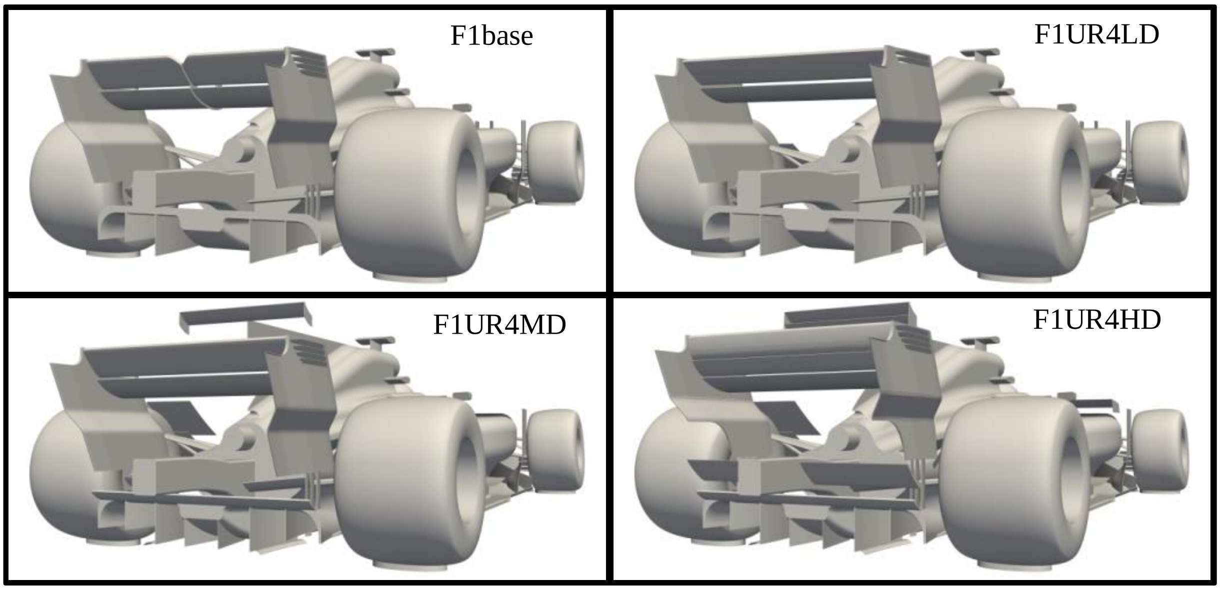

Figure 60: Rear view of the vehicle - baseline, low (LD), medium (MD) and high-downforce (HD) configurations

6.2 Results and Discussion

The performance of the vehicles described above was numerically evaluated in terms of drag, downforce, efficiency and front balance. In order to pursue a consistent comparison, all the conceived configurations were tested under the same setup (15-55): in accordance with the results discussed in section 5.3, this combination of front and rear ride height ensures a good compromise in terms of overall downforce and balance. Table 18 and Figure 61 summarize the global performance coefficients related to the four vehicles tested. The low-downforce package develops less drag than the baseline (-8%), despite benefiting from higher downforce (+4%): as a result, its efficiency greatly improves (+13%). While reaching higher peaks of downforce (+25% and +48% for F1UR4MD and F1UR4HD, respectively), every change in vehicle geometry becomes more expensive in terms of drag, hence the efficiency of the high-downforce configuration is lower than that of the medium-downforce package, which, in turn, is lower than that of the low-downforce layout. Recalling that the weight distribution of a current F1 car is about 45% on the front and 55% on the rear, the aerodynamic front balance should be lower than 0.45 for high-speed cornering stability. The new aero packages comply with this requirement. Furthermore, the front balance of the high-downforce vehicle is the highest (0.43), so as to reduce understeering and improve responsiveness of the front axle in low-speed corners, which are typical of street circuits.

Focusing on the vehicle components makes it possible to better assess the differences between the four aerodynamic configurations. As shown in Table 19, the front bodywork benefits from the contribution of the canards: the extra downforce generated at the cost of negligible drag is more than enough to counterbalance the performance loss resulting from the new duct feeding the bottom of the car.

Vehicle	*SCx [m^2]*	*SCz [m^2]*	*Cz/Cx*	*FB*
F1base	1.18	-3.48	3.0	0.41
F1UR4LD	1.08	-3.63	3.4	0.42
F1UR4MD	1.34	-4.35	3.3	0.42
F1UR4HD	1.61	-5.16	3.2	0.43

Table 18: Performance coefficients of the baseline vehicle (F1base) and the new aero-packages (F1UR4LD, MD, HD)

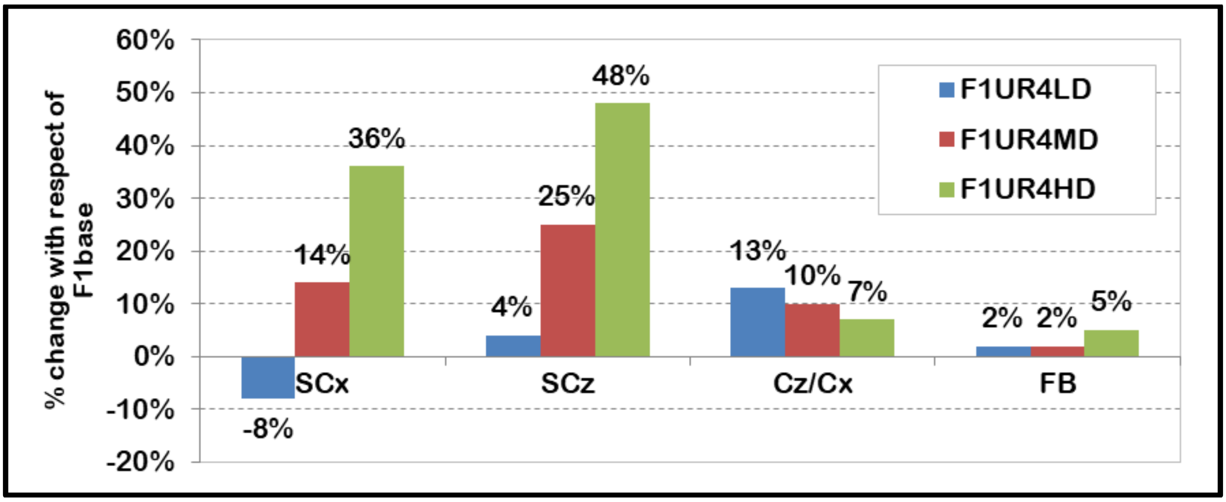

Figure 61: Performance of the new aero-packages: percentage change with respect of the baseline vehicle (F1base)

Front Bodywork	*SCx [m^2]*	*SCz [m^2]*
F1base	0.055	-0.11
F1UR4LD	0.065	-0.12
F1UR4MD	0.073	-0.12
F1UR4HD	0.074	-0.21

Table 19: Drag and downforce coefficients of the front bodywork

As documented by Table 20, the low-downforce front wing was mainly designed to minimize drag. On the contrary, the F1UR4HD configuration was not intended to be efficient, but aimed at ensuring the highest level of downforce. As regards the medium-downforce layout, the drag contribution of the add-ons described above is counterbalanced by a reduction of the flap incidence angles. In this respect, it should be noted that some of the devices mounted on the front wing do not aim at increasing the local performance, but rather at managing the flow towards the underfloor.

Front Wing	*SCx [m^2]*	*SCz [m^2]*
F1base	0.163	-0.92
F1UR4LD	0.143	-0.82
F1UR4MD	0.156	-0.90
F1UR4HD	0.206	-1.13

Table 20: Drag and downforce coefficients of the front wing

The underfloor (consisting of underbody and plank) underwent many changes, in order to find new ways to generate downforce and improve its behaviour in slipstream (Table 21). The new aero devices affect the diffuser behaviour, as well as its interaction with the rear wing. For instance, the baseline and the low-downforce underbodies have the same performance, although the latter is equipped with diffuser guide vanes and a vortex generator at the inlet: this is because the suction side of the low-downforce rear wing accelerates the flow less than the baseline one thus reducing its contribution in extracting the air underneath the car. In support of this hypothesis, it can be noted that the contribution to downforce of medium and high-downforce underfloor is different, despite their geometries are exactly the same: in fact, the F1UR4HD layout is equipped with a three-element rear wing and an additional beam wing that heavily deflect upwards the flow in synergy with the diffuser. In order to distinguish the effects of the diffuser/wing interaction from the contribution of the new underbody devices, one should compare the baseline configuration with the medium-downforce layout, which has the same rear wing geometry: the results put in evidence that the new underbody components provide a large amount of downforce at the cost of negligible drag.

Underfloor	*SCx [m^2]*	*SCz [m^2]*
F1base	0.197	-1.99
F1UR4LD	0.196	-2.00
F1UR4MD	0.215	-2.45
F1UR4HD	0.261	-2.69

Table 21: Drag and downforce coefficients of the underfloor

As in the front wing case, the low-downforce rear wing (Table 22) aims at reaching the lowest drag, in compliance with the downforce requirements deriving from the aerodynamic balance. The reduction of the angle of attack led to a significant improvement in efficiency, defined as the ratio between Cz and Cx. As a result of a specific design choice, the medium-downforce rear wing was penalized in favour of numerous aerodynamic devices along the vehicle bodywork such as the nose cone duct, the canards and the tyre ramps. In addition, the high-downforce rear wing assembly was designed for the purpose of improving the underbody performance in wake flows. The benefits associated with these choices will be quantified in Chapter 8, specifically dedicated to tandem-running simulations of the above described vehicles, equipped with the new aero packages.

Rear Wing	*SCx [m^2]*	*SCz [m^2]*
F1base	0.239	-0.92
F1UR4LD	0.175	-0.77
F1UR4MD	0.253	-0.75
F1UR4HD	0.371	-0.77

Table 22: Drag and downforce coefficients of the rear wing

The additional sidepod-mounted devices are as simple as effective (Table 23): in fact, the new layouts equipped with tyre ramps and winglets can convert the original lifting component into an important downforce-generating element. Extracting downforce from sidepods does not create particular problems in vehicle aero-balance, because they are located in the middle region of the chassis, close to the centre of gravity.

Sidepod	*SCx [m^2]*	*SCz [m^2]*
F1base	0.033	+0.22
F1UR4LD	0.086	-0.13
F1UR4MD	0.149	-0.18
F1UR4HD	0.123	-0.21

Table 23: Drag and downforce coefficients of the sidepod

A similar line of thought was applied to the engine cover (Table 24): the original engine cover, mounted also on the low-downforce configuration, creates undesirable lift. The so called “T-wing” assembly can lessen or almost completely eliminate this effect, at the cost of few points of drag.

The next section aims at analysing the features of the four aerodynamic configurations from a qualitative point of view. Figures 62 and 63 show the pressure coefficient plots, looking at the top and bottom of the vehicle, respectively. The F1UR4HD front wing gives its extra contribution to downforce not only by means of additional flaps and add-ons, but also by strengthening the low-pressure area on the suction side of the first two wing profiles. On the one hand, the presence of the nose duct inlet deprives the upper side of the front bodywork of a useful high-pressure region; on the other hand, it ensures better feeding of the underfloor. There are no other significant differences among the front ends of the vehicles, apart from the contribution of the canards. Looking at the upper view of the cars, it can be noted that the new guide vanes produce a pressure increase on the sidepod front edge. The entire surfaces of tyre ramps and T-wings are well exploited to generate downforce: on the contrary, Figure 62 puts in evidence that medium and high downforce rear wings suffer from the presence of upstream devices. Looking at Figure 63, it can be pointed out that the underbody inlet of the F1UR4LD car works harder than that of the baseline, thanks to the above mentioned solutions for improving the suction effect underneath the car; however, despite the new advanced design, the low-downforce diffuser is less effective than the baseline because of the limited rear wing/diffuser interaction. Similarly, medium and high-downforce configurations are characterized by significant differences in the diffuser region, although the underfloor geometries are identical: the better performance of the F1UR4HD diffuser can be attributed to the interaction with the new rear wing assembly, described previously. Finally, the high-downforce layout can provide a slightly better performance than the medium-downforce configuration in correspondence of the plank and the step plane inlet, most probably thanks to the stronger vortex system coming from the front wing.

Engine cover	*SCx [m^2]*	*SCz [m^2]*
F1base	0.021	+0.18
F1UR4LD	0.019	+0.17
F1UR4MD	0.048	+0.08
F1UR4HD	0.070	+0.01

Table 24: Drag and downforce coefficients of the engine cover

Figures 64-70 are dedicated to the study of the vortical structures around the car by means of iso-Q surface plots and X-vorticity slices, providing complementary information about shape, spatial development and strength of the vortices and rotation of the flow. Starting from the front wing, shape and persistence of the Y250 vortex depend on flap geometry and incidence. Figures 65 and 66 display that the updated add-ons mounted on the side of the wing generate stronger and larger vortices than the baseline: consequently, the flow has more chances to counteract the tyre disturbance and reach the underbody with higher energy. Furthermore, the new geometry of the lower side of the nose cone allows the generation of a couple of additional vortices, thus stabilising the flow underneath the front bodywork.

Alongside the Y250 vortex, the medium and high-downforce configurations can also benefit from the vortex generated by the turning vane mounted on the front suspension, well visible in Figures 64 and 67: this vortex travels down the middle region of the vehicle and works together with the couple of counter-rotating vortices generated by the bargeboard (Figures 64 and 68). The iso-Q surfaces at the inlet of the underbody (Figure 65) and the axial vorticity slice at X = 1.6 m (Figure 69) reveal the contribution of the vortex generators in creating low-pressure cores underneath the car: medium and high-downforce configurations are characterized by four distinct vortex tubes acting alongside the vortex coming from the delta-shaped part of the underbody.

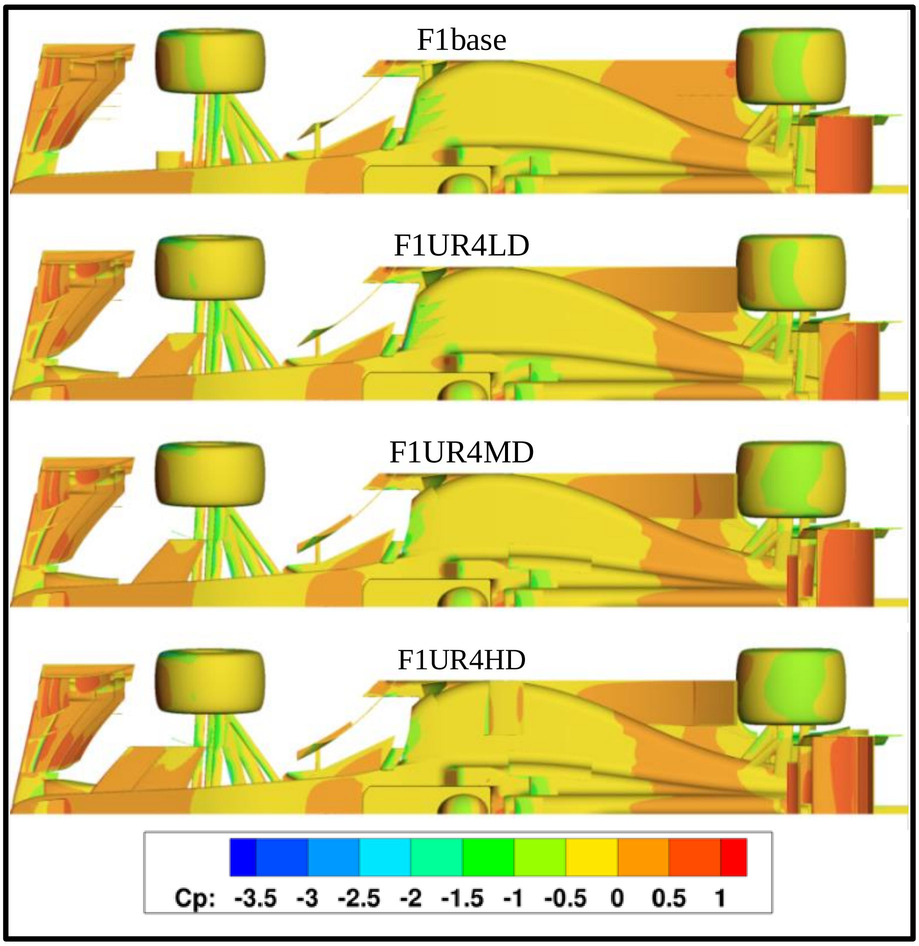

Figure 62: Pressure coefficient plot - top view – baseline, low (LD), medium (MD), high-downforce (HD) vehicles

The slice at X = 3.9 m (Figure 70) helps to clarify the flow structures composing the wake. As already described in Chapter 4, the flow coming from underneath the baseline vehicle is highly three-dimensional: medium and high-downforce layouts make the vortex system even more complex, thanks to the additional middle diffuser channel and the strengthening of the Venturi vortex, detaching from the side region of the diffuser. As reported earlier, the vehicle rear-end is heavily affected by the interaction between the rear wing assembly and the underbody: in fact, because of this phenomenon, the vortical structures characterizing the F1UR4HD diffuser are larger than those of the F1UR4MD configuration, despite the same geometry.

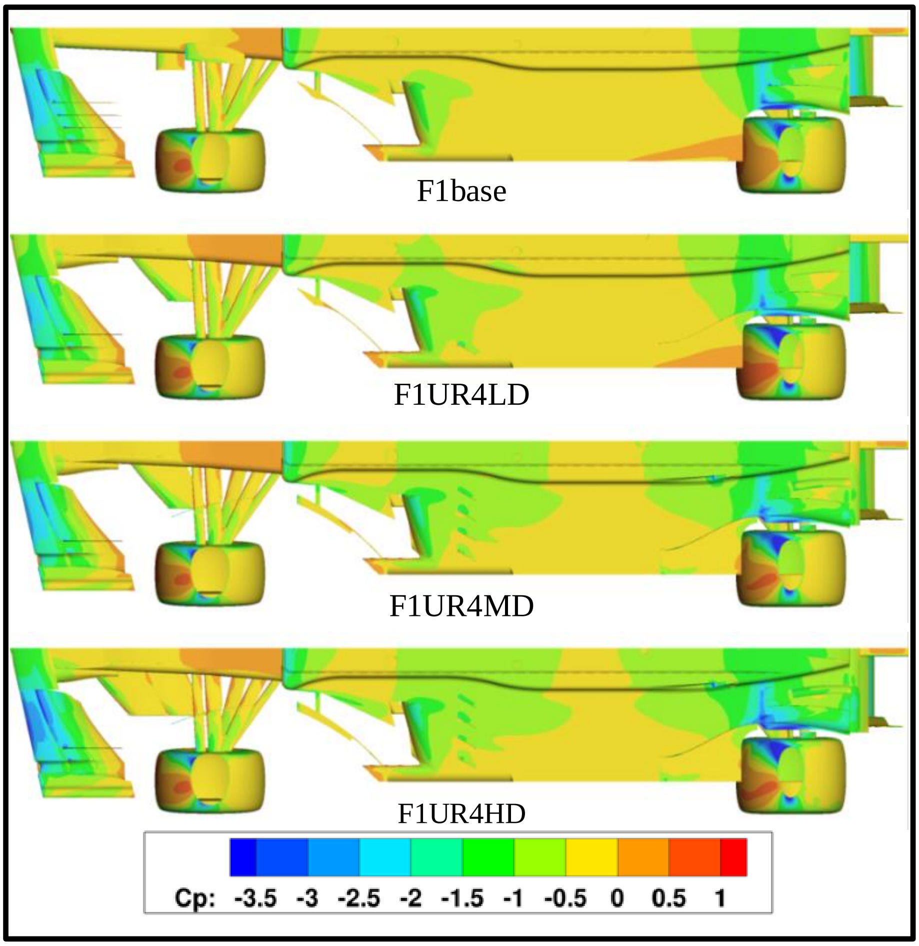

Figure 63: Pressure coefficient plot - bottom view – baseline, low (LD), medium (MD), high-downforce (HD) vehicles

Concerning the behaviour of the rear wing, one can see that wingtip vortices detaching from the F1UR4LD layout are the smallest, thanks to the reduced angle of incidence of main plane and flap. However, although the high angle of attack adopted, the vortices generated by the high-downforce configuration are just a bit larger than the others, because the aerodynamics features of the vehicle do not provide an adequate amount of clean airflow feeding the rear wing. The high drag coefficient of the F1UR4HD rear wing results from parasitic drag, rather than from induced drag linked to the axial vorticity.

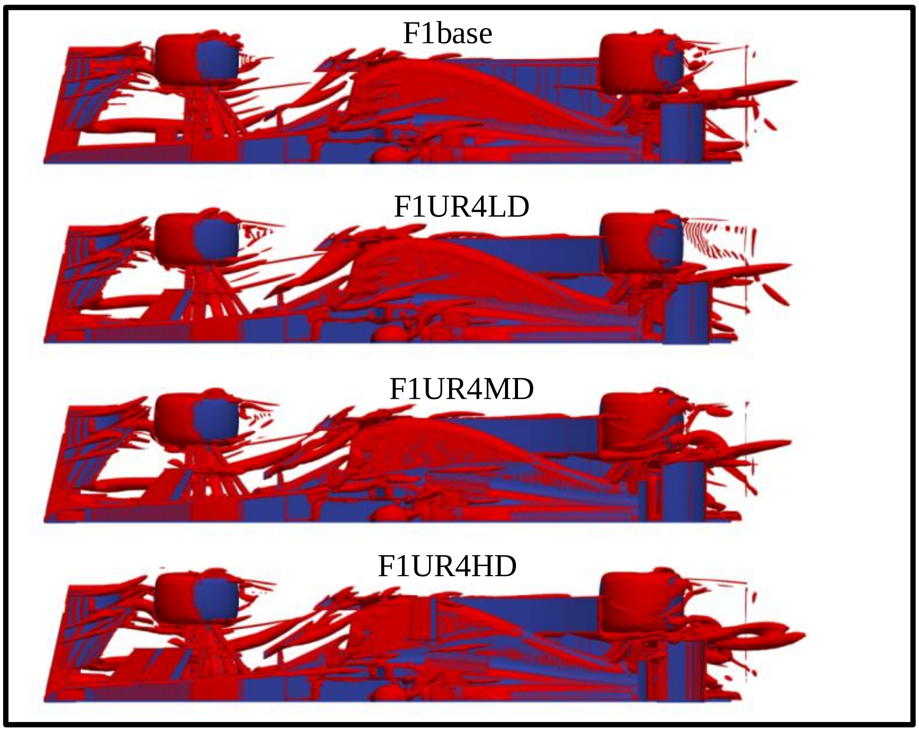

Figure 64: Iso-contour of Q = 50000 $1/s^2$ – top view - baseline, low (LD), medium (MD), high-downforce (HD) vehicles

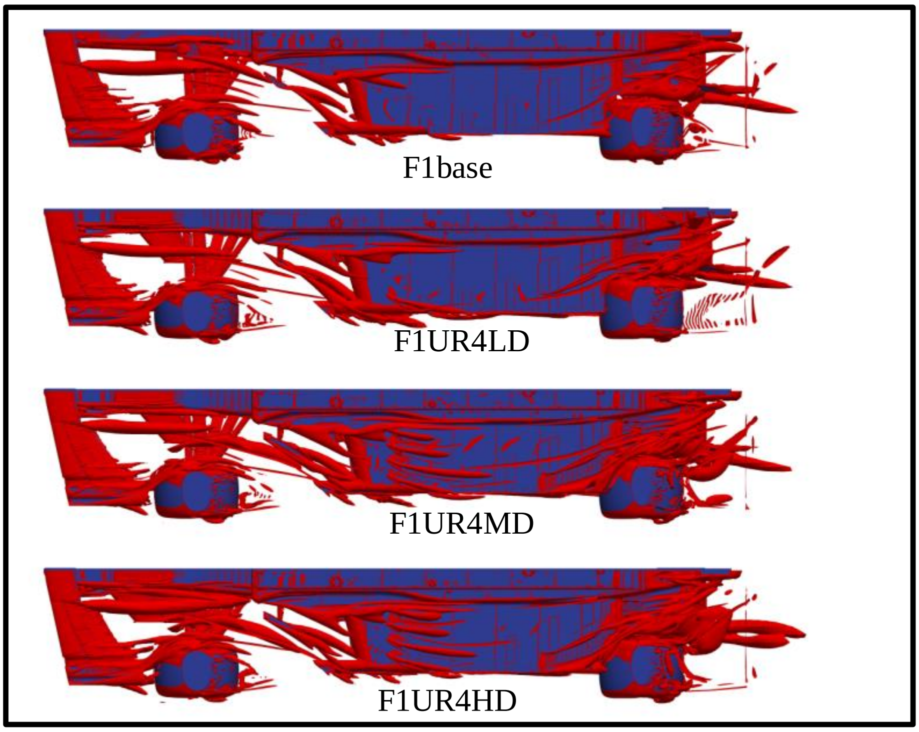

Figure 65: Iso-contour of Q = 50000 $1/s^2$ – bottom view - baseline, low (LD), medium (MD), high-downforce (HD) vehicles

Still talking about wings, the slice at X = 3.9 m shows the trace of the wingtip vortices generated by the T-wings mounted on medium and high downforce configurations.

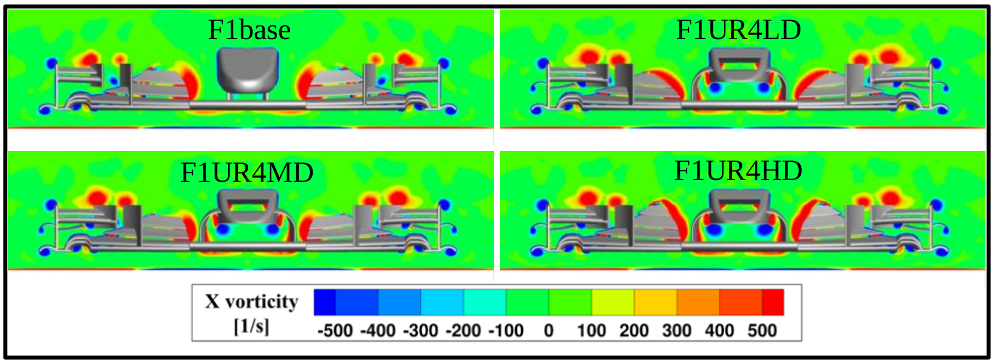

Figure 66: Axial vorticity contours – cross section X = -0.75 m

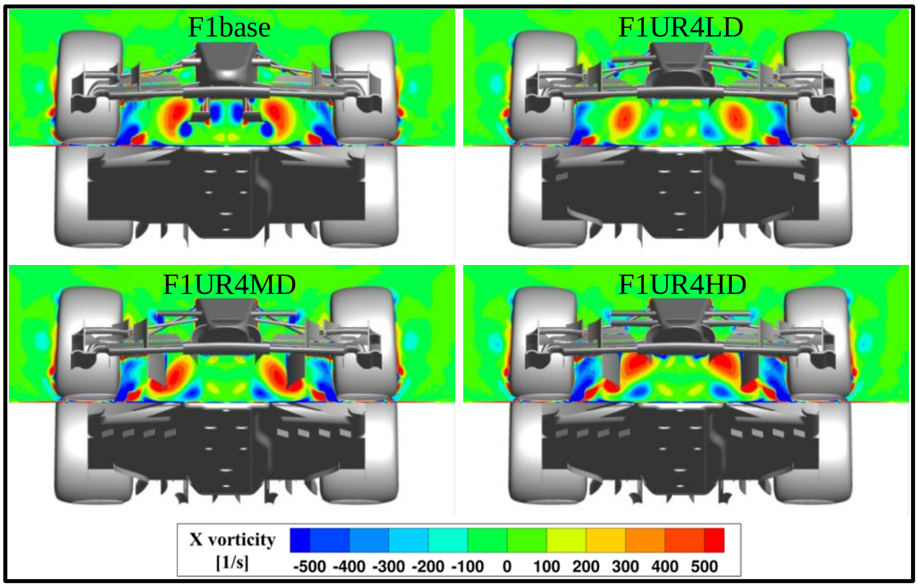

Figure 67: Axial vorticity contours – cross section X = 0.15 m

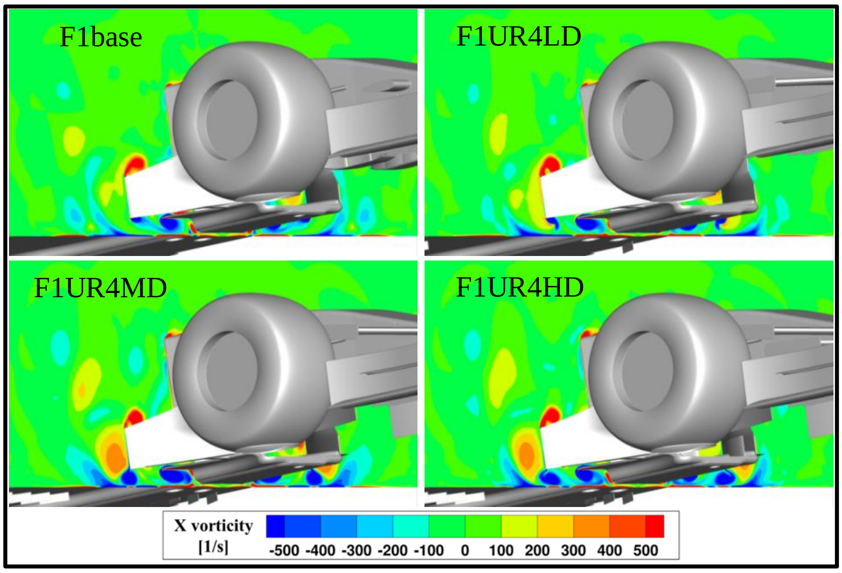

Figure 68: Axial vorticity contours – cross section X = 0.9 m

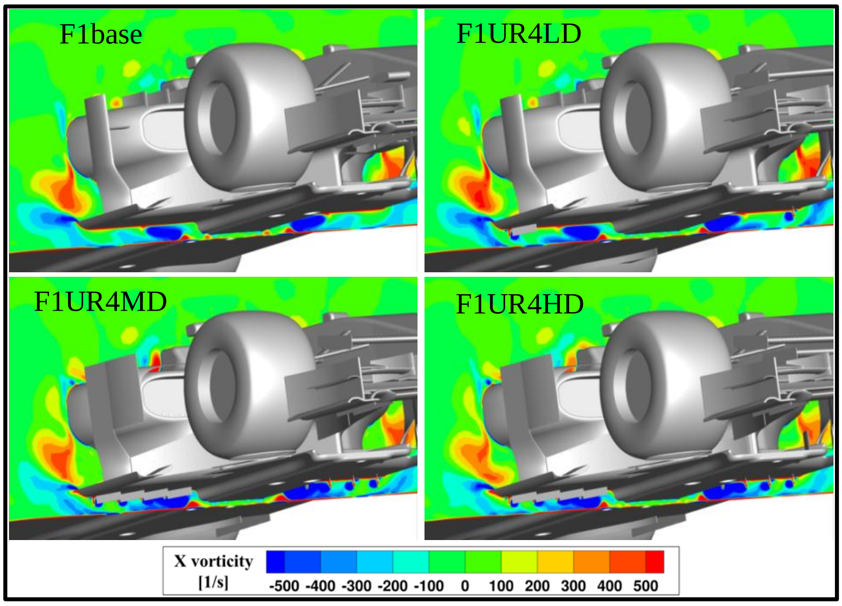

Figure 69: Axial vorticity contours – cross section X = 1.6 m

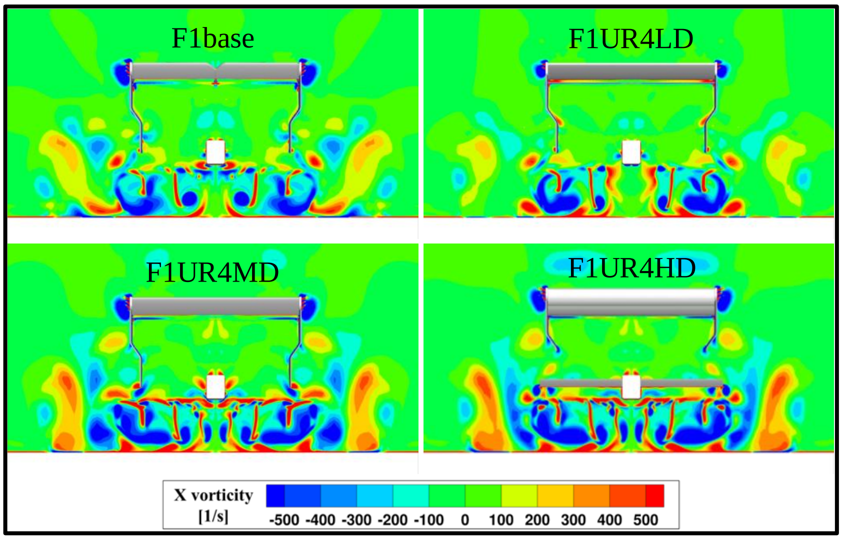

Figure 70: Axial vorticity contours – cross section X = 3.9 m

In order to complete the analysis of the aerodynamic packages running in freestream flow, the pattern of the streamlines feeding the most important component of the car will be examined below. Figure 71 demonstrates that tyre ramps, front canards, sidepod winglets and T-wings perturb the flow around the main rear wing: however, it should be remembered that, on balance, the overall impact of these aerodynamic devices on downforce is positive. Accordingly, it is obvious that the F1UR4HD rear wing is the most penalized by the large number of add-ons mounted on the vehicle. The rear view of the vehicle (Figure 72) shows how the wing influences the wake of the vehicle. Even though the baseline and the medium-downforce vehicles are equipped with the same rear wing layout, the flow downstream of the F1UR4MD configuration is characterized by a more pronounced deflection: this can be associated with the above mentioned add-ons and the mutual interaction between rear wing and diffuser. The upward deflection is even greater in the F1UR4HD vehicle, thanks to the new flap design and the addition of the beam wing.

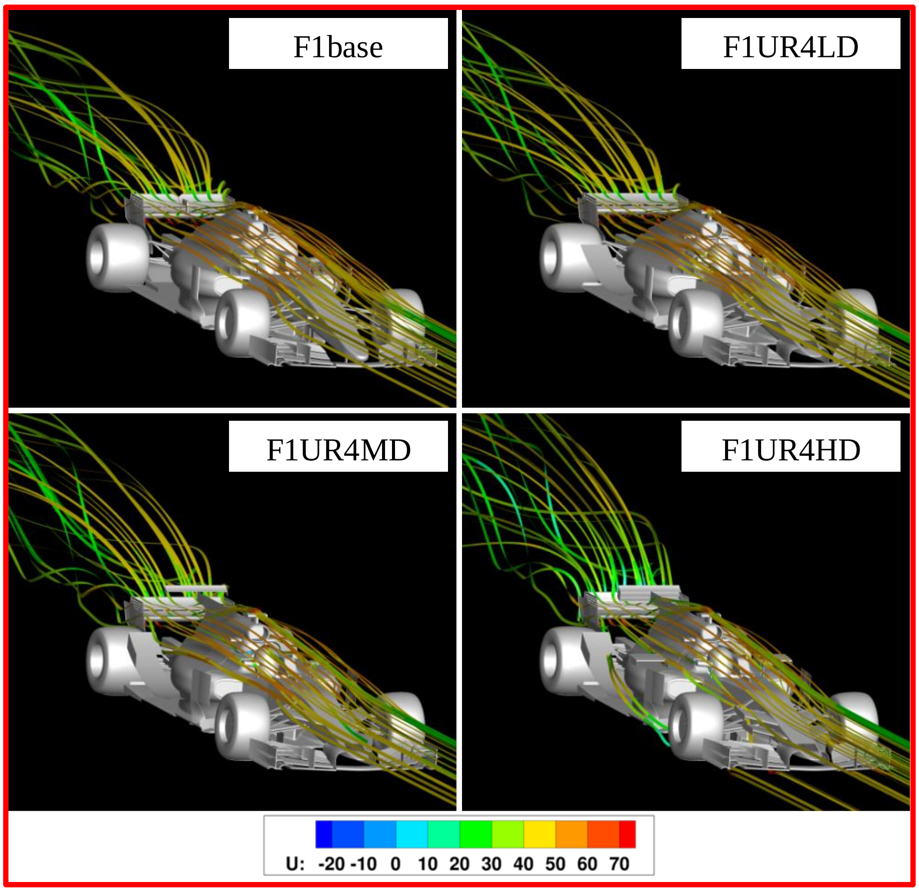

Figure 71: Streamlines feeding the rear wing – front view - baseline, low (LD), medium (MD), high-downforce (HD) vehicles

To corroborate the diffuser/rear wing interaction, one can look at Figure 73, where the streamlines at the diffuser exit follow the same direction as those of the corresponding rear wing.

The top view (Figure 74) highlights the features of the flow at the diffuser exit, such as the different wake width in the spanwise direction. The streamlines, at each side of medium and, principally, high-downforce vehicle, are deflected inward at a shorter distance from the rear-end with respect of those of the baseline. It might be that the high-strength vortices generated by the new underbody drive the side flow inboard so that the wake produced by the rear-end of the vehicle is shortened.

Then, the focus shifts to the underbody performance, depending on the quantity and the quality of the flow underneath the car: to this end, the seed points of the streamlines displayed in Figure 75 are placed precisely at the underbody inlet. The strong three-dimensionality of the medium and high-downforce streamlines testifies that the flow feeding the bottom of the car is well exploited by those configurations.

Moreover, the high-downforce configuration can better confine the flow in the middle region of the step plane, thus reducing the losses on the sides of the underfloor.

As touched upon in the paragraphs above, the proper functioning of the underfloor strongly depends on the design of important upstream devices: in this respect, some of the add-ons aimed at preparing the flow to run underneath the car are mounted on the front wing. In Figure 76 the seed points are located immediately upstream of the front wing.

Following the fluid threads downstream, it appears that the F1UR4HD configuration benefits the most from the cooperation between the front wing and the corresponding underbody: most of the flow bypassing the front tyres and the front suspensions can reach the rear underfloor of the car and maintain correct direction and adequate kinetic energy, as witnessed by the presence of highly three-dimensional structures at the diffuser exit.

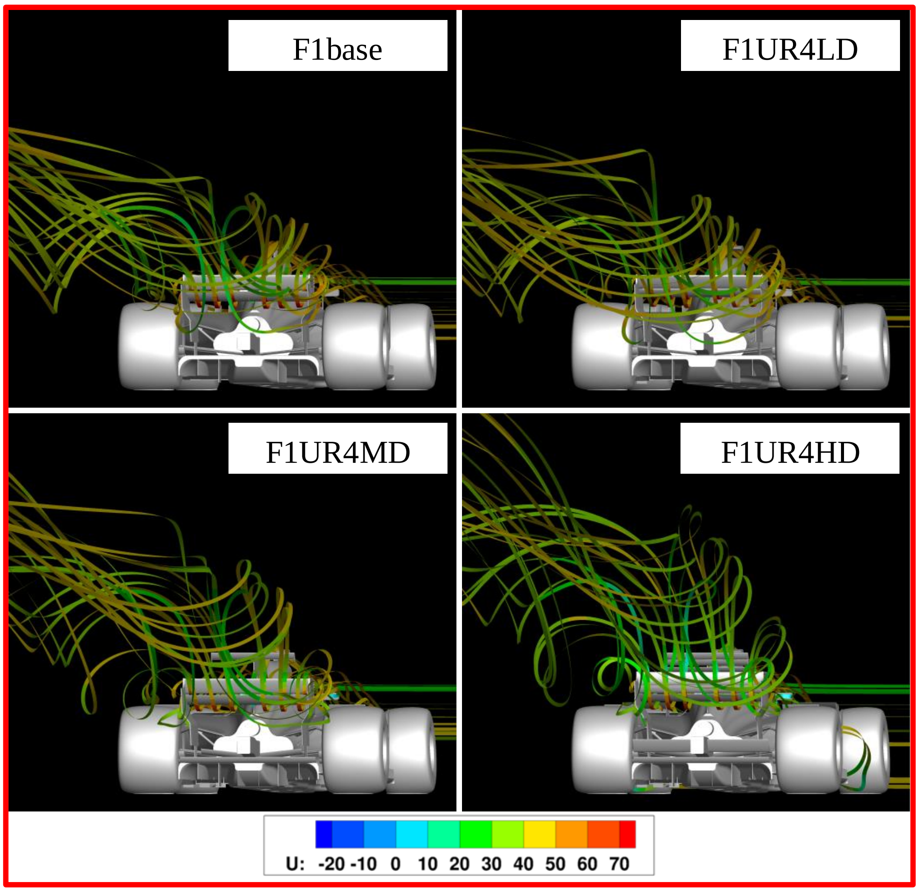

Figure 72: Streamlines feeding the rear wing – rear view - baseline, low (LD), medium (MD), high-downforce (HD) vehicles

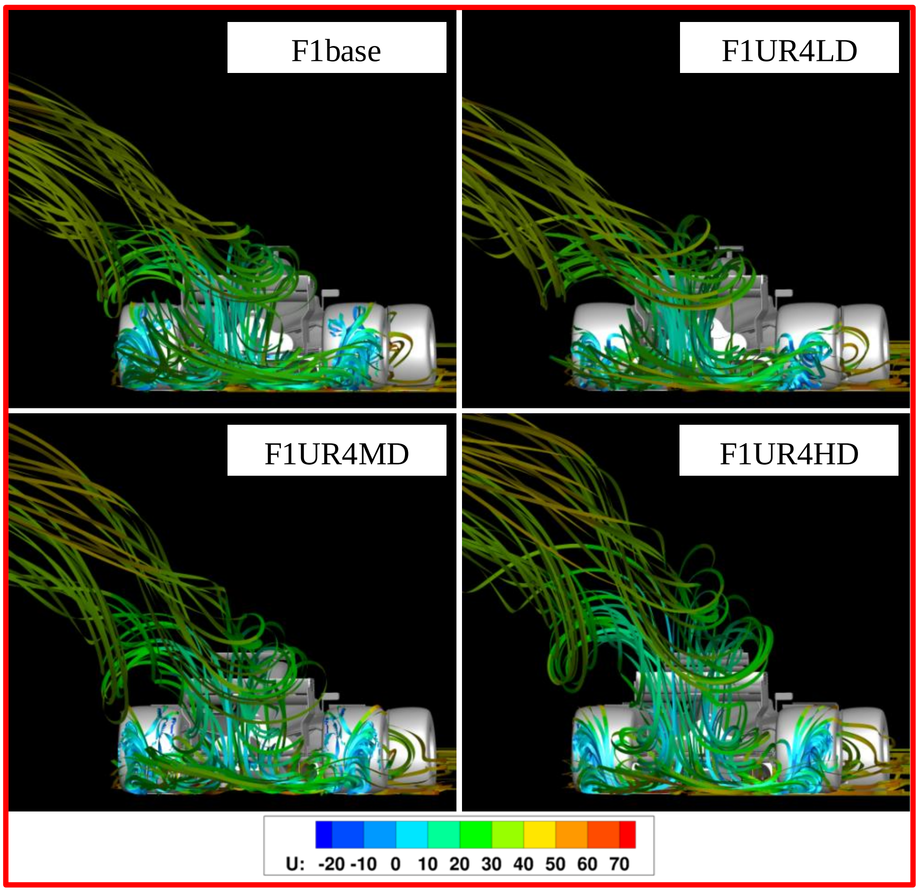

Figure 73: Streamlines at the diffuser exit – rear view - baseline, low (LD), medium (MD), high-downforce (HD) vehicles

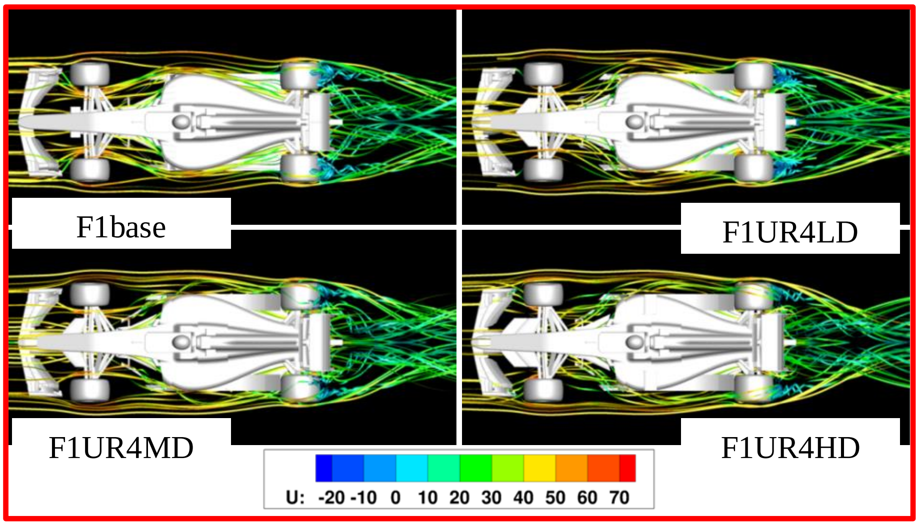

Figure 74: Streamlines at the diffuser exit – top view - baseline, low (LD), medium (MD), high-downforce (HD) vehicles

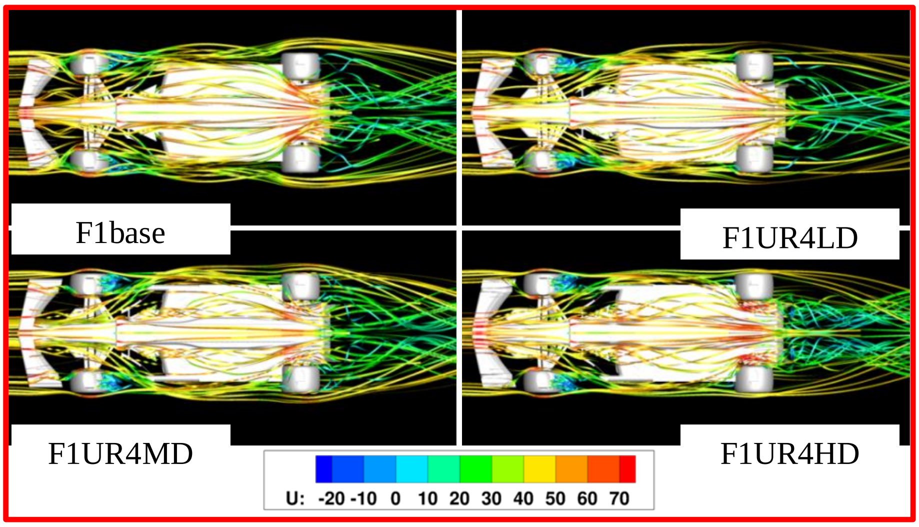

Figure 75: Streamlines at the underbody inlet – bottom view - baseline, low (LD), medium (MD), high-downforce (HD) vehicles

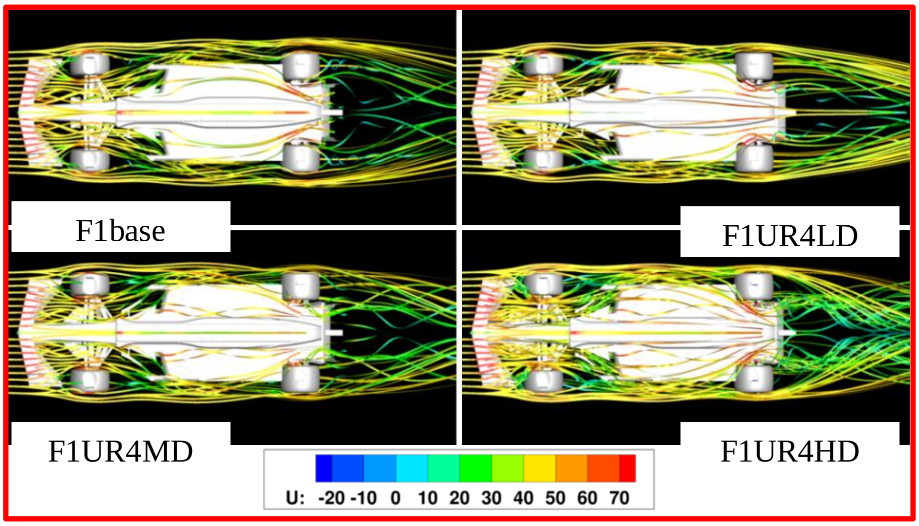

Figure 76: Streamlines upstream the front wing – bottom view - baseline, low (LD), medium (MD), high-downforce (HD) vehicles

6.3 Conclusions

The baseline vehicle designed by ©PERRINN was developed improving both downforce and efficiency, by means of simple and cheap aerodynamic components. Some of the new devices, such as the front wing add-ons, follow the 2017 F1 Technical Regulations; instead, other elements were designed on the basis of past regulations or completely original approaches. Particular attention was paid to the underbody and the rear wing, whose performance deteriorates significantly by running in wake flows.

The high-downforce vehicle is characterized by a 48% increase in downforce and a 7% efficiency improvement, testifying the validity of the ideas behind the aerodynamic development. The conceived evolutions of the baseline vehicle could be a good solution for building cheap and reliable racing cars, whose behaviour gradually approaches real F1 vehicles.

In the next stages of the research, the new aerodynamic packages will be the subject of additional investigation, for the purpose of understanding their behaviour in different operating conditions: as mentioned previously, driveability in slipstream is a fundamental aspect of the research, as well as sideslip angle sensitivity.

Chapter 7. Low, Medium and High-Downforce Layouts in Wake Flows

The development of the F1 car designed by ©PERRINN led to three new aerodynamic packages, characterized by different levels of sophistication (low, medium and high-downforce). This part of the study is intended to analyse the new vehicles in slipstream and compare their behaviour with the baseline configuration. As described in the previous chapter, many details of the new components were designed specifically with the aim of improving aerodynamic performance in wake flow, namely reducing downforce losses and front balance forward shift. The underfloor was heavily modified in order to make it more robust to the low-energy and chaotic flow coming from the leading car; many aerodynamic add-ons were added, so that the downforce can be evenly distributed on the entire bodywork. Finally, different configurations of rear wing assembly were tested, for the purpose of better understanding their interaction with the incoming wake flow. Accordingly, the following investigation will define the viability of the new ideas.

7.1 Results and Discussion

7.1.1 Comparison Between the Baseline and the New Aerodynamic Configurations

Baseline (F1base), low (F1UR4LD), medium (F1UR4MD) and high-downforce (F1UR4HD) vehicles were tested in tandem-running simulations. For the purpose of saving computational resources, only the most critical distance (0.5L) was considered in the first set of simulations; only at a later stage, the most promising aerodynamic configuration has been analysed in greater detail. The chosen setup for each vehicle was 15-55, in accordance with the freestream flow simulations reported in Chapter 7.

Table 25 summarizes the performance of the car in 2nd position (P2) and the percentage change of the global coefficients with respect of the isolated vehicle in freestream flow (see Table 18 in the previous chapter). Drag, downforce, efficiency and front balance were taken into account to assess aerodynamic performance.

A first analysis of the results puts in evidence that low and medium-downforce configurations show more or less the same drag gain as the baseline vehicle (≈ 30%), along with a lower downforce loss; however, a better efficiency is accompanied by a greater increase in front balance. On the contrary, the high-downforce vehicle is characterized by a more robust behaviour in slipstream: smaller downforce and efficiency losses go hand in hand with a lower increase in front balance. To sum up, the F1UR4HD configuration is the best option from all points of view: pure performance, driveability and safety during overtaking.

P2 Car	*SCx*	*SCz*	*Cz/Cx*	*FB*
F1base	0.80	-1.64	2.1	0.49
F1UR4LD	0.77	-1.97	2.6	0.52
F1UR4MD	0.94	-2.31	2.5	0.52
F1UR4HD	1.26	-3.14	2.5	0.49

P2 Car	*SCx*	*SCz*	*Cz/Cx*	*FB*
F1base	-32%	-53%	-30%	+20%
F1UR4LD	-29%	-46%	-24%	+24%
F1UR4MD	-30%	-47%	-24%	+24%
F1UR4HD	-22%	-39%	-22%	+14%

Table 25: Performance coefficients of the car in 2nd position (d = 0.5L) and percentage change with respect of the vehicle in freestream flow

These preliminary results are particularly encouraging for two main reasons: on the one hand, downforce level of the F1UR4HD configuration is the closest to that of current F1 cars; on the other hand, high-downforce layouts are usually affected by the most serious performance worsening. Indeed, among all motorsport categories, F1 suffers the most from running in slipstream. When a huge amount of horsepower is available, as is the case in F1, aerodynamic drag is not the most limiting performance factor. On the contrary, lap-time can be consistently penalised by lack of downforce, and hence tyre grip. Except in very specific cases, such as low-downforce tracks, F1 car performance is generally “grip-limited”: reaching higher values of downforce usually brings more benefits than optimising efficiency.

As already done in Chapter 6, the analysis of the contributions from the different aerodynamic devices is necessary to better understand the global behaviour of the vehicle: the outcomes related to front wing, rear wing and underfloor are provided by Tables 26, 27 and 28, respectively. The percentage changes are calculated with respect of the vehicle in freestream flow.

Front Wing - P2 car	*SCx [m^2]*	*SCz [m^2]*
F1base	0.127	-0.62
F1UR4LD	0.133	-0.64
F1UR4MD	0.158	-0.74
F1UR4HD	0.204	-0.97

Front Wing - P2 car	*SCx [m^2]*	*SCz [m^2]*
F1base	-19%	-33%
F1UR4LD	-7%	-22%
F1UR4MD	-0%	-18%
F1UR4HD	-5%	-14%

Table 26: Performance of the front wing in 2nd place (P2): absolute values and percentage change with respect of the isolated vehicle in freestream flow

All three new front wings, but particularly the high-downforce one, show a better behaviour than the baseline in terms of downforce loss: the reasons for this do not only depend on the geometry of the wings themselves, but above all on the features of the wake generated by the underfloor and the rear wing of the leading car.

Rear Wing - P2 car	*SCx [m^2]*	*SCz [m^2]*
F1base	0.127	-0.43
F1UR4LD	0.076	-0.30
F1UR4MD	0.114	-0.35
F1UR4HD	0.185	-0.39

Rear Wing - P2 car	*SCx [m^2]*	*SCz [m^2]*
F1base	-46%	-53%
F1UR4LD	-55%	-61%
F1UR4MD	-56%	-57%
F1UR4HD	-49%	-49%

Table 27: Performance of the rear wing in 2nd place (P2): absolute values and percentage change with respect of the isolated vehicle in freestream flow

The results related to the rear wing lead to some important comments. Although this may not appear immediately obvious, the reduction of the wing incidence brings no benefits in slipstream: in fact, the F1UR4LD layout is subjected to a serious downforce loss. On the opposite, the three-element rear wing mounted on the high-downforce vehicle improves the baseline performance both in terms of drag and downforce.

Thinking in terms of slipstream performance, the vehicle rear-end is crucial in managing the wake flow coming from the front-end and the underfloor of the car. It might be that the rear wing acts like a shield which deviates upwards the wake flow: the low-incidence wing mounted on the lead car is inadequate for this purpose, because of its small frontal area and the limited deflection provided to the incoming dirty flow. If this chaotic and low-energy flow is allowed to reach the following car, its aerodynamic performance will be strongly affected. On the contrary, the high-downforce rear wing, thanks to the double high-incidence flaps and the large frontal area, is able to intercept and deviate upwards a large amount of wake flow. Also, the beam wing mounted on the rear crash helps in this aim, channelling the flow between the diffuser and the suction side of the rear wing.

In light of the worsened rear wing behaviour and the simultaneous improvement of the front wing performance in slipstream, it can be explained why low and medium-downforce configurations suffer from a significant front balance shift.

Concerning the underfloor (plank plus underbody), all three new configurations show improved performance compared to the baseline: the new aerodynamic devices can re-organize the chaotic airflow underneath the car, thus leading to a more robust behaviour in wake flows. However, the high-downforce layout benefits from a greater improvement than the medium-downforce configuration, for the same underfloor geometry. In wake flows, even more than in freestream, the interaction between the diffuser and the rear wing assembly is crucial for performance enhancement. So, the high-downforce rear wing plays a key role in slipstream even if it is not efficient in freestream flow: in other words, it is no longer a mere device for generating downforce, but an important component for wake control.

Underfloor - P2 car	*SCx [m^2]*	*SCz [m^2]*
F1base	0.102	-0.84
F1UR4LD	0.112	-1.09
F1UR4MD	0.109	-1.20
F1UR4HD	0.187	-1.55

Underfloor - P2 car	*SCx [m^2]*	*SCz [m^2]*
F1base	-47%	-58%
F1UR4LD	-45%	-54%
F1UR4MD	-48%	-51%
F1UR4HD	-26%	-42%

Table 28: Performance of the underfloor in 2nd place (P2): absolute values and percentage change with respect of the isolated vehicle in freestream flow

Figures 77 and 78 show the pressure coefficient contours on the slipstreaming vehicles from top and bottom view, respectively. The four different rear wings are characterized by similar pressure contours on the upper side. On the contrary, the cascade winglets mounted on the front wing improve progressively their performance, moving from baseline to high-downforce package.

The T-wings mounted on F1UR4MD and F1UR4HD vehicles maintain a good pressure level (Cp of about 0.5), because they are positioned higher than the rear wing. Also, the tyre ramps provide their contribution to downforce, without experiencing a significant performance penalty.

As far as the bottom of the vehicle is concerned, the low-pressure area on the suction side of the front wing becomes larger while increasing the downforce level of the vehicle. The vortex generators at the step plane inlet and the guide vane in correspondence of the diffuser work as local downforce-generating devices, re-energizing the wake flow in the most sensitive regions of the underfloor. Since the front wing is not particularly affected by operating in slipstream, the performance of diffuser and rear wing is important for maintaining a good distribution of downforce between front and rear axle, namely an acceptable value of front balance.

The iso-contours of the scalar Q plotted in Figures 79 and 80 are in accordance with the previous observations. As already discussed in Chapter 6, the Y250 vortex is more affected by wake flow than the vortex system generated by the side-mounted front wing devices. In particular, the high-downforce configuration can preserve the vortices detaching from endplate, strakes and turning vanes in almost full strength. Despite the adverse conditions, the vortex tubes at the underbody inlet are clearly visible in F1UR4MD and F1UR4HD layouts, as well as the Venturi vortex at the side of the diffuser, certifying the effectiveness of the underfloor. The near absence of the rear wingtip vortices in all aerodynamic configurations confirms the poor contribution to downforce by the rear wing.

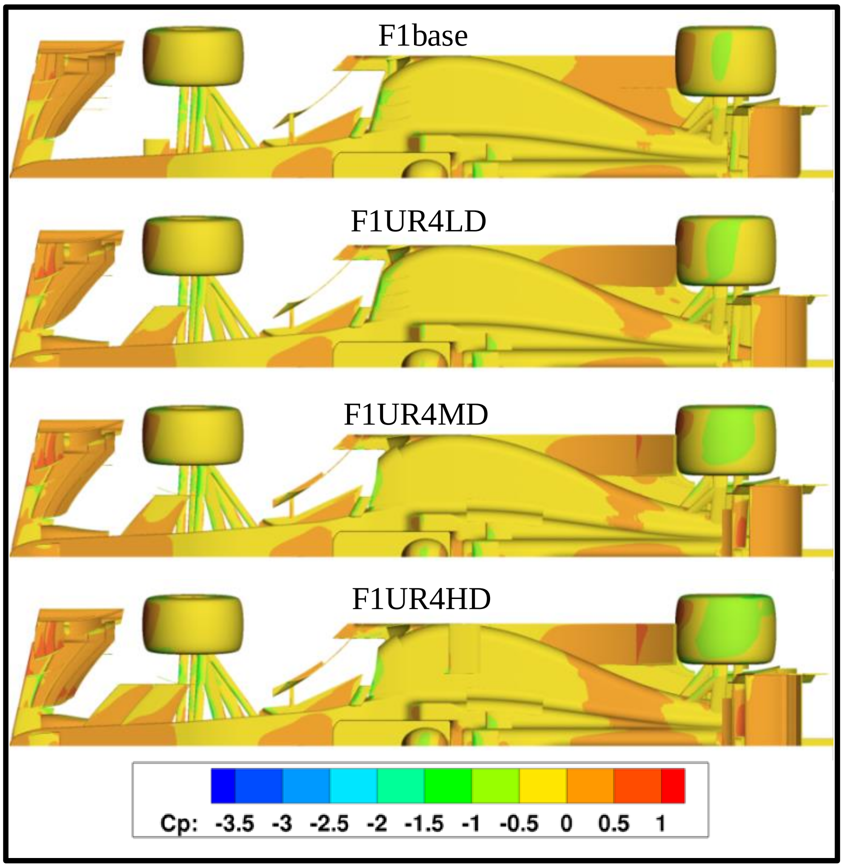

Figure 77: Pressure coefficient plot of the P2 car (d = 0.5L) - top view – baseline, LD, MD, HD vehicles

After describing the performance of the aerodynamic devices mounted on different vehicles, it is necessary to investigate the reason of their behaviour in slipstream: as already demonstrated, the same component can deliver different results depending on the features of the surrounding flow. The streamwise velocity contours in the longitudinal symmetry plane (Figure 81) aim at investigating this aspect. It is evident that the wake structure depends on the aerodynamic configuration. Considering that the diffuser size was maintained constant, the rear wing assembly is largely responsible for controlling the exit angle of the flow and hence the height of the wake.

Moving from low to high-downforce design, the wake becomes shorter and taller so cleaner flow can reach the car in 2nd position. When comparing medium and high-downforce layouts, one can see that the former is affected by reversed flow in the diffuser region, while the latter is characterized by attached flow. This difference between the two configurations reveals that the underbody devices for re-organizing low-energy flow work better when interacting with the beam wing and the three-element rear wing. The stall of the diffuser, together with the worsening of the rear wing performance, is one of the reasons why the front balance of low and medium-downforce configurations seriously increases, although the overall downforce loss is lower than the baseline.

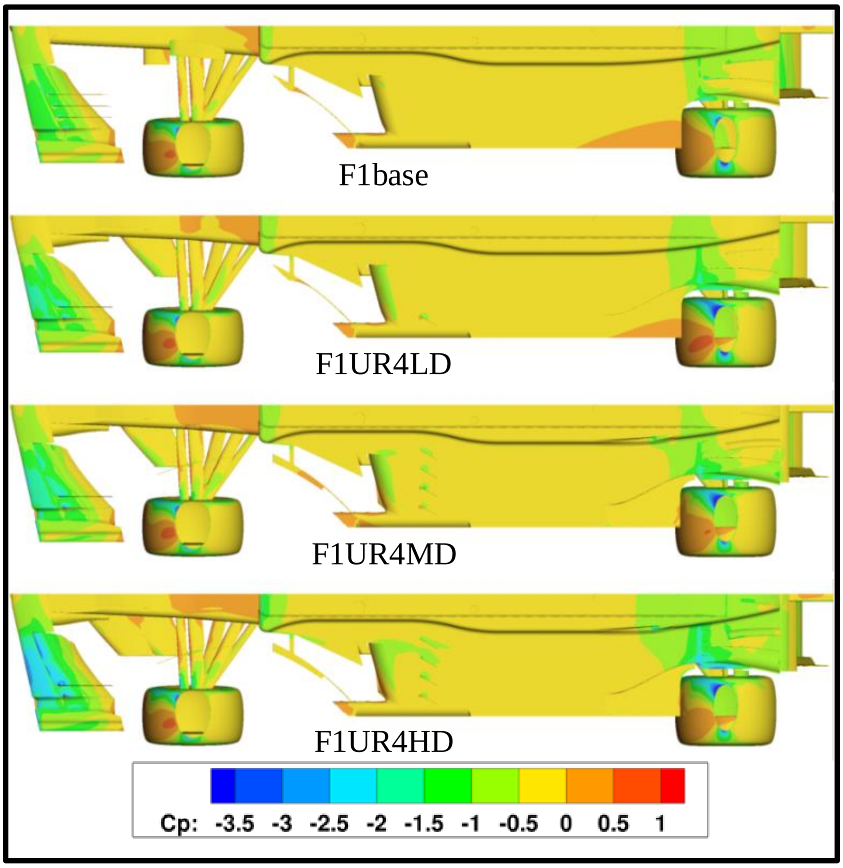

Figure 78: Pressure coefficient plot of the P2 car (d = 0.5L) - bottom view – baseline, LD, MD, HD vehicles

In Figures 82 and 83, streamwise velocity contours are plotted in XY planes, at two different heights (Z = 0.1 m and Z = 0.2 m, respectively): the goal is to look deeper into the flowfield which is closest to the ground and affects the front wing and the underfloor. The benefits inherent in the use of high-downforce layout are evident: the wake produced by the leading car is so much narrow and slender that the velocity of the flow feeding the front wing of the following car is very close to the freestream (40÷50 m/s). When the front wing is properly fed, its aerodynamic devices are able to create energetic vortical structures which travel down the front bodywork and help the underfloor to work harder: that is why improvements in front wing performance go hand in hand with underfloor enhancements.

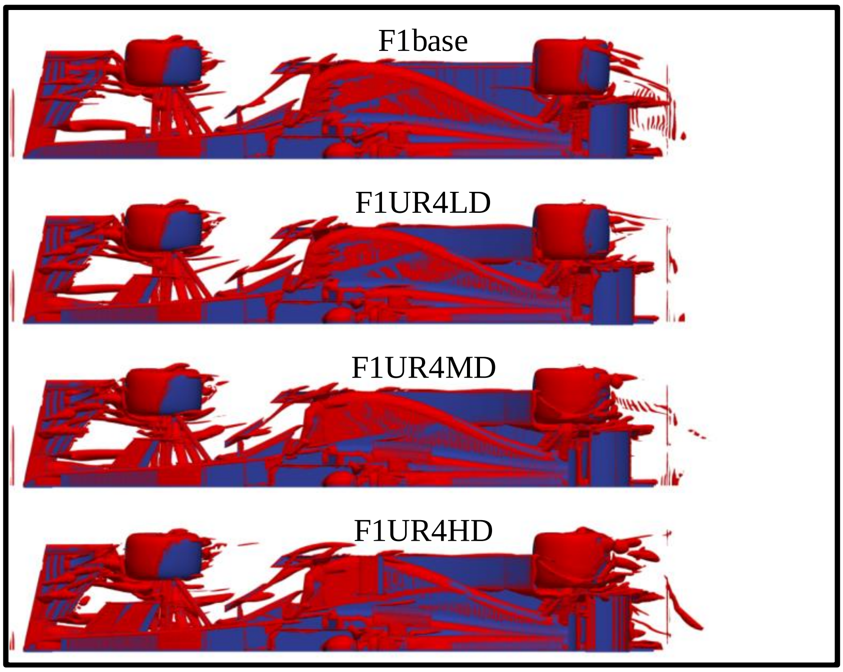

Figure 79: Iso-contour of Q = 50000 1/s^2 – P2 car (d = 0.5L) - top view - baseline, LD, MD, HD vehicles

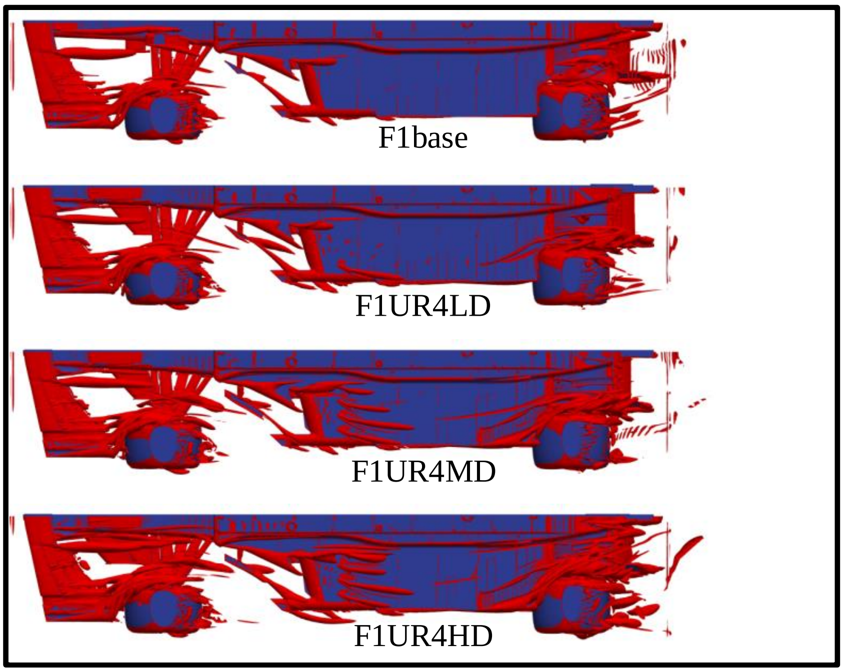

Figure 80: Iso-contour of Q = 50000 1/s^2 – P2 car (d = 0.5L) - bottom view - baseline, LD, MD, HD vehicles

Looking at the cars in 2nd position, it is really difficult to find common features between the four wakes, as different geometries have to deal with different types of flow coming from the leading car. In order to complete the analysis of the four aerodynamic configurations in wake flow, the plots of the streamlines feeding front wing, rear wing and underbody of the car in 2nd position (P2) are illustrated in Figures 84, 85, and 86, respectively.

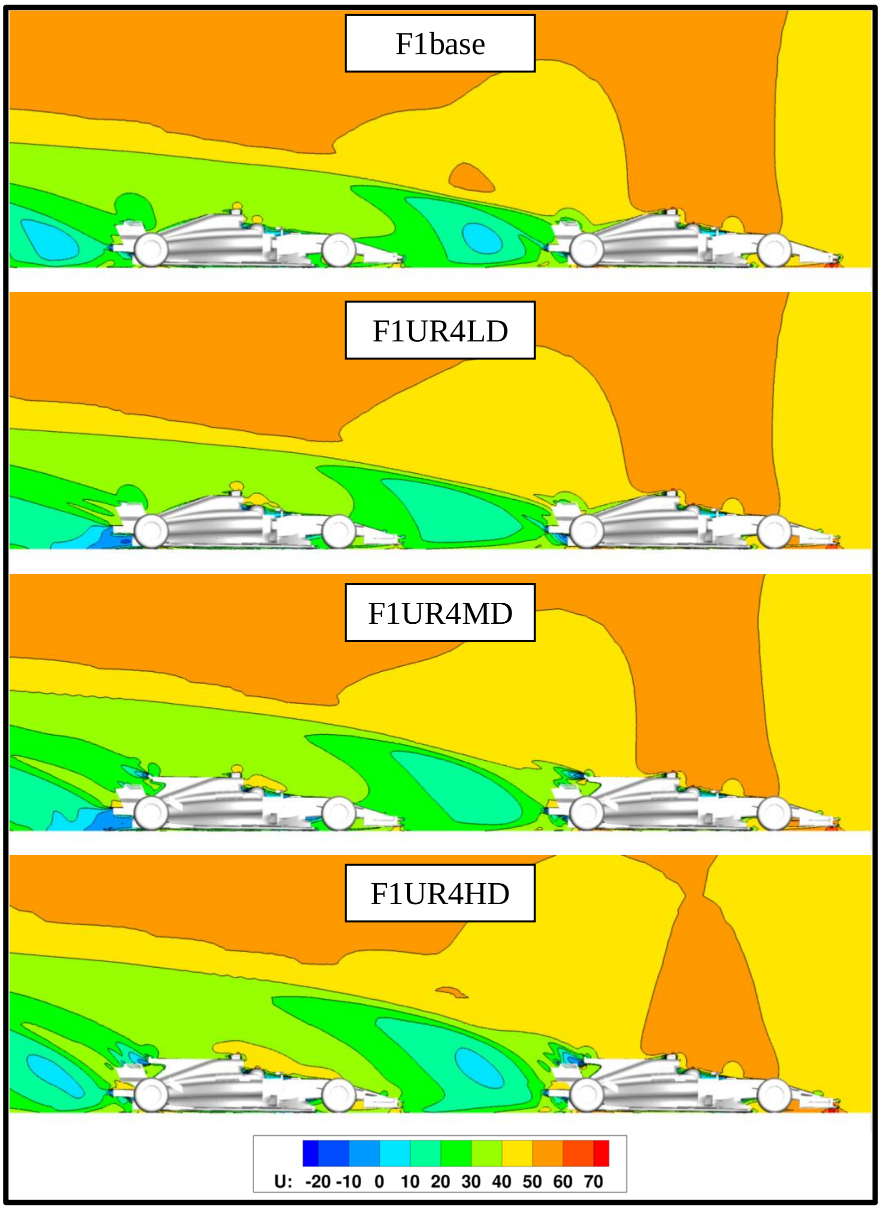

Figure 81: Streamwise velocity plot (U) on the symmetry plane (XZ plane) – d = 0.5L - baseline, low, medium, high-downforce vehicles

As already underlined in Chapter 6, front wings running in wake flow suffer the most in correspondence of the FIA control section: this region does not directly provide downforce, but, unfortunately, flap tips are responsible for the Y250 vortex. In this regard, the high-downforce configuration is by far the best, both in terms of airflow direction and kinetic energy content, thanks to the fact that the streamlines feeding the front wing almost entirely bypass the leading car. The more the wake of the P1 car is short and directed inwards, the fresher flow at each side of the vehicle can fill the region in front of the P2 car.

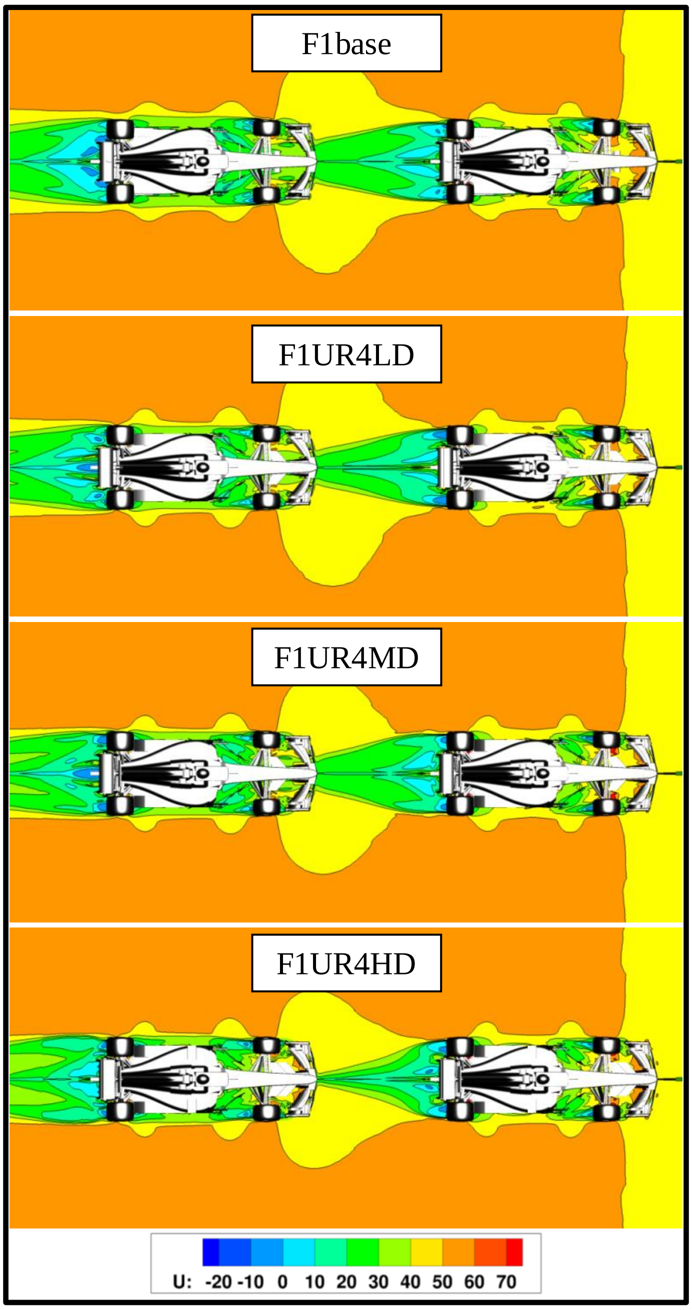

Figure 82: Streamwise velocity plot (U) on XY plane (Z = 0.1 m) – d = 0.5L - baseline, low, medium, high-downforce vehicles

Concerning the rear wing, none of the new aerodynamic configurations seems to have distinct advantages over the baseline vehicle: the airflow is initially able to bypass the leading car, but thereafter it loses its energy and deviates from the X-direction, because of the interaction with the front bodywork of the following vehicle. Also the high-downforce rear wing, which evidences a lower downforce loss than the baseline, was designed for other purposes than reaching pure performance: on the one hand, it has got the specific task of deflecting upwards the wake of the P1 car; on the other hand, it helps to avoid separation in the diffuser of the P2 car.

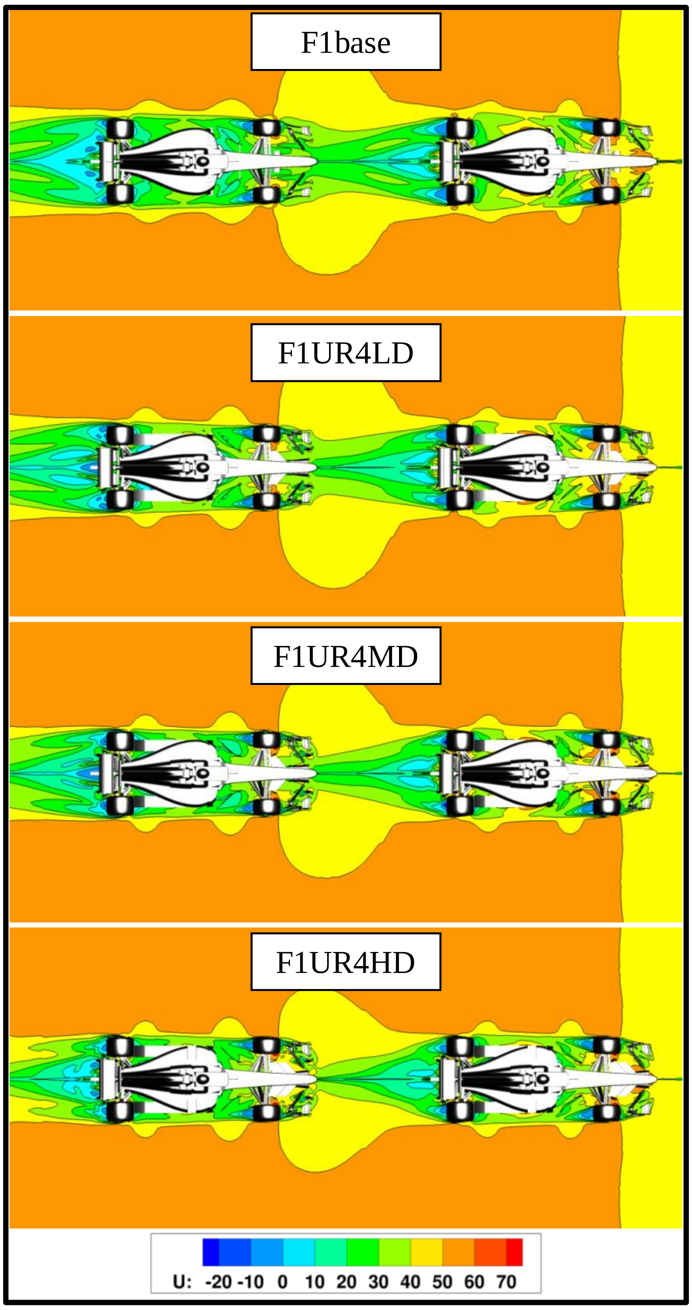

Figure 83: Streamwise velocity plot (U) on XY plane (Z = 0.2 m) – d = 0.5L - baseline, low, medium, high-downforce vehicles

As mentioned previously, the behaviour of the underfloor in slipstream is one of the most serious issues of this research. The skid bock, which works at very low ride heights and makes extensive use of ground effect, has more need than any other device to receive two-dimensional and clean flow. Unfortunately, as documented by Figure 86, this region is the most affected by low-energy and chaotic flow, coming from rear tyres and front bodywork of the lead car. The operating conditions of the baseline vehicle in slipstream are critical: only few streamlines are able to properly feed the underbody bypassing the P1 car.

The new aerodynamic configurations improve step by step the underbody performance. In low-downforce layout, the kinetic energy of the side streamlines begins to increase.

The medium-downforce vehicle reduces the width of the disturbed region. Lastly, the high-downforce configuration can minimize the impact of the tyre wake in the middle region of the underfloor and to entrain high-energy flow from the outer side of the vehicle.

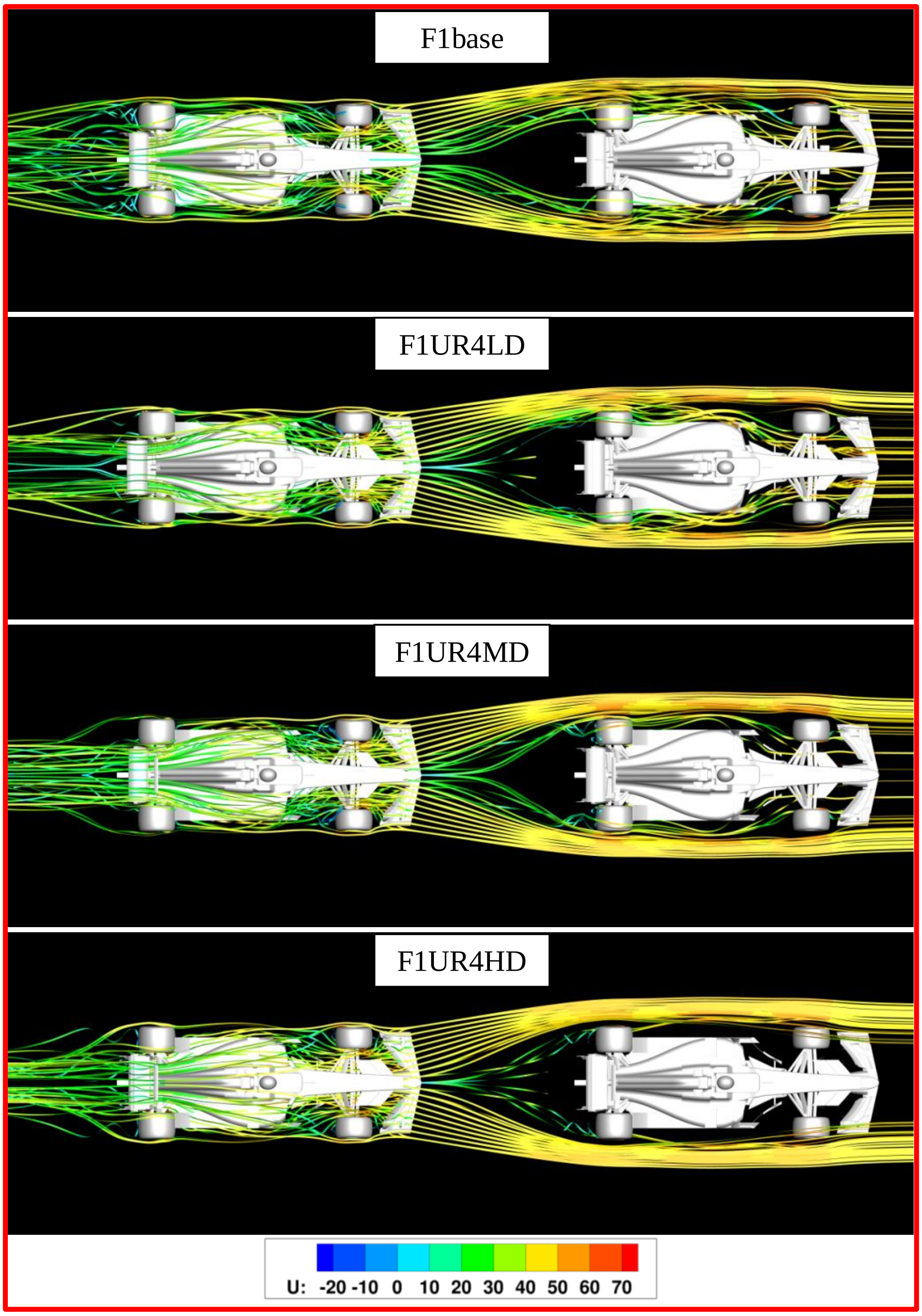

Figure 84: Streamlines feeding the front wing of the car in 2nd position (P2) – baseline, low, medium, high-downforce vehicles

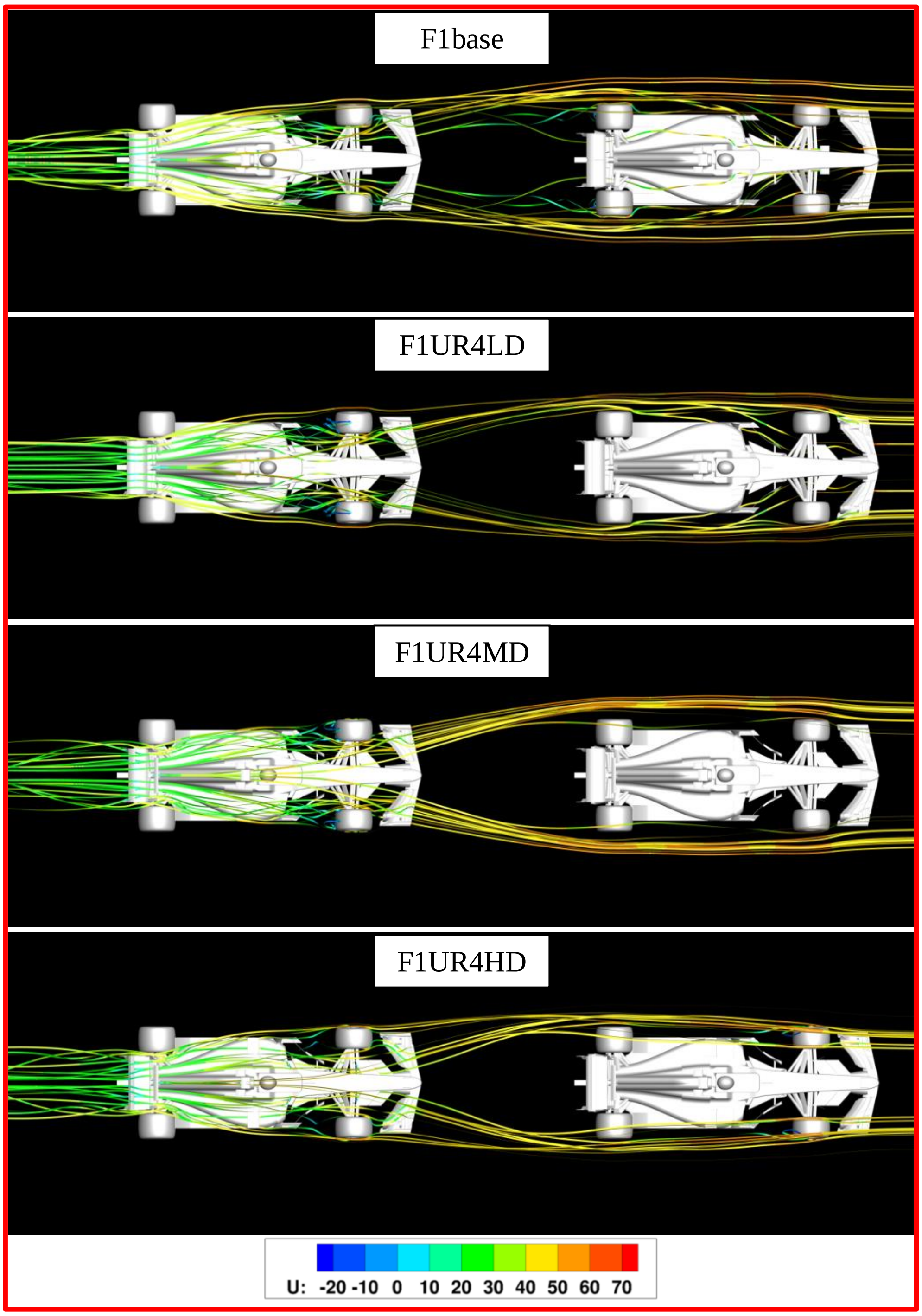

Figure 85: Streamlines feeding the rear wing of the car in 2nd position (P2) – baseline, low, medium, high-downforce vehicles

7.1.2 Focus on High-Downforce Vehicle

Once established that the F1UR4HD layout is by far the best solution for improving the aerodynamic behaviour of two vehicles racing very close to each other (0.5L), a supplementary simulation set was developed in order to better quantify the performance of the above mentioned aerodynamic configuration.

The baseline (F1base) and the high-downforce (F1UR4HD) layouts were analysed in tandem-running simulations at three additional distances: L, 2L, 4L. The designated setup was 15-55. Table 29 compares the two configurations in terms of absolute performance coefficients; in addition, the percentage changes of the P2 car performance with respect of the isolated vehicle in freestream flow are graphically displayed in Figures 87-90.

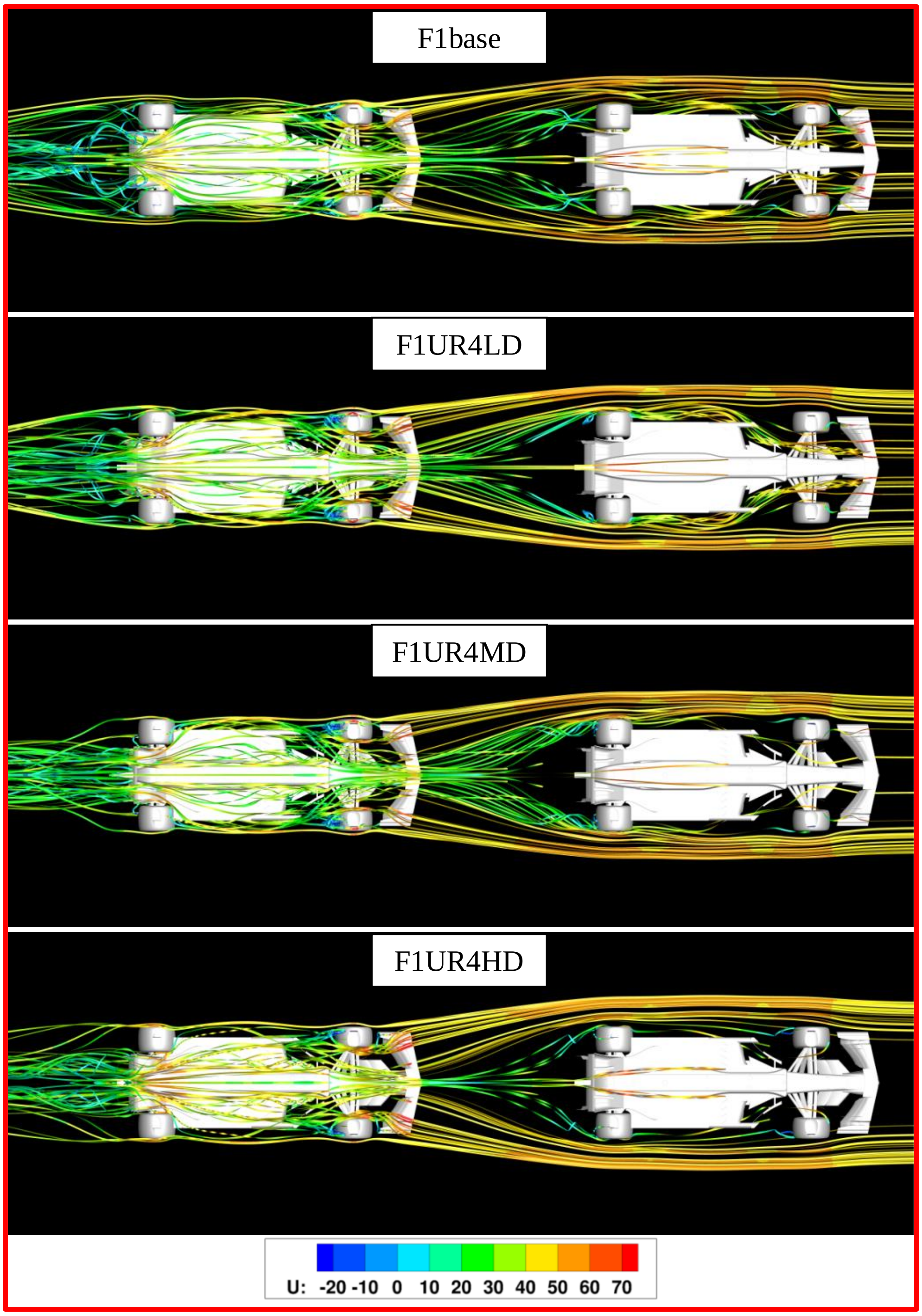

Figure 86: Streamlines feeding the underfloor of the car in 2nd position (P2) – baseline, low, medium, high-downforce vehicles

The benefits of the high-downforce design go beyond the specific case where the distance between the two vehicles is very short (d = 0.5L). Indeed, the F1UR4HD aero package is able to drastically reduce downforce and efficiency losses during the approach to the leading car (d = L, d = 2L); also, the front balance is much more stable, improving driveability and safety. These results are very significant and confirm the potential of the considered aerodynamic design in facilitating overtaking in F1: indeed, most of the time, the following car is not even capable of approaching the vehicle ahead, especially in medium and high-speed corners, because of the aerodynamic performance worsening and the consequent decrease in tyre grip. In other words, if the approach to the leading car is difficult, also the places on track where overtaking is easier cannot be exploited by the following driver (for instance, the braking point at the end of long straights, where drag reduction in slipstream is significant and the downforce loss is not particularly harmful).

0.5L	*SCx [m^2]*	*SCz [m^2]*	*Cz/Cx*	*FB*
F1base	0.80	-1.64	2.1	0.49
F1UR4HD	1.26	-3.14	2.5	0.49

L	*SCx [m^2]*	*SCz [m^2]*	*Cz/Cx*	*FB*
F1base	0.92	-1.95	2.1	0.55
F1UR4HD	1.39	-3.89	2.8	0.48

2L	*SCx [m^2]*	*SCz [m^2]*	*Cz/Cx*	*FB*
F1base	1.02	-2.62	2.6	0.49
F1UR4HD	1.52	-4.56	3.0	0.45

4L	*SCx [m^2]*	*SCz [m^2]*	*Cz/Cx*	*FB*
F1base	1.09	-3.14	2.9	0.44
F1UR4HD	1.57	-4.80	3.1	0.44

Table 29: Comparison between the performance coefficients of baseline (F1base) and high-downforce configurations (F1UR4HD) at different distances (d = 0.5L, L, 2L, 4L)

As usual, the contribution of the most important aerodynamic components was quantified. Table 30 collects coefficients of drag and downforce, related to the front wing. When the distance between the two vehicles is greater than or equal to 2L, wing performance is almost equivalent; for shorter distances, the advantages of the high-downforce layout are undeniable.

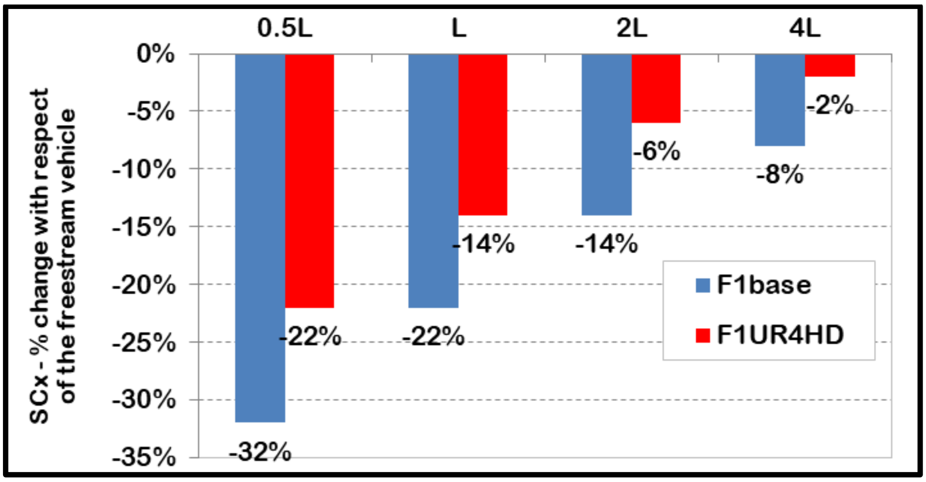

Figure 87: Comparison between the drag (SCx) of baseline and high-downforce vehicles at different distances (d = 0.5L, L, 2L, 4L): % change with respect of the vehicle in freestream flow

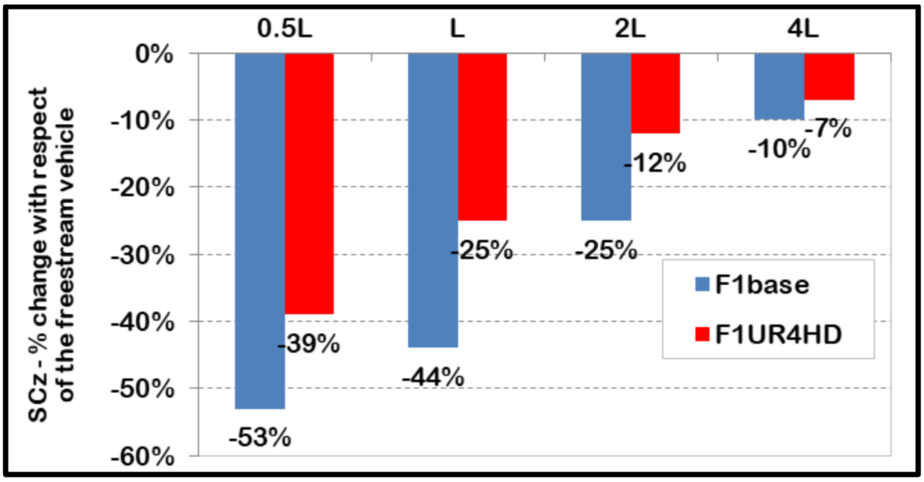

Figure 88: Comparison between the downforce (SCz) of baseline and high-downforce vehicles at different distances (d = 0.5L, L, 2L, 4L): % change with respect of the vehicle in freestream flow

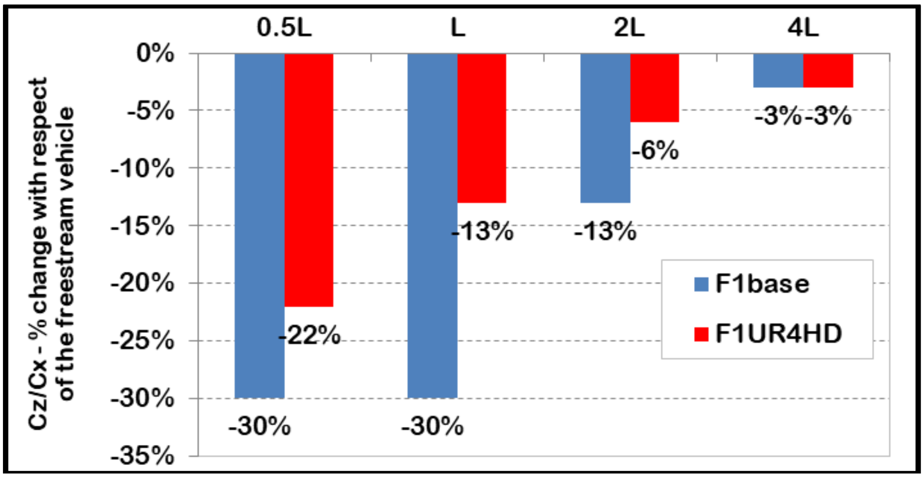

Figure 89: Comparison between the efficiency (Cz/Cx) of baseline and high-downforce vehicles at different distances (d = 0.5L, L, 2L, 4L): % change with respect of the vehicle in freestream flow

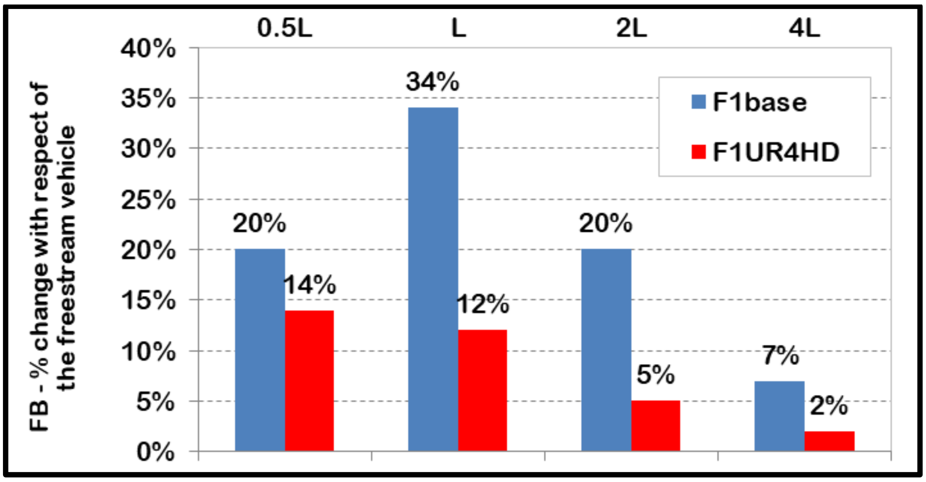

Figure 90: Comparison between the front balance (FB) of baseline and high-downforce vehicles at different distances (d = 0.5L, L, 2L, 4L): % change with respect of the vehicle in freestream flow

0.5L	*SCx [m^2]*	*SCz [m^2]*
F1base	0.127	-0.62
F1UR4HD	0.204	-0.97

0.5L	*SCx [m^2]*	*SCz [m^2]*
F1base	-19%	-33%
F1UR4HD	-5%	-14%

L	*SCx [m^2]*	*SCz [m^2]*
F1base	0.155	-0.78
F1UR4HD	0.218	-1.07

L	*SCx [m^2]*	*SCz [m^2]*
F1base	+0%	-15%
F1UR4HD	+5%	-5%

2L	*SCx [m^2]*	*SCz [m^2]*
F1base	0.168	-0.87
F1UR4HD	0.215	-1.10

2L	*SCx [m^2]*	*SCz [m^2]*
F1base	+6%	-5%
F1UR4HD	+5%	-3%

4L	*SCx [m^2]*	*SCz [m^2]*
F1base	0.169	-0.91
F1UR4HD	0.213	-1.12

4L	*SCx [m^2]*	*SCz [m^2]*
F1base	+6%	-1%
F1UR4HD	+0%	-1%

Table 30: Comparison between baseline and high-downforce configurations at different distances (d = 0.5L, L, 2L, 4L): performance coefficients of the P2 front wing and % change with respect of the vehicle in freestream flow

As explained before, the high-downforce rear wing is not designed for pure performance, but for enhancing the interaction with the diffuser and shielding the wake flow. Nevertheless, the simulations conducted at greater distances (d = L, 2L and 4L) reveal that the behaviour of the new rear wing is even better than that at d = 0.5L. Unlike the front wing, the high-downforce rear wing shows its biggest improvement when working at d = L and d = 2L (Table 31).

0.5L	*SCx [m^2]*	*SCz [m^2]*
F1base	0.127	-0.43
F1UR4HD	0.185	-0.39

0.5L	*SCx [m^2]*	*SCz [m^2]*
F1base	-46%	-53%
F1UR4HD	-49%	-49%

L	*SCx [m^2]*	*SCz [m^2]*
F1base	0.135	-0.48
F1UR4HD	0.233	-0.49

L	*SCx [m^2]*	*SCz [m^2]*
F1base	-42%	-48%
F1UR4HD	-38%	-36%

2L	*SCx [m^2]*	*SCz [m^2]*
F1base	0.175	-0.63
F1UR4HD	0.295	-0.61

2L	*SCx [m^2]*	*SCz [m^2]*
F1base	-25%	-32%
F1UR4HD	-19%	-21%

4L	*SCx [m^2]*	*SCz [m^2]*
F1base	0.210	-0.77
F1UR4HD	0.330	-0.68

4L	*SCx [m^2]*	*SCz [m^2]*
F1base	-13%	-16%
F1UR4HD	-11%	-12%

Table 31: Comparison between baseline and high-downforce configurations at different distances (d = 0.5L, L, 2L, 4L): performance coefficients of the P2 rear wing and % change with respect of the vehicle in freestream flow

Finally, the underfloor performance was taken into account (Table 32). The biggest downforce improvements occur when d = L and d = 2L, proving once again the strong link between the rear wing and the diffuser: at the end of the analysis, it can be reasonably concluded that this concept is the key to solving the problem of overtaking.

7.2 Conclusions

The new aero packages described in Chapter 7 (F1UR4LD, F1UR4MD and F1UR4HD) and the baseline vehicle (F1base) were tested in tandem-running simulations at a distance of 0.5L. All the new configurations proved to suffer lower downforce and efficiency losses than the original, when running in wake flow. However, low and medium downforce vehicles, as well as the baseline, are characterized by a significant increase in front balance, which undermines driveability and driver safety during braking and high-speed corners. Surprisingly, the high-downforce configuration showed the best performance in slipstream: in light of this, an additional set of simulations was carried out at larger distances (d = L, 2L, 4L), in order to quantify in detail the benefits of this aero package over the baseline. The results are encouraging: the high-downforce configuration is much better not only when the two vehicles are racing very close to each other, but also during the approaching phase, making overtaking much easier and safer. This significant performance improvement in slipstream was reached by means of some design innovations. First of all, a lot of aero devices, such as winglets and canards, were added on the vehicle bodywork, in order to distribute the downforce all over the vehicle. If only few components are dedicated to the generation of downforce, even a small disturbance can potentially have massive consequences for the entire vehicle aerodynamics. For instance, the vortex tubes generated by the front-end of the vehicle survive for a shorter time when working in wake flow so they cannot properly feed the downstream aero devices, such as the underfloor. Furthermore, in light of the simulation results documented in Chapter 6, the bottom of the car underwent a lot of changes. An array of vortex generators re-energizes the flow at the step plane inlet, while a turning vane accelerates the flow in correspondence of the diffuser: thanks to these local devices, the low-pressure areas of the underfloor are partially restored, despite the low-energy flow feeding the bottom of the car. Apart from the local benefits on the car in slipstream, the above described devices make the wake coming from the underfloor of the leading vehicle very narrow in Y-direction.

0.5L	*SCx [m^2]*	*SCz [m^2]*
F1base	0.102	-0.84
F1UR4HD	0.187	-1.55

0.5L	*SCx [m^2]*	*SCz [m^2]*
F1base	-47%	-58%
F1UR4HD	-27%	-42%

L	*SCx [m^2]*	*SCz [m^2]*
F1base	0.125	-1.07
F1UR4HD	0.215	-1.99

L	*SCx [m^2]*	*SCz [m^2]*
F1base	-37%	-46%
F1UR4HD	-15%	-26%

2L	*SCx [m^2]*	*SCz [m^2]*
F1base	0.153	-1.50
F1UR4HD	0.232	-2.42

2L	*SCx [m^2]*	*SCz [m^2]*
F1base	-21%	-25%
F1UR4HD	-8%	-10%

4L	*SCx [m^2]*	*SCz [m^2]*
F1base	0.176	-1.80
F1UR4HD	0.248	-2.50

4L	*SCx [m^2]*	*SCz [m^2]*
F1base	-5%	-10%
F1UR4HD	-4%	-7%

Table 32: Comparison between baseline and high-downforce configurations at different distances (d = 0.5L, L, 2L, 4L): performance coefficients of the P2 underfloor and % change with respect of the vehicle in freestream flow

At last, also the rear-end geometry was heavily modified. The mutual collaboration between the three-element rear wing and the beam wing mounted on the rear crash enhances the diffuser extraction and consequently prevents the flow separation afflicting the car in slipstream. In addition to the above described improvements, the new rear wing assembly minimizes the impact of the wake generated by the lead vehicle, giving the streamlines underneath the car a strong upward deviation and shielding the following vehicle against the incoming low-energy flow: as a result, the overall wake is very short in X-direction. Tyre ramps and T-wings perform the same function, although their contribution seems to have a reduced impact.

In conclusion, the features of the new wake in terms of width (XY plane) and height (XZ plane) allow high-energy flow to fill the gap between the two vehicles from the outside, thus improving the aerodynamic performance of the car in slipstream.

Chapter 8. Sideslip Angle Sensitivity

As already seen in previous chapters, a racing car should have good performance when running in freestream flow as well as in slipstream. Off-design conditions are not limited to wake flows: when racing on a real track, every vehicle is constantly subjected to sudden direction changes. During cornering, where the downforce plays a key role in ensuring tyre grip, the flow is not perfectly aligned with the longitudinal axis of the vehicle. On the contrary, it is characterized by a certain incidence in XY plane, which is called sideslip angle: its value is not much different from that of the tyre slip angle (5÷8° for typical racing car applications). In the above described operating conditions, vehicle aerodynamics must provide adequate values of downforce and front balance. As indicated by Hucho et al. (1998), the resulting yawed flow normally causes an increase in drag and a decrease in downforce. In particular, the downforce loss at the rear axle should be equal or smaller than that at the front axle, in order to ensure both driveability and safety. The yawed flow is also responsible for the generation of a side force on the vehicle: if the centre of pressure is located behind the centre of gravity, the resulting yawing moment helps to turn the vehicle to the airflow, thus increasing stability. This chapter deals with the numerical simulations of baseline, low, medium and high-downforce vehicles running in yawed flow: the aerodynamic performance will be evaluated in terms of downforce and drag coefficients, efficiency, front balance and side force coefficient.

8.1 Mesh and Simulation Setup

The simulation set for sideslip angle analysis differs in some respects from the previous cases. The flow at the inlet of the virtual wind tunnel, while maintaining the original velocity magnitude (50 m/s), is tilted to the right (DX) by the sideslip angle (α) with respect to the longitudinal axis (Figure 91). As a result of asymmetric flow, the entire geometry of the car needs to be simulated in a double-width volume mesh.

8.2 Results and Discussion

All four aerodynamic configurations (F1base, F1UR4LD, F1UR4MD and F1UR4HD) were investigated at two sideslip angles: 10° and 20°. The chosen values are greater than those indicated in the introduction of this chapter, in order to stress the vehicle aerodynamics in critical conditions, such as sliding and abrupt loss of mechanical grip. The chosen setup for each vehicle was 15-55.

Table 33 summarizes the results of the simulations at 10° in terms of global performance coefficients and percentage change with respect of the isolated vehicle running in freestream flow.

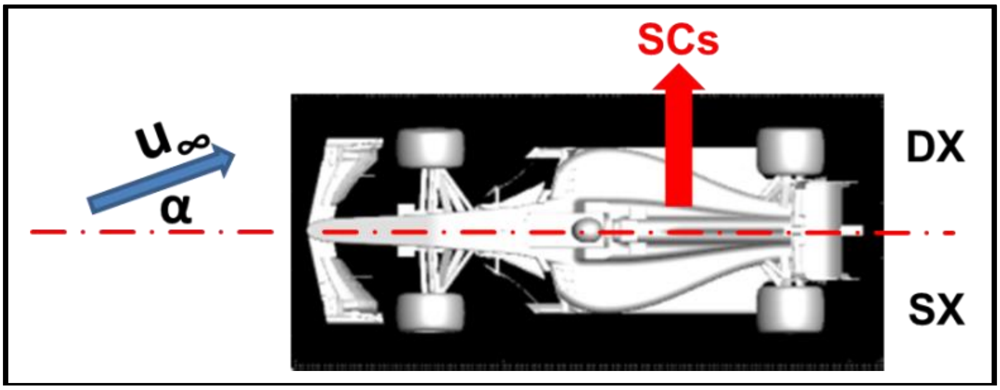

Figure 91: Definition of sideslip angle

$\alpha = 10°$	$SCx\ [m^2]$	$SCz\ [m^2]$	Cz/Cx	FB	FB_{DX}	FB_{SX}	$SCs\ [m^2]$
F1base	1.16	-3.40	2.9	0.40	0.34	0.46	0.08
F1UR4LD	1.07	-3.60	3.4	0.41	0.35	0.47	0.10
F1UR4MD	1.31	-4.15	3.2	0.41	0.36	0.46	0.13
F1UR4HD	1.58	-4.96	3.1	0.42	0.39	0.46	0.14

$\alpha = 10°$	$SCx\ [m^2]$	$SCz\ [m^2]$	Cz/Cx	FB
F1base	-2%	-2%	-9%	-2%
F1UR4LD	-1%	-1%	-0%	-2%
F1UR4MD	-2%	-5%	-3%	-2%
F1UR4HD	-2%	-4%	-3%	-0%

Table 33: Performance coefficients of baseline, low, medium and high-downforce configurations in yawed flow (10°): absolute values and percentage change with respect of the vehicle in freestream flow

At first, the downforce losses occurred in the 10° case are less than or equal to 5% for all the aerodynamic configurations. The slight worsening of downforce performance is accompanied by a little decrease in drag. This latter result seems to be in contradiction with what reported above: nevertheless, the data by Hucho et al. (1998) refer to a sport car, where the induced drag is of lesser importance than the pressure drag. On the contrary, the induced drag of a modern F1 car, associated with axial vorticity and hence with generation of downforce, is the great majority of total drag: if the aerodynamic devices do not work properly, the related three-dimensional vortices are weaker and dissipate less energy in X-direction. Moreover, part of the energy contained in the freestream flow is spent on generating a side force (SCs): as stated in Table 33, its magnitude is rising with the downforce level of the considered aerodynamic configuration and hence with the lateral area of the vehicle. The side force magnitudes range from 7 to 10% of the overall drag. The performance of the three new layouts (F1UR4LD, F1UR4MD, F1UR4HD) are more or less on the same level as the baseline when working with a 10° sideslip angle, except insofar as the efficiency losses are lower.

Having determined that the downforce losses are not significant, the focus moves on front balance results: luckily, in all cases the centre of pressure tends to shift rearward or remains in the same position. It is also interesting to note that the two sides of the vehicle show different behaviour: the centre of pressure of the left half is located much more forward than that of the right half, due to the relative angle between the longitudinal axis of the vehicle and the flow velocity vector, pointing to the right. Looking at the results of the 20° case (Table 34) one can see that downforce losses become more pronounced, as well as efficiency worsening: in this respect, the new aerodynamic configurations seem to have a slightly better performance than the baseline.

α = 20°	*SCx [m^2]*	*SCz [m^2]*	*Cz/Cx*	*FB*	*FB_{DX}*	*FB_{SX}*	*SCs [m^2]*
F1base	1.13	-2.97	2.6	0.42	0.28	0.60	0.20
F1UR4LD	1.08	-3.37	3.1	0.42	0.29	0.56	0.26
F1UR4MD	1.31	-3.98	3.0	0.41	0.31	0.51	0.31
F1UR4HD	1.58	-4.72	3.0	0.42	0.34	0.51	0.32

α = 20°	*SCx [m^2]*	*SCz [m^2]*	*Cz/Cx*	*FB*
F1base	-4%	-15%	-13%	+2%
F1UR4LD	-0%	-7%	-9%	-0%
F1UR4MD	-2%	-9%	-9%	-2%
F1UR4HD	-2%	-9%	-6%	-2%

Table 34: Performance coefficients of baseline, low, medium and high-downforce configurations in yawed flow (20°): absolute values and percentage change with respect of the vehicle in freestream flow

The same is true for front balance: while the baseline aerodynamics suffers from a forward shift of the centre of pressure, the new configurations become more stable (F1UR4MD and F1UR4HD) or, at least, maintain the original driveability (F1UR4LD). Moreover, with a greater sideslip angle, the difference between the front balance of each side of the vehicle becomes more significant and the side force magnitude grows up to 18÷24% of the overall drag.

Once established the asymmetric behaviour of the vehicle, a further investigation was carried out on the most important aerodynamic devices equipping the car, in order to better understand their functioning. Table 35 shows that the left half of the front wing works slightly better than the right part.

Front Wing (α = 10°)	*SCz [m^2] DX*	*SCz [m^2] SX*
F1base	-0.44	-0.46
F1UR4LD	-0.39	-0.41
F1UR4MD	-0.43	-0.45
F1UR4HD	-0.54	-0.56

Front Wing (α = 20°)	*SCz [m^2] DX*	*SCz [m^2] SX*
F1base	-0.41	-0.43
F1UR4LD	-0.37	-0.42
F1UR4MD	-0.41	-0.45
F1UR4HD	-0.52	-0.56

Table 35: Downforce coefficients related to the front wing: comparison between right and left sides - α = 10° and 20°

Conversely, as reported in Tables 36 and 37, rear wing and underfloor show the opposite behaviour: this explains why the centre of pressure of the right half of the car is shifted rearward, while the downforce generated by the left part of the vehicle is more concentrated on the front axle.

Rear Wing (α = 10°)	*SCz [m^2] DX*	*SCz [m^2] SX*
F1base	-0.45	-0.43
F1UR4LD	-0.38	-0.36
F1UR4MD	-0.37	-0.35
F1UR4HD	-0.38	-0.37

Rear Wing (α = 20°)	*SCz [m^2] DX*	*SCz[m^2] SX*
F1base	-0.41	-0.30
F1UR4LD	-0.36	-0.31
F1UR4MD	-0.36	-0.32
F1UR4HD	-0.37	-0.32

Table 36: Downforce coefficients related to the rear wing: comparison between right and left sides - α = 10° and 20°

Underfloor (α = 10°)	*SCz [m^2] DX*	*SCz [m^2] SX*
F1base	-0.98	-0.95
F1UR4LD	-1.03	-0.99
F1UR4MD	-1.18	-1.15
F1UR4HD	-1.30	-1.27

Underfloor (α = 20°)	*SCz [m^2] DX*	*SCz [m^2] SX*
F1base	-0.97	-0.90
F1UR4LD	-1.03	-0.96
F1UR4MD	-1.20	-1.13
F1UR4HD	-1.30	-1.23

Table 37: Downforce coefficients related to the underfloor: comparison between right and left sides - α = 10° and 20°

No further investigations on drag and downforce of the single components were reported, because the percentage changes with respect of the isolated vehicle are not very significant and the performance of the new aerodynamic configurations are in line with those of the baseline vehicle.

The following section aims at investigating from a qualitative point of view the features of the flow and their effect on force distribution. Only the 20° case was taken into account to highlight the differences between the two sides of the bodywork. Figures 92 and 93 show the pressure coefficient plots related to the four aerodynamic configurations, from top and bottom view. Looking at the pressure side of the front wing, no difference can be found between the left and right part; on the contrary, the low-pressure core on the left suction side is slightly larger than the right one. The pressure discrepancies on the underfloor are hard to notice, because of the large surface on which they are distributed: the diffuser seems to be almost symmetrical, while the underbody inlet is characterized by a little larger low-pressure core on the right side. The behaviour of the rear wing is rather clear: in all four cases, the left pressure side does not provide the expected performance, perhaps because the large endplate obstructs the airflow passage.

As seen in previous chapters, axial vorticity plays a key role in generation of downforce: Figures 94 and 95 help in understanding how the sideslip angle affects direction and position of the most significant vortical structures.

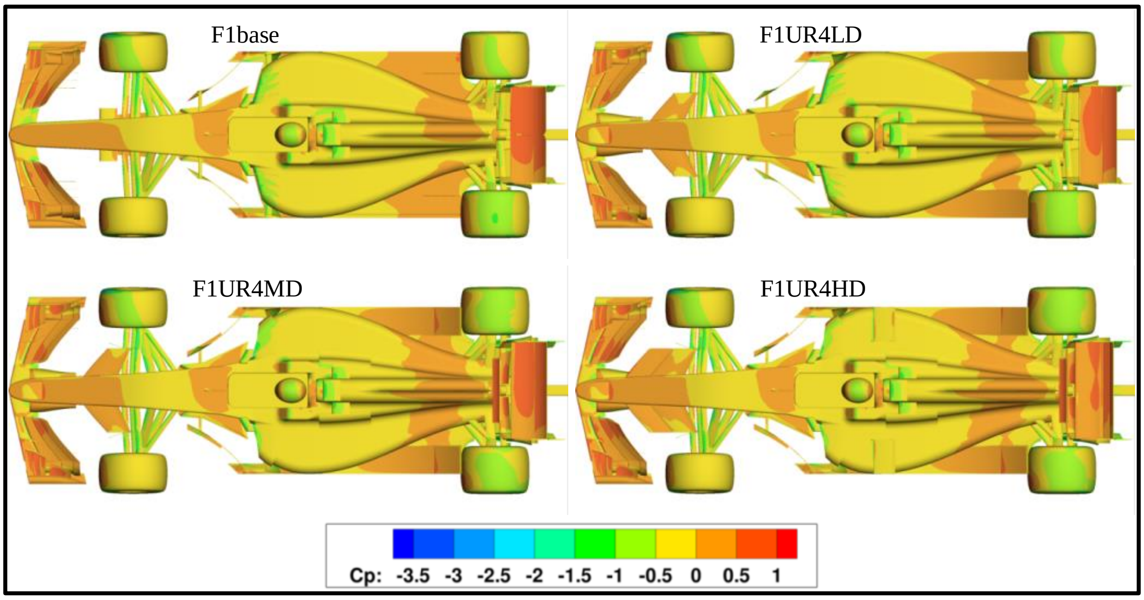

Figure 92: Pressure coefficient plot – α = 20° – top view – baseline, low, medium and high-downforce vehicles

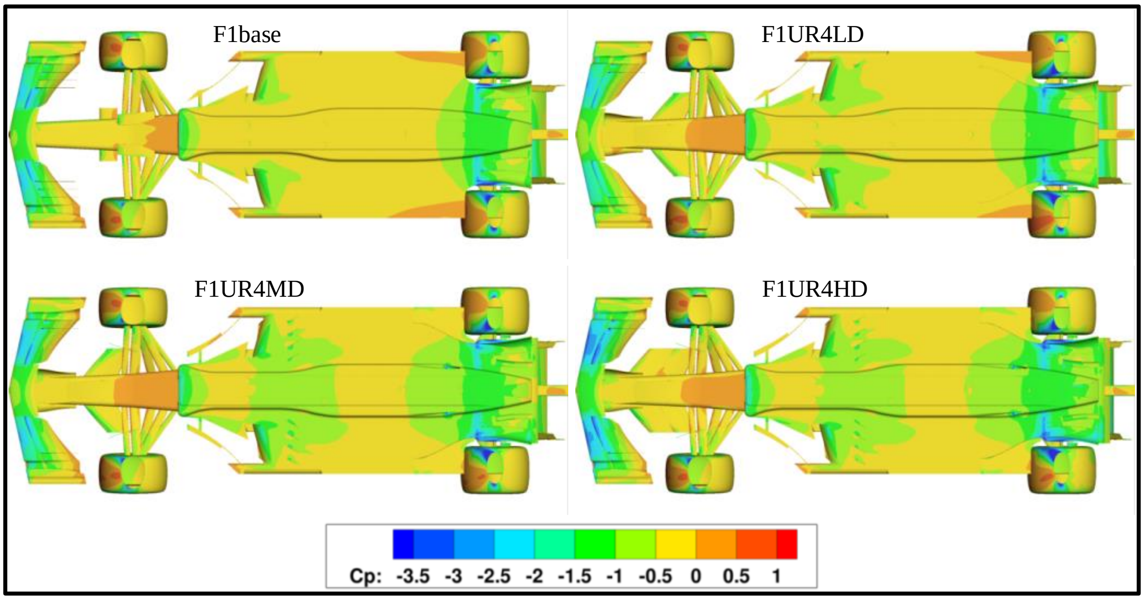

Figure 93: Pressure coefficient plot – α = 20° – bottom view – baseline, low, medium and high-downforce vehicles

The Y250 vortex does not undergo substantial changes: no rotation or shift in the direction of the main flow can be noticed; however, things are different when it comes to the side devices of the front wing: the vortex system aimed at bypassing the front tyres is almost non-existent on the right, while maintaining its original features on the left. Visually, the underfloor vortical structures, such as those generated by the bargeboard and the step plane inlet, are essentially symmetrical; only in the diffuser region the right Venturi vortex seems to be a little bit stronger than the left one. As already witnessed by the pressure coefficient plots, the left span of the rear wing is not properly fed by the airflow: as a consequence, the corresponding vortex is very weak. On the contrary, the right wingtip vortex is persistent and aligned with the direction of the main flow.

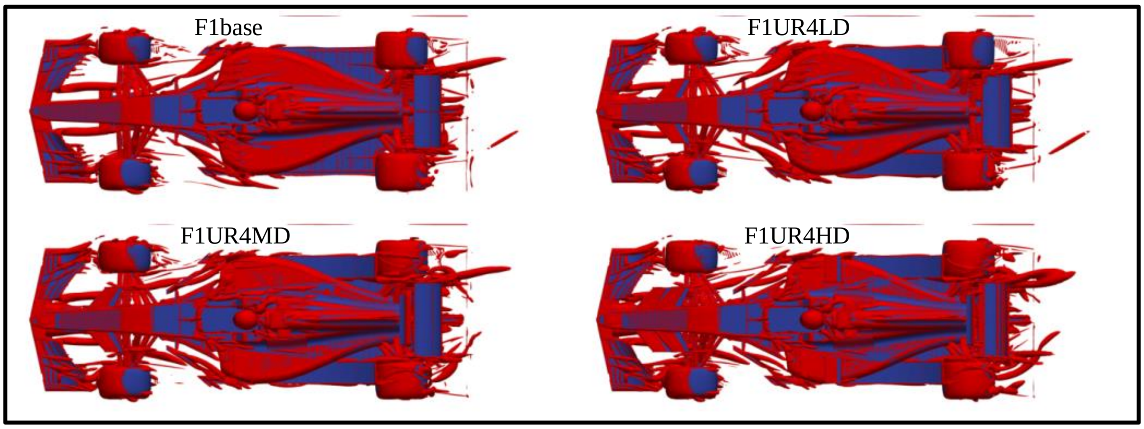

Figure 94: Iso-contour of Q = 50000 1/s^2 – α = 20° – top view – baseline, low, medium and high-downforce vehicles

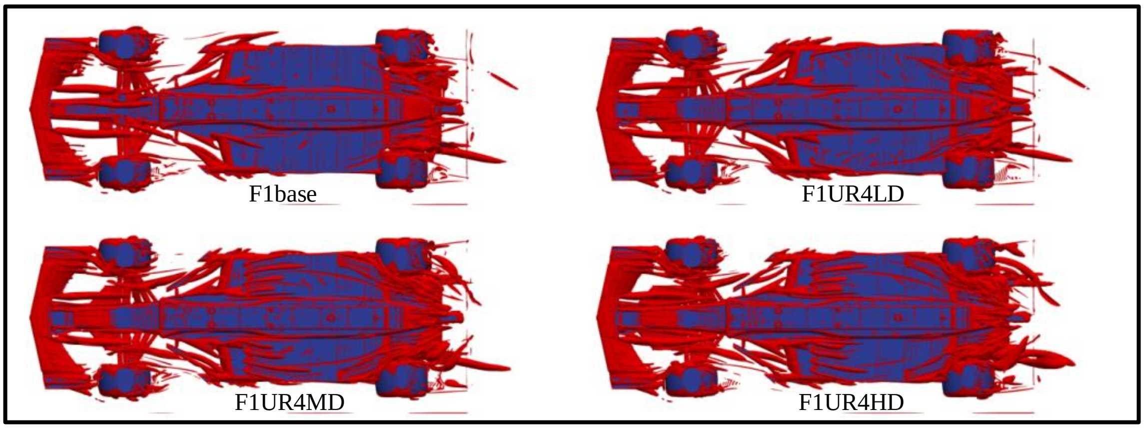

Figure 95: Iso-contour of Q = 50000 1/s^2 – α = 20° – bottom view – baseline, low, medium and high-downforce vehicles

8.3 Conclusions

The baseline layout and the three new aerodynamic configurations were simulated during cornering, where the freestream flow forms an angle with the longitudinal axis of the vehicle. This angle is the so called "sideslip angle". Downforce and front balance play a key role in these operating conditions: for this reason, the evaluation of the resulting performance changes is particularly important.

Luckily, in all cases, the worsening of downforce is not particularly significant. Apart from the baseline configuration working at 20° incidence, the front balance generally decreases or remains constant during cornering, leading to a stabilizing effect on the car.

The aerodynamic behaviour of the car is inevitably asymmetrical: when the freestream flow is pointing to the right, the centre of pressure of the left side moves forward; on the contrary, the centre of pressure of the right side moves towards the rear-end of the vehicle. In accordance with these results, the left side of the front wing generates more downforce than the right one; on the other hand, the right sides of underfloor and rear wing show better performance than the left ones.

Finally, it is noteworthy that the side force magnitude is rising with the sideslip angle and the lateral surface of the vehicle.

Chapter 9. Lap-time Simulations

The last part of the research is intended to quantify the performance of the new aerodynamic configurations in terms of lap-time. Depending on the features of the considered track, the best lap-time can be reached by means of a dedicated aerodynamic layout. In most cases, downforce is the key factor for competitiveness; sometimes efficiency is more important than vertical load; in some further circumstances, it is not easy to establish which performance parameter may take precedence over the other. Nevertheless, it goes without saying that drag reduction alone is no longer useful to optimize lap-time performance, in light of the current features of F1 cars and tracks.

It should be recalled that higher vertical load leads to an increase in lateral and longitudinal tyre grip, allowing faster cornering and better performance during acceleration and braking; on the other hand, the generation of downforce is always accompanied by induced drag: as a consequence, the vehicle is penalised by lower maximum speed on straights.

Different sets of lap-time simulations were carried out by means of the free software OptimumLap 1.4.2, in order to compare the performance of the new aerodynamic packages on the most important tracks of the F1 championship.

9.1 Simulation Tools

OptimumLap is a free software developed by ©OptimumG, an international company which offers engineering consulting, software solutions, data acquisition and training for motorsport teams, automotive manufacturers and race car industry (http://www.optimumg.com). It makes use of a quasi-steady-state point mass vehicle model: in spite of its simplicity, it is accurate due to the combined states that the vehicle can achieve, for instance accelerating and cornering simultaneously as well as decelerating and cornering simultaneously. Despite the model does not account for weight transfer, vehicle yaw and sophisticated tire models, its outputs can be very close to track logged data, with a 10% margin of error (OptimumLap v1.4 user guide).

9.2 Simulation Setup

Several inputs need to be set up, in order to define all the physical features of the vehicle. Table 38 summarizes the information required in the “General Data” section: the object of study in these simulations is a two-wheel drive (2WD) open wheeler single seat car. According to 2017 FIA Technical Regulations (https://www.fia.com/regulations), the weight of the car, without fuel, must always not be less than 728 kg during the entire race weekend. In 2018 the minimum weight has grown up to 733 kg, because of the introduction of the Halo safety system. Two different weights were simulated: 750 kg and 833 kg. The former choice is suitable for qualifying, where the driver needs to push the vehicle to its limits for a few laps: considering that over 10500 rpm the fuel mass flow must not exceed 100kg/h, a fuel load of about 20 kg allows the driver to run on track for approximately 10 minutes. The latter solution keeps into account the fuel necessary to complete an entire race: in fact, in addition to the fuel mass flow limitations, cars may use no more than 105 kg of fuel in each race.

General Data	*Input*
Vehicle type	Open wheeler car
Mass	750, 833 kg
Driven type	2WD

Table 38: Vehicle setup – General Data

In the section labelled “Aero Data” (Table 39) the differences between the three different aerodynamic configurations are highlighted. Air density, vehicle frontal area and performance coefficients are required for calculating drag and downforce. Front balance is not useful because the mathematical model does not consider the presence of front and rear axle.

Aero Data	*Input*
Air Density	1.225 kg/m^3
Front Area	1 m^2
Drag Coefficient	F1UR4LD: 1.08; F1UR4MD: 1.34; F1UR4HD: 1.61
Downforce Coefficient	F1UR4LD: 3.63; F1UR4MD: 4.35; F1UR4HD: 5.16

Table 39: Vehicle setup – Aero Data

“Tire Data” are shown in Table 40: the setup of these parameters is particularly important, because of their strong influence on the final performance of the car. Tire radius can be measured on the CAD model; the rolling resistance coefficient depends on several factors, such as tire pressure, slip angle and vehicle speed. However, as a first approximation, a constant value of 0.025 could be realistic for high-performance formula tires (http://hpwizard.com/tire-friction-coefficient.html and Milliken, 1995). The lateral friction coefficient indicates the tire capability to convert the vertical load in lateral force between the ground and the tire itself; the longitudinal friction coefficient is an expression of the link between the vertical load and the longitudinal forces, responsible for acceleration and braking. In both cases these coefficients are not constant, but they decrease as the vertical load increases: lateral and longitudinal load sensitivity keep into account this physical effect. On the basis of the information provided by the website motorsportmagazine.com, Valentini (2008), Lopez (2001) and the OptimumLap user guide, a realistic value of 2 defined at 102 kg (1000 N) was attributed both to lateral and longitudinal friction coefficients; the load sensitivity was set to 0.001.

Tire Data	*Input*
Tire Radius	0.33 m
Rolling Resistance	0.025
Longitudinal Friction	2 @ 102 kg
Longitudinal Load Sensitivity	0.001
Lateral Friction	2 @ 102 kg
Lateral Load Sensitivity	0.001

Table 40: Vehicle setup – Tire Data

Introduced in 2014, the latest F1 power units are really complex (https://www.formula1.com). They consist of six separate elements: the 1.6 litres V6 internal combustion engine (ICE), the motor generator unit-kinetic (MGU-K), the motor generator unit-heat (MGU-H), the energy store (ES), turbocharger (TC) and control electronics (CE). In terms of pure performance, the most important feature of this compound engine is the huge torque at low engine speed provided by the turbocharger and the electric motor generators.

The “Torque vs RPM” curve is the main input required by the “Engine Data” section: starting from an XY-chart in input (Table 41), the model calculates the “Power vs RPM” curve. These input data were obtained by updating the curve displayed in Figure 96, which refers to a 2014 engine (https://www.f1analisitecnica.com). Research and development in the last four years led to a significant increase in available maximum power: engine manufactures claim that 2018 engines are able to develop more or less 1000 hp (https://www.thisisf1.com). In accordance with the Technical Regulations, crankshaft rotational speed must not exceed 15000 rpm. The maximum torque can be achieved at very low engine speed, owing to the characteristics of the energy recovery system (MGU-H and MGU-K), while maximum power (≈ 1000 hp) is reached between 10000 and 12000 rpm.

Engine Speed [RPM]	*Engine Torque [Nm]*
5000	650.00
6000	650.00
7000	645.00
8000	640.00
9000	640.00
10000	640.00
11000	635.00
12000	600.00
13000	550.00
14000	460.00
15000	390.00

Table 41: Vehicle setup – Engine Data

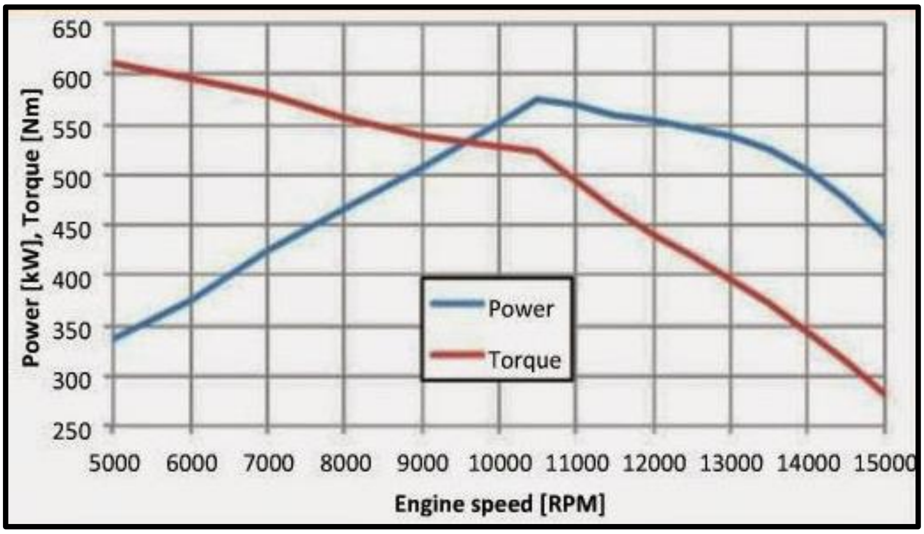

Figure 96: Torque and Power curves of a 2014 F1 Engine (https://www.f1analisitecnica.com)

With the aim of analysing the engine fuel consumption, optional parameters such as thermal efficiency, type of fuel and fuel energy density can be set up. Thanks to the significant contribution of the energy recovery system, current F1 engines can break the 50% thermal efficiency barrier on dyno. This value, which has not yet been reached on track, is much higher than a reported 29% efficiency peak that old normally aspirated V8 engines produced before the technical revolution in 2014 (https://www.autosport.com). Gasoline with 47.2 MJ/kg of mass energy density was chosen from among the available options.

Power gets transmitted to the wheels by means of a sequential gearbox (see “Transmission Data” section) and a limited slip differential. The calculation of gear ratios is a particularly sensitive issue, because it involves a lot of variables and heavily affects lap-time performance. The assumptions underlying the gear ratio calculation are the following: gear shifting occurs at the engine speed corresponding to maximum power (≈ 12000 rpm) and the highest gear ratio must ensure the achievement of the maximum available speed, depending on the considered vehicle.

When the maximum power available at the wheel is equal to the total power load, the vehicle reaches its constant maximum speed (Equation 2).

$$P_{wheel}^{MAX} = P_{load}^{v_{MAX}}$$

Equation 2: Power balance at the wheel

The power available at the wheel is not equal to the engine power, because of the losses through the driveline: the transmission efficiency was estimated at 0.95 (Equation 3).

$$P_{wheel}^{MAX} = P_{eng}^{MAX} \cdot \eta_{tr}$$

Equation 3: Calculation of the power available at the wheel

As reported by Genta (2000) and Innocenti (2012), the power load comprises a series of elements, such as aerodynamic drag and rolling resistance (Equation 4).

$$P_{load}^{V\_MAX} = [mg(f_0 \cos\alpha + \sin\alpha)]v_{MAX} + \left[mgK\cos\alpha + \frac{1}{2}\rho(SCx - SCzf_0)\right]{v_{MAX}}^3 - \frac{1}{2}\rho KSCz{v_{MAX}}^5$$

Equation 4: Calculation of the power load

Table 42 summarizes the parameters required to evaluate the power at wheel and the power load. By means of a simple iterative calculation, it is possible to find the speed that satisfies Equation 2: this value is the maximum speed that the vehicle can achieve. The high-downforce configuration does not exceed the maximum speed of 307 km/h, while medium and low-downforce layouts reach 325 and 348 km/h, respectively. These values are realistic, but it should be recalled that real F1 cars make use of the Drag Reduction System (DRS) for the purpose of increasing top speed under special conditions.

When maximum speed becomes known, it is possible to calculate the highest gear ratio (8th gear), as illustrated by Equation 5.

Max speed calculation	*Symbol*	*Value*
Vehicle mass	m	750/833 kg
Gravitational acceleration	g	9.81 m/s^2
1st Rolling resistance coefficient (static)	f_0	0.025
2nd Rolling resistance coefficient	K	0.0000065 s^2/m^2
Road gradient	α	0 rad
Drag coefficient	Cx	LD: 1.08; MD: 1.34; HD: 1.61
Lift coefficient	Cz	LD: -3.63; MD: -4.35; HD: -5.16
Frontal area of the vehicle	S	1 m^2
Air density	ρ	1.225 kg/m^3
Tire radius	R	0.33 m
Transmission efficiency	η_{tr}	0.95
Engine speed @ P_{max}	$\omega_{eng}^{P_{MAX}}$	12000 rpm = 1256.637 rad/s
Maximum engine power	P_{eng}^{MAX}	1011 hp = 743589 W

Table 42: Parameters for the calculation of the highest gear ratio

$$\tau_8 = \frac{\omega_{INPUT}}{\omega_{OUTPUT}} = \frac{\omega_{eng}^{P_{MAX}}}{v_{MAX}} R$$

Equation 5: Calculation of the 8th gear ratio

The spacing between the other gears (from 1st to 7th) was decided on the basis of the information provided by Valentini (2008). Table 43 shows an example of gear ratio spacing, in the case of high-downforce vehicle with a light fuel load. The other drive ratios, such as the differential ratio and the primary shaft ratio, were incorporated into the gear coefficients.

The last section of the vehicle setup offers the user the chance to easily add or subtract power, drag and downforce, lateral and longitudinal friction coefficients, by means of scaling factors (Table 44). The grip factor is particularly important because it evidences how tire and track conditions influence the choice of the best aerodynamic layout and hence the final lap-time performance. Two grip factors were taken into account: 100% and 90%: in the former case, tires perform at their best, whereas, in the latter case, they lose 10% of grip, probably due to dirty track, low temperatures or normal wear.

Once a track is selected and downloaded from the ©OptimumG website database, the lap-time simulation is ready to run.

Gear	*Gear Ratio*
8th	4.8615
7th	5.1532
6th	5.9262
5th	6.8744
4th	7.7681
3rd	8.8556
2nd	11.9551
1st	15.5416

Table 43: Vehicle setup – Transmission Data – example of high-downforce vehicle (m = 750 kg)

Scaling Factors	*Value*
Power Factor	100%
Aero Factor	100%
Grip Factor	90%; 100%

Table 44: Vehicle setup – Scaling Factors

9.3 Results and Discussion

9.3.1 Lap-Time Comparison

Eighteen tracks used during the most recent FIA F1 World Championships were chosen to test the following aerodynamic configurations: low, medium and high downforce. Two vehicle weights were taken into account (750 kg and 833 kg), in order to simulate both qualifying run and full race. At last, two different grip conditions (90% and 100%) were considered, for better understanding the relation between tyres behaviour and aerodynamic performance. All the investigated parameters are summarized in Table 45.

Simulation pattern	*Value*
Track	18 F1 tracks
Aerodynamic Configuration	F1UR4LD; F1UR4MD; F1UR4HD
Vehicle mass	750kg (qualifying run); 833 kg (full race)
Grip Factor	90%; 100%

Table 45: Investigated parameters

The first simulation set involves the vehicles with light fuel load (m = 750 kg) and optimal grip (100%). The related results are collected in Table 46. Lap-times are expressed in seconds (s) and the best performance on every circuit is highlighted in green.

It is evident that the F1UR4HD layout is the best choice for most of the considered tracks. On the one hand, since F1 engines provide a huge amount of power, induced drag is an acceptable side effect when downforce helps to transfer all that power to the ground. In other words, it is very often that performance is "grip limited" rather than "power limited". On the other hand, most of current tracks were modified or built ex-novo, limiting straight length and top speed for safety reasons.

The Monza circuit is the only racetrack where efficiency is still clearly the predominant performance factor: in fact, the F1UR4LD configuration allows to consistently improve the lap-time achieved by medium and high-downforce layouts (-0.7 and -2.4 s, respectively).

	Austin USA	*Montreal CANADA*	*Spa BELGIUM*	*Monte-Carlo MONACO*	*Barcelona SPAIN*	*Sakhir BAHRAIN*
F1UR4LD	98.8	73.3	108.1	77.9	83.7	91.8
F1UR4MD	98.0	72.7	108.6	76.7	83.3	91.3
F1UR4HD	97.5	72.5	108.5	75.6	82.8	90.6

	São Paulo BRASIL	*Monza ITALY*	*Melbourne AUSTRALIA*	*Budapest HUNGARY*	*Istanbul TURKEY*	*Marina Bay SINGAPORE*
F1UR4LD	73.4	81.1	85.3	80.8	88.8	98.9
F1UR4MD	72.3	81.8	85.0	79.9	88.4	97.6
F1UR4HD	72.2	83.5	84.3	78.8	87.4	96.1

	Spielberg AUSTRIA	*Sepang MALAYSIA*	*Shanghai CHINA*	*Silverstone UK*	*Suzuka JAPAN*	*Yas Marina ABU DHABI*
F1UR4LD	69.0	95.7	98.4	90.5	93.6	102.8
F1UR4MD	68.3	95.3	97.9	89.3	93.0	102.2
F1UR4HD	68.4	94.4	97.7	89.0	93.4	101.4

Table 46: Lap-time simulation results – m = 750 kg, grip factor = 100%

Also the Spa circuit requires a low downforce setup, but the advantages over medium and high-downforce layouts are not conspicuous: the three calculated lap-times are within half a second of each other because this track is characterized by both long straights and medium/high speed corners, where downforce is pretty important for reaching high values of lateral acceleration.

The choice of the best setup is not a trivial matter in some other circuits, such as São Paulo, where medium and high-downforce vehicle lap-times are more or less the same (±0.1s): this track is characterized by a pretty long straight section and a combination of medium-speed S-corners (http://www.formula1-dictionary.net), where aerodynamic balance is more important than reaching high values of downforce (https://www.racefans.net).

Tracks like Istanbul and Sepang, despite the presence of a couple of long straights, require a high-downforce setup, because they are also characterised by multi-apex corners and hairpins. Suzuka is a very comprehensive track, because very high-speed corners coexist with significant sections spent at full-throttle: for this reason, a compromise solution consisting of medium-downforce setup is needed. Silverstone is, in some respects, like Suzuka, but in this case the choice of high-downforce setup is driven by the presence of a slow understeering corners (https://www.racefans.net).

In general, the optimum downforce level for street circuits is high; however, some issues must be clarified in detail. Montreal, for example, is characterized by a very long straight, a critical hairpin and a lot of chicanes where downforce is important but not decisive: in this case, medium and high-downforce configurations provide more or less the same performance. Melbourne is quite similar to Montreal, but the average cornering speed increases with the increase of the corner radii: in this context, the high-downforce setup gives more benefits than the medium-downforce one.

At last, tracks such as Monaco and Singapore require the highest possible downforce level: despite the average cornering speed is not very high, maximum effort is made in increasing tire grip during braking ad acceleration in tight and bumpy corners, characterized by slippery and dirty asphalt. Budapest is not a street circuit, but its layout reminds of a karting track: for this reason the level of required downforce is very high.

Table 47 collects the results of the second simulation set: the mass of the vehicle is increased up to 833 kg, because of the fuel load, while tire grip is still optimal. With higher mass, the vehicle is subjected to higher centrifugal forces during cornering: as a consequence, in the same tire conditions, the cornering speed decreases.

The simulation results put in evidence that, in general, a heavier vehicle needs higher downforce for achieving the best lap-time. Only racing in Monza still requires beyond any doubt the low-downforce setup; the Spa lap-time calculations say that medium-downforce setup is becoming a viable option. The best choice for Suzuka and Spielberg is no longer the medium-downforce layout: indeed, the high-downforce configuration guarantees slightly better lap-time performance.

	Austin USA	*Montreal CANADA*	*Spa BELGIUM*	*Monte-Carlo MONACO*	*Barcelona SPAIN*	*Sakhir BAHRAIN*
F1UR4LD	101.3	75.1	110.8	79.4	85.8	93.8
F1UR4MD	100.4	74.6	111.0	78.5	85.2	93.5
F1UR4HD	100.0	74.3	111.4	77.3	85.1	93.1

	São Paulo BRASIL	*Monza ITALY*	*Melbourne AUSTRALIA*	*Budapest HUNGARY*	*Istanbul TURKEY*	*Marina Bay SINGAPORE*
F1UR4LD	75.4	82.9	87.4	83.0	90.9	101.3
F1UR4MD	74.2	83.6	87.2	82.0	90.7	100.1
F1UR4HD	73.9	84.9	87.0	81.3	90.2	98.9

	Spielberg AUSTRIA	*Sepang MALAYSIA*	*Shanghai CHINA*	*Silverstone UK*	*Suzuka JAPAN*	*Yas Marina ABU DHABI*
F1UR4LD	70.8	98.0	100.7	93.4	96.7	105.1
F1UR4MD	70.3	97.7	100.1	92.3	95.5	104.6
F1UR4HD	69.9	97.4	100.0	91.7	95.4	104.1

Table 47: Lap-time simulation results – m = 833 kg, grip factor = 100%

A decrease in tire grip has the same effect as increasing the vehicle weight (Table 48): now low and medium downforce configurations provide identical lap-times at Spa racetrack. The simultaneous increase in vehicle weight and decrease in tire grip (Table 49) consolidates the above described trend for Spa, establishing a clear advantage of medium-downforce layout over the low-downforce one, whereas the best option for Monza remains the low-downforce setup. Only in full wet condition, which involves a heavy grip reduction (-40%) and hence a lap-time worsening of about 20 s, the low-downforce setup is no longer adequate for reaching the best performance on Monza race track: in this case, higher downforce is essential to guarantee acceptable levels of grip during traction and braking.

In addition to lap-time calculation, OptimumLap provides qualitative and graphical results, in order to illustrate the dynamic behaviour of the tested vehicles. In the following paragraphs all the aerodynamic configurations (LD, MD and HD) are compared in critical sections of the most remarkable F1 tracks. Light fuel load (m = 750 kg) and maximum grip (grip factor = 100%) were considered for the following analysis.

	Austin *USA*	*Montreal* *CANADA*	*Spa* *BELGIUM*	*Monte-Carlo* *MONACO*	*Barcelona* *SPAIN*	*Sakhir* *BAHRAIN*
F1UR4LD	103.0	76.1	112.0	81.4	87.3	95.2
F1UR4MD	101.9	75.4	112.0	80.3	86.6	94.8
F1UR4HD	101.3	74.8	112.3	78.8	86.4	94.0

	São Paulo *BRASIL*	*Monza* *ITALY*	*Melbourne* *AUSTRALIA*	*Budapest* *HUNGARY*	*Istanbul* *TURKEY*	*Marina Bay* *SINGAPORE*
F1UR4LD	76.4	83.5	88.1	84.2	91.8	103.3
F1UR4MD	75.1	84.1	87.9	83.0	91.5	101.8
F1UR4HD	74.6	85.4	87.6	82.3	91.0	100.4

	Spielberg *AUSTRIA*	*Sepang* *MALAYSIA*	*Shanghai* *CHINA*	*Silverstone* *UK*	*Suzuka* *JAPAN*	*Yas Marina* *ABU DHABI*
F1UR4LD	71.7	99.4	102.1	94.3	98.1	106.8
F1UR4MD	71.0	99.0	101.5	93.0	96.6	106.1
F1UR4HD	70.4	98.5	101.2	92.3	96.3	105.4

Table 48: Lap-time simulation results – m = 750 kg, grip factor = 90%

	Austin *USA*	*Montreal* *CANADA*	*Spa* *BELGIUM*	*Monte-Carlo* *MONACO*	*Barcelona* *SPAIN*	*Sakhir* *BAHRAIN*
F1UR4LD	105.4	77.8	115.7	82.9	89.4	97.4
F1UR4MD	104.5	77.3	114.7	82.0	88.6	97.0
F1UR4HD	103.8	76.7	115.3	80.9	88.3	96.7

	São Paulo *BRASIL*	*Monza* *ITALY*	*Melbourne* *AUSTRALIA*	*Budapest* *HUNGARY*	*Istanbul* *TURKEY*	*Marina Bay* *SINGAPORE*
F1UR4LD	78.2	85.3	90.4	86.4	94.0	105.7
F1UR4MD	77.7	86.0	90.1	85.2	93.7	104.3
F1UR4HD	76.6	86.9	90.0	84.5	93.6	103.2

	Spielberg *AUSTRIA*	*Sepang* *MALAYSIA*	*Shanghai* *CHINA*	*Silverstone* *UK*	*Suzuka* *JAPAN*	*Yas Marina* *ABU DHABI*
F1UR4LD	73.4	101.9	104.4	96.7	100.8	109.3
F1UR4MD	73.0	101.2	103.8	96.3	99.8	108.3
F1UR4HD	72.5	101.1	103.5	94.8	98.8	108.0

Table 49: Lap-time simulation results – m = 833 kg, grip factor = 90%

9.3.2 Post-Processing of the Results

Figure 97 shows the map of the Monte Carlo circuit: Saint Devote is a 90-degree tight corner usually taken in 1st or 2nd gear (Smith, 1995), located immediately at the end of the start/finish straight.

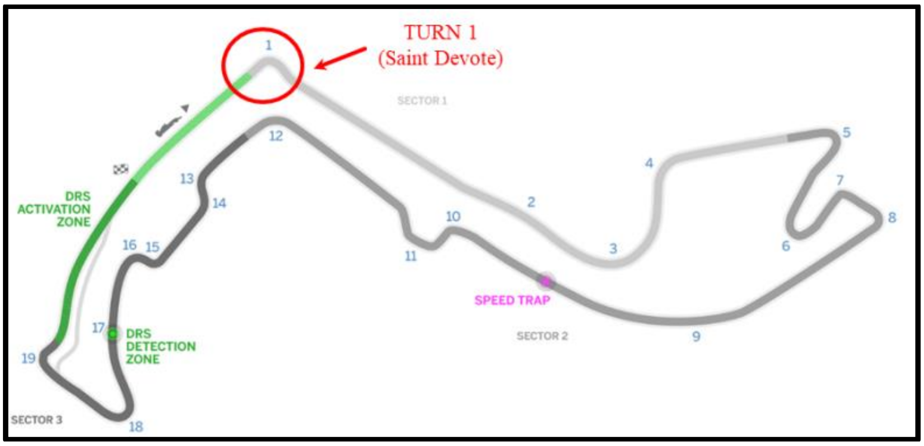

Figure 97: Monte Carlo track map

As illustrated in Figure 98, lateral acceleration and speed of the three vehicles are essentially the same when cornering: the drivers are subject to scarcely relevant lateral forces (≈ 2.5 g), because the low cornering speed (≈ 100 km/h) is dictated by the narrow roadside. At this velocity, the vertical load generated by the vehicle is not able to significantly affect the lateral g-force: indeed, the most relevant differences between the aerodynamic configurations are the brake percentage and the consequent longitudinal acceleration on corner entry. The high-downforce layout allows the driver to brake later and hence exploit more fully the high speed reached at the end of the start/finish straight. The differences in top speed just before the braking point are not very relevant: in fact, the LD and MD layouts cannot express their full potential, because of the short length of the upstream straight. To sum up, in this corner the advantages given by the high-downforce configuration are mainly connected to more effective braking: the transient phase between throttle and braking generates a negative longitudinal acceleration of about 58 m/s^2 (≈ 5.9 g).

Silverstone circuit represents another category of track (Figure 99): the required downforce is still high, but the dynamic behaviour of the vehicle is very different in comparison with Monte Carlo. Turn 1 (Abbey) is the first portion of the track under analysis: this right-hand corner, located at the end of the start/finish straight, is characterized by some interesting features, as illustrated in Figure 100. Medium (MD) and high-downforce (HD) vehicles, unlike the low-downforce (LD) one, can take the curve without braking: the driver only needs to lift off the throttle on corner entry. Moreover, the medium-downforce car shows higher cornering speed and lateral acceleration than the high-downforce one, because its downforce level is high enough to take the curve safely, but, at the same time, it does not penalize top speed. The high-downforce vehicle would be able to reach the same or even higher cornering speed, but its low efficiency does not permit this. Focusing on the acceleration map, one can see that a 2017 F1 car can develop a lateral force of about 5.3 g: these results are in line with the predicted values provided by motorsport.com (2016).

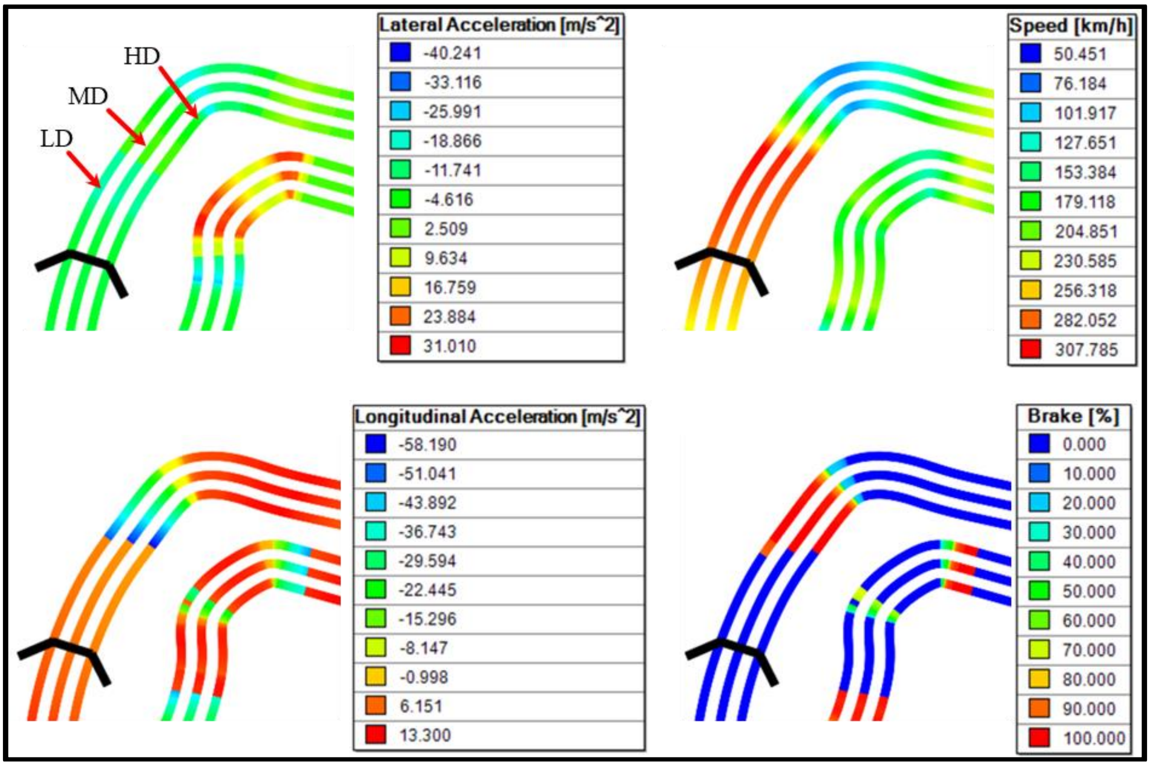

Figure 98: Lateral acceleration, speed, longitudinal acceleration and percentage brake at Turn 1 (Saint Devote, Monte Carlo) – low (LD), medium (MD) and high-downforce (HD) aerodynamic configurations

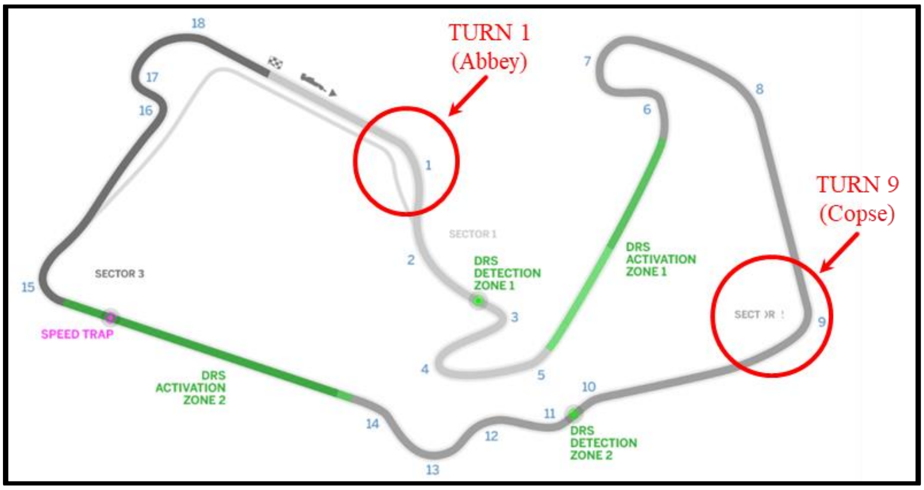

Figure 99: Silverstone track map

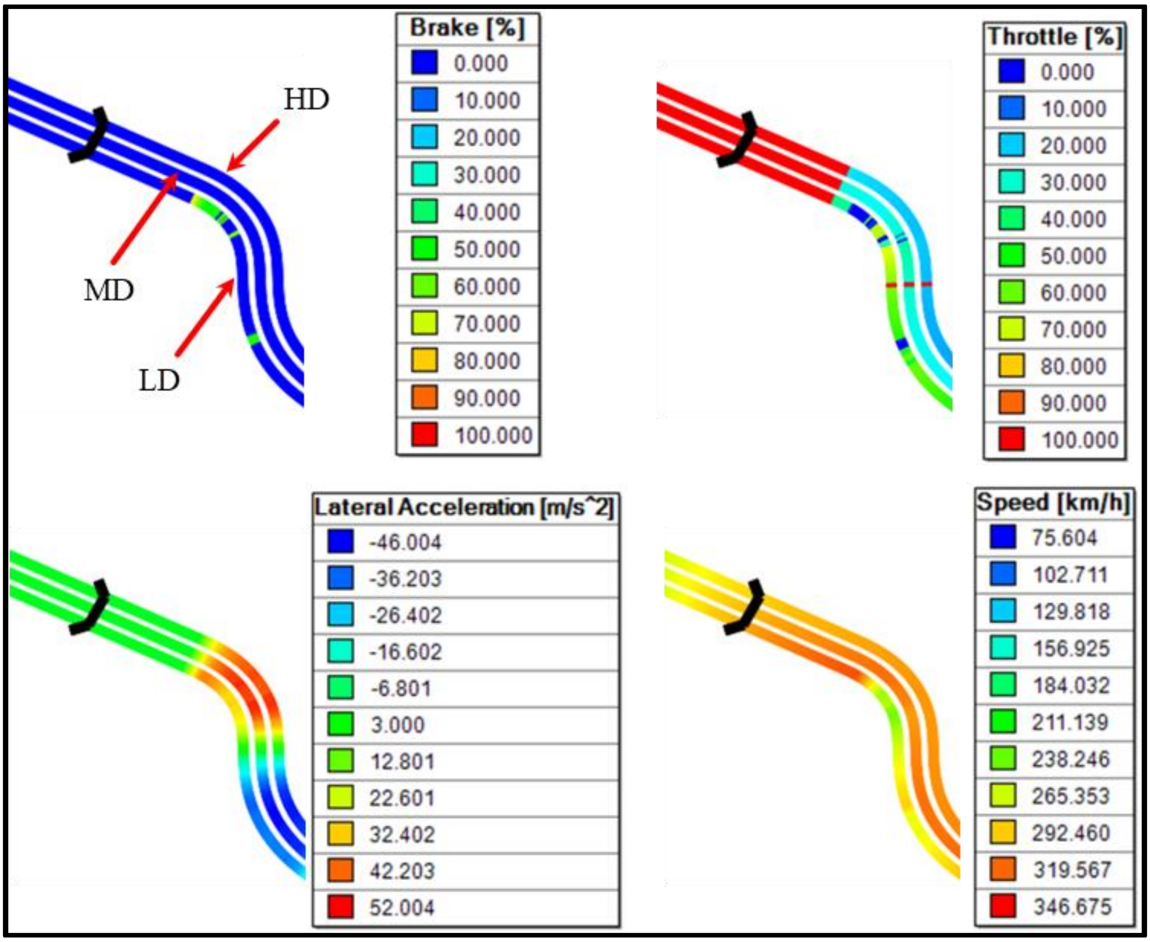

Figure 100: Percentage brake, percentage throttle, lateral acceleration and speed at Turn 1 (Abbey, Silverstone) - low (LD), medium (MD) and high-downforce (HD) aerodynamic configurations

Another turn worth of attention is the Copse (Figure 99), a quasi-90-degree right-hand corner characterized by a large track width. As shown in Figure 101, the high-downforce configuration (HD) is by far the best option. It can entry the corner without braking and reach very high lateral g-forces (≈ 5.3 g). Even if aerodynamic drag penalizes top speed at the end of the upstream straight, the cornering velocity achieved by the high-downforce car is considerably higher than the others and remains almost constant along the entire bend, leading to a quicker corner exit.

One of the most challenging tracks in the world is the Suzuka International Racing Course, whose map is illustrated in Figure 102. The 1^{st} sector of the track is characterized by the so called First Curve, at the end of the start/finish straight, and the famous S-curves. Results in Figure 103 show that all three vehicles are able to reach their respective top speed at the end of the main straight but, as usual, the high-downforce configuration ensures later braking point and very high lateral acceleration at the corner entry (≈ 5.5 g). Conversely, the analysed aerodynamic configurations are equivalent in the S-curves, where the optimum racing line strongly depends on mechanical responsiveness and aerodynamic balance rather than pure downforce.

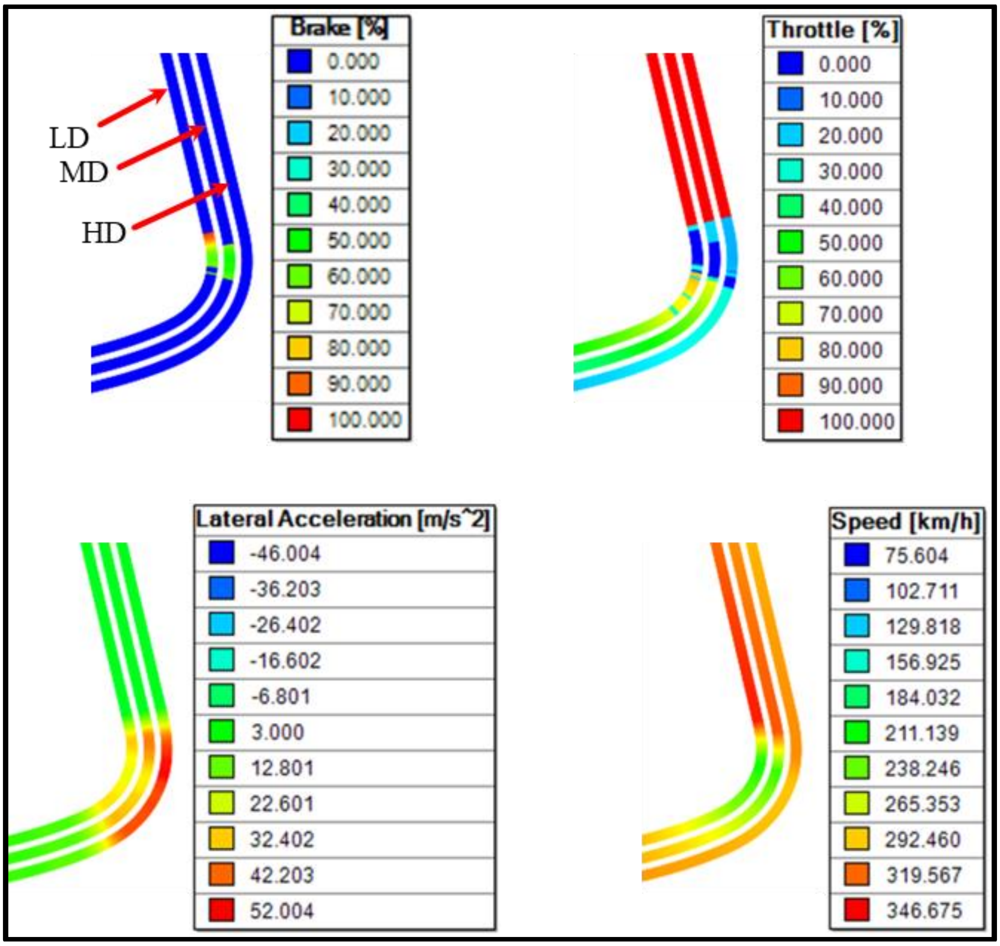

Figure 101: Percentage brake, percentage throttle, lateral acceleration and speed at Turn 9 (Copse, Silverstone) - low (LD), medium (MD) and high-downforce (HD) aerodynamic configurations

Figure 104 illustrates the behaviour of the three vehicles in the infamous 130R Curve, which owes its name to the 130 m corner radius of the original layout. Located in the 3rd sector of the track, it underwent some changes over the last years in order to improve safety, but, despite that, drivers are still able to take the corner flat-out, thanks to the grip improvement of current F1 cars. Since the corner radius is very wide, the low downforce setup (LD) seems to guarantee the grip required to take the corner at maximum speed or so. The lateral acceleration provided by the low-downforce vehicle exceeds 5.3 g: in this case, in contrast to the Copse curve at Silverstone, the high lateral g-force is the result of high velocity rather than low corner radius.

The last track considered is the legendary Spa-Francorchamps Circuit, characterised by one of the longest full-throttle sections in F1 and a very difficult 2nd sector, with medium-speed corners and chicanes (Figure 105).

Two peculiar corners are analysed: Pouhon (Turn 10-11) and Blanchimont (Turn 17). The former is a double apex left-hander, with a very difficult entry phase (https://driver61.com), due to the downhill approach. Since the cornering speed abundantly exceeds 200 km/h, the steering movements need to be very smooth, in order not to unsettle the car. The latter is a very high-speed left-hand turn, located in the 3rd sector of the track, just before the last chicane. A wrong approach to this corner could lead to massive crashes, as already happened in the past. Its layout resembles the above mentioned 130R curve, at Suzuka: in fact, as happens in Japan, F1 drivers are able to take the Blanchimont corner flat-out.

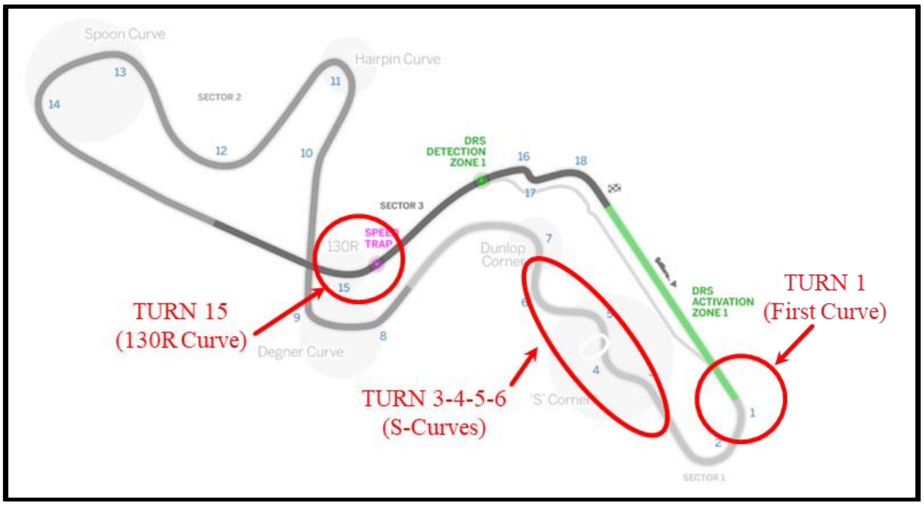

Figure 102: Suzuka track map

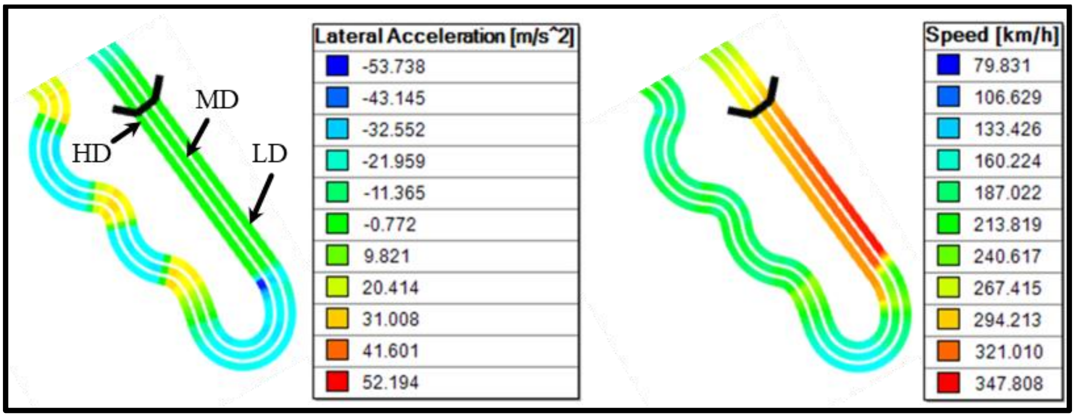

Figure 103: Lateral acceleration and speed at Turn 1 and S-Curves (Suzuka circuit) - low (LD), medium (MD) and high-downforce (HD) aerodynamic configurations

Approaching the Pouhon entry, the high-downforce vehicle (HD) can brake later and lighter than the other aerodynamic configurations. Moreover, a more aggressive corner entry leads to higher lateral acceleration, as witnessed by Figure 106. In the middle of the turn and at the corner exiting, the performance of the three vehicles are almost equivalent, both in terms of speed and lateral acceleration. Concerning the Blanchimont, the low-downforce layout is by far the best option, since its downforce level is high enough to guarantee an adequate lateral grip.

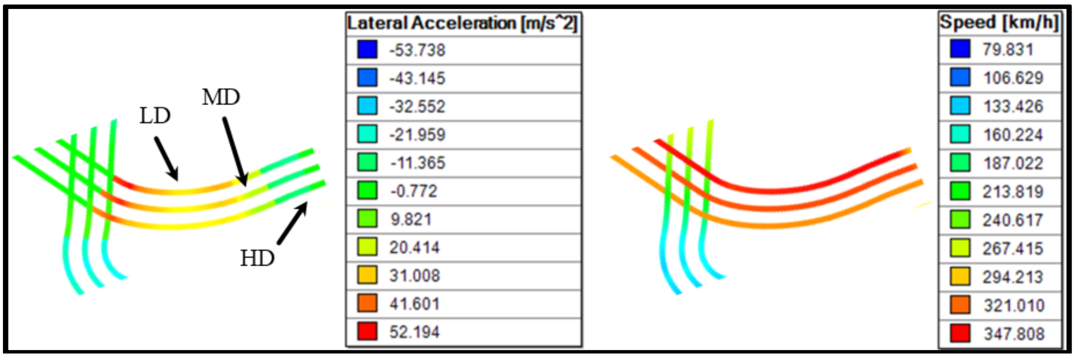

Figure 104: Lateral acceleration and speed at Turn 15 (130R, Suzuka circuit) - low (LD), medium (MD) and high-downforce (HD) aerodynamic configurations

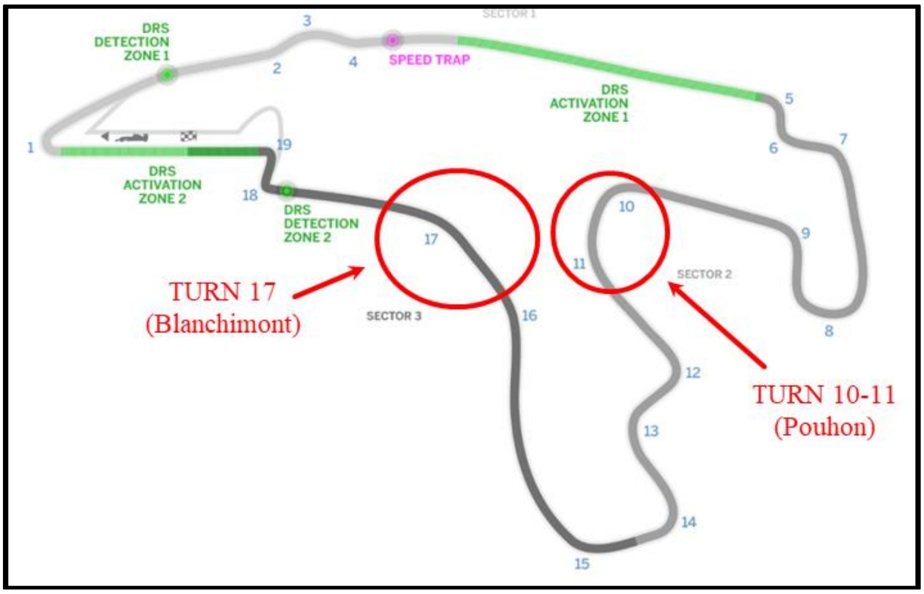

Figure 105: Spa-Francorchamps track map

As already highlighted by previous analyses, the most challenging circuits of the world present very contrasting features, depending on the considered section: this makes it very difficult to properly identify the best aerodynamic setup, resulting from the most effective trade-off between the split-times of different sectors.

9.4 Conclusions

The results of the lap-time simulations carried out by means of the free-software OptimumLap clearly evidence the importance of adjusting the aerodynamic design in accordance with the considered track: a wrong choice in aerodynamic configuration could lead to significant performance losses. A rough estimation of the optimum downforce level for a given track is the preliminary procedure which leads to a fine tuning of the vehicle setup, both from mechanical and aerodynamic point of view.

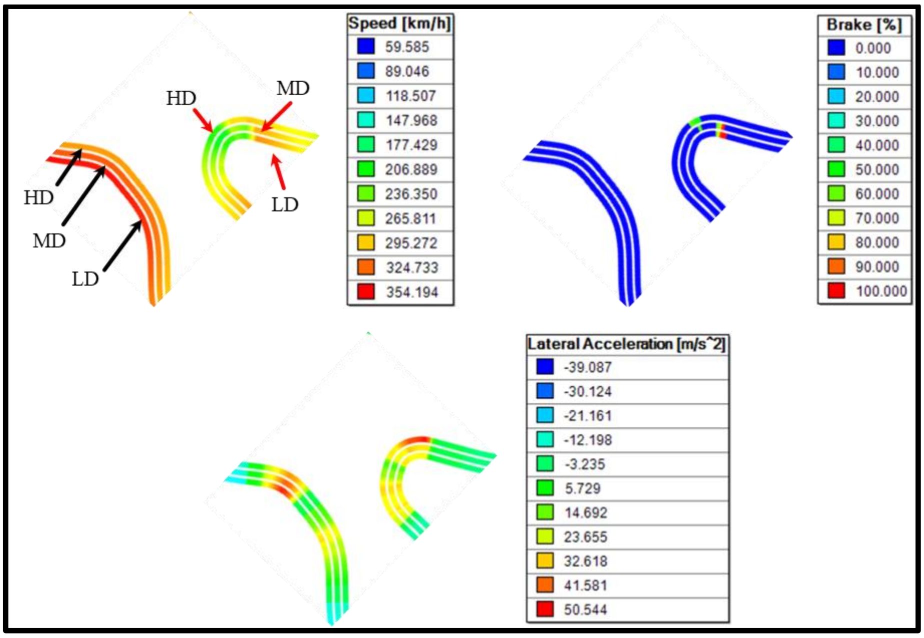

Figure 106: Speed, percentage brake and lateral acceleration at Pouhon (Turn 10-11) and Blanchimont (Turn 17) (Spa-Francorchamps) - low (LD), medium (MD) and high-downforce (HD) aerodynamic configurations

Most of the modern F1 circuits require medium or high levels of downforce, in light of the huge amount of engine power available and the layout of modern tracks, which tend to penalise top speed: in other words, performance of current F1 cars are “grip limited” rather than “power limited”. However, within the same track, different downforce requirements may be present, making it difficult to find the best compromise setup. The choice of the most suitable aerodynamic configuration also depends upon other factors: typically, heavier vehicles and lower tire grip require higher levels of downforce.

References

Bearman, P. W., De Beer, D., Hamidy, E., & Harvey, J. K. (1988) ‘The effect of a moving floor on wind-tunnel simulation of road vehicles’, SAE Technical Paper, No. 880245.

Benzing, E. (2012) ‘Wings – Their design and application to racing cars’, Giorgio Nada Editore, ISBN-13: 978-8879115391.

Carr, G. W. (1988) ‘A comparison of the ground-plane-suction and moving-belt ground-representation techniques’, SAE Technical Paper, No. 880249.

Casiraghi, C. (2010) ‘Race Car Aerodynamics’, Seminar at KTH – Royal Institute of Technology, Stockholm, Sweden.

Chandra, S., Lee, A., Gorrell, S., & Jensen, C., G. (2011) ‘CFD Analysis of PACE Formula-1 Car’, Brigham Young University, Provo, USA.

Cogotti, A. (1998) ‘A parametric study on the ground effect of a simplified car model’, SAE Technical Paper, No. 980031.

Cooper, K. R., Bertenyi, T., Dutil, G., Syms, J., & Sovran, G. (1998) ‘The aerodynamic performance of automotive underbody diffusers’, SAE paper 980030.

Cooperman, A., McLennan, A., Baker, J., van Dam, C., & Chow, R. (2010) ‘Aerodynamic performance of thick blunt trailing edge airfoils’, 28th AIAA Applied Aerodynamics Conference (p. 4228).

Correia, J. (2016) ‘The influence of external disturbances on the aerodynamic performance of a wing in ground effect’, Unpublished Ph. D. Thesis, Cranfield University, Cranfield, Great Britain.

Dominy, R., G. (1990) ‘The influence of slipstreaming on the performance of a Gran Prix racing car’, IMechE Journal of Automobile Engineering.

Dominy, R., & G., Ryan, A., Sims-Williams, D. (2000) ‘The aerodynamic stability of a Le Mans prototype race car under off-design pitch conditions’, SAE Technical Paper No. 2000-01-0872.

Genta, G. (2000) ‘Meccanica dell’autoveicolo’, Levrotto & Bella Editrice, Torino, ISBN: 88-8218-042-5.

George, A. R. (1981) ‘Aerodynamic effects of shape, camber, pitch, and ground proximity on idealized ground-vehicle bodies’, Journal of Fluids Engineering, Vol. 103(4), pp. 631 - 637.

George, A. R., & Donis, J. E. (1983, December) ‘Flow patterns, pressures, and forces on the underside of idealized ground effect vehicles’, Paper presented at the ASME Fluids Engineering Division Symposium on Aerodynamics of Transportation-II, Vol. 7, pp. 69-79.

Guilmineau, E. (2008) ‘Computational study of flow around a simplified car body’, Journal of wind engineering and industrial aerodynamics, 96(6-7), 1207-1217.

Haller, G. (2005) ‘An objective definition of a vortex’, J. Fluid Mech., Vol. 525, pp.1–26, doi:10.1017/S0022112004002526.

Hanna R. K. (2012) ‘CFD in Sport-a Retrospective; 1992-2012’, Procedia Engineering 34, pp. 622-627.

Howell, J., & Hickman, D. (1997) ‘The influence of ground simulation on the aerodynamics of a simple car model’, SAE Technical Paper, No. 970134.

Hucho, W., H., Ahmed, S., R., Bayer, B., E., Callister, J., R., Deußen, N., Emmelmann, H., J., Flegl, H., George, A., R., Gilhaus, A., Götz, H., Großmann, H., Hoffmann, R., Hummel, D., Kohl, W., R., Mayr, G., Necati, G., A., Piatek, R., Schlenz, D., Schmitt, J., Sebbeße, W., Singer, N., & Steinberg, P. (1998) ‘Aerodynamics of Road Vehicles – From Fluid Mechanics to Vehicle Engineering’, 4th Edition, SAE International, ISBN 0-7680-0029-7.

Innocenti, C. (2012) ‘Appunti del corso di Meccanica del Veicolo’, Università degli Studi di Modena e Reggio Emilia.

Islam, M., Decker, F., de Villiers, E., Jackson, A., Gines, J., Grahs, T., Gitt-Gehrke, A., & Comas i Font, J. (2009) ‘Application of detached-eddy simulation for automotive aerodynamics development’, No. 2009-01-0333, SAE Technical Paper.

Jowsey, L., & Passmore, M. (2010) ‘Experimental study of multiple-channel automotive underbody diffusers’, Proceedings of the Institution of Mechanical Engineers, Part D: Journal of Automobile Engineering, Vol. 224 No. 7, pp. 865-879.

Kuya, Y., Takeda, K., Zhang, X., Beeton, S., & Pandaleon, T. (2009) ‘Flow physics of a race car wing with vortex generators in ground effect’, Journal of Fluids Engineering, 131(12), 121103.

Larsson, T. (2009) ‘Formula One Aerodynamics - BMW Sauber F1.09 – Fundamentally Different, EASC 2009’, 4th European Automotive Simulation Conference, Munich, Germany.

Larsson, T., Sato, T., & Ullbrand, B. (2005) ‘Supercomputing in F1 - Unlocking the Power of CFD’, 2nd European Automotive CFD Conference, Frankfurt, Germany.

Linfield, K., W., & Mudry, R., G. (2008) ‘Pros and Cons of CFD and Physical Flow Modelling’, White Paper by Airflow Sciences Corporation ©.

Lombardi, G., Maganzi, M., Cannizzo, F., & Cardile, E. (2009) ‘Use of the CFD for the Aerodynamic Optimization of the Car Shape: Problems and Application’, 4th European Automotive Simulation Conference, Munich, Germany.

Lopez, C. (2001) ‘Going Faster – Mastering the Art of Race Driving’, Bentley Publishers, ISBN 0-8376-0226-2.

Mahon, S., Zhang, X. and Gage, C. (2004) ‘The evolution of edge vortices underneath a diffuser equipped bluff body’, 1-10, Unpublished Paper, Southampton University, Southampton, Great Britain.

McBeath, S. (2006) ‘Competition Car aerodynamics – A Practical Handbook’, Haynes Publishing, ISBN 1-84425-230-2.

McBeath, S. (2017) ‘Follow the leader’, Racecar Engineering.

Menter, F. R. (1994) ‘Two-equation eddy-viscosity turbulence models for engineering applications’, AIAA journal, 32(8), 1598-1605.

Milliken, W. F., & Milliken D. L. (1995) ‘Race Car Vehicle Dynamics’, SAE International, ISBN 1-56091-526-9.

Nebenführ, B. (2010) ‘OpenFOAM: A tool for predicting automotive relevant flow fields’. Unpublished Master’s Thesis in Automotive Engineering, Chalmers University of Technology, Goteborg, Sweden.

Newbon, J., Sims-Williams, D., & Dominy, R., G. (2017) ‘Aerodynamic Analysis of Grand Prix Cars Operating in Wake Flows’, SAE Int. J. Passeng. Cars - Mech. Syst. / Volume 10, Issue 1.

OpenFOAM Guide [online] https://openfoamwiki.net/index.php/OpenFOAM_guide/ (Accessed 11 July 2017)

OptimumLap v1.4 User guide (provided by ©OptimumG 2018)

Perry, R., L., & Marshall, D. D. (2008) ‘An Evaluation of Proposed Formula 1 Aerodynamic Regulations Changes Using Computational Fluid Dynamics’, 26th AIAA Applied Aerodynamics Conference.

Piola, G., & Somerfield, M. (2016) ‘Video analysis: How different will F1 cars be in 2017’, motorsport.com.

Ravelli, U., & Savini, M. (2018) ‘Aerodynamic investigation of blunt and slender bodies in ground effect using OpenFOAM’, International Journal of Aerodynamics, Volume 7, Issue 1, DOI: 10.1504/IJAD.2020.107161.

Ravelli, U., & Savini, M. (2018) ‘Aerodynamic Simulation of a 2017 F1 Car with Open-Source CFD Code’, Journal of Traffic and Transportation Engineering, 6, 155-163, DOI: 10.17265/2328-2142/2018.04.001.

Romberg, G. F., Chianese, F., & Lajoie, R. G. (1971) ‘Aerodynamics of race cars in drafting and passing situations’, SAE Technical Paper No. 710213.

SCAI Cineca. [online] http://www.hpc.cineca.it/content/hardware/ (Accessed 10 July 2017)

Smith, B. (1995) ‘Formula 1 Pocket Annual’, Words on Sport Limited, ISBN 978-1-898351-25-2.

Somerfield, M., & Piola, G. (2017) ‘Retro F1 tech: The ground effect era’, motorsport.com.

Spalart, P.R. and Allmaras, S.R. (1992) ‘A one equation turbulence model for aerodynamic flows’, Paper presented at the 30th Aerospace Sciences Meeting and Exhibit, p. 439, January.

Valentini, G. (2008) ‘Formula 1 e Prototipi – Come progettare le vetture da competizione’, Giorgio Nada Editore, ISBN: 978-88-7911-402-8.

Wright, P. G. (1982) ‘The influence of aerodynamics on the design of Formula One racing cars’, International Journal of Vehicle Design, 3(4), 383-397.

Zaya, J. (2013) ‘Aerodynamic Optimization of Ground Vehicles with the Use of Fluent’s Adjoint Solver’, Master’s Thesis in the Master Programme Automotive Engineering, Chalmers University of Technology, Goteborg, Sweden.

Zerihan, J., & Zhang, X. (2000) ‘Aerodynamics of a single element wing in ground effect’, Journal of Aircraft, 37(6), 1058-1064.

Zerihan, J., & Zhang, X. (2001) ‘Aerodynamics of Gurney flaps on a wing in ground effect’, AIAA journal, 39(5), 772-780.

Zhang, X., Senior, A., & Ruhrmann, A. (2004) ‘Vortices behind a bluff body with an upswept aft section in ground effect’, International Journal of Heat and Fluid Flow, 25(1), 1-9.

Zhang, X., Toet, W., & Zerihan J. (2006) ‘Ground effect aerodynamics of race cars’, Applied Mechanics Reviews, 59.1, 33-49.

Zhang, X., & Zerihan, J. (2002) ‘Turbulent Wake behind a Single Element Wing in Ground Effect’, transition, 1(1.5), 1-6.

Zhang, X., & Zerihan, J. (2003) ‘Aerodynamics of a double-element wing in ground effect’, AIAA journal, 41(6), 1007-1016.

Zhang, X., Zerihan, J., Ruhrmann, A., & Deviese, M. (2002, July) ‘Tip vortices generated by a wing in ground effect’. Paper presented at the 11th International Symposium on Applications of Laser Techniques to Fluid Mechanics.

https://www.autosport.com/f1/news/131772/mercedes-engine-hits-remarkable-dyno-target

https://driver61.com/resources/circuit-guide/spa/

https://www.f1analisitecnica.com/2014/04/simulazione-di-una-power-unit-di.html

https://www.fia.com/regulations

https://www.formula1.com/en/championship/inside-f1/rules-regs/Power_Unit_and_ERS.html

http://www.formula1-dictionary.net/plank_or_skidblock.html

http://formula1-dictionary.net/rake_angle.html http://www.formula1-dictionary.net/set_up_track_specific.html

http://hpwizard.com/tire-friction-coefficient.html

https://www.motorsport.com/f1/news/analysis-5-5g-revelation-prompts-fresh-concerns-about-2017-f1-cars-682998/682998/

https://www.motorsportmagazine.com/archive/article/july-1999/51/slick-tyre

http://www.optimumg.com/

https://www.openfoam.com/documentation/cpp-guide/html/guide-fos-field-q.html

https://www.racefans.net/f1-information/going-to-a-race/autodromo-jose-carlos-pace-carlos-pace-interlagos-circuit-information/

https://www.racefans.net/f1-information/going-to-a-race/silverstone-circuit-information/

https://www.thisisf1.com/2018/01/24/2018-ferrari-f1-knocking-the-door-of-1000hp-engine/

List of figures

List of tables